Searching for Dark Matter with the Cryogenic Dark Matter Search Experiment

Dissertation

zur
Erlangung der naturwissenschaftlichen Doktorwürde
(Dr. sc. nat.)

vorgelegt der
Mathematisch-naturwissenschaftlichen Fakultät
der
Universität Zürich

von
Sebastian Arrenberg
aus
Deutschland

Promotionskomitee

Prof. Dr. Laura Baudis (Vorsitz)
Dr. Marc Schumann
Dr. Tobias Bruch

Zürich 2011

Zusammenfassung

Es gibt eine überwältigende Fülle von Hinweisen dafür, dass lediglich ∼5% der Gesamtenergie des Universums aus gewöhnlicher baryonischer Materie besteht aus der wiederum die Planeten, Sterne und wir selbst aufgebaut sind. Die restlichen ∼95% können noch weiter in Dunkle Energie (∼72%), die das gesamte Universum durchdringt und von der man annimmt, dass sie für seine beobachtete beschleunigte Expansion verantwortlich ist, und Dunkle Materie (∼23%), deren gravitative Kraft dieser Expansion entgegenwirkt, aufgeteilt werden. Diese Zusammensetzung basiert auf Beobachtungen aus unterschiedlichen Richtungen, wie umfangreichen Analysen der kosmologischen Hintergrundstrahlung, von Gravitationslinseneffekten oder von Rotationskurven von Galaxien. Obwohl beide, Dunkle Energie und Dunkle Materie, noch nicht direkt gemessen wurden, hat sich eine Klasse von Dunkle Materie Teilchen, genannt "Weakly Interacting Massive Particles" (WIMPs), also schwach wechselwirkende massive Teilchen, als führender Kandidat innerhalb der Forschungsgemeinschaft, die sich mit Dunkler Materie beschäftigt, etabliert. Die Existenz von WIMPs geht aus vielen Erweiterungen des Standardmodels der Teilchenphysik wie "Supersymmetry" oder "Universal Extra Dimensions" hervor. Es wird vermutet, dass WIMPs in einem Dunklen Halo von Galaxien wie der Milchstrasse verteilt sind, was eine direkte Detektion der Dunkle Materie Teilchen in Detektoren auf der Erde möglich macht.

Das "Cryogenic Dark Matter Search" (CDMS) Experiment ist dafür ausgelegt nach WIMPs zu suchen, die mit den Atomkernen in geeigneten Halbleiterdetektoren aus Germanium und Silizium elastisch streuen. Die Charakteristiken dieses Signals sorgen dafür, dass dieser Ansatz ein äußerst herausforderndes Unterfangen darstellt: Die erwartete Rate ist extrem klein, es könnte ein gemessenens Ereignis pro Tonne und Jahr oder sogar noch weniger sein, und das Signal im "Standard" WIMP Szenario wird bei sehr geringen Rückstossenergien in der Größenordnung von 1 keV oder 10 keV erwartet. Daher ist eine niedrige Energieschwelle und eine hervorragende Reduzierung des Hintergrundes zwingend erforderlich. Aus diesem Grund werden die CDMS Detektoren im Bereich von Millikelvin Temperaturen betrieben, und sie sind von einer umfangreichen Abschirmung umgeben. Eine weitere wichtige Eigenschaft im Hinblick auf die Reduzierung des Hintergrundes ist die Messung zweier Signale: Ionisation und Phononen. Eine Kombination dieser Signaturen ermöglicht eine leistungsstarke Diskriminierung des Hintergrundes.

Diese Doktorarbeit beinhaltet eine detaillierte Beschreibung einer WIMP-Analyse basierend auf Daten von CDMS mit besonderem Schwerpunkt auf Techniken im Zusammenhang mit der Reduktion des Hintergrundes. Nach einer allgemeinen Betrachtung des erwarteten Signals, wobei Abweichungen von dem "Standard" WIMP Modell bezüglich der Geschwindigkeitsverteilung der WIMPs und des Streuprozesses selbst diskutiert werden, werden Grenzen von Experimenten, die auf direkter Detektion von WIMPs basieren, für ein spezielles WIMP Modell, das auf der vorgeschlagenen Existenz von zusätzlichen Raumdimensionen basiert, vorgestellt. Danach werden der Aufbau und die Detektoren

sowie der Hintergrund des CDMS Experimentes diskutiert und die WIMP-Analyse wird erläutert. Die Beschränkungen auf spin-unabhängige Wechselwirkungen, die aus dieser Analyse hervorgingen, waren zum Zeitpunkt der Publikation die führenden oberen Grenzen für WIMP Massen oberhalb von $\sim$44 GeV/c^2. Danach wird ein Szenario diskutiert, bei dem die WIMPs inelastisch mit den Atomkernen streuen. In diesem Zusammenhang wird die auf "cuts" basierende Technik, die üblicherweise von der CDMS Kollaboration für die Reduzierung des Hintergrundes verwendet wird, präsentiert. Schließlich wird noch ein anderer Ansatz basierend auf einer "Maximum-Likelihood Methode" entwickelt, der insbesondere im Hinblick auf eine mögliche Detektion von WIMPs sehr vielversprechend ist.

Abstract

There is overwhelming evidence that only around ∼5% of the energy content of the universe is made up of ordinary baryonic matter, the building blocks of planets, stars and ourselves. The remaining ∼95% can be further divided into dark energy (∼72%), which permeates the whole universe and which ought to be responsible for its observed accelerated expansion, and into dark matter (∼23%), whose gravitational force thwarts this expansion. This recipe is based on observations from different directions like extensive analyses of the cosmic microwave background, gravitational-lensing effects or rotation curves of galaxies. While both, dark energy and dark matter, have not been detected directly, a class of dark matter particles referred to as Weakly Interacting Massive Particles (WIMPs) has been established as the leading candidate among the dark matter community. The existence of WIMPs naturally arises from many extensions of the standard particle physics model like Supersymmetry or Universal Extra Dimensions. WIMPs should be distributed in dark halos of galaxies such as the Milky Way, enabling the direct detection of the dark matter particles via their interactions in terrestrial detectors.

The Cryogenic Dark Matter Search (CDMS) experiment is designed to search for WIMPs elastically scattering off the target nuclei in dedicated semiconductor detectors made of germanium and silicon. The regime of the signal makes this approach an extremely challenging endeavour: The expected event rate is extremely small, it could be one event/ton/year or even less, and the signal in the "standard" WIMP scenario is expected at very low recoil energies of order 1 keV or 10 keV. Therefore, a low energy threshold and exceptional background rejection capabilities are mandatory. Thus, CDMS detectors are operated at Millikelvin temperatures and surrounded by substantial shielding. Another important feature regarding background rejection is the measurement of two signals: ionization and phonons. A combination of these signatures allows a powerful discrimination against background.

This thesis provides a detailed description of a WIMP-search analysis based on CDMS data with a special emphasis on background rejection techniques. After general considerations regarding the expected signal, where deviations from the "standard" WIMP model, regarding the WIMP-velocity distribution and the scattering process itself, are discussed, constraints from direct detection experiments on a particular WIMP model, based on the suggested existence of extra space dimensions, are presented. Subsequently, the CDMS setup and detectors as well as the background are discussed and the WIMP search analysis is elucidated. The limits on spin-independent interactions emerging from this analysis were the leading constraints for WIMP masses above ∼44 GeV/c^2 at the time, when the results were published. Subsequently, constraints on a scenario, where the WIMPs scatter inelastically off the target nuclei, are discussed. In this context the background-rejection technique typically used by CDMS, which is based on "cuts", is presented in great detail. Finally, a different approach based on a maximum-likelihood method is developed, which is very promising particularly regarding a possible WIMP detection.

Contents

List of Figures

List of Tables

Preface

The CDMS experiment is a collaborative effort of numerous scientists and technicians. Therefore, this thesis contains work carried out by other members of the collaboration. In the following I give a brief summary of my own work.

I derived the correct formulae for the differential event rate expected from WIMP-nucleon interactions given in (2.21). As discussed in chapter 2.1.4, this is an update to the expression given in the standard reference [1]. Even though I cannot exclude that it was published before I calculated it, the correct formulae were not known to anybody in the CDMS collaboration. This correction was of crucial importance for the inelastic dark matter analysis as emphasized in chapter 2.1.4. The inelastic dark matter model predicts a signal at tens of keV recoil energy, while the "standard" WIMP model yields a signal at low energies.

I analyzed the velocity distributions from dark matter simulations (chapter 2.1). The results indicated that the standard Maxwell-Boltzmann distribution is a valid approximation to the WIMP-velocity distribution unless a model, which is extremely sensitive to the high-velocity tail, is considered.

Regarding spin-independent interactions I investigated advanced parametrizations of the nuclear form factors (chapter 2.2.1). It was shown that the simple formulae, given in the standard reference [1], are a good approximation and that it is not necessary to use more advanced approaches.

Considering the inelastic dark matter model I calculated the regions in parameter space preferred by the DAMA/LIBRA data based on the observed annual modulation (chapter 2.3).

I was a lead author of a (non-CDMS) publication constraining the parameter space of WIMPs arising from the proposed existence of Universal Extra Dimensions [2]. I determined all direct detection constraints which are presented in chapter 3 of this thesis. It was demonstrated that direct and collider searches are highly complementary and that the expected sensitivity of the next-generation direct detection experiments should be sufficient to cover the whole parameter space for the Kaluza-Klein photon. These prospects are very promising for dark matter searches in the near future.

I significantly contributed to the "standard" WIMP analysis. Regarding the lifetime-reducing cuts, discussed in chapter 6.4.1, I was responsible for a cut based on the time elapsed after the last LED flash, which was one of the two criteria defined in order to preserve proper neutralization of the detectors (chapter 6.4.1.6). Besides, I defined the cut removing data series with a bad resolution regarding various fit parameters from the pulse

reconstruction (chapter 6.4.1.7). Considering the energy-independent efficiency-reducing cuts, discussed in chapter 6.4.2, I was responsible for a cut rejecting events with negative phonon energies (chapter 6.4.2.2). Regarding the energy-dependent efficiency-reducing cuts, discussed in chapter 6.4.3, I defined the ionization goodness-of-fit cut (chapter 6.4.3.1) and the ionization threshold cut (chapter 6.4.3.4). I also performed noise stability studies of the phonon and charge channels as shown exemplarily in Fig. 6.12. Besides, I determined the correct detector masses given in Table 6.2 and subsequently the exposure of the analysis given in (6.3). T. Bruch and I evaluated the final signal efficiency as discussed in chapter 6.4.4. I contributed to the likelihood analysis of the two obtained WIMP candidates, presented in chapter 6.7, by performing the calculations of the method denoted KDE-3D with signal and background distributions based on kernel density estimates. Finally, I calculated constraints from this analysis on the inelastic dark matter interpretation of the DAMA/LIBRA results, which are shown in Fig. 6.26. The results from the standard analysis (including Fig. 6.26) were published in Science [3]. The constraints on the spin-independent WIMP-nucleon cross section were the world-leading upper limit on WIMP masses above $\sim$44 GeV/c^2 at the time of publication.

I performed the whole dedicated inelastic dark matter analysis documented in chapter 7 (except for the determination of the neutron background), which was optimized for the signal expected in this scenario. For this analysis, I investigated all energy-dependent efficiency-reducing cuts discussed in chapter 6.4.3 in the context of the standard analysis. Besides, I used an advanced algorithm to improve the experimental sensitivity by optimization of the tradeoff between the primary background (surface events) and the expected signal (chapter 7.1). I also performed a Bayesian leakage estimate to calculate the final background (chapter 7.2). Subsequently, I applied all selection criteria to the WIMP-search data (chapter 7.3) and determined constraints on the inelastic dark matter interpretation of the DAMA/LIBRA results (7.4). The analysis was published in a paper which I produced [4].

I developed a new analysis framework based on a maximum-likelihood method (chapter 8), which is expected to be more powerful than the standard cut-based method currently used by most direct detection experiments. All aspects of this approach originate from my work. It includes modelling of multidimensional distributions with kernel density estimates (chapter 8.1), treatment of various nuisance parameters (chapters 8.2 and 8.3) and a comparison of Frequentist (chapter 8.2) and Bayesian (chapter 8.3) methods. A Frequentist Feldman and Cousins approach is outlined in chapter 8.4. The analysis framework has been developed (applying the "original" CDMS data) and is foreseen to be applied to the CDMS data, which was recently reprocessed using an improved pulse fitting algorithm (chapter 6.6). A publication can be expected at the beginning of 2012. Depending on the final performance, this new approach has the potential to become the primary analysis method for future CDMS analyses. The method is of particular importance regarding a possible detection of dark matter and the characterization of its properties like the WIMP mass and WIMP-nucleon cross section.

Moreover, I was a member of the small CDMS subgroup which performed the first CDMS axion search [5]. My main responsibilities were the evaluation of cuts at low energies

and systematic studies to verify the significance of the obtained results. Besides, I contributed to the axion rate calculation. I worked on all of these topics in collaboration with T. Bruch. A competetive upper limit (in the theoretically preferred axion mass region) on the Primakov coupling was determined for solar axions. It benefited from the first precise measurement of the crystal plane orientations in this type of experiment. This analysis showed that the CDMS experiment was capable of exploring new physics beyond the scope of WIMP dark matter, which it was actually designed for. Such extensions are an important asset for every experiment. A discussion of this analysis was omitted due to time constraints, but an extensive description can be found in the thesis of T. Bruch [6].

Chapter 1

Dark matter - Properties and Evidence

Extensive analyses from many different directions led to the recipe of the universe shown in Fig. 1.1. It is remarkable that the origin of only ∼5% of the whole energy content of the universe is well established. As indicated in the diagram, current observations indicate a division of the remaining ∼95% into dark energy (∼72%) and dark matter (∼23%). Dark energy is believed to be responsible for the accelerated expansion of the universe. Very little is known about its properties, so that theoretical models based on a cosmological constant, as introduced by Einstein, or dynamic scalar fields like quintessence [7] are highly speculative. Gravitational effects, caused by dark matter, have been observed on various different scales from single galaxies over galaxy clusters to the universe as a whole. Even though knowledge of most of its properties is still lacking, too, theoretical predictions regarding its origin can be based on a more "solid" grounding. For example, there exist dark matter candidates in extensions of the standard model of particle physics, that satisfy basic requirements like being weakly interacting, stable and "cold", and additionally yield

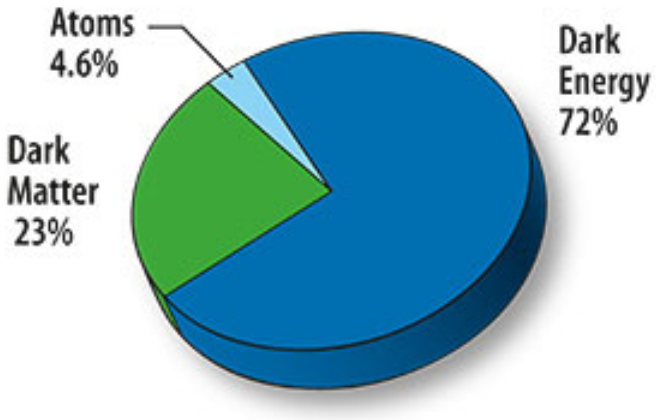

Figure 1.1: Recipe of the universe based on cosmological measurements. Figure taken from [8].

the observed relic density necessary to account for the dark matter in the universe. A direct discovery and specification of the dark energy and dark matter is one of the most important issues in modern science.

Since this thesis is concerned with dark matter, its aforementioned properties are briefly discussed, and some evidence for its existence are presented in the following.

1.1 Properties of dark matter

The three most important properties of dark matter were already mentioned in the introductory paragraph. In the following it is assumed that dark matter consists of one or more new elementary particles, which is the currently preferred picture.

First of all, dark matter must be weakly interacting, since otherwise it would have been already detected directly. In particular, this means that dark matter does not interact electromagnetically or via the strong force.

Besides, it must be stable, which means that its lifetime must be longer than the age of the universe, since otherwise it would have been already decayed. This feature is evident from the fact that its influences can be measured today.

Moreover, dark matter has to be "cold", i.e. non-relativistic during the times the galaxies were formed. Relativistic ("hot") dark matter would have washed out the growing fluctuations, which finally culminated in the current structure of the universe.

A class of dark matter candidates, referred to as Weakly Interacting Massive Particles (WIMPs) [9], has been established as the leading candidate among the dark matter community. The existence of WIMPs naturally arises from many extensions of the standard particle physics model like Supersymmetry (SUSY) [10] or Universal Extra Dimensions (UED) [11][1]. The remainder of this thesis is concerned with the *direct detection* of WIMPs.

1.2 Evidence for the existence of dark matter

Probably the most convincing evidence for the existence of dark matter arises from the analysis of the rotation curves of spiral galaxies, so plots of a galaxy's rotation velocity v vs. the distance from its center r. Theoretical predictions for v can be calculated based on simple Newtonian dynamics:

$$\frac{v^2}{r} = \frac{G\,M(r)}{r^2}\,, \tag{1.1}$$

where G denotes the gravitational constant and $M(r)$ is the mass within a given radius r:

$$M(r) = 4\pi \int_0^r \mathrm{d}r'\, r'^2 \rho(r')\,, \tag{1.2}$$

[1] WIMP candidates from UEDs are discussed in more detail in chapter 3.

where it is assumed that the mass density ρ solely depends on r, which is a reasonable approximation for spiral galaxies. Solving for v directly yields

$$v(r) = \sqrt{\frac{G\,M(r)}{r}}\,. \tag{1.3}$$

It could be expected that the velocity of objects outside the visible part of a galaxy should decrease according to $v(r) \propto \frac{1}{\sqrt{r}}$. However, as shown for example in Fig. 1.2, the rotation curves are nearly constant at a large distance from the galactic center, which implies the existence of a dark matter halo yielding $M(r) \propto r$ and thus $\rho(r) \propto \frac{1}{r^2}$ for large radii. It is evident that the visible mass is not sufficient to explain this density profile.

A direct empirical proof for the existence of dark matter was obtained by the investigation of the Bullet Cluster 1E 0657–558 [13], which is a pair of two colliding galaxy clusters. The collision was analyzed based on observations of X-rays, which trace the visible baryonic matter, and applying techniques based on gravitational lensing [14], which map the distribution of the total mass dominated by dark matter. A clear separation between the visible matter and the dark matter is apparent from Fig. 1.3. The dark matter halos passed through each other, while the baryonic matter decelerated and dragged behind the dark matter due to electromagnetic interactions.

The last evidence for the recipe of the universe (shown in Fig. 1.1), that is about to be discussed, arises from studies of the cosmic microwave background, which is the primordial blackbody radiation (at 2.73 K) left over from the Big Bang. Although this radiation

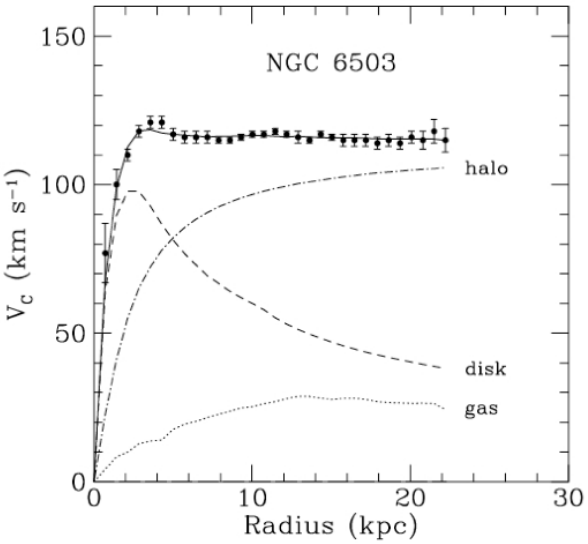

Figure 1.2: Measured rotation curve of the spiral galaxy NGC 6503 (solid). The dashed and the dotted curves represent the contributions from the visible part of the galaxy and the gas within the galaxy respectively. The dashed-dotted curve denotes the inferred contribution from the dark matter halo, which is needed to explain the observation. Figure taken from [12].

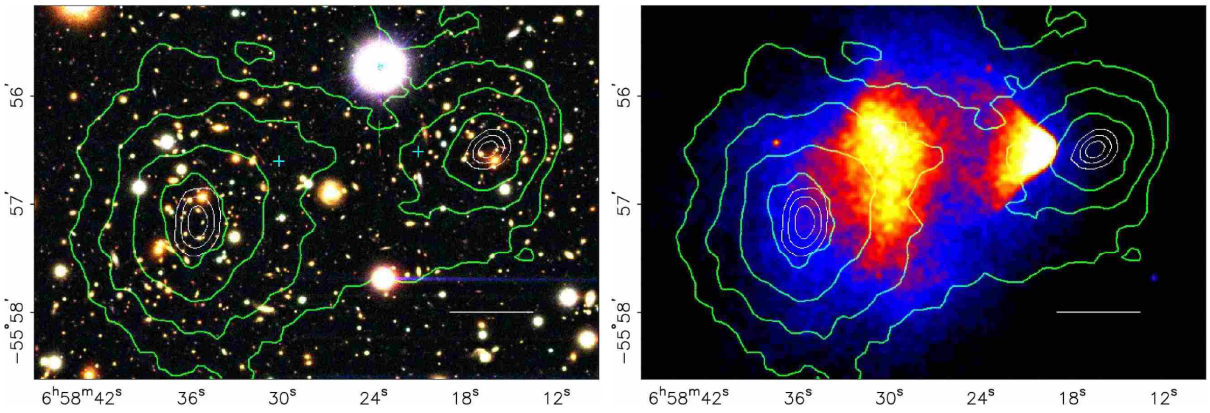

Figure 1.3: Images of the Bullet Cluster. An optical photograph from the Hubble Space Telescope is shown on the left and an X-ray image from the Chandra X-Ray Observatory is shown on the right. The overlaid lines represent contours of the mass distribution, obtained from an analysis based on gravitational lensing. Figure taken from [13].

is quite uniform and isotropic, precise measurements show that there are anisotropies regarding the polarization and temperature. The latter, which are illustrated in Fig 1.4, are of order 10 μK. The corresponding power spectrum (shown in Fig. 1.5), which was measured by the Wilkinson Microwave Anisotropy Probe (WMAP), can be used to extract detailed information regarding the content of the universe. In fact, the recipe shown in Fig. 1.1 is mainly based on this analysis. It should be noted that these measurements also

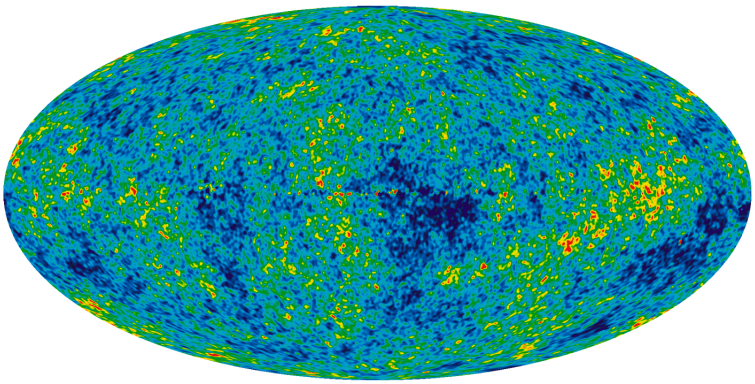

Figure 1.4: Temperature anisotropies of the cosmic microwave background from WMAP. The color-code represents temperature fluctuations of order 10 μK. Figure taken from [8].

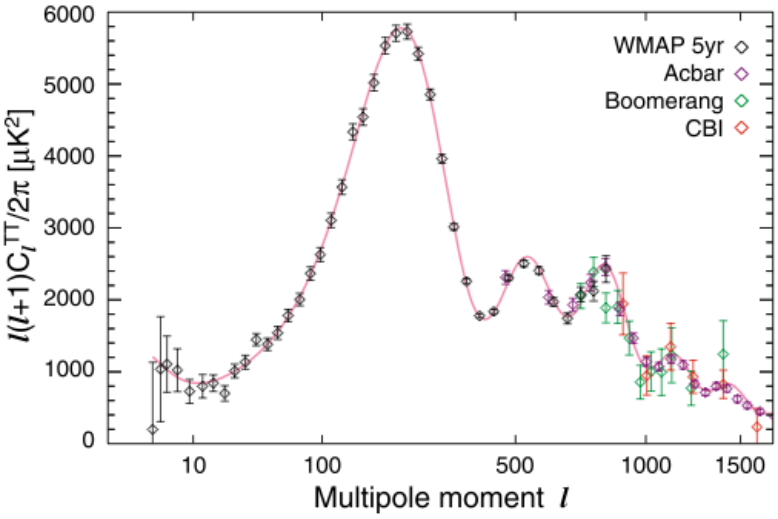

Figure 1.5: Power spectrum of the temperature anisotropies of the cosmic microwave background from WMAP. Figure taken from [15].

allow to draw conclusions regarding the curvature of the universe. It turns out that they are perfectly consistent with a flat universe.

Chapter 2

Direct detection of dark matter

As shortly discussed in the previous chapter, there is overwhelming evidence that around $\sim$23% of the energy content of the universe is made up of dark matter. Moreover, it was pointed out that WIMPs are the leading dark matter candidate.

Essentially, there are three ways to detect this new kind of particle: Direct searches, where WIMPs elastically scatter off nuclei in a given target; indirect searches, where the decay products like neutrinos from WIMP annihilation in locations with increased WIMP density are detected; and accelerator experiments like the LHC, where WIMPs should be produced in high-energy collisions of standard model particles. It is indeed important to attack the problem of the missing mass in the universe from different directions, since it has been shown, e.g. in [2] (also summarized in the next chapter) for the case of direct detection and collider constraints on UED, that the different methods are highly complementary in the sense that they are sensitive to different regions in the WIMP parameter space.

The Cryogenic Dark Matter Search (CDMS) experiment was designed to detect WIMPs, which are supposed to be distributed in the Milky Way's dark halo, via their scattering off germanium and silicon nuclei. This chapter discusses the formalism relevant to calculate the expected event rate and the two possible types of interaction. A particular particle physics model (UED) is discussed in the next chapter.

2.1 Event rate calculations for direct detection experiments

The event rate calculation itself is independent of the actual particle physics model. However, it is necessary to make some assumptions regarding the WIMP-velocity distribution. The most important issues considering this formalism are discussed in great detail in [1]. This is the standard reference for the differential rate calculation. However, the derived result is only approximately correct, which is discussed here in some detail. At fist, it is necessary to summarize some ingredients for the event rate calculation.

2.1.1 The Earth velocity

The velocity of the Earth $\vec{v}_E$ has to be parameterized with respect to the stationary dark matter halo. There are three contributions to $\vec{v}_E$: the galactic rotation velocity $\vec{v}_r$, the velocity of the Sun with respect to the galactic disc $\vec{v}_s$ and the velocity of the Earth around the Sun $\vec{v}_{\rm orb}$. Thus, $\vec{v}_E$ is given by

$$\vec{v}_E = \vec{v}_r + \vec{v}_s + \vec{v}_{\rm orb}\,. \tag{2.1}$$

The motion of the Local Standard of Rest is taken to be

$$\vec{v}_r = \begin{pmatrix} 0 \\ 220 \\ 0 \end{pmatrix} \text{km/s}\,, \tag{2.2}$$

according to [16], while

$$\vec{v}_s = \begin{pmatrix} 10.00 \\ 5.25 \\ 7.17 \end{pmatrix} \text{km/s} \tag{2.3}$$

is used for the Sun's peculiar velocity [17]. The time-dependent Earth's orbital velocity relative to the Sun is parameterized as discussed in [1]:

$$\begin{aligned} \vec{v}_{\rm orb} &= 29.79 \cdot \Big(1 - 0.016722 \cdot \sin(\lambda - 13)\Big) \\ &\quad \cdot \begin{pmatrix} \cos(-5.5303) \cdot \sin(\lambda - 266.141) \\ \cos(59.575) \cdot \sin(\lambda + 13.3485) \\ \cos(29.812) \cdot \sin(\lambda - 179.3212) \end{pmatrix} \text{km/s}\,, \end{aligned} \tag{2.4}$$

with the parameter λ given by

$$\begin{aligned} \lambda(n) &= \Big(280.460 + 0.9856474 \cdot n\Big) + 1.915 \cdot \sin\Big(357.528 + 0.9856003 \cdot n\Big) \\ &\quad + 0.020 \cdot \sin\Big(2 \cdot \big(357.528 + 0.9856003 \cdot n\big)\Big)\,, \end{aligned} \tag{2.5}$$

where n denotes the fractional day number with respect to noon (universal time) December 31$^{\rm st}$, 1999. As discussed later on, the time-dependence introduced by $\vec{v}_{\rm orb}$ is of great importance regarding an annual modulation of the expected WIMP signal. The modulation of the mean velocity is about $\pm 6.5\%$.

2.1.2 The WIMP-velocity distribution

The next issue that needs to be discussed is the velocity distribution of the dark matter particles. Two cases are introduced in the following. The first one is the standard assumption of an isothermal and isotropic sphere of an ideal WIMP gas obeying a Maxwell-Boltzmann velocity distribution

$$f(\vec{v}, \vec{v}_E) \propto e^{-\frac{(\vec{v}+\vec{v}_E)^2}{v_0^2}}\,, \tag{2.6}$$

where $\vec{v}$ denotes the velocity of the WIMPs in the rest frame of the Earth and v_0 is the characteristic velocity of the distribution, which is assumed to be equal to the non-zero component of the galactic rotation velocity $\vec{v}_r$ ($v_0 = 220$ km/s). The velocity distribution is limited by the escape velocity of the WIMPs v_{esc} from the galactic halo, which is taken to be $v_{\mathrm{esc}} = 544$ km/s [18]. Taking this cutoff into account, the normalized velocity distribution is given by

$$f(\vec{v}, \vec{v}_E) = \frac{e^{-\frac{(\vec{v}+\vec{v}_E)^2}{v_0^2}}}{\sqrt{\pi}\,\pi\,v_0^3 \left(\mathrm{erf}\left(\frac{v_{\mathrm{esc}}}{v_0}\right) - \frac{2}{\sqrt{\pi}} \frac{v_{\mathrm{esc}}}{v_0} e^{-\frac{v_{\mathrm{esc}}^2}{v_0^2}} \right)}\,, \tag{2.7}$$

where erf denotes the error function.

Since it cannot be expected that the velocity distribution of WIMPs indeed closely follows a Maxwell-Boltzman distribution, it is important to consider other possible shapes. Such analyses have indeed been carried out (see e.g. [19]). They are comparably simple considering isotropic velocity distributions, since, in that case, a one-to-one transformation exists between the velocity distribution and the density profile of the dark halo, which is given by Eddington's formula [20]. However, for the current analysis, the velocity distributions were directly obtained from GHalo [21], a numerical simulation of galactic dark matter structure. A few samples of a ∼1 kpc-radius sphere carved out the simulation's 7–9 kpc shell, which is the appropriate scale, given that the Sun is located at ∼8.5 kpc from the galactic center, were used. Each sample contained ∼10000 particles. An analysis, based on these samples, was performed as a quick cross-check of the validity of the Maxwell-Boltzman approximation. Much more detailed investigations based on dark matter simulations can be found for example in [22] and [23]. As an illustration, Fig. 2.1 shows the velocities of the particles in a particular sample.

In the case of the simulation, the velocity distribution is written as a sum of Dirac's delta functions over the n particles within a given sample:

$$f(\vec{v}, \vec{v}_E) = \frac{1}{n} \sum_{i=1}^{n} \delta\big(\vec{v} - (\vec{v}_i - \vec{v}_E)\big)\,, \tag{2.8}$$

where $\vec{v}_i$ is the velocity of the i^{th} particle in the galactic rest frame. No upper boundary is considered regarding the simulation, since any cutoff related to an escape velocity is intrinsically included in the simulation. Note, that from Fig. 2.1 it can be observed that some of the particles in the simulation have higher velocities than v_{esc} applied to the Maxwell-Boltzmann distribution. A comparison of an example of the velocity distribution from a representative sample (already used for Fig. 2.1) with the Maxwell-Boltzmann distribution is shown in Fig. 2.2. A typical feature is the wider shape of the distribution from the simulation. Thus, the Maxwell-Boltzmann distribution is expected to underestimate the low and high velocity tails of the actual distribution. Moreover, the distributions from the simulations exhibit bumps and dips even though statistics are quite high in the bulk of the distributions, indicating that these are real features within the simulations, which reflect local structures. Similar observations were also reported in [22] and [23].

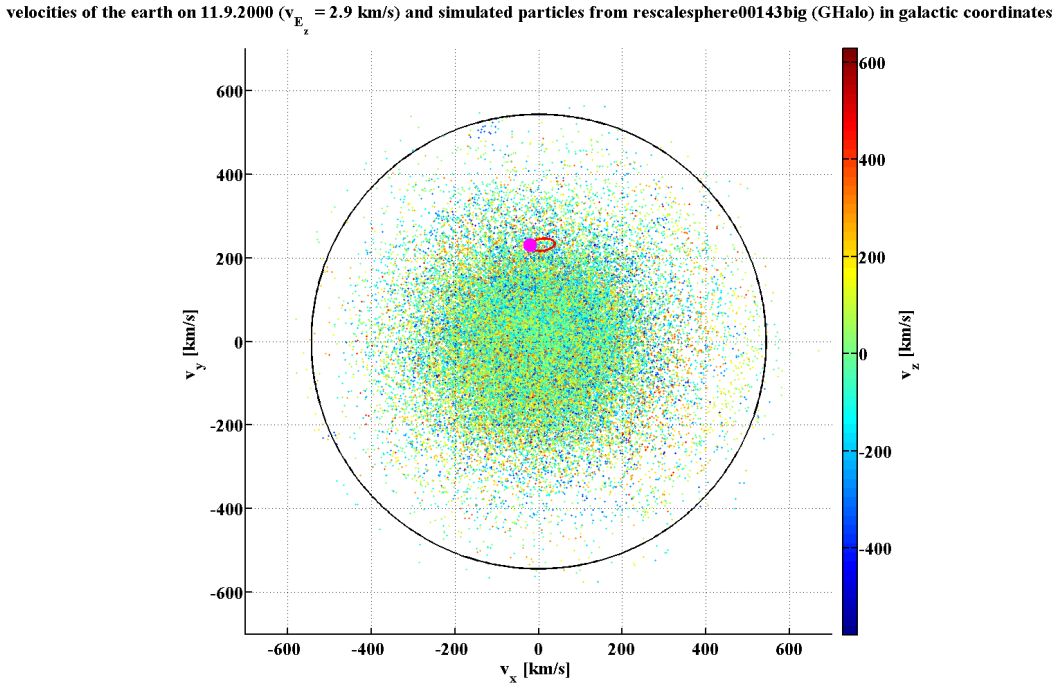

Figure 2.1: Velocities in galactic coordinates of the particles from a sample with 55760 particles of the GHalo simulation projected onto the v_y vs. v_x plane. The color-code denotes the v_z-component. The black circle represents the escape velocity cutoff introduced in the context of the Maxwell-Boltzmann distribution. The red circle represents the movement of the Earth in the velocity space over the course of a year, as discussed in the previous section. The big magenta point marks its velocity at a particular date (11.09.2000).

Before continuing, some shortcomings of the simulations should be mentioned. First, the samples, used for this analysis, were taken from spheres with a quite large radius of $\sim$1 kpc. Actually, it would be desirable to resolve the structure on much smaller scales (sub-pc), but even current state-of-the-art simulations are not capable of achieving such resolutions. Moreover, in particular the central region near the galactic center is difficult to resolve [24]. Note, that the Sun is located comparably close to the center given a virial radius of 200–300 kpc of the Milky Way's dark matter halo. Finally, the particle masses in the simulations are typically of the order of 1000 $m_\odot$, where $m_\odot$ ($= 2.0 \cdot 10^{30}$ kg $= 1.1 \cdot 10^{57}$ GeV/c^2) represents the mass of the Sun, which is many orders of magnitude higher than the typical range of WIMP masses considered as dark matter candidates (10–1000 GeV/c^2). In summary, applying the velocity distributions from dark matter simulations to dark matter direct detection experiments involves extrapolations, whose validity cannot be taken for granted. Nevertheless, it is certainly interesting to investigate the implications of distributions obtained from simulations.

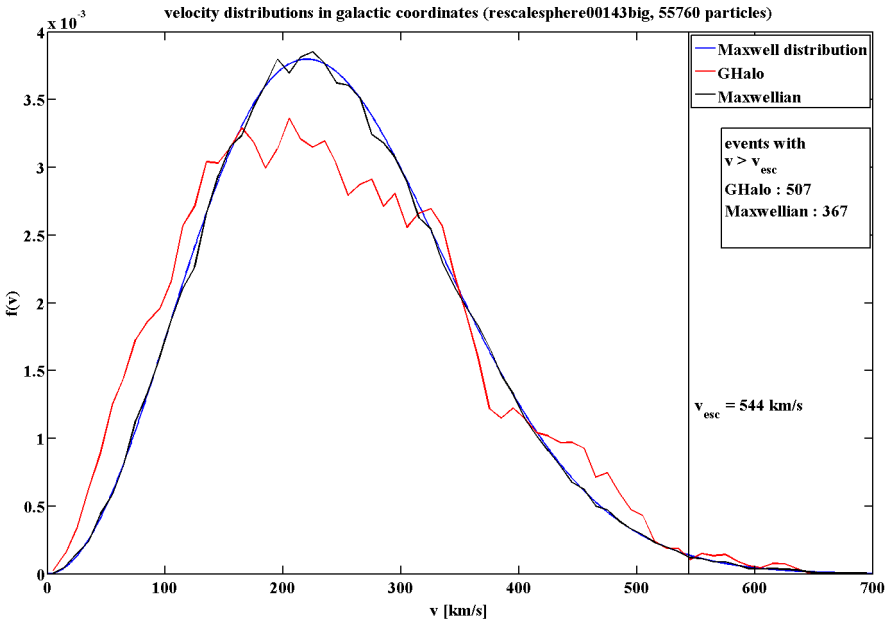

Figure 2.2: Comparison of a velocity distribution in galactic coordinates obtained from a sample with 55760 particles of the GHalo simulation (red) with the standard Maxwell-Boltzmann distribution (blue). The most prominent feature, which is typical for the results obtained from the simulation, is the wider shape. The distribution shown in black is based on a Monte Carlo simulation from the standard distribution with the same number of particles as in in the GHalo sample (55760). It closely follows the original distribution emphasizing the non-maxwellian behaviour of the distribution based on the GHalo sample. Note, that the shown Maxwell-Boltzmann distribution is normalized in the range from 0 km/s to ∞.

2.1.3 WIMP scattering and the inelastic dark matter model

As shown in the previous section, where the velocity distribution of dark matter particles was discussed, WIMPs are expected to have velocities of order 100 km/s. In particular, they are non-relativistic. Thus, the scattering process of WIMPs and the target nuclei can be analyzed applying simple Newtonian mechanics. In the standard scenario, it is assumed that the scattering process is elastic. However, especially for following investigations, it is appropriate to include inelastic dark matter (iDM) scattering in this discussion. The inelastic scenario [25] assumes that WIMPs (χ) can only scatter off baryonic matter (N) by transition into an excited state at a certain energy above the ground state ($\chi\, N \rightarrow \chi^*\, N$), while elastic scattering is forbidden or highly suppressed. Given a particular mass splitting δ between both WIMP states, the scattering process can only occur, if

$$\delta < \frac{1}{2}\,\mu\, v^2\,, \tag{2.9}$$

where μ is the reduced mass of the WIMP-nucleus system

$$\mu = \frac{m_W\, m_N}{m_W + m_N}\,. \tag{2.10}$$

The masses of the WIMP and the target nucleus are denoted m_W and m_N respectively. There is a minimal velocity required to produce recoil energy E:

$$v_{\min} = \frac{1}{\sqrt{2 m_N E}}\left(\frac{m_N E}{\mu} + \delta\right). \tag{2.11}$$

This formula is valid for elastic and inelastic scattering with the former case being equivalent to $\delta = 0$ keV. If E is too small or too large, $v_{\min}$ is above the cutoff imposed by the galactic escape velocity, and the event cannot occur. In the next section important consequences of this model for direct detection experiments are discussed in the context of differential event rates.

2.1.4 Expected event rates

Following the arguments in [1] the differential event rate, which is expressed in terms of counts/kg/day/keV, is given by

$$\frac{\mathrm{d}R}{\mathrm{d}E} = \frac{2\, N_0\, \rho\, \sigma}{r\, A_u\, m_W^2} \iiint_{v_{\min}<v<v_{\max}} \mathrm{d}^3\vec{v}\, \frac{f(\vec{v}, \vec{v}_E)}{v}\,, \tag{2.12}$$

where N_0 is the Avogadro constant and A_u is the atomic mass unit. The local dark matter density is taken to be $\rho = 0.3$ GeV/cm^3, a standard value, which is in good agreement with the results from a recent publication [26]. Moreover, σ denotes the total WIMP-nucleus cross section and r is a kinematic factor defined by

$$r = \frac{4\, m_W\, m_N}{(m_W + m_N)^2}\,. \tag{2.13}$$

Since the result for the evaluation of this integral, assuming a truncated Maxwell-Boltzmann distribution (2.7), given in [1] is not quite correct and until recently nearly all dark matter direct detection collaborations based their analysis on this incorrect result, the integration is discussed here in some detail.

The problems regarding the integration are related to the boundaries of the integral. The lower boundary is given by $v_{\min}$ (2.11), which is obviously independent of the scattering angle. The upper boundary is related to the escape velocity v_{esc}:

$$|\vec{v} + \vec{v}_E| \leq v_{\mathrm{esc}}\,, \tag{2.14}$$

which yields a maximum WIMP velocity

$$v_{\max}(\theta) = \sqrt{v_{\mathrm{esc}}^2 - v_E^2\,(1 - \cos^2\theta)} - v_E \cos\theta\,, \tag{2.15}$$

with θ being the scattering angle in the galactic rest frame.

This situation is illustrated in Fig. 2.3. The norm of the Earth velocity v_E is projected onto the x-axis with the magenta point indicating its value at a particular data (11.09.2000). The thin horizontal black line, which is partly concealed by this point, represents the variation of v_E during the year due to the time dependence of the Earth's orbital motion around the Sun. However, this has no significant impact on the following reasoning. The y-axis points into an arbitrary direction perpendicular to the vector, which points into the direction of v_E. So the figure essentially shows cuts through the velocity space in galactic coordinates putting the norm of the Earth velocity on the x-axis. Thus, the real three-dimensional space is axially symmetric around the x-axis, and the shown circles actually represent three-dimensional spheres. The thick black circle stands for the restriction from v_{esc}, while the thin lines represent v_{min} for elastic scattering ($\delta = 0$ keV) off a ^{73}Ge nucleus for WIMP masses of 15 GeV/c^2 (left) and 100 GeV/c^2 (right) and a few chosen recoil energies as given in the legends. To evaluate the integral correctly it is necessary to integrate over the velocity space from an inner v_{min}-circle (or rather three-dimensional sphere) to the circle (or rather three-dimensional sphere) corresponding to v_{esc}. E.g. for a WIMP mass of 100 GeV/c^2 and a recoil energy of 10 keV the red v_{min}-circle is totally inside the v_{esc}-circle, and thus it is valid to simply integrate from v_{min} to v_{esc} for all possible scattering angles. The formula, given in the standard reference [1], is based on

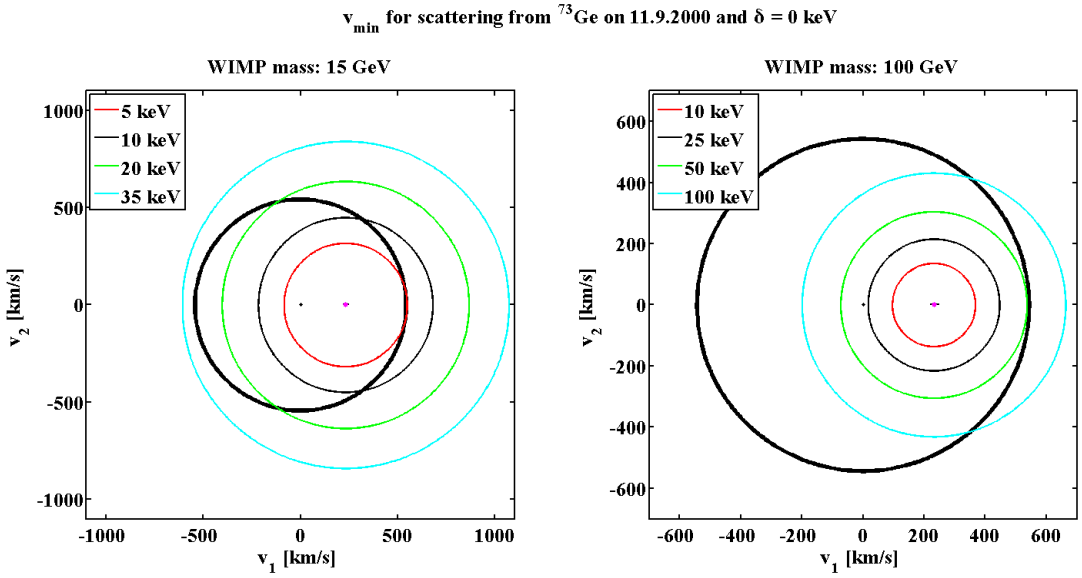

Figure 2.3: Illustration regarding the velocity-space integration to calculate the differential event rate for dark matter direct detection experiments in galactic coordinates. The thick black line represents the cutoff from the galactic escape velocity. The norm of the Earth velocity v_E is projected onto the x-axis with the magenta point indicating its value at a particular data (11.09.2000). The thin lines represent v_{min} assuming elastic scattering ($\delta = 0$ keV) off a ^{73}Ge nucleus for WIMP masses of 15 GeV/c^2 (left) and 100 GeV/c^2 (right) and a few chosen recoil energies as given in the legends. See text for more details.

the assumption that this is always the case, so that $v_{\mathrm{min}} + v_E \leq v_{\mathrm{esc}}$ holds. However, the situation is different e.g. for a WIMP mass of 15 GeV/c^2 and a recoil energy of 35 keV. Here, the cyan v_{min}-circle is totally outside the v_{esc}-circle, and thus the integral should simply be set to zero. Just integrating from v_{min} to v_{esc} leads to a negative differential event rate, which is certainly not correct. Apart from these two simple cases there is also the possibilty that the two circles have points of intersection, which can be seen assuming again a WIMP mass of 15 GeV/c^2 but a recoil energy of 10 keV (thin black circle) for example. Hence, there are three distinct cases which need to be considered:

$$\begin{aligned} 0 &\leq v_{\mathrm{min}} \leq v_{\mathrm{esc}} - v_E \\ v_{\mathrm{esc}} - v_E &\leq v_{\mathrm{min}} \leq v_{\mathrm{esc}} + v_E \\ v_{\mathrm{esc}} + v_E &\leq v_{\mathrm{min}} \leq \infty \end{aligned} \tag{2.16}$$

The derivation of the correct differential event rate is outlined in the following. At first (2.12) can be written as

$$\frac{\mathrm{d}R}{\mathrm{d}E} \propto \int_{-1}^{1} \mathrm{d}(\cos\theta) \int_{v_{\mathrm{min}}}^{v_{\mathrm{max}}(\cos\theta)} \mathrm{d}v\, v\, e^{-\frac{(v^2+2vv_E\cos\theta+v_E^2)}{v_0^2}}, \tag{2.17}$$

where all constant factors have been omitted, since they are unimportant for the following reasoning. Note, that the integration regarding the azimuth angle simply yields a factor of 2π. The area in the v vs. $\cos\theta$ space, which the two-dimensional integral runs over, is shown as the yellow region in Fig. 2.4 for the cases $0 \leq v_{\mathrm{min}} \leq v_{\mathrm{esc}} - v_E$ (left) and $v_{\mathrm{esc}} - v_E \leq v_{\mathrm{min}} \leq v_{\mathrm{esc}} + v_E$ (right). The third case $v_{\mathrm{esc}} + v_E \leq v_{\mathrm{min}} \leq \infty$ is trivial and simply yields a rate of zero, as already mentioned.

Since the integration over $\cos\theta$ is simple, it is appropriate to change the order of the integration. Therefore, (2.15) has to be inverted yielding an upper boundary on $\cos\theta$ for a given velocity:

$$\cos\theta_{\mathrm{max}}(v) = \frac{1}{2}\left(\frac{v_{\mathrm{esc}}^2}{v_E\, v} - \frac{v_E}{v} - \frac{v}{v_E}\right). \tag{2.18}$$

From Fig. 2.4 it can be concluded that for $0 \leq v_{\mathrm{min}} \leq v_{\mathrm{esc}} - v_E$, the integral is given by

$$\frac{\mathrm{d}R}{\mathrm{d}E} \propto \left(\int_{v_{\mathrm{min}}}^{v_{\mathrm{esc}}-v_E} \mathrm{d}v\, v \int_{-1}^{1} \mathrm{d}(\cos\theta) + \int_{v_{\mathrm{esc}}-v_E}^{v_{\mathrm{esc}}+v_E} \mathrm{d}v\, v \int_{-1}^{\cos\theta_{\mathrm{max}}(v)} \mathrm{d}(\cos\theta)\right) e^{-\frac{(v^2+2vv_E\cos\theta+v_E^2)}{v_0^2}}, \tag{2.19}$$

and for $v_{\mathrm{esc}} - v_E \leq v_{\mathrm{min}} \leq v_{\mathrm{esc}} + v_E$ by

$$\frac{\mathrm{d}R}{\mathrm{d}E} \propto \int_{v_{\mathrm{min}}}^{v_{\mathrm{esc}}+v_E} \mathrm{d}v\, v \int_{-1}^{\cos\theta_{\mathrm{max}}(v)} \mathrm{d}(\cos\theta)\, e^{-\frac{(v^2+2vv_E\cos\theta+v_E^2)}{v_0^2}}. \tag{2.20}$$

After integration over $\cos\theta$ and rearrangement of terms the differential event rate is obtained:

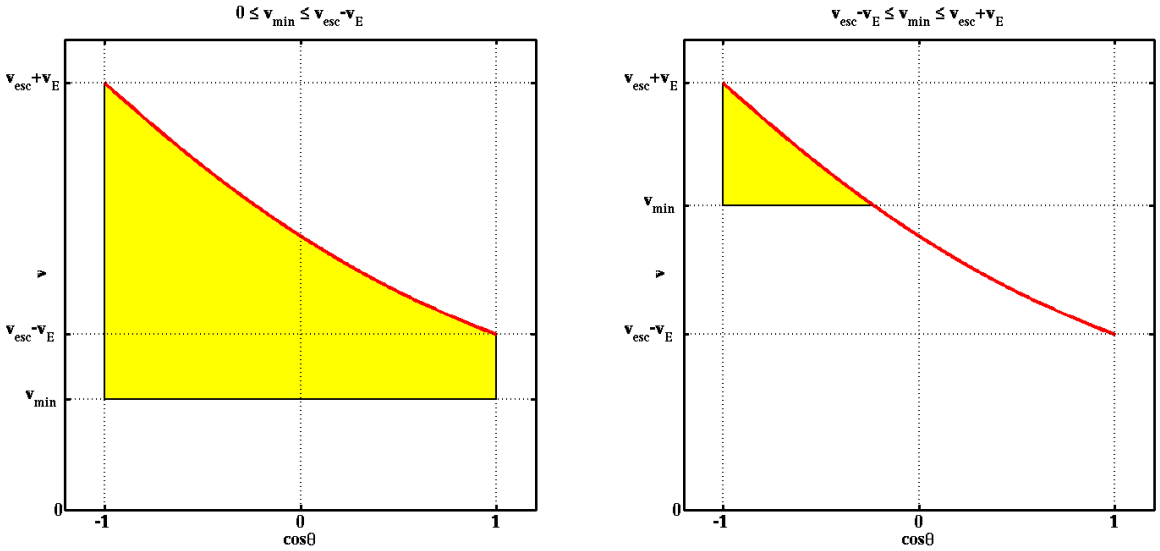

Figure 2.4: Regions relevant for the velocity-space integration yielding the formulae for the differential event rate expected in direct dark matter search experiments. The maximum velocity $v_{\max}$ (2.15) is indicated by the red line. The area, which the integral runs over, is shown for the case $0 \leq v_{\min} \leq v_{\rm esc} - v_E$ in the left plot and the case $v_{\rm esc} - v_E \leq v_{\min} \leq v_{\rm esc} + v_E$ in the right plot.

$$\frac{\mathrm{d}R}{\mathrm{d}E} = \frac{4\,N_0\,\rho\,\sigma}{\sqrt{\pi}\,r\,A_u\,m_W^2\,v_0\left(\mathrm{erf}\left(\frac{v_{\rm esc}}{v_0}\right) - \frac{2}{\sqrt{\pi}}\frac{v_{\rm esc}}{v_0}e^{-\frac{v_{\rm esc}^2}{v_0^2}}\right)}\cdot$$

$$\begin{cases} \frac{\sqrt{\pi}v_0}{4v_E}\left(\mathrm{erf}\left(\frac{v_{\min}(E)+v_E}{v_0}\right) - \mathrm{erf}\left(\frac{v_{\min}(E)-v_E}{v_0}\right)\right) - e^{-\frac{v_{\rm esc}^2}{v_0^2}} & \text{if } 0 \leq v_{\min} \leq v_{\rm esc} - v_E \\ \frac{\sqrt{\pi}v_0}{4v_E}\left(\mathrm{erf}\left(\frac{v_{\rm esc}}{v_0}\right) - \mathrm{erf}\left(\frac{v_{\min}(E)-v_E}{v_0}\right)\right) - \frac{v_{\rm esc}+v_E-v_{\min}(E)}{2v_E}e^{-\frac{v_{\rm esc}^2}{v_0^2}} & \text{if } v_{\rm esc} - v_E \leq v_{\min} \leq v_{\rm esc} + v_E \\ 0 & \text{if } v_{\rm esc} + v_E \leq v_{\min} \leq \infty\,, \end{cases} \tag{2.21}$$

which is continuous at the saltus. As discussed before, the result, which is valid in the range $0 \leq v_{\min} \leq v_{\rm esc} - v_E$ and given by the authors of [1], has previously often been applied for all values of $v_{\min}$. Since this is certainly not correct, it is interesting to check the validity of that approximation.

Figure 2.5 shows the recoil-energy dependence of $v_{\min}$ for mass splittings of 0 keV (top), hence elastic scattering, and 100 keV (bottom) for various WIMP masses as given in the legends, considering scattering off a ^{73}Ge nucleus. The horizontal blue line in the middle represents the escape velocity, while the upper and lower blue lines show the boundaries of the validities of the three formulae, given by $v_{\rm esc} - v_E$ and $v_{\rm esc} + v_E$. The red bands around these lines are related to the time dependence of the Earth's orbital motion. The

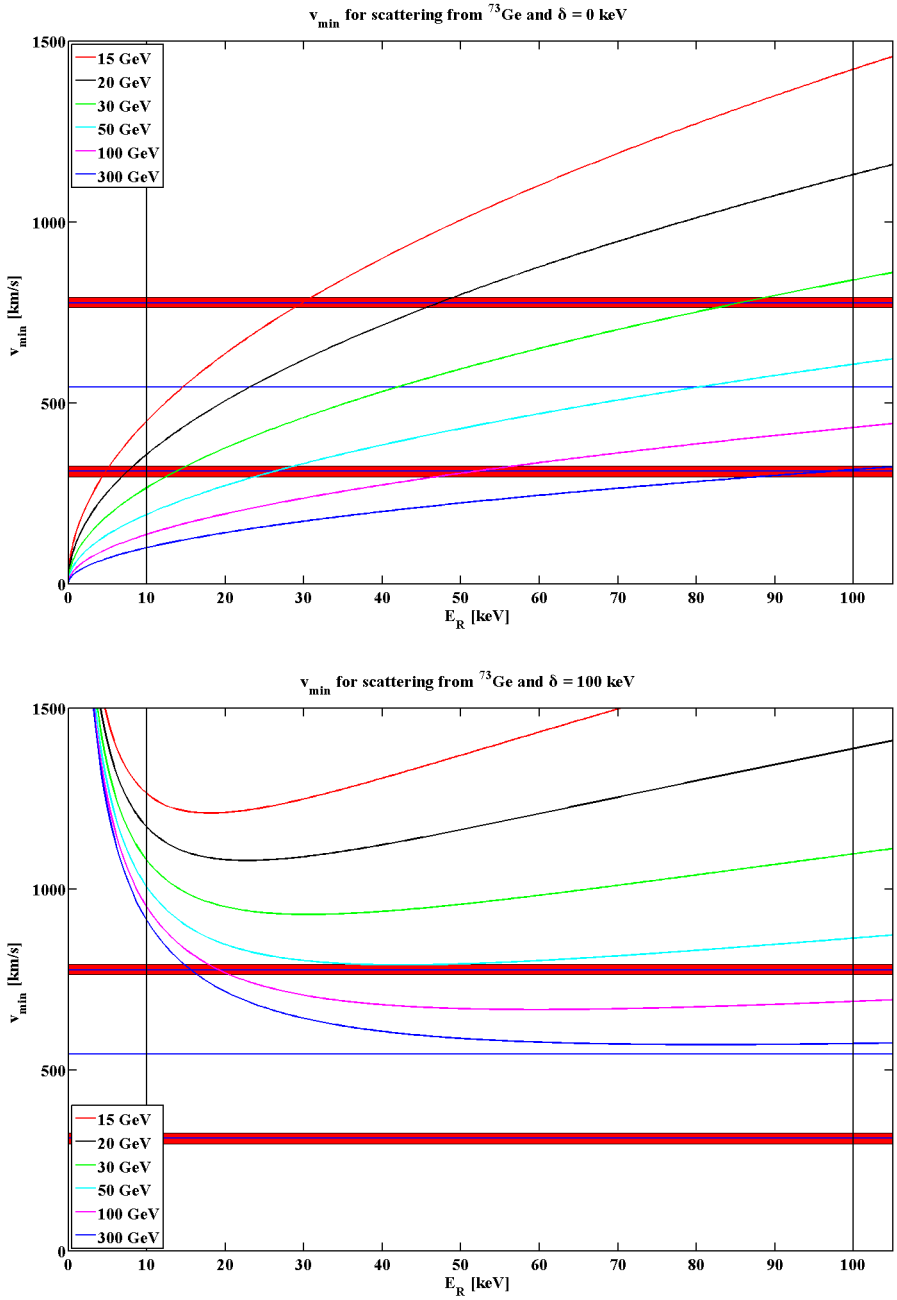

Figure 2.5: Recoil energy dependence of the minimum velocity $v_{\min}$ considering scattering off a ^{73}Ge nucleus for mass splittings of 0 keV (top), hence elastic scattering, and 100 keV (bottom) for various WIMP masses as given in the legends. The horizontal blue line in the middle represents the escape velocity, while the upper and lower blue lines show the boundaries of the validities of the three formulae (2.21), given by $v_{\rm esc} - v_E$ and $v_{\rm esc} + v_E$. See text for more details.

"standard" formula has to be used in the lowest part. Regarding elastic scattering, it is valid over the whole recoil-energy range considered by CDMS (10–100 keV) for WIMP masses above ∼300 GeV/c^2. For a WIMP with $m_W = 100$ GeV/c^2 it is only valid up to ∼50 keV. The second formula, given in (2.21), has to be used for higher recoil energies. It can be concluded that significant deviations from simply applying the "standard" formula are only expected for comparably low WIMP masses. Considering the iDM scenario the minimum velocity is no longer a monotonically increasing function of the recoil energy. Instead it is infinity for $E = 0$ keV and $E = \infty$ with a local minimum in-between. The most important difference regarding the calculation of the differential event rate is the fact that the exact result (2.21) has to be used. The "standard" formula is a bad approximation because of the increased minimum velocity. Regarding the shown example of $\delta = 100$ keV it is incorrect for all shown WIMP masses. To quantify the importance of the usage of the corrected rate formulae it should be noted that the (incorrect) results from the "standard" formula can be lower by a factor of 10 or even more for such high mass splittings. From this analysis it can also be observed that the inelastic dark matter scenario is much more sensitive to the actual value of the escape velocity than the standard model assuming elastic scattering.

The evaluation of the differential rate formula regarding the GHalo simulation is much less involved, since no explicit escape velocity cutoff has to be considered as discussed before. Thus, v_{max} can be simply set to ∞. Plugging (2.8) into (2.12) directly yields:

$$\frac{\mathrm{d}R}{\mathrm{d}E} = \frac{2\,N_0\,\rho\,\sigma}{r\,A_u\,m_W^2}\,\frac{1}{n}\sum_i \frac{1}{|\vec{v}_i - \vec{v}_E|}\,, \tag{2.22}$$

where the sum has to be restricted by the constraint $v_{\mathrm{min}} \leq |\vec{v}_i - \vec{v}_E|$, which corresponds to the lower boundary of the integral. Thus, the number of events contributing to the sum decreases for increasing minimum velocity. To investigate this behaviour, Fig. 2.6 shows the recoil energy dependence of the number of particles from a sample with 55760 particles (the same sample considered before) of the GHalo simulation contributing to the rates considering scattering off a ^{73}Ge nucleus for mass splittings of 0 keV (top), so elastic scattering, and 100 keV (bottom) for various WIMP masses as given in the legends. Regarding elastic scattering it can be observed that, except for very small WIMP masses ($\lesssim$ 30 GeV/c^2), the number of particles, which the differential event rate (2.22) is based on, is sufficiently high, so that the outcome should be trustworthy. This is different for the shown example considering inelastic scattering with $\delta = 100$ keV. The number of events contributing to the rate for a WIMP of 50 GeV/c^2 is $\lesssim 20$, while it is larger than 1000 considering elastic scattering for the same WIMP mass over the whole considered recoil-energy range. It should be noted that the sample used for this plot had particularly high statistics. Most samples contained just around 20000 particles. In summary it can be concluded that for small minimum velocities the rates, calculated according to (2.22), should yield reasonable results, so particularly considering elastic scattering except for very small WIMP masses. On the other hand, the results for comparably high minimum velocities, which put a higher emphasis on the high-velocity tail of the distribution, can be

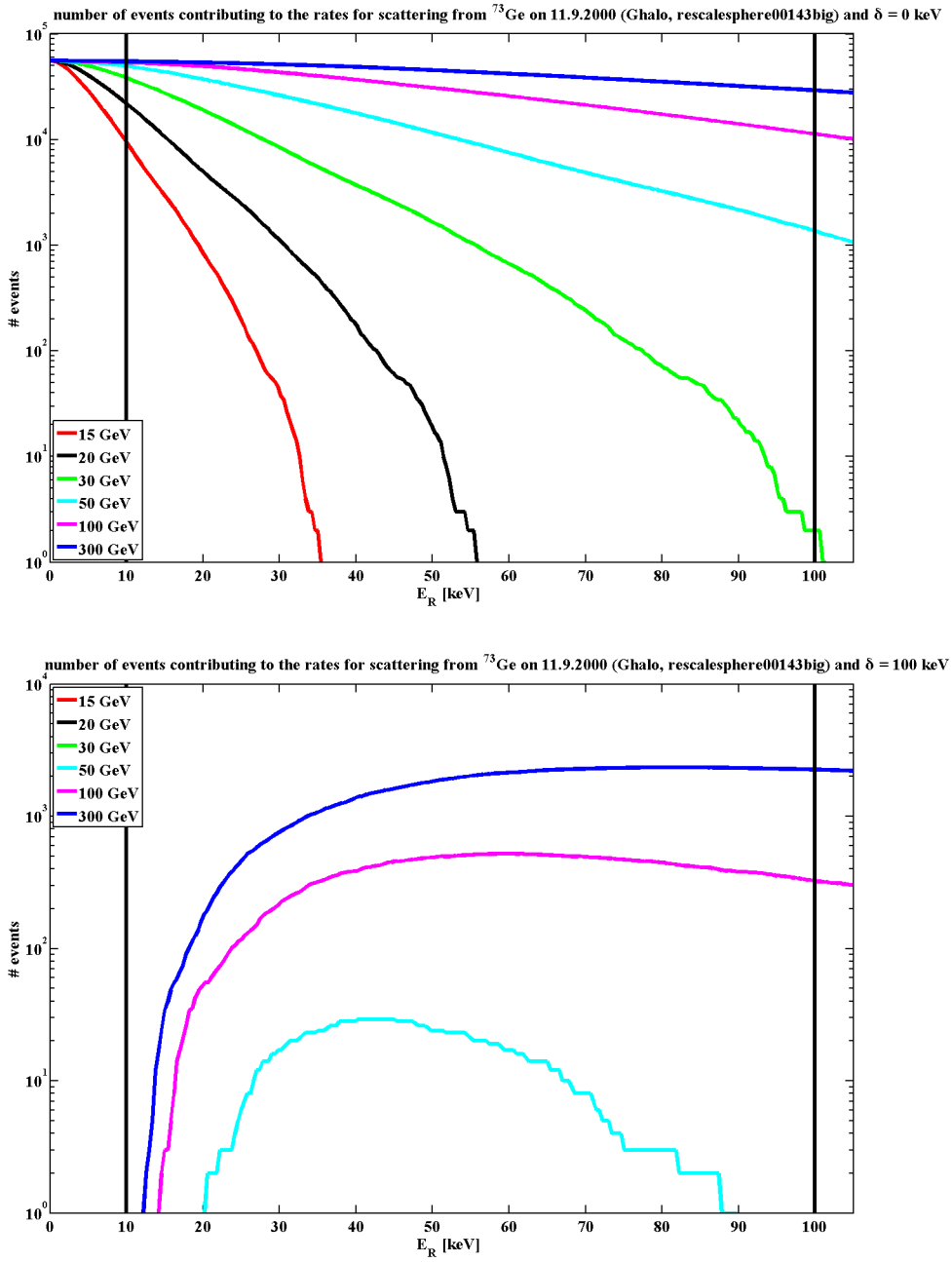

Figure 2.6: Recoil energy dependence of the number of particles from a sample with 55760 particles of the GHalo simulation contributing to the rates, considering scattering off a ^{73}Ge nucleus for mass splittings of 0 keV (top), so elastic scattering, and 100 keV (bottom) for various WIMP masses as given in the legends.

expected to be dominated by low statistics. This is the case regarding inelastic scattering for high mass splittings.

Finally, Fig. 2.7 shows differential event rates assuming elastic scattering ($\delta = 0$ keV) off Ge and a representative WIMP mass of 100 GeV/c^2 based on the truncated Maxwell-Boltzmann distribution (blue), calculated according to (2.21), and on the GHalo sample with 55760 particles investigated throughout this chapter (black), calculated according to (2.22). A spin-independent (see chapter 2.2.1) WIMP-nucleon cross section of $\sigma = 10^{-8}$ pb was used for the plot. It can be observed that the rates have a featureless exponential shape, which is the most important property of the expected WIMP spectrum. It shows that in this scenario a WIMP signal is expected at low recoil energies. Thus, a low threshold is important. Moreover, it can be seen that both spectra are quite similar. This was observed for all investigated GHalo samples, which indicates that the Galilean transformation from galactic coordinates into the Earth's rest frame and the integration over the velocity space wash out most of the features in the simulation. This is a convenient result, since it shows that the simple Maxwell-Boltzmann distribution is appropriate to analyze the results from

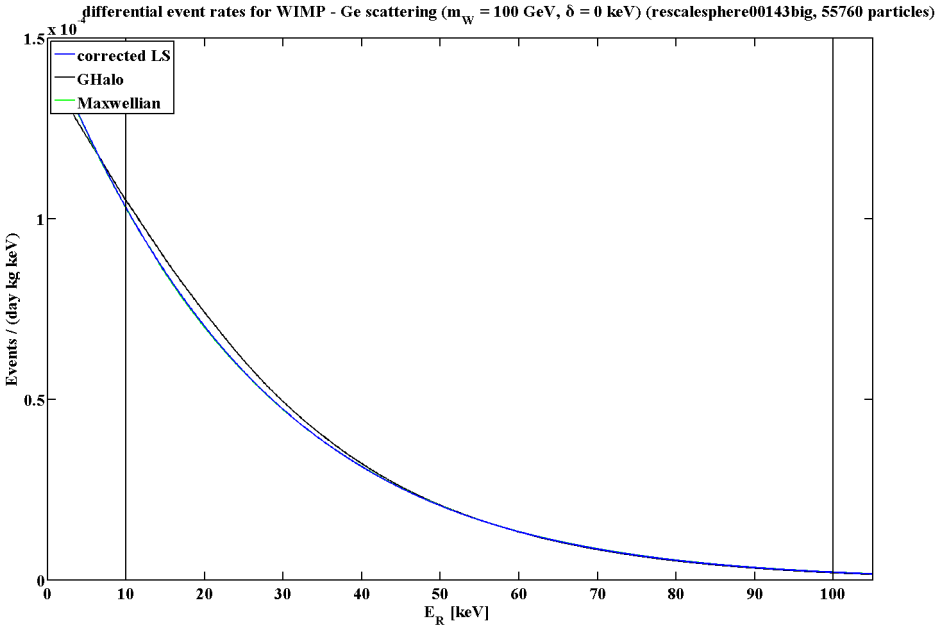

Figure 2.7: Differential event rates assuming elastic scattering ($\delta = 0$ keV) off Ge, a spin-independent WIMP-nucleon cross section of $\sigma = 10^{-8}$ pb and a representative WIMP mass of 100 GeV/c^2. The blue line was calculated assuming a Maxwell-Boltzmann distribution following (2.21). The black line corresponds to the rate calculated according to (2.22) based on the GHalo sample with 55760 particles investigated throughout this chapter. The plot also contains the rate based on a Monte Carlo simulation with 55760 particles drawn from the non-truncated Maxwell-Boltzmann distribution (green). The corresponding velocity distribution was shown in Fig. 2.2. This line lies directly under the black line, so it cannot be seen easily. A difference can be observed in the next figure, where a different mass splitting was used.

direct detection experiments assuming elastic scattering.

The shape of the spectra regarding inelastic scattering is significantly different, which is shown in Fig. 2.8. The differential rates peak at tens of keV recoil energy and exhibit a significant suppression of the recoil spectrum at low recoil energies. It can be observed from the top plot that the Maxwell-Boltzman distribution is still a reasonable approximation to the rates obtained from the simulation for comparably small mass splittings. For higher mass splittings, as shown in the bottom plot, the differential rates are only based on the high velocity tails of the distributions, since v_{min} gets very large. As the Maxwell-Boltmann distribution is truncated at the escape velocity, no signal is expected for $\delta = 150$ keV. Nevertheless, some particles within the simulations have velocities, which are high enough that the differential event rate based on the simulations does not vanish. However, as discussed before, the number of particles in the tails is limited, so that the calculated rates suffer from low statistics. It is thus difficult to judge whether features, as shown in the bottom plot, represent real properties of the WIMP distribution or just reflect the low statistics issue. An analysis of several GHalo samples suggests that they are due to low statistics. Note, that on the contrary the authors of [23] conclude that these features are real. Given that they investigated samples of similar size ($\sim$20000 particles) this conclusion is questionable, particularly since no information is given regarding the numbers of events contributing to the rates at high mass splittings. Nevertheless, it should be admitted that they investigated a much larger number of samples (100), while only half a dozen were investigated for the quick analysis performed here, so that the validity of their conclusion cannot be excluded. However, for the analysis presented in the remainder of this thesis, it seems appropriate to simply use the standard Maxwell-Boltzmann distribution, since the corresponding rates are similar to the ones obtained from the simulation assuming elastic scattering and the simulation yields questionable results assuming inelastic scattering with high mass splittings.

2.2 Spin-independent and spin-dependent cross sections

As discussed in the previous section, WIMPs are expected to have velocities of order 100 km/s, which means that they are non-relativistic. It can be shown quite generally that only two kinds of interactions between WIMPs and the target nuclei exist in this regime [27]. These are spin-independent and spin-dependent interactions. All other possible terms in the interaction Lagrangian vanish in the non-relativistic limit or can be absorbed in one of the two mentioned terms. These processes are discussed in the following.

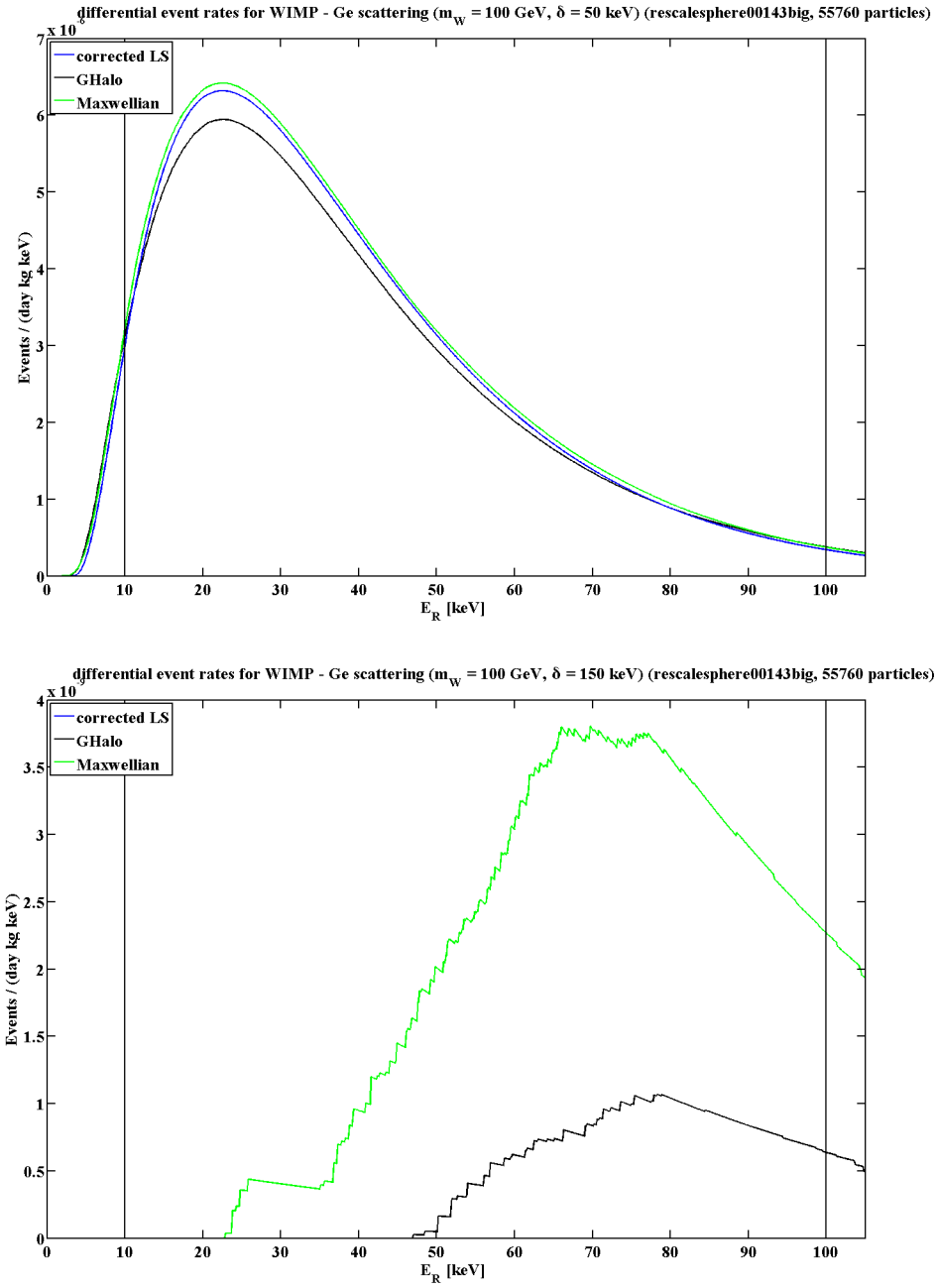

Figure 2.8: Differential event rates assuming inelastic scattering with $\delta = 50$ keV (top) and $\delta = 150$ keV (bottom) off Ge, a spin-independent WIMP-nucleon cross section of $\sigma = 10^{-8}$ pb and a representative WIMP mass of 100 GeV/c^2. The blue line was calculated assuming a Maxwell-Boltzmann distribution following (2.21). The black line corresponds to the rate calculated according to (2.22) based on the GHalo sample with 55760 particles investigated throughout this chapter. The plot also contains the rate based on a Monte Carlo simulation with 55760 particles drawn from the non-truncated Maxwell-Boltzmann distribution (green). The corresponding velocity distribution was shown in Fig. 2.2. Due to the high minimum velocity no signal is observed for $\delta = 150$ keV assuming that the velocity distribution is a truncated Maxwell-Boltzmann distribution. The features in the two rates from simulations are related to the low statistics of the samples rather than to real properties of the WIMP distribution.

2.2.1 Spin-independent interactions

The spin-independent (or scalar) WIMP-nucleus cross section at zero momentum transfer is given by

$$\sigma_{\text{scalar}} = \frac{m_N^2}{4\pi\,(m_W + m_N)^2} \cdot \Big(Z\,f_p + (A - Z)\,f_n\Big)^2\,, \tag{2.23}$$

where Z and A are the nuclear charge and atomic number respectively. The coupling constants, considering interactions with protons and neutrons, are denoted f_p and f_n. In most theoretical models they have similar size, so that $f_n \approx f_p$. As an example, WIMPs arising from UEDs are discussed in the next chapter. This cross-section can be normalized to a single nucleon:

$$\sigma_{scalar}^{p,n} = \frac{1}{A^2}\,\frac{\mu_{p,n}^2}{\mu^2}\,\sigma_{scalar}\,. \tag{2.24}$$

It is typically referred to when constraints regarding scalar interactions are discussed. Due to the A^2-scaling heavy target nuclei are much more sensitive to spin-independent interactions than light nuclei except for very small WIMP masses.

Owing to the finite size of the target nucleus, these cross sections are valid only for the case of zero momentum transfer ($q = \sqrt{2m_N E} = 0$). For non-zero momentum transfer, a form factor correction needs to be considered:

$$\sigma_{SI} = \sigma_{\text{scalar}}\,F_{SI}^2\,, \tag{2.25}$$

where F_{SI} is the nuclear form factor. It is defined as the Fourier transform of the mass density distribution, which is usually assumed to be equivalent to the charge density distribution:

$$F_{SI}(q) \sim \int \mathrm{d}^3\vec{r}\,\rho(\vec{r})\,e^{-i\vec{q}\cdot\vec{r}} = \frac{4\pi}{q}\int_0^\infty \mathrm{d}r\,\rho(r)\,r\,\sin(qr)\,, \tag{2.26}$$

with the second term being valid for isotropic densities with $\rho(\vec{r}) = \rho(r)$, which is an appropriate assumption for most nuclei. A realistic density profile is given by the two-parameter Fermi distribution:

$$\rho(r) = \frac{\rho_0}{e^{\frac{r-c}{a}} + 1}\,. \tag{2.27}$$

For the analysis discussed in this thesis Helm's model [28] was used:

$$F_{SI}(qr_n) = 3\frac{j_1(qr_n)}{qr_n}e^{-\frac{(qs)^2}{2}}\,, \tag{2.28}$$

with the spherical Bessel function of the first kind j_1, the effective nuclear radius $r_n = \sqrt{c^2 + \frac{7}{3}\pi^2 a^2 - 5s^2}$ with $a = 0.52$ fm and $c = 1.23\sqrt[3]{A} - 0.60$ fm, and the nuclear skin thickness $s = 1$ fm [1]. This parametrization was found by fitting (2.28) to the numerically calculated Fourier transform of (2.27). The charge densities were obtained from muonic atom spectroscopy data [29]. Since a muon is ∼200 times more massive than an electron, the corresponding Bohr orbit is much smaller, and thus the muon has a much larger

probability to be close to the nucleus than in ordinary atoms. Therefore, the transition energies in muonic atoms are strongly affected by the charge distribution of the nucleus. The main issue with the given parametrization of the form factors is the fact that they are fits to measurements, which were based on a specific nuclear density model, in this case the two-parameter Fermi distribution. Hence, the form factor parametrization is essentially obtained from fits to fitted data, which can introduce some uncertainties. This issue is discussed in great detail in [30]. Therefore, it is desirable to investigate differences between form factors directly obtained from the Fourier transform of the two-parameter Fermi distribution and form factors based on the given parametrization. As already mentioned, parameters of this distribution for various isotopes obtained from muonic atom spectroscopy data are given in [29]. For some isotopes this paper also contains parameters from two-parameter Fermi distribution fits based on elastic electron scattering measurements. Moreover, there also exists the following ansatz, called Fourier-Bessel expansion, for the charge distribution [31]:

$$\rho(r) = \begin{cases} \sum_{i=1}^{n} a_i \, j_0\left(\frac{i\,\pi\,r}{R}\right) & \text{if } r \leq R \\ 0 & \text{if } r \geq R\,, \end{cases} \tag{2.29}$$

with the zeroth-order spherical Bessel function j_0, and where the cutoff R is 10 fm for Ge isotopes. The parameters for various isotopes are also given in [31]. All charge densities are normalized by requiring:

$$\int \mathrm{d}^3\vec{r}\,\rho(\vec{r}) = Ze\,. \tag{2.30}$$

A comparison of the three discussed density profiles for the ^{72}Ge nucleus is shown in Fig 2.9.

In order to obtain the form factors based on these densities, the Fourier transforms (2.26) have to be computed and normalized to $F_{SI}(0) = 1$. There exists an analytic expression in the case of the Fourier-Bessel expansion, which is already normalized [30]:

$$F_{SI}(q) = \frac{\sin(qR)}{qR} \frac{\sum_{i=1}^{n} \frac{(-1)^i\,a_i}{(i\pi)^2 - (qR)^2}}{\sum_{i=1}^{n} \frac{(-1)^i\,a_i}{(i\pi)^2}}\,. \tag{2.31}$$

The charge densities of the two-parameter Fermi distribution have to be Fourier transformed numerically. Despite of the oscillating $\sin(qr)$ term in the integrand this is a quite simple calculation, since the charge densities drop off very fast, so that the integrand stops oscillating after at least one period.

Finally, Fig. 2.10 shows a comparison of the just discussed form factors with the simple parametrization given in (2.28) for the ^{72}Ge nucleus. From the top plot, which shows the direct comparison, it can be observed that there are only slight differences. To take a better look at the deviations from the simple parametrization the bottom plot shows the

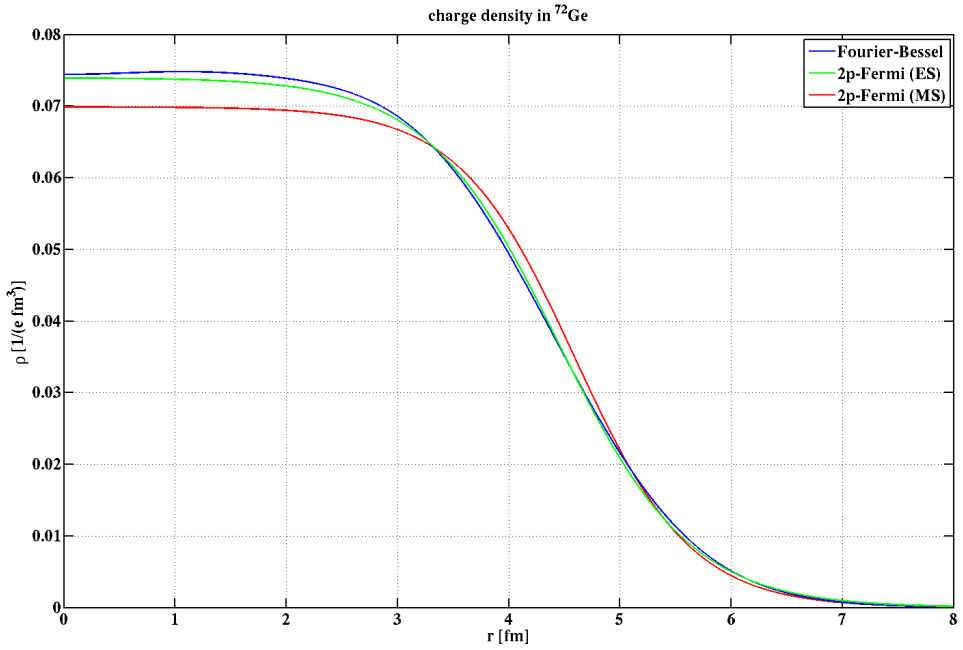

Figure 2.9: Comparison of the three charge density profiles of ^{72}Ge as discussed in the text. These are the two-parameter Fermi distribution with parameters obtained from muonic atom spectroscopy (red), the two-parameter Fermi distribution with parameters obtained from electron scattering measurements (green) and the Fourier-Bessel expansion (blue).

squared ratio of the form factors based on (2.28) and the other three form factors. The alternative estimates deviate from the simple parametrization by just a few percent for high recoil energies, which indicates that it is a very good approximation and that using more advanced approaches is not necessary.

Considering a specific model, which makes predictions about the couplings f_p and f_n, the spin-independent differential event rate for finite-momentum transfer can then be obtained by replacing σ in (2.21) with σ_{SI} given in (2.25). If the WIMP target consists of more than one element, the respective abundances of each isotope f_i have to be considered. The total differential event rate for a specific WIMP target is

$$\frac{\mathrm{d}R_{SI}}{\mathrm{d}E} = \sum_i f_i \frac{\mathrm{d}R^i_{SI}}{\mathrm{d}E} \,. \tag{2.32}$$

The expected number of events for spin-independent interactions for a given experiment can then be written as

$$\mu_{SI} = \mathrm{MT} \cdot \int_{E_{\mathrm{lower}}}^{E_{\mathrm{upper}}} \mathrm{d}E \, \frac{\mathrm{d}R_{SI}}{\mathrm{d}E} \cdot \mathrm{eff}(E) \,, \tag{2.33}$$

where MT denotes the total detector exposure in kg-days, and eff(E) denotes the WIMP

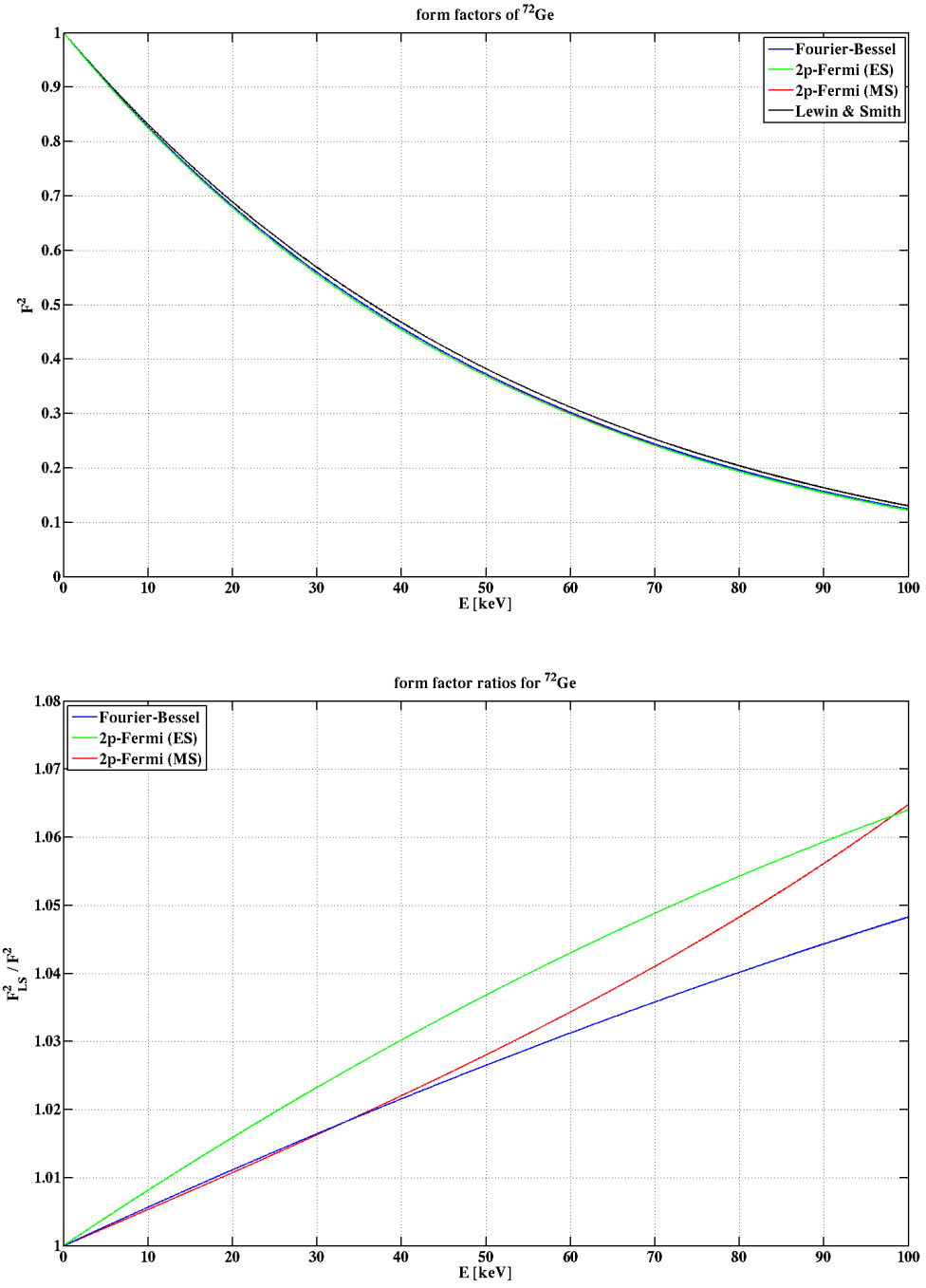

Figure 2.10: *Top*: Comparison of the three spin-independent form factors of ^{72}Ge, as discussed in the text, with the simple parametrization given in (2.28) (black). They are based on the Fourier transform of the two-parameter Fermi distribution with parameters obtained from muonic atom spectroscopy (red), the two-parameter Fermi distribution with parameters obtained from electron scattering measurements (green) and the Fourier-Bessel expansion (blue). *Bottom*: Squared ratio of the form factors based on (2.28) and the other three discussed form factors. Even at high energies there are deviations of just a few percent.

detection efficiency as a function of the recoil energy. E_{lower} and E_{upper} denote the lower and upper bound of the recoil energy, which is considered in the data analysis.

2.2.2 Spin-dependent interactions

In the case of spin-dependent interactions the WIMPs do not couple to the number of nucleons but to their spins. Since paired nucleons have opposite spin, which leads to a vanishing interaction strength, only nuclei with an odd number of nucleons yield a significant cross section. Other nuclei can be neglected regarding this type of interaction.

Following [32], at zero momentum transfer, the spin-dependent cross section can be written in the form

$$\sigma_{\text{spin}} = \frac{32}{\pi} G_F^2 \, \mu^2 \, \frac{J_N + 1}{J_N} \Big(a_p \langle S_p \rangle + a_n \langle S_n \rangle \Big)^2 , \tag{2.34}$$

where G_F is the Fermi constant and J_N is the total nuclear spin. $\langle S_p \rangle$ and $\langle S_n \rangle$ denote the expectation values of the proton and neutron spins within the nucleus respectively. The spin-dependent couplings to protons and neutrons are a_p and a_n. In contrast to their scalar brethren f_p and f_n it is typically not a good approximation to assume that they have similar size. An example is discussed in the next chapter.

Nevertheless, given the spin-dependent cross section (2.34) and the differential event rate (2.21), the expected event rate calculation is similar to the spin-independent case. At first, it is again convenient to normalize the cross section to the scattering from a single nucleon. The nucleon spin expectation values are $\langle S_p \rangle = \frac{1}{2}$ and $\langle S_n \rangle = 0$ and $\langle S_p \rangle = 0$ and $\langle S_n \rangle = \frac{1}{2}$, for a proton and a neutron respectively. Using these values the spin-dependent cross section for a single nucleon is

$$\sigma_{\text{spin}}^{p,n} = \frac{24}{\pi} G_F^2 \, \mu_{p,n}^2 \, a_{p,n}^2 \, . \tag{2.35}$$

Comparing (2.35) to (2.34) the spin-dependent cross section can be written as

$$\sigma_{spin}^{p,n} = \frac{3}{4} \frac{\mu_{p,n}^2}{\mu^2} \frac{J_N}{J_N + 1} \frac{1}{\langle S_{p,n} \rangle^2} \sigma_{\text{spin}} \, . \tag{2.36}$$

Similar to the spin-independent case a form factor has to be introduced to account for non-zero momentum transfer

$$\sigma_{SD} = \sigma_{\text{spin}} \, F_{SD}^2 \, , \tag{2.37}$$

where F_{SD}^2 can be written in the form [33]

$$F_{SD}^2(q) = \frac{S(q)}{S(0)} \, , \tag{2.38}$$

with the spin structure function $S(q)$. What makes the calculation of constraints on the model parameters in the spin-dependent case involved is the fact that $S(q)$ depends on

the WIMP-nucleon couplings. In the zero-momentum transfer limit, the spin structure function $S(q)$ can be evaluated:

$$S(0) = \frac{2J_N + 1}{\pi} J_N(J_N + 1)\Lambda^2 \,, \tag{2.39}$$

where Λ is defined as

$$\Lambda = \frac{a_p \langle S_p \rangle + a_n \langle S_n \rangle}{J_N} \,. \tag{2.40}$$

For finite-momentum transfer it is a common procedure to translate the WIMP-proton and WIMP-neutron couplings a_p and a_n into isoscalar and isovector spin couplings a_0 and a_1 using

$$\begin{aligned} a_0 &= a_p + a_n \\ a_1 &= a_p - a_n \,, \end{aligned} \tag{2.41}$$

so that the spin structure function can be written as

$$S(q) = a_0^2 S_{00}(q) + a_1^2 S_{11}(q) + a_0 a_1 S_{01}(q) \,. \tag{2.42}$$

S_{00}, S_{11} and S_{01} represent isoscalar, isovector and interference terms respectively. Appropriate parametrizations of these functions based on nuclear shell model calculations can be found e.g. in [34] for ^{73}Ge and in [35] for ^{129}Xe and ^{131}Xe, which are the only naturally occurring odd-nucleon isotopes of Ge and Xe. The shape of $S(q)$ is determined by the ratio $\frac{a_p}{a_n}$, while its magnitude is proportional to $a_p^2 + a_n^2$. Following [36] it is convenient to use polar coordinates in the (a_p, a_n) subspace:

$$\begin{aligned} a_p &= a \, \sin\theta \\ a_n &= a \, \cos\theta \,. \end{aligned} \tag{2.43}$$

Pure proton and neutron couplings are obtained by setting $\theta = 90°$ and $\theta = 0°$, respectively. Inserting this ansatz into (2.42) yields

$$S(q) = a^2 \Big((\sin\theta + \cos\theta)^2 \, S_{00}(q) + (\sin\theta - \cos\theta)^2 \, S_{11}(q) - \cos(2\theta) \, S_{01}(q) \Big) \,. \tag{2.44}$$

Similar to (2.33) the number of events is obtained by evaluating the integral

$$\mu_{SD} = \mathrm{MT} \cdot \sum_i f_i \cdot \int_{E_{\mathrm{lower}}}^{E_{\mathrm{upper}}} \mathrm{d}E \, \frac{\mathrm{d}R_{SD}^i}{\mathrm{d}E} \cdot \mathrm{eff}(E) \,. \tag{2.45}$$

μ_{SD} can be rewritten in the form

$$\mu_{SD} = A \, a_p^2 + 2 \, B \, a_p a_n + C \, a_n^2 \,, \tag{2.46}$$

with A, B and C being constant for a given WIMP mass. Inserting (2.43) yields

$$\mu_{SD} = a^2 \Big(A \, \sin^2\theta + 2 \, B \, \sin\theta \cos\theta + C \, \cos^2\theta \Big) \,. \tag{2.47}$$

In order to investigate constraints on the WIMP-nucleon spin-dependent couplings, for any WIMP mass of interest a scan can be performed over the angle θ from 0°–360°. Thus, for given θ a limit can be set on a^2. Since (2.47) is a quadratic equation, the limits are expected to be ellipses in the (a_p, a_n) subspace. The allowed (a_p, a_n) parameter space is restricted to the inner region of these ellipses.

2.3 Annual modulation and the DAMA/LIBRA results

The Earth's orbital velocity introduces a time-dependence to the differential rate. Thus, the movement of the Earth around the Sun would provide an annual modulation of the counting rate, caused by the change in the relative velocity of the dark matter particles with respect to the earthbound target [37]. The time dependence of the differential rate can be written as

$$\frac{\mathrm{d}R}{\mathrm{d}E}(E,t) = S_0(E) + S_m(E) \cdot \cos\left(\omega(t-t_0)\right), \tag{2.48}$$

where t_0 corresponds to the 2$^{\text{nd}}$ June, which is the day when the Earth velocity reaches its maximum. S_0 denotes the average differential rate over a year. This part of the formula contains the constant part of a possible WIMP signal and background contributions, which are assumed to be time-independent. S_m is referred to as the modulation amplitude, which would be solely due to WIMP interactions. It is given by:

$$S_m(E) = \frac{1}{2}\left(\frac{\mathrm{d}R}{\mathrm{d}E}(E,t_0) - \frac{\mathrm{d}R}{\mathrm{d}E}(E,t_1)\right), \tag{2.49}$$

where t_1 denotes the 2$^{\text{nd}}$ December, which is the day when the Earth velocity reaches its minimum. Note, that the given formulae are valid for the standard halo model based on the Maxwell-Boltzmann velocity distribution discussed before, where the rate exhibits a sinusoidal time dependence to a very high accuracy. This is not valid for halo models including for example dark matter streams [38] but this is beyond the scope of this study.

The DAMA collaboration claims the observation of such a modulation in two different NaI(Tl) scintillation detector arrays [39, 40]. The observed signal is in the 2–6 keV electron-equivalent energy range with a periodicity of 0.999±0.002 years and a phase of 146±7 days [41]. The observed modulation signature is consistent with the expected signature of galactic dark matter particles interacting in a terrestrial detector. Other experimental results [3, 42, 43, 44, 45, 46], however, are inconsistent with the interpretation of the DAMA result as a signal from Weakly Interacting Massive Particles (WIMPs) elastically scattering off nuclei.

Inelastic dark matter scattering, as introduced in chapter 2.1.3, has been proposed as a way to resolve this tension. In this model the annual modulation signature is significantly enhanced because of the increased dependence on the high-velocity tail of the WIMP-velocity distribution, which in turn is due to the larger minimal velocity (2.11). At the

same time, the scattering rate is enhanced for heavy target nuclei (e.g. Xe and I), which circumvents the strong constraints e.g. from previous CDMS runs.

In order to set constraints on an iDM interpretation of the DAMA claim, it is necessary to determine the regions in parameter space which are allowed by the DAMA results. This analysis is presented in the current section, where only spin-independent inelastic scattering is considered, which means that the parameter space is three-dimensional consisting of the WIMP mass m_W, WIMP-mass splitting δ and the WIMP-nucleon cross section σ. The corresponding constraints from CDMS are presented in a later chapter, after the CDMS analysis and the corresponding limits were discussed.

The DAMA experiment was divided into two data runs designed as DAMA/LIBRA with an exposure of 0.53 ton-years[1] and its predecessor DAMA/NaI with an exposure of 0.29 ton-years. The DAMA collaboration has published the modulation amplitude S_m from their analysis for several energy bins averaged over the corresponding intervals in [40], where both mentioned runs have been combined. In fact, the authors of [47] provide a table with the values taken from the plot in the DAMA paper, which are shown in the top plot of Fig. 2.11. Following the extensive discussion in the same paper, the bins between 10 keV and 20 keV were combined into a single bin, since the signal is only evident in the low-energy range, while the rate seems to vary randomly around zero at higher energies, which would dilute the power of the χ^2-goodness-of-fit test, that is about to be performed. A detailed discussion regarding this issue can be found in [48]. Thus, the 17 data points shown in blue color in the plot are used for the determination of the DAMA allowed regions. For completeness it should be noted that apart from the modulated spectrum, the DAMA collaboration also published the constant part of the rate S_0 [40]. Since they do not strongly discriminate between WIMPs and background events, an unknown and possibly large fraction of this rate is due to background, which is assumed to be time independent. The spectrum is shown in the bottom plot of Fig. 2.11. Note, that, contrary to the published modulated rate, it only contains the DAMA/LIBRA results, thus only from the second, longer run.

It is important to keep in mind that in contrast to the CDMS experiment, which is capable of measuring the recoil energy from a WIMP-nucleus interaction directly, the DAMA experiment only detects the energy transferred into the electron system of the detectors. Only a small fraction of the recoil energy goes into scintillation, while the rest is converted into phonons/heat and thus cannot be measured. The detected energy E_{det}, measured in keVee (keV electron-equivalent), is related to the actual recoil energy E, measured in keV, by $E_{\mathrm{det}} = q \cdot E$ with the quenching factor q. They have been determined to be 0.30 for Na and 0.09 for I, which are the two components of the DAMA detectors, with errors of 0.01 [49].

To be as accurate as possible the detector resolutions given by the DAMA collaboration were included for this analysis. As mentioned before, the whole experiment was divided into two data runs designed as DAMA/LIBRA and its predecessor DAMA/NaI. The cor-

[1] In the meantime this exposure was increased to 0.87 ton-years [41]. These updated results where used in later chapters as indicated.

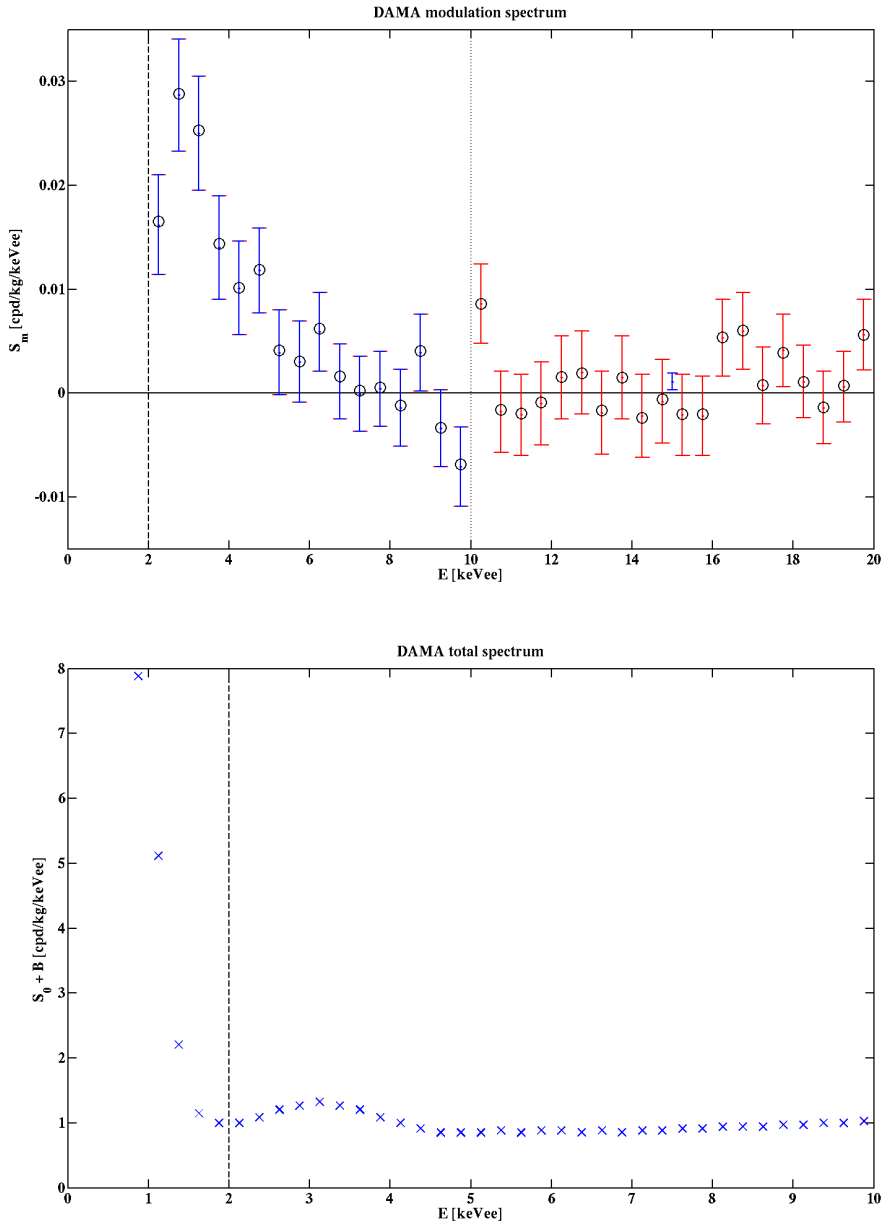

Figure 2.11: *Top*: Modulation spectrum S_m of the DAMA experiment, based on the combined results from DAMA/LIBRA and DAMA/NaI as given in Table 3 in [47] (all data points except for the single blue point at 15 keV). The data in the range 10–20 keV, which fluctuates around zero, was combined into a single bin yielding the blue data point at 15 keV. The following analysis is based on the blue data points. The black circles denote the data points exctracted directly from Fig. 9 in [40]. This was done as a cross check. *Bottom*: Constant (regarding time) part of the rate S_0 of the DAMA experiment, based only on the results from DAMA/LIBRA. The vertical lines at 2 keV denote the threshold of the DAMA experiment. The energies are given in keVee (keV electron-equivalent). See text for details.

responding detector resolutions can be found in [50] and [51] respectively. As shown in Fig. 2.12 the measurements can be well approximated by the parametrizations [52]:

$$\begin{aligned} \sigma_{\text{DAMA/LIBRA}} &= 0.448 \cdot \sqrt{E_{\text{det}}} + 0.0091 \cdot E_{\text{det}} \\ \sigma_{\text{DAMA/NaI}} &= 0.76 \cdot \sqrt{E_{\text{det}}} - 0.024 \cdot E_{\text{det}} \,. \end{aligned} \tag{2.50}$$

Thus, the differential rate (2.21), considered as a function of E_{det}, is corrected by convolving the rate with a Gaussian representing the detector resolution:

$$\frac{\mathrm{d}R}{\mathrm{d}E'_{\text{det}}}(E'_{\text{det}}) = \int_0^\infty \mathrm{d}E_{\text{det}} \frac{1}{\sqrt{2\pi}\,\sigma(E_{\text{det}})} e^{-\frac{1}{2}\left(\frac{E'_{\text{det}} - E_{\text{det}}}{\sigma(E_{\text{det}})}\right)^2} \cdot \frac{\mathrm{d}R}{\mathrm{d}E_{\text{det}}}(E_{\text{det}}) \tag{2.51}$$

Since the DAMA collaboration published S_m averaged over the respective energy bins, it is necessary to consider the integrated differential rate:

$$R = \int_{E_1}^{E_2} \mathrm{d}E'_{\text{det}} \frac{\mathrm{d}R}{\mathrm{d}E'_{\text{det}}}(E'_{\text{det}}) = \int_0^\infty \mathrm{d}E_{\text{det}} \frac{\mathrm{d}R}{\mathrm{d}E_{\text{det}}}(E_{\text{det}}) \cdot \Phi\big(E_{\text{det}}, E_1, E_2\big) \tag{2.52}$$

with the detector response function

$$\Phi\big(E_{\text{det}}, E_1, E_2\big) = \frac{1}{2}\left(\operatorname{erf}\left(\frac{E_2 - E_{\text{det}}}{\sqrt{2}\sigma(E_{\text{det}})}\right) - \operatorname{erf}\left(\frac{E_1 - E_{\text{det}}}{\sqrt{2}\sigma(E_{\text{det}})}\right)\right). \tag{2.53}$$

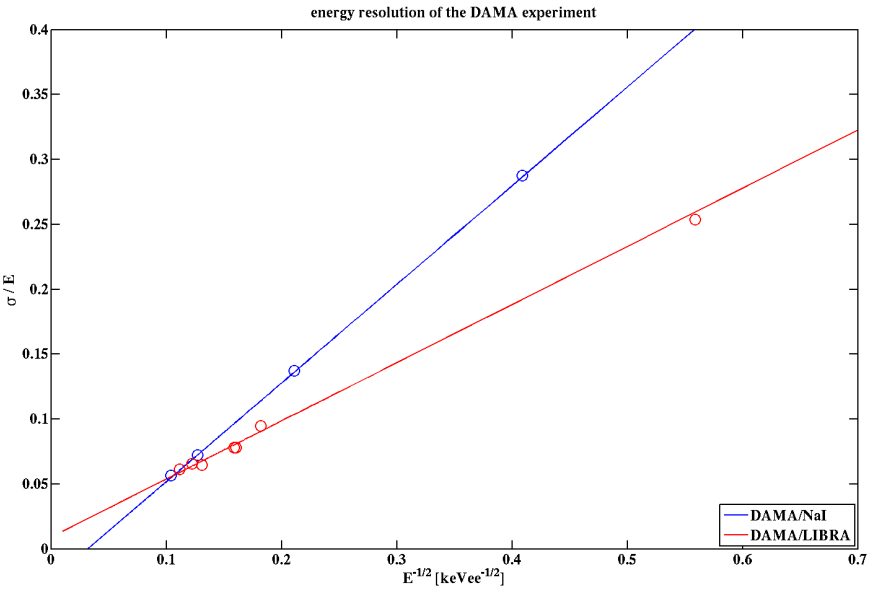

Figure 2.12: Detector resolutions of the DAMA experiment for DAMA/LIBRA (red) and DAMA/NaI (blue). The circles represent measurements as given in [50] and [51], and the lines represent fits parameterized by (2.50).

Thus instead of integrating the differential rate from E_1 to E_2, it is multiplied with the response function and integrated from 0 to ∞. This function has the feature to peak in the corresponding interval and fall off quickly outside of it, which can be used to impose a finite cutoff for the integration. The detector response functions for all 17 intervals, considered in the analysis of the modulation spectrum, are shown in Fig. 2.13. Note, that the functions corresponding to DAMA/LIBRA have a sharper peak due to the better energy resolution.

First, the theoretically expected modulated rate S_m (2.49) has to be computed for both isotopes contained in the DAMA detectors separately. Per definition the rate (2.21) is given as a function of the recoil energy, so that it is necessary to convert E to E_{det}. For the final result, the contributions of both isotopes have to be added, weighted by the mass fractions, to get $S_{m,\mathrm{tot}}$, which yields

$$S_{m,\mathrm{tot}}(E_{\mathrm{det}}) = \frac{m_{\mathrm{Na}}}{m_{\mathrm{Na}}+m_{\mathrm{I}}}\frac{1}{q_{\mathrm{Na}}}S_{m,\mathrm{Na}}\left(\frac{E_{\mathrm{det}}}{q_{\mathrm{Na}}}\right) + \frac{m_{\mathrm{I}}}{m_{\mathrm{Na}}+m_{\mathrm{I}}}\frac{1}{q_{\mathrm{I}}}S_{m,\mathrm{I}}\left(\frac{E_{\mathrm{det}}}{q_{\mathrm{I}}}\right), \tag{2.54}$$

where the indices Na and I denote the parameters/functions for the respective isotopes in the DAMA detectors. It is important not to forget the factor $1/q_{\mathrm{Na/I}}$ in front of $S_{m,\mathrm{Na/I}}$ from the partial derivative.

At this stage, a short annotation regarding the so-called channeling effect is appropriate, which was assumed to be important regarding the discrepancies between the DAMA claim and the results from other experiments. As stated before, typically only the small fraction q of the recoil energy is measured by the DAMA detectors. However, nuclei that recoil along characteristic axes through the crystal can in principal travel large distances without colliding with other nuclei. Thus, in this case, they transfer their whole energy to the electrons rather than nuclei, which effectively leads to a quenching factor of order unity. The DAMA collaboration has used simulations to determine the energy dependent fractions of recoils with $q = 1$ for Na (f_{Na}) and I (f_{I}), and they obtained the result that the channeling effect is indeed significant [53]. Given these results, the CDMS collaboration included these fractions of channeled events in the computations. In this case, the theoretical predictions for $S_{m,\mathrm{tot}}$ are given by:

$$\begin{aligned} S_{m,\mathrm{tot}}^{\mathrm{channeling}}(E_{\mathrm{det}}) \;=\; & \frac{m_{\mathrm{Na}}}{m_{\mathrm{Na}}+m_{\mathrm{I}}}\left(f_{\mathrm{Na}}\big(E_{\mathrm{det}}\big)\cdot S_{m,\mathrm{Na}}\Big(E_{\mathrm{det}}\Big) + \frac{1-f_{\mathrm{Na}}\left(\frac{E_{\mathrm{det}}}{q_{\mathrm{Na}}}\right)}{q_{\mathrm{Na}}}\cdot S_{m,\mathrm{Na}}\left(\frac{E_{\mathrm{det}}}{q_{\mathrm{Na}}}\right)\right) \\ & + \frac{m_{\mathrm{I}}}{m_{\mathrm{Na}}+m_{\mathrm{I}}}\left(f_{\mathrm{I}}\big(E_{\mathrm{det}}\big)\cdot S_{m,\mathrm{I}}\Big(E_{\mathrm{det}}\Big) + \frac{1-f_{\mathrm{I}}\left(\frac{E_{\mathrm{det}}}{q_{\mathrm{I}}}\right)}{q_{\mathrm{I}}}\cdot S_{m,\mathrm{I}}\left(\frac{E_{\mathrm{det}}}{q_{\mathrm{I}}}\right)\right) \end{aligned} \tag{2.55}$$

However, an advanced analysis recently published in [54] has shown that the fractions of channeled events determined by the DAMA collaboration are only valid for ions starting their motion close to the middle of a channel, but not for the case of the direct detection of WIMPs. It was concluded that regarding WIMP interactions the effect of channeling is nearly negligible.

In the next step, theoretical expectations, calculated according to (2.54), have to be compared to the spectrum shown in the top plot of Fig. 2.11. In order to be as precise as

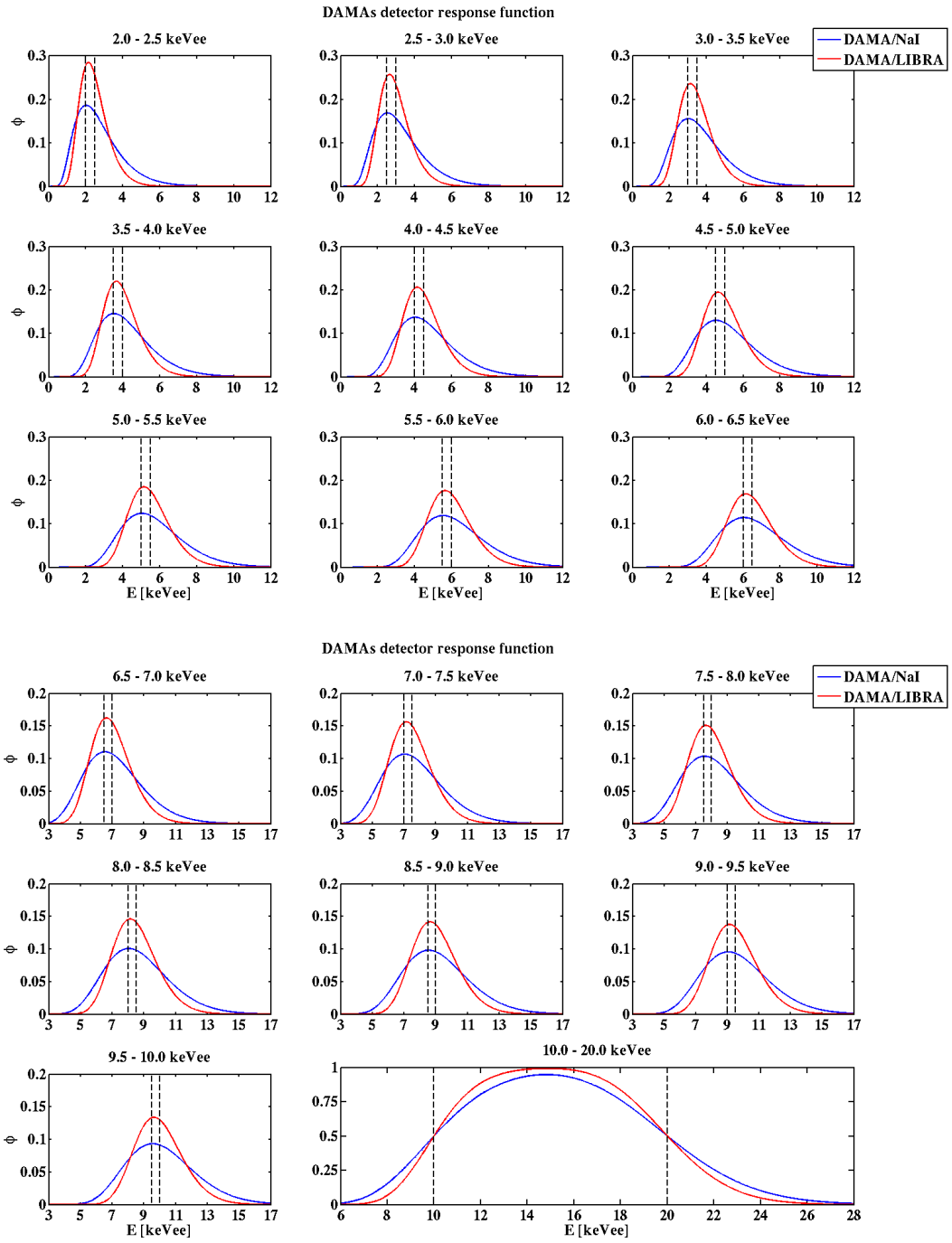

Figure 2.13: Detector response functions for all energy ranges considered in the analysis of the modulation spectrum S_m, shown in the top plot of Fig. 2.11. The function corresponding to DAMA/LIBRA (red) has a sharper peak than the function corresponding to DAMA/NaI (blue) due to the better energy resolution.

possible, these rates are averaged over each energy bin convolving $S_{m,\mathrm{tot}}$ with a Gaussian representing the detector resolution. Since the measured spectrum contains the combined results from DAMA/LIBRA and DAMA/NaI, the resolutions are weighted with the corresponding exposure MT of the respective runs. Thus, the following prediction has to be compared to the DAMA rate in the i^{th} energy bin:

$$\begin{aligned} S_{m,i} &= \frac{1}{E_{i+1}-E_i}\int_0^\infty \mathrm{d}E_{\mathrm{det}}\, S_{m,\mathrm{tot}}(E_{\mathrm{det}}) \\ &\quad \cdot\left(\frac{\mathrm{MT}_{\mathrm{DAMA/LIBRA}}}{\mathrm{MT}_{\mathrm{DAMA/NaI}}+\mathrm{MT}_{\mathrm{DAMA/LIBRA}}}\,\Phi_{\mathrm{DAMA/LIBRA}}\big(E_{\mathrm{det}},E_i,E_{i+1}\big)\right. \\ &\quad \left.+\frac{\mathrm{MT}_{\mathrm{DAMA/NaI}}}{\mathrm{MT}_{\mathrm{DAMA/NaI}}+\mathrm{MT}_{\mathrm{DAMA/LIBRA}}}\,\Phi_{\mathrm{DAMA/NaI}}\big(E_{\mathrm{det}},E_i,E_{i+1}\big)\right). \end{aligned} \tag{2.56}$$

Since it is the idea to perform a χ^2-goodness-of-fit test and since there are three free parameters (m_W, δ, σ), it is useful to write this theoretical expectation in an appropriate form. The dependence of $S_{m,i}$ on m_W and δ is rather complicated, but it is just proportional to σ. Therefore, it is convenient to define:

$$S_{m,i} = \sigma \cdot A_i(m_W,\delta)\,. \tag{2.57}$$

Thus, the χ^2 can be written as

$$\chi^2 = \sum_{i=1}^{17}\left(\frac{S_i-\sigma\cdot A_i(m_W,\delta)}{\sigma_i}\right)^2 = U\cdot\left(\sigma-\frac{V}{U}\right)^2-\frac{V^2}{U}+W\,, \tag{2.58}$$

where S_i denotes the rate measured by DAMA, and σ_i represents the corresponding error as shown in Fig. 2.11. The new parameters U, V and W are given by:

$$\begin{aligned} U &= \sum_{i=1}^{17}\left(\frac{A_i}{\sigma_i}\right)^2 \\ V &= \sum_{i=1}^{17}\left(\frac{A_i\,S_i}{\sigma_i^2}\right) \\ W &= \sum_{i=1}^{17}\left(\frac{S_i}{\sigma_i}\right)^2. \end{aligned} \tag{2.59}$$

U and V depend on m_W and δ. Since U is always positive, considering χ^2 just as a function of σ for a given WIMP mass and mass splitting, it is a simple parabola with a minimum at V/U, which turns out to be very useful. For the χ^2-goodness-of-fit test it is demanded that the absolute value of χ^2 is below a certain value, which depends on the number of free parameters (17) and the desired level of compatibility between the expectation and the data (90%). This value C is given by:

$$C = F^{-1}_{\chi^2,17}(0.9) \approx 24.77\,, \tag{2.60}$$

where $F_{\chi^2,17}$ denotes the cumulative distribution function of the χ^2-distribution with 17 degrees of freedom. The application of this formula implies that the χ^2, given in (2.58), indeed follows the just mentioned χ^2-distribution. Note, that the χ^2 was not minimized in order to find an absolute minimum and to subsequently define a confidence region by restricting $\Delta\chi^2$ with respect to the value at this minimum, which would correspond to finding the "most likely" parameters. Instead the absolute value of χ^2 was constrained yielding "allowed" regions in parameter space, which are suited for comparisons with other experiments. An extensive discussion regarding the difference between both kinds of regions can be found in [47]. The actual determination of the DAMA allowed regions was performed by scanning over the parameters m_W and δ and calculating the respective minimum for σ, given by $\sigma_{\min} = V/U$. If this minimum yielded a χ^2 below C (2.60), the tested WIMP mass and mass splitting was "accepted". In this case an allowed interval for σ existed, which was bounded by:

$$\sigma_{1,2} = \frac{V \pm \sqrt{V^2 + U\,(C - W)}}{U} \tag{2.61}$$

Defining the allowed regions in this way, it was only necessary to scan over two parameters instead of all three and to compute as much as possible analytically. Finally, the outcome is the three-dimensional allowed parameter space shown in Fig. 2.14. The allowed high-mass region is due to scattering from I. The small low-mass region, which disappears for higher mass splittings, is caused by scattering from Na. Constraints on the DAMA allowed part of the parameter space emerging from CDMS data are shown in chapters 6.8 and 7.4 after an extensive discussion of the CDMS analysis.

Figure 2.15 is a repetition of Fig 2.11 showing the measured values of S_m (top) and S_0 (bottom). However, the theoretical predictions, which yield the minimum χ^2, are overlaid here. It should be mentioned again that these lines were not just obtained by fitting the rate, but the averaged rate in each energy bin, to the data. In order to investigate the results assuming only elastic scattering, the case where δ was fixed to 0 keV was separately considered. Moreover, both plots also include the results of both cases, assuming that the aforementioned calculations from the DAMA collaboration regarding channeling were correct. Thus, they were based on (2.55) rather than on (2.54). As discussed before, these results are now obsolete regarding the advanced analysis presented in [54]. All relevant values are given in the legend of the plot. The parameters

$$\begin{aligned} \delta &= 115 \text{ keV} \\ m_W &= 56.5 \text{ GeV/c}^2 \\ \sigma &= 2.3 \cdot 10^{-3} \text{ pb}\,, \end{aligned} \tag{2.62}$$

yield the best concordance with the measured modulated spectrum ($\chi^2 = 12.4$) if the channeling effect is discarded. Moreover, it is obvious from the bottom plot that all other scenarios yield a total rate, which is too high at low energies just above the threshold. The magenta/dotted line shows the correponding background obtained by subtracting the computed rate from the observed one. Obviously, most of the measured signal would be due to background. In this regard it would be interesting to get more input from the

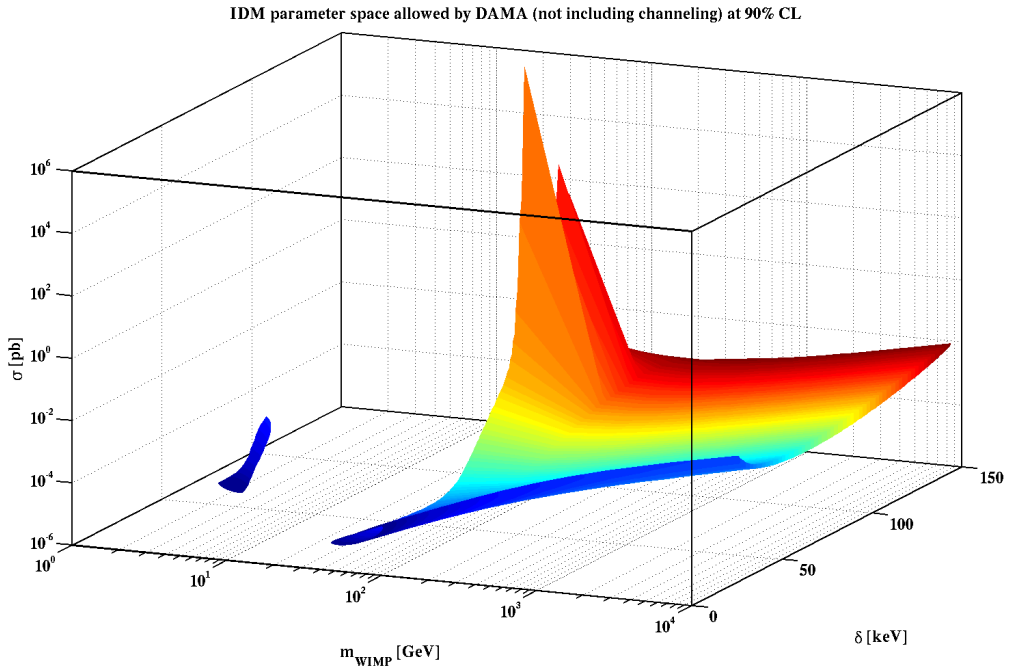

Figure 2.14: Regions allowed by DAMA considering spin-independent inelastic scattering in the three-dimensional parameter space, consisting of the WIMP mass m_W (m_{WIMP} in the plot), WIMP-mass splitting δ and WIMP-nucleon cross section σ. The high-mass region is due to scattering from I, and the small low-mass region is caused by scattering from Na. The "spikes" at the edges, where the allowed region curves up, are related to the binning used to scan over m_W and δ. The color-code was only used to improve the visibility of the three-dimensional region.

DAMA collaboration on the ^{40}K background peak at 3.2 keV [50]. Note, however, that the full allowed regions for a certain confidence level have to be considered to decide whether a certain scenario is excluded or not.

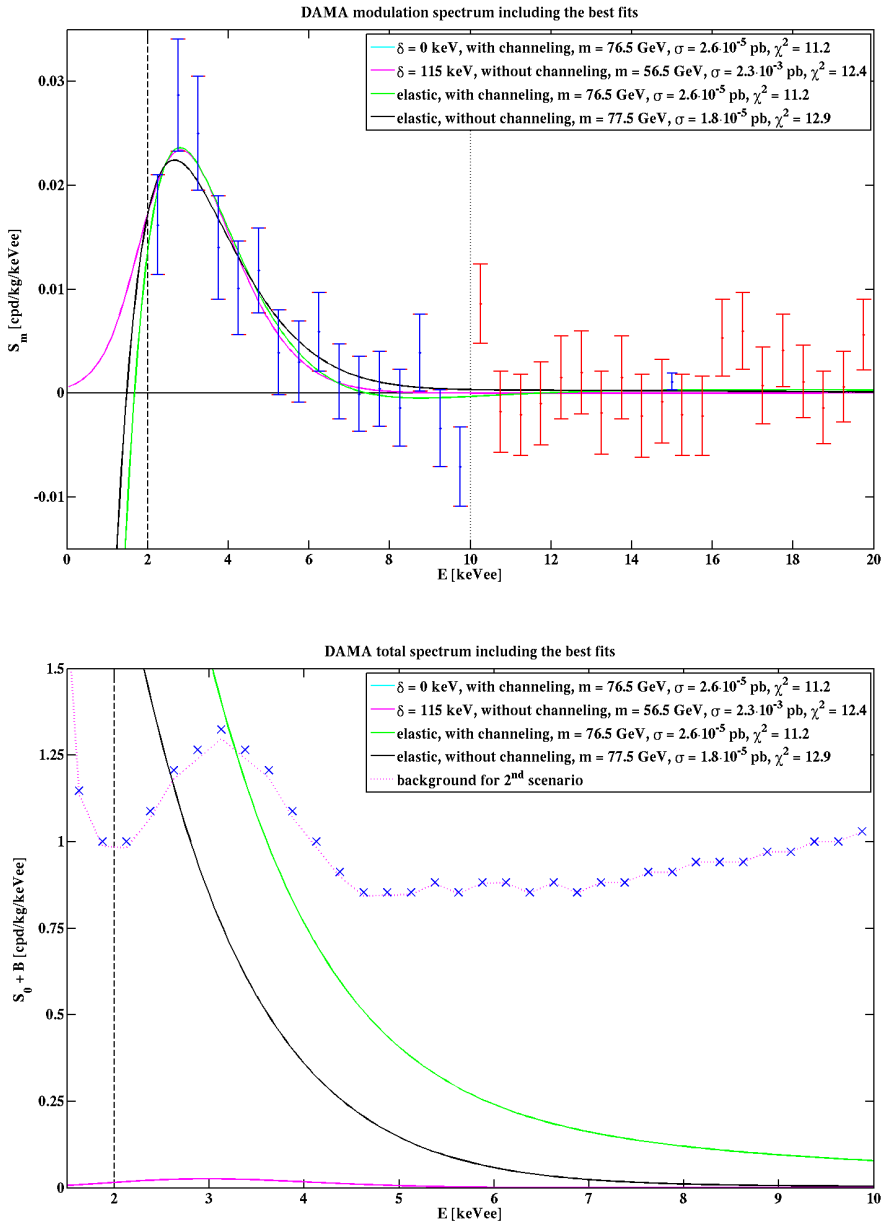

Figure 2.15: *Top*: Modulation spectrum S_m of the DAMA experiment, as shown in the top plot of Fig. 2.11, overlaid with the best fits considering several scenarios as discussed in the text. In the two scenarios labeled "elastic" δ was fixed to 0 keV, while it was treated as a free parameter in the other two cases. The corresponding parameters are given in the legend. Note, that, if channeling is included, the best fit for inelastic scattering accidently yields $\delta = 0$ keV. (So the cyan line is just below the green line.) *Bottom*: Constant part (regarding time) of the rate S_0 of the DAMA experiment, as shown in the bottom plot of Fig. 2.11, overlaid with the theoretical predictions considering the scenarios and parameters that provide the best fits to the modulation spectrum. The only valid scenario is the one with $\delta = 115$ keV (magenta/solid). The magenta/dotted line shows the corresponding background obtained by subtracting the computed rate from the observed one.

Chapter 3

Constraints on Kaluza-Klein dark matter

The direct detection of WIMP dark matter was presented in great detail in the previous chapter. In particular, the two possible types of interactions, spin-independent and spin-dependent scattering, were discussed. However, the given elucidations were rather general without a specific model determining the actual coupling constants. Such a discussion is presented in the current chapter. SUSY [10] is certainly by far the most extensively studied framework regarding physics beyond the standard model. However, in order to take "the less traveled road", WIMP candidates from UEDs [11] are examined in the following, and constraints are set on the parameters of that model. The WIMP candidates, emerging from this framework, are also referred to as Kaluza-Klein dark matter, since T. Kaluza and O. Klein were the first physicist who considered a theory based on additional space dimensions [55, 56].[1] The plots shown in this chapter include upper limits from various experiments. The status of these limits is not up-to-date, since the study was performed a few years ago and published in 2008 [2].

3.1 A brief summary of Universal Extra Dimensions

In models with universal extra dimensions [11, 57] all standard model particles are promoted to one or more compactified flat extra dimensions. The simplest version considers just one additional dimension with a compactification on a simple interval. The corresponding topology is denoted S_1/Z_2, which means that opposite sides of a circle are identified to create a line segment with two endpoints. After removing the additional dimension from the Lagrangian via integration, the effective four-dimensional theory contains all standard model particles (as it should be) and a so-called tower of additional particles for each of the standard model particles. They are labeled by an integer n. At tree level their masses

[1] Note, that it was their intention to unify the theories of electrodynamics and gravitation, which was unsuccessful as is known.

are given by

$$m_n^2 = m^2 + \frac{n^2}{R^2}\,, \tag{3.1}$$

where R is the compactification scale, and m is the mass of the corresponding standard model particle. It turns out that the so-called Kaluza-Klein parity $(-1)^n$ is a conserved quantity, which follows from invariance under reflections with respect to the center of the interval constituting the compactified extra dimension. It ensures that the lightest Kaluza-Klein particle with $n = 1$ is stable and thus naturally constitutes a valid WIMP candidate. A nice feature of the UED model is the fact that the Langrangian only contains standard model parameters, which are all well determined except for the Higgs mass m_h. However, additional parameters can arise from boundary interactions in the compactified extra dimension. These interactions are in principle arbitrary. For simplicity, they are usually assumed to vanish at a certain cutoff scale Λ. Since there are no compelling reasons corroborating this assumption, the UED model should be considered to be an effective theory, which is only valid up to Λ. In this so-called minimal UED model (MUED) the compactification scale R and the cutoff scale Λ are the only additional parameters.

From (3.1) it can be observed that R basically determines the masses of the Kaluza-Klein particles, since it is expected that $1/R \sim$ TeV, so that the standard model particle masses only yield a subdominant contribution to the Kaluza-Klein particle masses. This also means that the latter are highly degenerated. This is an important property of the UED model with significant implications regarding the detectability of the proposed new particles in direct detection and collider experiments as discussed below in great detail. It also indicates that radiative corrections are very important to determine the actual particle masses of all modes with $n = 1$. This is necessary since only the lightest of these particles could constitute the WIMP candidate emerging from this theory. Nevertheless, given that the boundary interactions are assumed to vanish at the cutoff scale, it is possible to determine radiative corrections to the masses applying standard renormalization methods. In the MUED framework it turns out that the lighest Kaluza-Klein particle is the Kaluza-Klein photon γ_1. However, given that the made assumption regarding the boundary interactions is arbitrary, it seems advisable to consider more general scenarios. A typical procedure is to completely ignore the physics at the cutoff scale and to simply assume that other particles could be the lightest Kaluza-Klein particle. In the following, apart from the γ_1, the Kaluza-Klein Z boson Z_1 is also considered as a possible dark matter candidate. Similar reasonings also hold for two additional extra dimensions. The spinless Kaluza-Klein photon γ_H, emerging from this framework, is also investigated below. So in total three different possible WIMPs are considered.

In each case the generic framework consists of three free parameters, the standard model Higgs mass m_h, the mass of the considered WIMP candidate m_W, which is related to the compactification scale R (3.1), and the mass splitting

$$\Delta_{q_1} = \frac{m_{q_1} - m_W}{m_W} \tag{3.2}$$

between the lightest particle (the WIMP candidate) and the Kaluza-Klein quark. The

Kaluza-Klein modes with $n = 1$ of the quarks are assumed to be degenerated. Regarding the phenomenology of UED dark matter it should be mentioned that the parameters m_W and Δ_{q_1} are much more important than m_h. More details on UEDs are given in the summary article [11].

3.2 Spin-independent cross sections and experimental constraints

The general form of the spin-independent cross section is given in (2.23). In order to investigate the three mentioned WIMP candidates it is necessary to calculate the respective WIMP-nucleon couplings f_p and f_n. The Feynman diagrams contributing to the γ_1 scattering with quarks are shown in Fig. 3.1. In general, the WIMP-nucleon couplings are given by

$$f_p = \sum_{u,d,s} (\beta_q + \gamma_q) \langle p|\bar{q}q|p\rangle = \sum_{u,d,s} \frac{\beta_q + \gamma_q}{m_q} m_p f^p_{T_q} \ , \tag{3.3}$$

and similarly for f_n. The contributions from heavy quarks, which only contribute at the loop level through the gluon content of the nucleon, are conservatively ignored. m_p (m_n) stands for the proton (neutron) mass and m_q denotes the quark masses. The nucleon matrix elements are given by $f^p_{T_u} = 0.020 \pm 0.004$, $f^p_{T_d} = 0.026 \pm 0.005$, $f^n_{T_u} = 0.014 \pm 0.003$, $f^n_{T_d} = 0.036 \pm 0.008$, and $f^{p,n}_{T_s} = 0.118 \pm 0.062$ [58]. The numerical coefficients β_q and γ_q are defined as [59]

$$\begin{aligned}
\beta_q &= \frac{e^2}{\cos^2\theta_W}\left[E_q(Y^2_{q_L}\cos^2\alpha + Y^2_{q_R}\sin^2\alpha)\frac{m^2_{q^1_L} + m^2_{\gamma_1}}{(m^2_{q^1_L} - m^2_{\gamma_1})^2} + \frac{Y_{q_L} Y_{q_R} m_{q^1_L} \sin 2\alpha}{m^2_{\gamma_1} - m^2_{q^1_L}} + (L \to R)\right] \\
&\overset{\alpha=0}{\approx} E_q \frac{e^2}{\cos^2\theta_W}\left[Y^2_{q_L}\frac{m^2_{\gamma_1} + m^2_{q^1_L}}{(m^2_{q^1_L} - m^2_{\gamma_1})^2} + (L \to R)\right] \qquad (3.4) \\
\gamma_q &= m_q \frac{e^2}{2\cos^2\theta_W}\frac{1}{m^2_h} \ , \qquad (3.5)
\end{aligned}$$

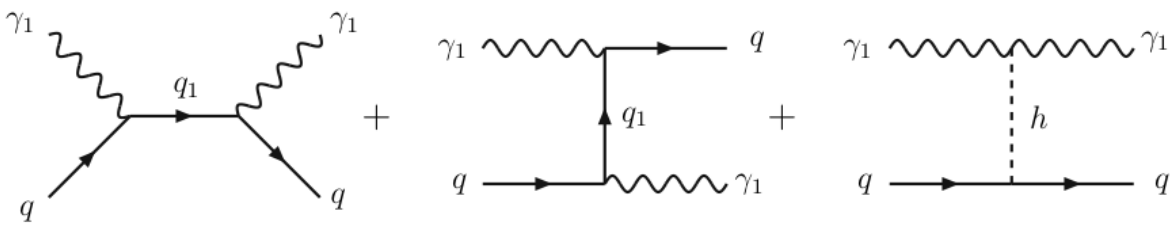

Figure 3.1: Tree-level diagrams for the elastic scattering of the γ_1 with quarks. The diagrams for the case of the Z_1 are similar.

where e is the electric charge, θ_W is the Weinberg angle, $m_{q_L^1}$ ($m_{q_R^1}$) is the mass of an $SU(2)_W$-doublet ($SU(2)_W$-singlet) Kaluza-Klein quark, and α is the mixing angle in the Kaluza-Klein quark mass matrix given by

$$\sin 2\alpha = \frac{2m_q}{(m_{q_L^1} + m_{q_R^1})} \,. \tag{3.6}$$

The first formula for β_q includes the mixing effect between two Kaluza-Klein quarks, while the second one is obtained in the limit when $\alpha = 0$. The mixing effect gives a minor correction to the cross section (at a few percent level). The convention used for the standard model hypercharge is $Y_i = Q_i - I_{3i}$, where Q_i (I_{3i}) is the electric charge (weak isospin) of particle i. E_q in (3.4) is the energy of a bound quark, which is conservatively replaced by the quark mass m_q. Its actual value is inconsequential, since the m_q factors in (3.4) and (3.5) cancel against the m_q factor in the denominator of (3.3). Note, that the two contributions (3.4) and (3.5) to the scalar interactions interfere constructively: even with extremely heavy Kaluza-Klein quark masses (large Δ_{q_1}), there is an inescapable lower bound on the scalar cross section for a given Higgs mass, since the Higgs contribution from (3.5) scales with the standard model Higgs mass m_h and not the Kaluza-Klein quark masses.

The analogous results for the case of Z_1 can be obtained from the above formulae by simple replacements: $m_{\gamma_1} \to m_{Z_1}$, $Y_{q_L} \to \frac{1}{2}$ and $Y_{q_R} \to 0$, since Z_1 is mostly the neutral $SU(2)_W$ gauge boson, which has no interactions with the $SU(2)_W$-singlet Kaluza-Klein quarks (or equivalently, the right-handed standard model quarks). In addition, one should replace $\frac{e}{\cos\theta_W} \to \frac{e}{\sin\theta_W}$ to account for the different gauge coupling constant.

The parameters β_q and γ_q, regarding the WIMP candidate arising from two extra dimensions γ_H, were published in [60], where a different convention for the hypercharges Y_i was used. The sum $\beta_q + \gamma_q$ is given by

$$\begin{aligned} \beta_q + \gamma_q &= \frac{e^2}{\cos^2\theta_W}\left[m_q (Y_{q_L} + Y_{q_R})^2 \left(\frac{1}{m_{q_1}^2 - (m_q - m_{\gamma_H})^2} + \frac{1}{m_{q_1}^2 - (m_q + m_{\gamma_H})^2} \right) \right. \\ &+ \left. m_{\gamma_H} (Y_{q_L}^2 + Y_{q_R}^2) \left(\frac{1}{m_{q_1}^2 - (m_q + m_{\gamma_H})^2} - \frac{1}{m_{q_1}^2 - (m_q - m_{\gamma_H})^2} \right) + \frac{m_q}{2m_h^2} \right] \end{aligned} \tag{3.7}$$

where m_{γ_H} is the mass of the spinless photon, m_{q_1} is the (common) mass of the $SU(2)_W$-doublet and $SU(2)_W$-singlet Kaluza-Klein quarks, while m_q is the corresponding standard model quark mass.

Theoretical predictions for the spin-independent WIMP-nucleon elastic scattering cross section are shown in Fig. 3.2 for all three considered WIMP candidates. The boundaries of the shown regions are selected for 0.01 (upper boundaries of the regions) $< \Delta_{q_1} <$ 0.5 (lower boundaries of the regions), while the Higgs mass m_h is fixed to 120 GeV/c^2. In all cases the cross sections decrease as a function of the WIMP mass. This is due to the inverse scaling of the Kaluza-Klein quark exchange contributions with the Kaluza-Klein mass scale. It can be noticed that the scalar cross section for Z_1 is more than one

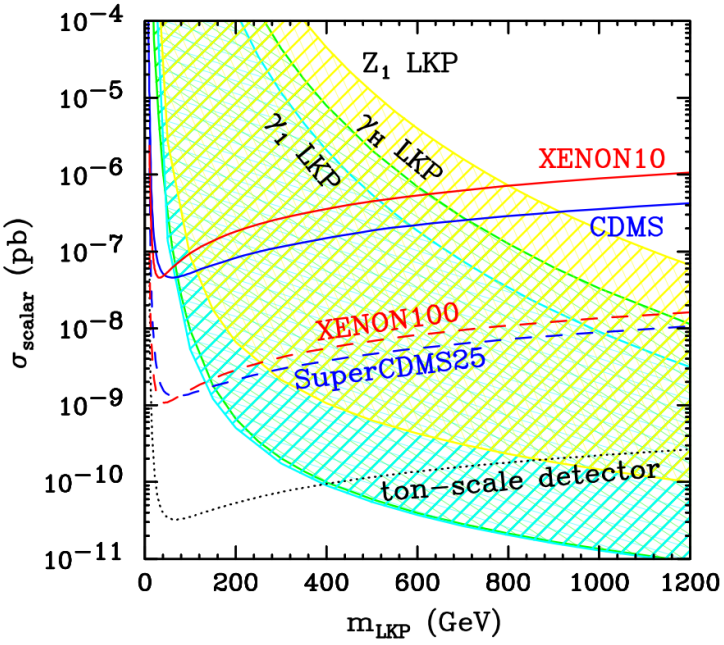

Figure 3.2: Current (in 2008) and projected experimental limits on the spin-independent WIMP-nucleon-scattering cross section together with the theoretically expected γ_1 (blue/shaded), Z_1 (yellow/shaded) and γ_H (green/shaded) regions. The boundaries of the predicted regions are selected for 0.01 (upper boundaries of the regions) $< \Delta_{q_1} <$ 0.5 (lower boundaries of the regions), while the Higgs mass m_h is fixed to 120 GeV/c^2. The solid lines are the current (in 2008) experimental upper bounds (90% C.L.) from the CDMS (blue) and XENON10 (red) experiments. The dashed lines are expected sensitivities for the SuperCDMS 25 kg (blue) and XENON100 (red) experiments, which will be operated in the near future. The dotted line is the expected sensitivity for a ton-scale detector.

order of magnitude larger than the scalar cross section for γ_1 of the same mass. This is mostly due to the larger $SU(2)_W$ gauge coupling. The size of the γ_H signal is about the same order as the γ_1 cross sections. Notice, that even when the Kaluza-Klein quarks are very heavy, there is still a reasonable cross section, which is due to the Higgs mediated contribution. Perhaps the most noteworthy feature is the significant enhancement of the direct detection signals at small Δ_{q_1}, often by several orders of magnitude. This greatly enhances the prospects for detecting Kaluza-Klein dark matter, if the mass spectrum turns out to be rather degenerated. Moreover, the plot also contains upper bounds for the spin-independent cross section from CDMS [61] and XENON10 [62] together with projected sensitivities for SuperCDMS 25 kg [63], XENON100 [64] and for a ton-scale detector. The small mass splitting regions are excluded up to a mass of about 600 GeV/c^2, 900 GeV/c^2 and 700 GeV/c^2 for γ_1, Z_1 and γ_H, respectively. For large mass splittings of $\Delta_{q_1} = 0.5$, only masses below about 100 GeV/c^2 can be probed. Future ton-scale direct detection experiments should cover most of the interesting WIMP parameter space.

3.3 Spin-dependent cross sections and experimental constraints

Since the γ_H is a scalar particle, there is no spin-dependent cross section. Thus, only the γ_1 and Z_1 are discussed in this section.

The general form of the spin-dependent cross section can be found in (2.34). The couplings to protons and neutrons for the γ_1 are given by [59]

$$a_{p,n} = \frac{e^2}{4\sqrt{3}G_F \cos^2\theta_W} \sum_{u,d,s} \left[\frac{Y_{q_L}^2}{m_{q_L^1}^2 - m_{\gamma_1}^2} + (L \to R) \right] \Delta_q^{p,n} \,, \tag{3.8}$$

where $\Delta_q^{p,n}$ denotes the fraction of the nucleon spin carried by the quark q. The values $\Delta_u^p = \Delta_d^n = 0.78 \pm 0.02$, $\Delta_d^p = \Delta_u^n = -0.48 \pm 0.02$ and $\Delta_s^p = \Delta_s^n = -0.15 \pm 0.02$ were used [65]. The same replacements as in the spin-independent case can be used to obtain the couplings for the Z_1. Notice, that since in the given setup there are only two relevant model parameters: m_W and Δ_{q_1}, there is a certain correlation between a_p and a_n, depending on the nature of the WIMP.

Figure 3.3 shows predictions for the spin-dependent WIMP-nucleon cross section regarding both (a) pure neutron and (b) pure proton couplings for the γ_1 and Z_1 for a range

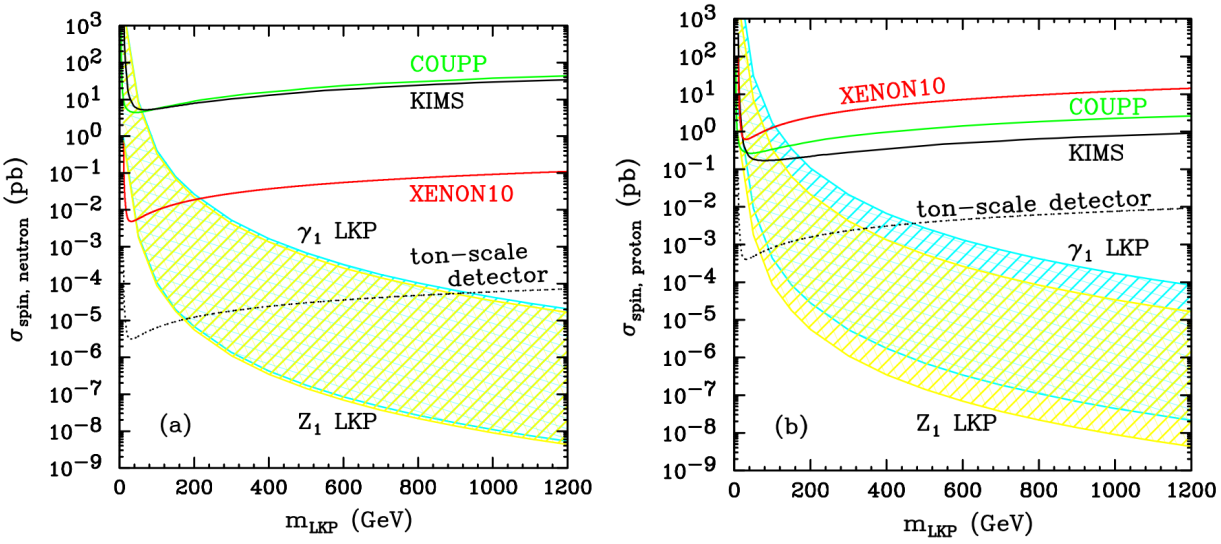

Figure 3.3: Current (in 2008) experimental limits on the spin-dependent (a) neutron- and (b) proton-scattering cross section together with the predicted spin-dependent WIMP-neutron (proton) cross sections for γ_1 (blue/shaded) and Z_1 (yellow/shaded). The boundaries of the predicted regions are selected for 0.01 (upper boundaries of the regions) $< \Delta_{q_1} <$ 0.5 (lower boundaries of the regions). The solid curves for each plot are the upper bounds (90% C.L.) from the COUPP (green), KIMS (black) and XENON10 (red) experiments. The dotted line shows the expected sensitivity for a ton-scale detector.

of mass splittings 0.01 (upper boundaries of the regions) $< \Delta_{q_1} <$ 0.5 (lower boundaries of the regions). The cross sections exhibit the same general trends as the spin-independent results: they decrease with the Kaluza-Klein mass scale, and they are enhanced for small mass splittings Δ_{q_1}. It is noteworthy that the theoretical γ_1 and Z_1 regions are overlapping for pure neutron couplings, while for pure proton coupling these can be distinguished for a given mass splitting. Besides, one peculiar feature is that the proton and neutron spin-dependent cross sections are equal in the case of Z_1. This is an exact statement, which is due to the fact that Z_1 does not particularly discriminate between the different quark flavors in the nucleon – it couples with equal strength to both up- and down-type (left-handed) quarks. On the other hand, γ_1 couples differently to u and d because of the different hypercharges of the right-handed quarks. As a result, the cross sections on protons and neutrons differ in the case of γ_1. Interestingly, for a given WIMP mass m_{γ_1} and mass splitting Δ_{q_1}, the proton cross section is larger than the neutron cross section by about a factor of 4, which is due to a numerical coincidence involving the values of the quark hypercharges and the $\Delta_q^{p,n}$ parameters. This can be simply understood in terms of the relative scaling of the a_p and a_n parameters. In the case of γ_1 they differ by a factor of -2, while in the case of Z_1 they are the same. Because of this simple scaling, for a given mass m_{γ_1}, the proton cross section at a certain Δ_{q_1} coincides with the neutron cross section for half the mass splitting $\Delta_{q_1}/2$ since to leading order both the proton and the neutron cross sections are proportional to $(\Delta_{q_1})^{-2}$. Besides, the plots also contain experimental constraints from XENON10 [43], COUPP [44] and KIMS [45]. The most stringent spin-dependent pure neutron upper bound is set by the XENON10 experiment, while the best spin-dependent cross section for pure proton couplings in the region of interesting WIMP masses (>500 GeV/c^2) comes from the KIMS experiment.

3.4 Limits on Kaluza-Klein Dark Matter

Three different dark matter candidates arising from UEDs were discussed in the previous sections: the γ_1, the Z_1 and the γ_H. In this section, the shown direct detection constraints on the respective cross sections are converted to limits on the model parameters particularly on the mass splitting parameter Δ_{q_1}. Where applicable, constraints from high energy collider experiments and from considerations of the relic density are included. The focus lies on the γ_1 and Z_1, whose relic density can be reliably calculated, including all relevant coannihilation processes [66, 67].

Figure 3.4 presents a combination of results for the case of (a) γ_1 and (b) Z_1. As mentioned earlier, the two most relevant parameters are the WIMP mass (m_{γ_1} or m_{Z_1}, correspondingly) and the mass splitting Δ_{q_1} between the WIMP and the Kaluza-Klein quarks. Therefore, both of these parameters are assumed to be free parameters without assuming the MUED relation among them. For simplicity, the $SU(2)_W$-doublet Kaluza-Klein quarks and the $SU(2)_W$-singlet Kaluza-Klein quarks are assumed to be degenerated, so that there is a single mass splitting parameter which has been called Δ_{q_1}. However, this assumption is only made for convenience and does not represent a fundamental limitation – all of the

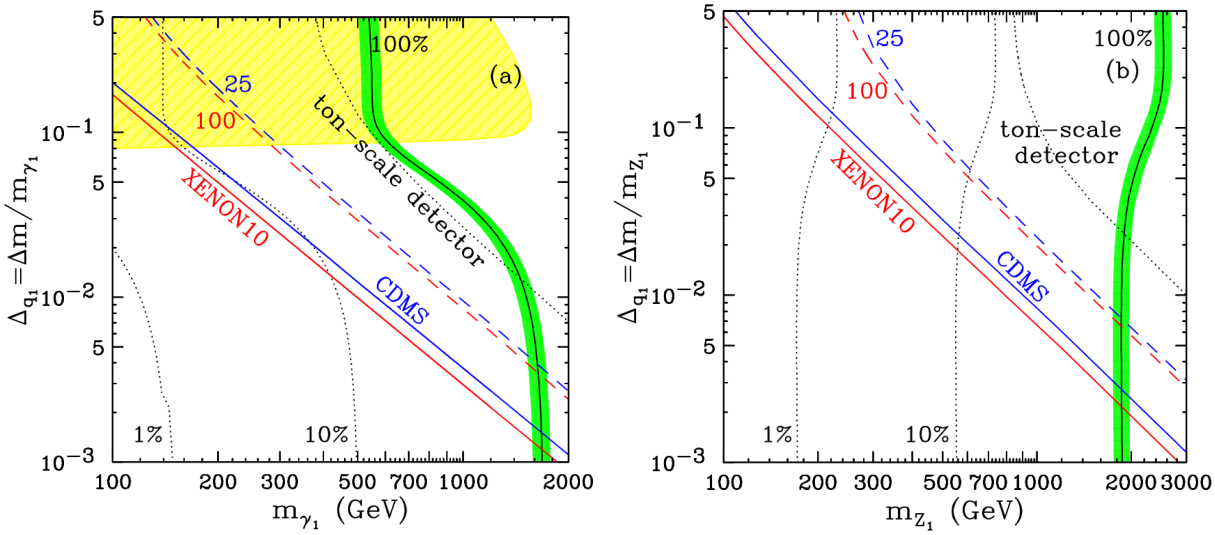

Figure 3.4: Combined plot of the direct detection limit on the spin-independent cross section, the limit from the relic abundance and the LHC reach for (a) γ_1 and (b) Z_1, in the parameter plane of the WIMP mass and the mass splitting Δ_{q_1}. The remaining Kaluza-Klein masses have been fixed as given in the text and the standard model Higgs mass is $m_h = 120\,\mathrm{GeV/c^2}$. The black/solid line accounts for all of the dark matter (100%) and the two black/dotted lines show 10% and 1%, respectively. The green band shows the WMAP range, $0.1037 < \Omega_{\mathrm{CDM}}h^2 < 0.1161$. The blue(red)/solid line labelled by CDMS (XENON10) shows the current (in 2008) limit of the experiment, whereas the dashed and dotted lines represent projected limits of future experiments as shown in Fig. 3.2. In the case of the γ_1, a ton-scale experiment will rule out most of the parameter space, while there is little parameter space left in the case of Z_1. The yellow region in the case of the γ_1 shows parameter space that could be covered by the collider search in the $4\ell + \not{E}_T$ channel at the LHC with a luminosity of 100 fb^{-1} [68].

results can be readily generalized for different Kaluza-Klein quark mass splittings (i.e. several individual Δ parameters). The masses of the remaining Kaluza-Klein particles in the spectrum are fixed as follows: in the case of γ_1, the MUED spectrum is used, while in the case of Z_1 the gluon and the remaining particles are taken to be respectively 20% and 10% heavier than the Z_1. This choice is only made for definiteness and does not carry a big impact on the validity of the results, as long as the remaining particles are sufficiently heavy, so that they do not participate in coannihilation processes.

In Fig. 3.4 the limit on the spin-independent elastic scattering cross section, the limit on the relic abundance [66, 67] and the LHC reach in the four leptons plus missing energy ($4\ell + \not{E}_T$) channel, which has been studied in [68], are imposed. This signature results from the pair production (direct or indirect) of $SU(2)_W$-doublet Kaluza-Klein quarks, which subsequently decay to Z_1's and jets. The leptons (electrons or muons) arise from the $Z_1 \to \ell^+\ell^-\gamma_1$ decay, whose branching fraction is approximately 1/3 [68]. Requiring a 5σ excess at a luminosity of 100 fb^{-1}, the LHC reach extends up to $R^{-1} \approx m_{\gamma_1} \sim 1.5\ \mathrm{TeV/c^2}$,

which is shown as the right-most boundary of the yellow/shaded region in Fig. 3.4(a). The slope of that boundary is due to the fact that as Δ_{q_1} increases, so do the Kaluza-Klein quark masses, and their production cross sections are correspondingly getting suppressed, diminishing the reach. The loss in cross section is accounted for according to the results from Ref. [69], assuming also that the level-2 Kaluza-Klein particles are about two times heavier than those at level 1. Points which are well inside the yellow/shaded region would be discovered much earlier at the LHC. Notice, however, that the LHC reach in this channel completely disappears for Δ_{q_1} less than about 8%. This is where the Kaluza-Klein quarks become lighter than the Z_1 (recall that in Fig. 3.4(a) m_{Z_1} was fixed according to the MUED spectrum) and the $q_1 \to Z_1$ decays are turned off. Instead, the Kaluza-Klein quarks all decay directly to the γ_1 and (relatively soft) jets, presenting a monumental challenge for an LHC discovery. So far, there have been no studies of the collider phenomenology of a scenario where the Z_1 is the lightest Kaluza-Klein particle, but it appears to be extremely challenging, especially if the Kaluza-Klein quarks are light and decay directly to the lightest Kaluza-Klein particle. This is why there is no LHC reach shown in Fig. 3.4(b). In conclusion of the discussion of the collider reaches exhibited in Fig. 3.4, it is important to draw attention once again to the lack of sensitivity at small Δ_{q_1}: such small mass splittings are quite problematic for collider searches (see, for example, [70, 71] for an analogous situation regarding SUSY).

The plots also contain relic density constraints. The green/shaded region labeled by 100% represents the 2σ WMAP band, $0.1037 < \Omega_{\rm CDM}h^2 < 0.1161$ [72] and the black/solid line inside this band is the central value $\Omega_{\rm CDM}h^2 = 0.1099$. The region above and to the right of this band is ruled out, since UED would then predict too much dark matter. The green/shaded region is where Kaluza-Klein dark matter is sufficient to explain all of the dark matter in the universe, while in the remaining region to the left of the green band the lightest Kaluza-Klein particle can make up only a fraction of the dark matter in the universe. The black/dotted contours indicate the parameter region where it would contribute only 10% and 1% to the total dark matter budget. Finally, the solid (CDMS in blue and XENON10 in red) lines show the current (in 2008) direct detection limits, while the dotted and dashed lines show projected sensitivities for future experiments. Note, that here and in the rest of this chapter, when presenting experimental limits in an underdense or an overdense parameter space region, the expected direct detection rates are not rescaled with the calculated relic density. The latter is much more model-dependent, e.g. the mismatch with the WMAP value may be fixed by non-standard cosmological evolution, having no effect on the rest of our analysis.

Figure 3.4 demonstrates the complementarity between the three different types of probes which were considered. First, the parameter space region at very large WIMP masses is inconsistent with cosmology – if the dark matter WIMP is too heavy, its relic density is too large. The exact numerical bound on the WIMP mass may vary, depending on the particle nature of the WIMP (compare Fig. 3.4(a) to Fig. 3.4(b)) and the presence or absence of coannihilations (compare the m_W bound at small Δ_{q_1} to the bound at large Δ_{q_1}). Nevertheless, it can be observed that, in general, cosmology provides an upper limit on the WIMP mass. On the other hand, colliders are sensitive to the region of relatively

large mass splittings Δ_{q_1}, while direct detection experiments are at their best at small Δ_{q_1} and small m_W. The relevant parameter space is therefore getting squeezed from opposite directions and is bound to be covered eventually. This can already be seen in the case of γ_1 from Fig. 3.4(a): the future experiments push up the current (in 2008) limit almost to the WMAP band. Unfortunately in the case of Z_1 the available parameter space is larger and will not be closed with the currently envisioned experiments alone. However, one should keep in mind that detailed LHC studies for that scenario are still lacking.

While it was previously argued that m_W and Δ_{q_1} are the most relevant parameters for UED dark matter phenomenology, the dependence on the standard model Higgs mass m_h, which is currently still unknown, is investigated for completeness. Therefore, in Fig. 3.5, the information from Fig. 3.2 is tranlated into the m_W-m_h plane, for a given fixed Kaluza-Klein mass splitting of $\Delta_{q_1} = 0.1$, now taking the Higgs mass m_h as a free parameter. In each panel the horizontal black/solid lines mark the Higgs mass bound of 114 GeV/c^2, while the diagonal black/solid lines show the indirect limit from the oblique corrections in this model [73]. One should keep in mind that the latter have been calculated only for the case of γ_1, and only within the framework of minimal UED. The line shown in Fig. 3.5(b) is therefore only for illustration. Furthermore, the γ_1 calculation itself may be subject to modifications in the more general scenarios, which are considered here. For low m_h, the limit on m_W (or equivalently, the compactification scale) is $m_W \sim R^{-1} \gtrsim 600$ GeV/c^2 (for $m_t = 173$ GeV/c^2), but it gets weaker for larger m_h, so that m_W values as low as 300 GeV/c^2

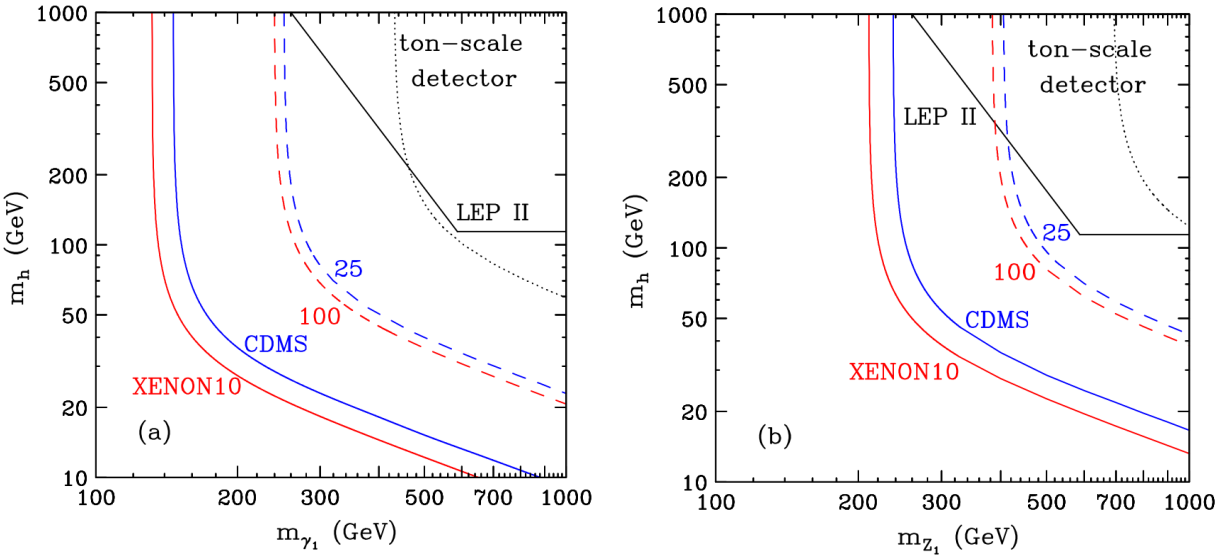

Figure 3.5: Limit on the standard model Higgs mass m_h for (a) γ_1 and (b) Z_1 for a given $\Delta_{q_1} = 0.1$. The horizontal black/solid line is the lower bound on m_h from LEP-II (90% C.L. at a top quark mass of 173 GeV/c^2). The diagonal black/solid line delineates the region disfavored by precision data. The solid curves are the current (in 2008) limits from CDMS (in blue) and XENON10 (in red). The dashed curves (SuperCDMS 25 kg and XENON100) and the dotted line (ton-scale detector) are the projected sensitivities for the future experiments.

are still allowed, if the standard model Higgs boson is very heavy [74]. Figure 3.5 also shows the current (solid lines) limits from CDMS (in blue) and XENON10 (in red), their projected near-future sensitivities, SuperCDMS 25 kg and XENON100 (dashed lines), and the projected sensitivity of a ton-scale detector (dotted line). The shape of these contours is easy to understand. At large m_h, the Higgs exchange diagram in Fig. 3.1 decouples, the elastic scattering rate becomes independent of m_h and the direct detection experimental sensitivity is only a function of m_W (since Δ_{q_1} is held fixed). In the other extreme, at small m_h, the Higgs exchange diagram dominates, and the sensitivity now depends on both m_h and m_W. Unfortunately, for $\Delta_{q_1} = 0.1$ the current (in 2008) direct detection bounds do not extend into the interesting parameter space region, but future experiments will eventually start probing the large m_h corner of the allowed parameter space. On the positive side, one important lesson from Fig. 3.5 is that the m_h dependence starts showing up only at very low values of m_h, which have already been ruled out by the Higgs searches at colliders. This observation confirms that when it comes to interpreting existing and future experimental limits on WIMPs from UEDs in terms of model parameters, m_W and Δ_{q_1} are indeed the primary parameters, while m_h plays a rather secondary role.

Note, that the LHC will be able to probe all of the parameter space shown in Fig. 3.5a through the $4\ell + \not{E}_T$ signature, while the discovery of UED in Fig. 3.5(b) appears quite problematic. Of course, the standard model Higgs boson will be discovered in both cases, for the full range of m_h masses shown.

In the following, constraints from spin-dependent elastic scattering are discussed. Similar to Fig. 3.4, in Fig. 3.6 existing limits from three different experiments (XENON10,

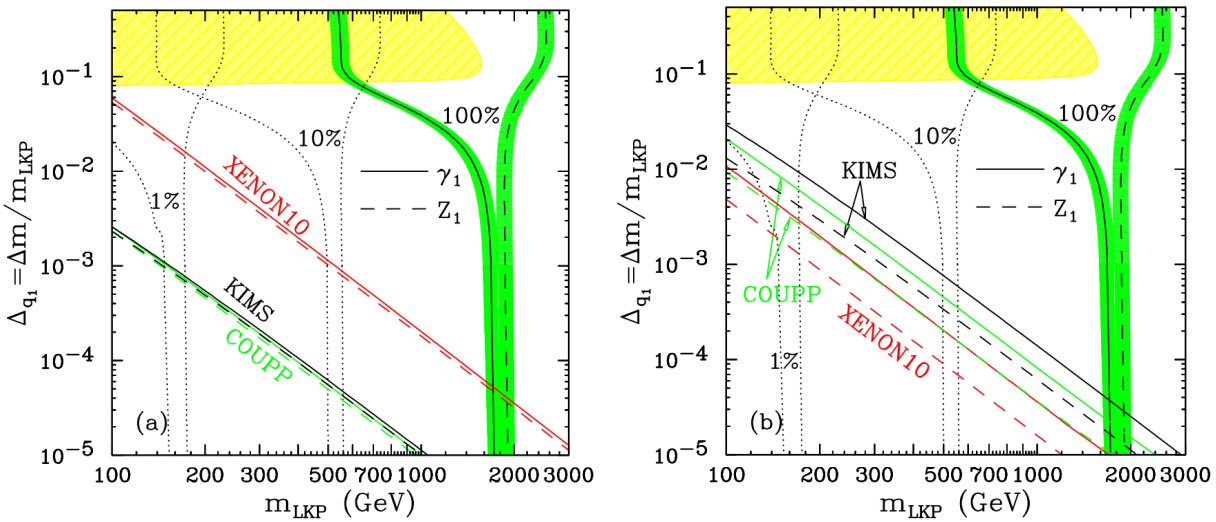

Figure 3.6: Experimental upper bounds (90% C.L.) on the spin-dependent elastic scattering cross sections on (a) neutrons and (b) protons in the m_W-Δ_{q_1} plane. The solid (dashed) curves are limits on γ_1 (Z_1) for each experiment. Shaded regions and dotted lines are defined in the same way as in Fig. 3.4. The depicted LHC reach (yellow/shaded region) applies only to the case of γ_1 being the lightest Kaluza-Klein particle.

KIMS and COUPP) are shown in the m_W-Δ_{q_1} plane. Panel (a) (panel (b)) shows the constraints from the WIMP-neutron (WIMP-proton) spin-dependent cross sections. The rest of the Kaluza-Klein spectrum has been fixed as mentioned earlier in this section and $m_h = 120$ GeV/c^2. The solid (dashed) curves are limits on γ_1 (Z_1) for each experiment. The constraints from LHC and WMAP on the m_W-Δ_{q_1} parameter space are the same as in Fig. 3.4.

By comparing Figs. 3.4 and 3.6 it can be seen that, as expected, the parameter space constraints from spin-independent interactions are stronger than those from spin-dependent interactions. For example, in perhaps the most interesting range of WIMP masses from 300 GeV/c^2 to 1 TeV/c^2, the spin-independent limits on Δ_{q_1} in Fig. 3.4 range from a few times 10^{-2} down to a few times 10^{-3}. On the other hand, the spin-dependent bounds on Δ_{q_1} for the same range of m_W are about an order of magnitude smaller (i.e. weaker). It can also be noticed that the constraints for γ_1 are stronger than for Z_1.

Figure 3.6 also reveals that the experiments rank differently with respect to their spin-dependent limits on protons and neutrons. For example, KIMS and COUPP are more sensitive to the proton cross section, while XENON10 is more sensitive to the neutron cross section. As a result, the current (in 2008) best spin-dependent limit on protons comes from KIMS, but the current (in 2008) best spin-dependent limit on neutrons comes from XENON10. Combining all experimental results can give a very good constraint on the a_p-a_n parameter space. Fig. 3.7 shows combined results for $m_W = 50$ GeV/c^2 and $m_W = 500$ GeV/c^2 in the (model-independent) a_p-a_n parameter space. The contours show limits from XENON10 (red/solid), KIMS (black/dotted) and COUPP (green/dashed). The blue near-horizontal bands show the evidence regions allowed by DAMA taken from [36], while the green region shows the parameter space allowed by all current (in 2008) experiments. Note, that these limits were computed in two different ways. The results from KIMS and COUPP are based on the method proposed in [32], whereas those from DAMA and XENON10 are calculated as advocated in chapter 2.2.2. The latter are more accurate, since limits are computed for all angles in the a_p-a_n plane separately, whereas the former solely rely on the limits calculated considering pure coupling to neutrons and protons respectively. The two straight lines originating from $a_n = a_p = 0$ are the theoretical predictions for a_p and a_n in the case of γ_1 or Z_1. These theory lines are parametrized by the value of Δ_{q_1} as indicated by a few representative points. The feature which is readily apparent in Fig. 3.7 is the orthogonality between the regions allowed by the a_p-sensitive experiments like KIMS and COUPP, on the one side, and the a_n-sensitive experiments like XENON10, on the other. This indicates the complementarity of the two groups of experiments: the green/shaded region allowed by the combination of all experiments is substantially narrower than the region allowed by each individual experiment.

Finally, the γ_H emerging from the model with two extra dimensions is considered. As a spin zero particle, it has no spin-dependent interactions and can only be detected through its spin-independent elastic scattering. Figure 3.8(a) (Fig. 3.8(b)) is the analogue of Fig. 3.4 (Fig. 3.5) for the case of γ_H. Figure 3.8(a) shows lower bounds on Δ_{q_1} versus the mass m_{γ_H} of the scalar photon for a fixed Higgs mass ($m_h = 120$ GeV/c^2). The solid lines indicate the current (in 2008) experimental limits from CDMS (blue) and XENON10 (red). The dashed

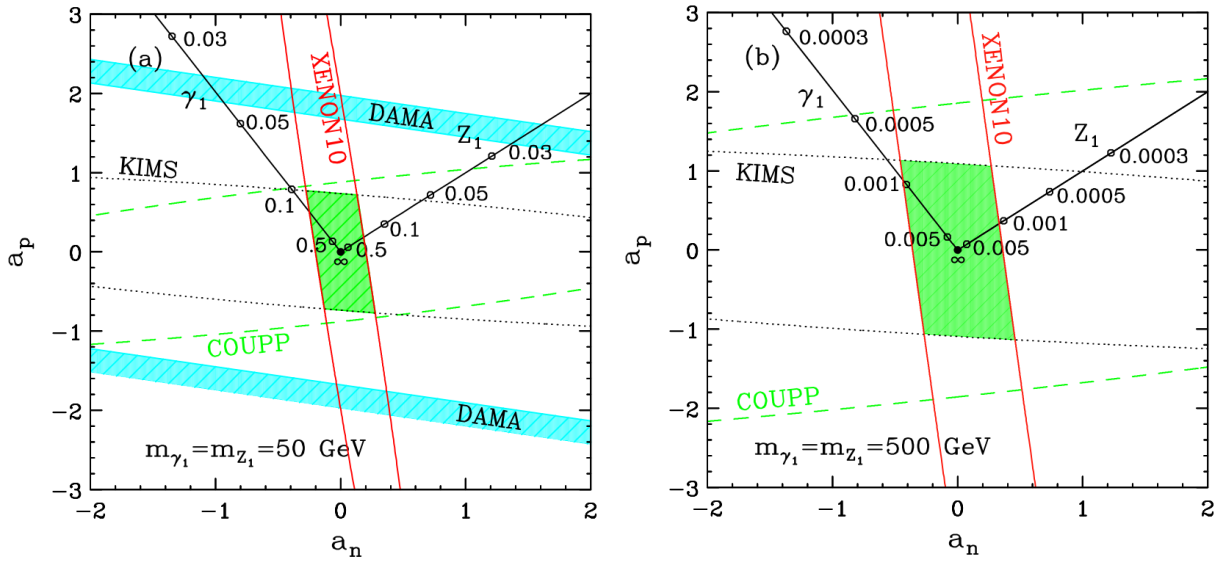

Figure 3.7: Experimental limits on the a_p-a_n parameter space for (a) $m_W = 50$ GeV/c^2 and (b) $m_W = 500$ GeV/c^2. The contours show limits from XENON10 (red/solid line), KIMS (black/dotted line) and COUPP (green/dashed line). The blue near-horizontal bands show the evidence regions allowed by DAMA taken from [36], while the green region shows the parameter space allowed by all current (in 2008) experimental results. The two straight lines originating from $a_n = a_p = 0$ are the theoretical predictions for a_p and a_n in the case of γ_1 or Z_1. These theory lines are parametrized by the value of Δ_{q_1} as indicated by a few representative points.

lines are the projected sensitivities of SuperCDMS 25 kg and XENON100, and the dotted line is the projected sensitivity of a ton-scale detector. Since the cosmologically preferred mass range for γ_H is much lower ($\sim$200 GeV/c^2 before accounting for coannihilations) than for the γ_1 and Z_1, the constraints are quite powerful – in particular, the future ton-scale experiments are expected to cover most of the interesting mass splitting (Δ_{q_1}) region.

Figure 3.8(b) shows lower bounds of the Higgs mass m_h as a function of m_{γ_H} for a fixed $\Delta_{q_1} = 0.1$. The WMAP preferred parameter space is marked as the green/shaded region, while the black/solid line is the LEP-II lower limit on m_h. The contours resemble in shape those seen earlier in Fig. 3.5. In particular, it can be noticed that within the LEP-II allowed range, the Higgs mass does not have a large impact on the direct detection bounds. However, if the LHC finds a standard model Higgs boson with a mass smaller than $\sim$300 GeV/c^2, the WMAP bound would constrain the mass of γ_H within a relatively narrow mass ranges at a given mass splitting (Δ_{q_1}). For example, in Fig. 3.8(b), where the fixed mass splitting is $\Delta_{q_1} = 0.1$, the corresponding constraint on the mass of γ_H would be 180 GeV/c^2 $< m_{\gamma_H} <$ 250 GeV/c^2. In fact, this conclusion is rather insensitive to the particular choice of Δ_{q_1}. This is due to the fact that γ_H self-annihilation is helicity-suppressed and gauge boson final states are dominant in the WMAP allowed regions. Therefore, Fig. 3.8(b) would look qualitatively similar, if a different value of Δ_{q_1} was used.

In summary, a comprehensive phenomenological analysis of Kaluza-Klein dark matter,

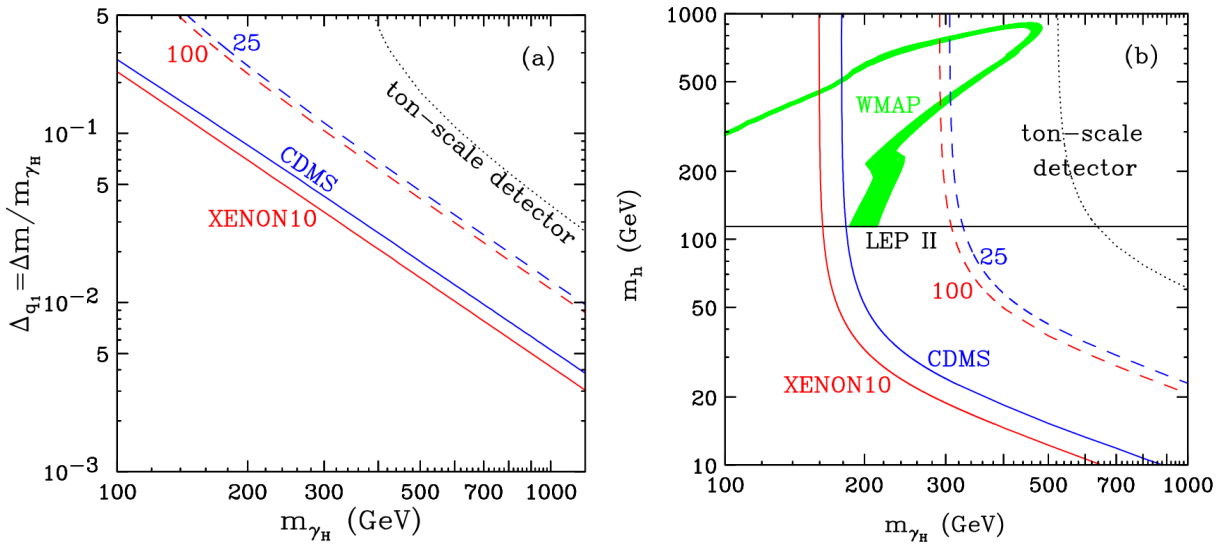

Figure 3.8: Experimental limits (90% C.L.) on γ_H. (a) Lower bound of Δ_{q_1} vs. m_{γ_H} for m_h =120 GeV/c^2. The solid lines are the current (in 2008) experimental lower bounds on Δ_{q_1} for a given m_{γ_H} from CDMS (blue) and XENON10 (red). SuperCDMS 25 kg and XENON100 projected sensitivities are drawn with dashed lines. The dotted line shows the projected sensitivity of a ton-scale experiment. (b) Lower bound of the Higgs mass (m_h) as a function of m_{γ_H} for a fixed $\Delta_{q_1} = 0.1$. The WMAP allowed range is the green/shaded region. The LEP-II lower bound on m_h is shown as the black/solid line.

including constraints from direct detection experiments, collider studies and cosmology considering one and two extra dimensions, was performed. It was shown that the three approaches are highly complementary, and that combining them substantially diminishes the relevant parameter space. Direct detection experiments restrict low values of m_W and small Δ_{q_1}, whereas colliders are sensitive to the region of relatively low m_W and sufficiently large Δ_{q_1}. On the other hand, cosmology rules out the region of very large m_W. As shown here, these two parameters (Δ_{q_1} and m_W) are the relevant quantities in analyzing UEDs. It can be seen that, at least in principle, the combination of all three types of constraints has the potential to completely cover the relevant parameter space. It was shown that with the expected sensitivity of the next-generation direct detection experiments, the coverage is almost complete in the case of γ_1.

Chapter 4

The CDMS setup

The Cryogenic Dark Matter Search (CDMS) experiment seeks to identify a small number of WIMP interactions amongst a very large population of background events. This is a very challenging effort and demands great care regarding the experimental setup and analysis. The most important issues in this kind of experiment are a low energy threshold and the understanding and suppression of all possible kinds of backgrounds. This requires the use of materials with very low radioactive contaminations, various kinds of shielding, operation at very low temperatures (∼10 mK) and advanced detection techniques.

This chapter provides a summary of the experimental setup. Except for a description of the detectors, the setup is treated rather shortly, since knowledge of the details is not necessary for understanding the main part of this thesis, which is concerned about various analysis techniques. In-depth treatments can be found in various theses, e.g. [75, 76, 77].

4.1 CDMS at the Soudan Underground Laboratory

The CDMS experiment is located in the Soudan Underground Laboratory in northern Minnesota, USA, close to the Canadian border. It is an experimental cavern at the 27^{th} level of the Soudan Mine, which is also host to the MINOS experiment [78], investigating neutrino oscillations, and the CoGeNT experiment [79], searching for dark matter particles like CDMS. The main benefit is the large reduction of the cosmogenic muon flux (by a factor of ∼50000 from its value at the surface) due to its 713 m rock overburden (2090 m water equivalent). The improvement regarding rejection of neutrons, induced by muons within the experimental setup and the surrounding rock, is of crucial importance since they impose a background, which is indistinguishable from a WIMP interaction. These cosmogenic neutrons were the dominant background at the Stanford Underground Facility, host of the CDMS experiment during previous operations before 2003.

4.2 Cryogenics

As illucidated in chapter 4.5 on the detector technology, apart from the ionization, CDMS also records the phonon signal from each interaction. Proper use of this measurement requires operation in the millikelvin regime. This is achieved by using an Oxford Instruments ^{3}He-^{4}He dilution refrigerator. After moving to Soudan, CDMS did not operate the five tower setup discussed later in this chapter, but only two towers. At that time the dilution refrigerator provided enough cooling power to reach a sufficiently low base temperature of ∼40 mK. In 2005 the system was upgraded and three additional towers were deployed, which increased the heat load significantly, mostly due to radiation from amplifier elements used for the readout system and conduction through new striplines. Thus, a Gifford-McMahon cryocooler was added as an additional cooling system. This update reduced the"cryogenic hold-time" to more than 24 hours, so that only one refill of liquid helium and nitrogen was necessary each day, an important aspect regarding that CDMS is operated in a location which, except for a case of an emergency, can only be accessed during regular working hours. Additional advantages are the increase of experimental lifetime and the reduction of costs of the expensive helium.

4.3 Shielding

In order to reduce the background of the experiment to a rate which is acceptable, the detectors are surrounded by several layers of active and passive shielding.

Even though the muon flux is significantly reduced with respect to the surface, it is still not negligible. Thus, the outermost layer of the shielding consists of a muon veto (active shielding), which is used to reject events coincident with a signal in the veto. This layer, which is arranged in a way such that adjacent panels have a slight overlap to cover the whole experimental setup, triggers approximately once every minute, supporting its necessity. Note, that some of these interactions are due to the ambient photon flux related to radioactive impurities within the experimental setup, whose spectrum extends up to about 2.6 MeV. Most muons typically deposit around 10 MeV within the veto, however this strongly depends on the incident angle. Thus, the threshold has to be kept much lower to keep the tagging efficiency high (∼99.99%).

Within the muon veto there are four layers of passive shielding. The next part of the shielding going inwards is a 40 cm thick layer of polyethylene bricks. Its purpose is to reduce the neutron flux from outside the apparatus. Within the polyethylene shield there are two layers of lead, which are necessary to suppress the external photon flux. The outer of these two layers, which has a thickness of 18 cm, is made of conventional lead. Thus, it contains the radioactive isotope ^{210}Pb, which has a half-life of 22.3 years and decays via two beta-decays. One of these betas has an energy of ∼1 MeV and thus emits Bremsstrahlung passing through the lead. Therefore, the inner lead layer consists of low-radioactive ancient lead, which was recovered from a ship that sunk near the French border. It has a thickness of 4 cm. The innermost part of the shielding is again a layer of polyethylene which is

10 cm thick. It is used to further moderate the neutron flux, primarily originating from production within the outer parts of the shield via spontaneous fission and (α,n) reactions.

The icebox, which hosts the detectors, resides within this shield. It is made of high-purity copper, which limits radioactive contaminations near the detectors. Its thickness (∼1 cm) is sufficient to stop alphas and betas from penetrating the detector assembly.

The described shielding is shown in Fig. 4.1.

4.4 Detector assembly and materials

The CDMS collaboration operates a total of 19 Ge (∼230 g each) and 11 Si (∼105 g each) detectors residing in the icebox in the center of the shielding. These semiconductors are stacked into five towers (T1–T5) with six detectors (Z1–Z6) each. Detector j in tower i is identified by the notation TiZj. The detectors within each tower are separated by 2 mm with no intervening material in-between. The arrangement is shown in Fig. 4.2. Figure 4.3 shows a photo of the open icebox from the top revealing the same configuration.

As discussed in chapter 2.2.1, except for very low WIMP masses the Ge detectors are much more sensitive to spin-independent WIMP-nucleon interactions than the Si detectors, which is due to their larger atomic mass. The presence of the Si detectors mainly goes

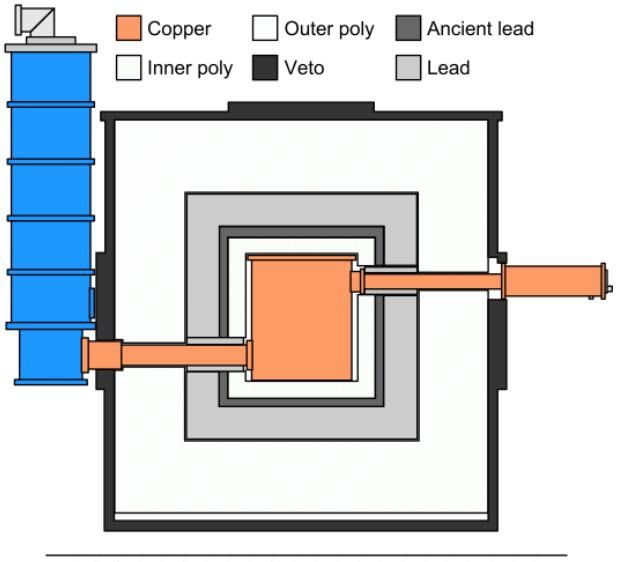

Figure 4.1: Cross section of the shielding of the CDMS experiment. Going from the inside to the ouside the icebox in the middle, which hosts the detectors, is surrounded by a layer of polyethylene, two layers of lead and an additional outer layer of polyethylene. The active muon veto constitutes the outermost shield. The fridge and the "fridge stem", which provides its connection to the icebox, is shown schematically on the left side. The "electronic stem" on the right side passes the wiring to the computer system.

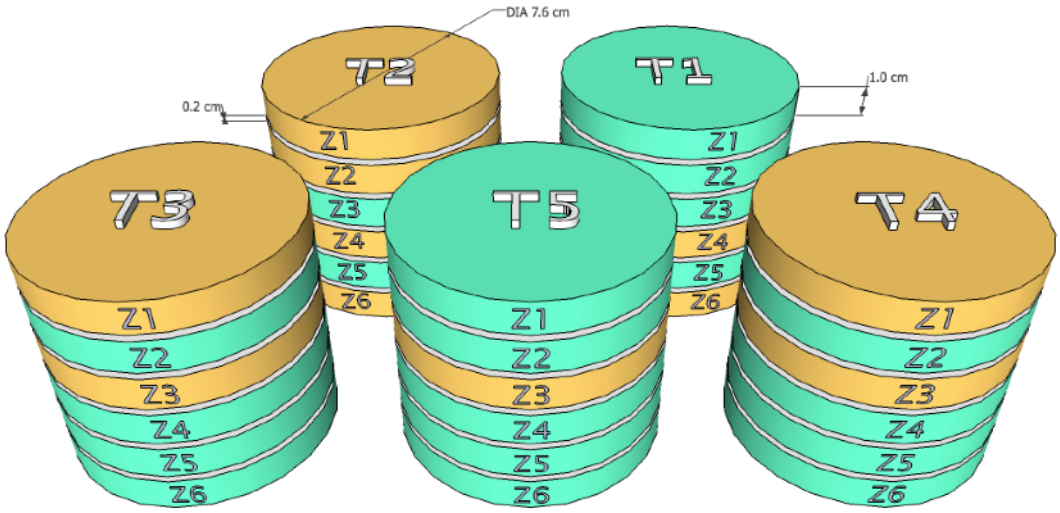

Figure 4.2: Arrangement of the detectors used by CDMS. Beige denotes Si detectors, while aqua represents Ge detectors. The latter are used for the dark matter searches described in this thesis.

back to the runs at the shallow side at the Stanford Underground Facility, where cosmogenic neutrons constituted the dominant background. This is because a comparison of the nuclear recoils within both types of detectors could be used to statistically discriminate a possible WIMP- from a neutron-interaction [80]. As discussed in great detail in chapter 5 the neutron background in the Soudan Underground Laboratory is much less significant. Therefore, for all analyses discussed in this thesis, the Si detectors were omitted. They were only used to tag multiple-scatter events, so events with a significant energy deposition in more than one detector. Multiple-scatter events are assumed to be induced by background

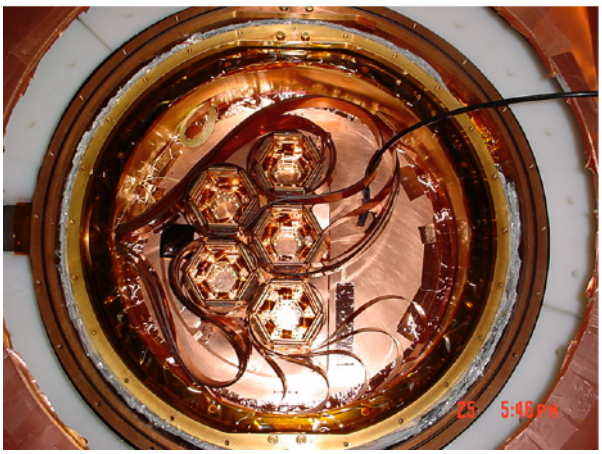

Figure 4.3: Photo of the open icebox showing the five towers. The holdings of the detectors constituting the towers have a hexagonal shape. The visible striplines assemble within the electronic stem which is on the left on this photo.

since the WIMP-nucleon cross section is expected to be very small.

4.5 The CDMS detectors

The main challenges regarding detector technology, used in a dark matter direct detection experiment, are the need for a very low threshold of order ∼1 keV, excellent background rejection capabilities and a very good energy resolution. For that purpose the CDMS collaboration has developed Z-sensitive ionization and phonon (ZIP) detectors. These detectors are instrumented to detect the phonons and ionization from a particle interaction within the crystal simultaneously. The great advantages of these detectors are the possibilities to obtain information regarding the event location from the phonon signal and to discriminate between nuclear recoils, which might be induced by WIMP interactions, and electron recoils, which are considered to be background. This chapter summarizes the working principles of the detection of both signals as well as the corresponding calibrations and primary signal processings.

4.5.1 Detector layout and characteristics

Each detector, Ge and Si, is a nearly cylindrical semiconductor with a diameter of approximately 7.6 cm and thickness of ∼1 cm. The exact geometry is shown in Fig. 4.4. The detectors have been fabricated with special care to limit impurities ($\sim 10^{11}/\mathrm{cm}^3$) and dislocation concentrations ($<5000/\mathrm{cm}^2$).

They are instrumented with four channels of superconducting transition-edge sensors on the top side to detect phonons and two concentric electrodes on the bottom side to

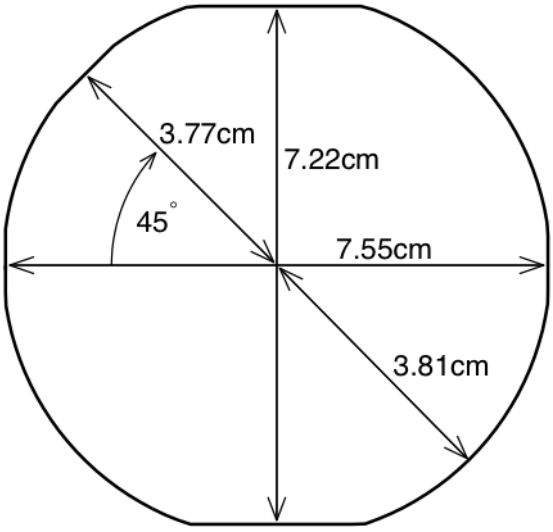

Figure 4.4: Geometry of the CDMS ZIP detectors.

detect ionization. The primary ionization signal is read out by an inner electrode covering ∼85% of the detector surface. A thin outer electrode, separated by a ∼1 mm wide gap from the inner electrode, serves as a guard ring to identify and reject events at the edge of the detector, which is subject to higher background and reduced charge collection. Moreover, this region is not well covered by the phonon sensors and thus the phonon response is degraded. Figure 4.5 shows a photo of a detector within its housing and a sketch of the layout of the four phonon and two ionization sensors.

4.5.2 Data acquisition

After a "global" trigger, initiated when the phonon signal exceeds a certain threshold, is issued during data acquisition (DAQ) all six channels of each detector are recorded and saved to disk. Each recorded signal consists of a 2048-sample trace with a 0.8 μs bin size, so that each trace is 1.6 ms long. The trigger itself occurs within the 512$^{\text{th}}$ bin, so that each trace contains a pre-pulse baseline of 409 μs, which can be used to reject events with unusually noisy traces.

The DAQ can handle events from all detectors at a rate of ∼20 Hz, which is set by the time required to reset the system so that it is able to record new events. This is sufficient regarding normal WIMP-search runs with an event rate of ∼0.2 Hz, thus smaller by a factor of 100. The event rates during calibration runs however can easily exceed ∼200 Hz. In order to decrease the dead time and corresponding loss of WIMP-search lifetime, barium calibration data was taken in "selective readout mode" which means that just those signals from detectors which trigger, typically not more than two or three, are read out and saved to disk instead of all 30 detectors as in standard readout mode. The standard readout was used for WIMP-search and also for the rare (compared to the barium calibrations) neutron calibration runs.

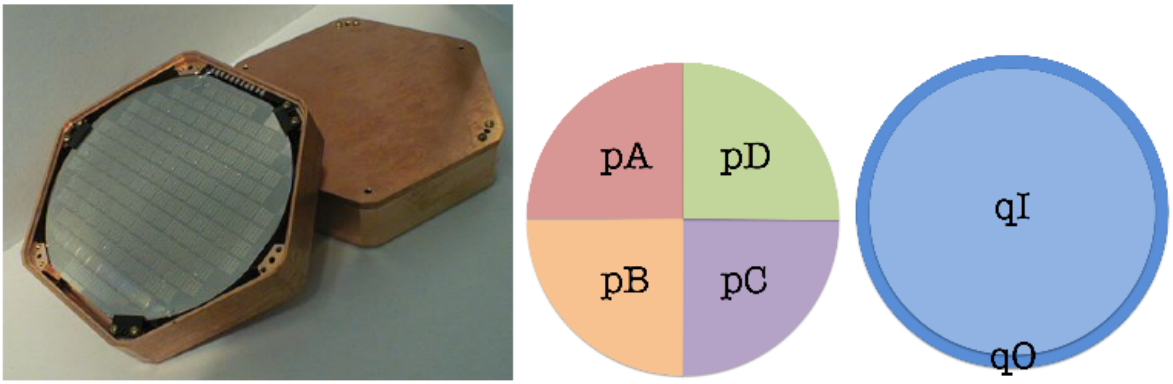

Figure 4.5: *Left*: Photo of a ZIP detector within its housing. *Right*: Sketch of a detector's four phonon (pA, pB, pC, pD) and two ionization sensors (qI, qO).

4.5.3 The ionization signal

4.5.3.1 Charge collection and neutralization

The ionization readout is in principle a simple process. When a particle interacts within the detector, electron-hole pairs are created as long as the deposited energy is above the semiconductor's band gap. At the operating temperature of CDMS (∼40 mK) this energy is 3.0 eV in Ge and 3.8 eV in Si. Directly after the particle impact, the electrons and holes propagate quasi-diffusely and would quickly recombine or be trapped by possible present impurities within the crystal. In order to prevent that and to collect the total amount of generated charges on the electrodes, a small voltage bias is applied to the electrodes, 3 V for the Ge and 4 V for the Si detectors, providing a nearly uniform electric field with the exception of the detector edges. These values have been shown to be sufficiently high to gain complete charge collection given the low crystal temperature and achieved purity. In fact 200 mV would already be sufficient [81]. To be more precise regarding the charge readout process: What actually is measured is the image charge induced by the migrating electrons and holes on the electrodes. Thus, in case of complete charge collection, the depth of the particle interaction has no effect on the obtained signal, since a drifting hole is equivalent to an electron drifting along the same track in the opposite direction.

Nevertheless, charge carriers can still be lost before reaching the surface electrodes. This is of particular importance since a reduced ionization signal, not related to detector issues but to the nature of the interaction, is typical for nuclear recoils from neutrons, as measured by calibrations with a californium source, and as expected from WIMPs. Since electron-hole pairs are generated from excitations of the atomic electrons, the ionization is reduced by a factor of ∼3 compared to an electron recoil of the same incident energy. Thus, electron recoils, regarded as background, with a severely diminished ionization signal can mimic a WIMP-nucleus interaction. As discussed in great detail in this thesis, such events constitute the dominant background for the CDMS experiment. The reason why charge carriers can still be lost is the presence of impurities, which cannot be perfectly circumvented even though great care is taken to manufacture the crystals from a highly pure substrate. In particular the equilibrium state of these donors and acceptors at the low temperatures is a state, where the trapping centers are ionized rather than neutralized. Fortunately, flashing the crystals with infrared LED light has proven to neutralize the detectors by generating a large number of free charge carriers, which subsequently recombine but also block the trapping centers. Note, that the detectors are not biased during this procedure. As just mentioned this does not yield a state of equilibrium, however it is stable over appropriate time scales requiring a flash every ∼12 hours.

4.5.3.2 Charge reconstruction

The charge collection process itself happens on a timescale typically lower than 1 μs. Thus, the traces of the charge pulses can be characterized by a spike and an exponentially falling edge. The characteristics of the charge amplifier fix the falltime of the trace to 40 μs, so that the shapes of all charge pulses are essentially identical, owing to possible saturation

effects, which however are not of concern regarding a WIMP-search in the keV regime. Simple time domain fits are not expected to yield good results, since noise fluctuations at different times are correlated. It is rather assumed that the power spectrum of the noise is constant, so-called "white noise". Thus, optimal filtering, which is a frequency domain fit of a fixed template to a recorded trace, is applied in the charge reconstruction process.

The optimal filter algorithm works as follows [77]: Let $\tilde{S}_n$ and $\tilde{A}_n$ be the values of the fourier transformations of a recorded trace and the template, which has been obtained by averaging over several well-formed pulses from calibration data, in the n^{th} digitizer bin respectively. J_n denotes the square of the corresponding noise contribution. Given that the start time of the pulse t_0 would be perfectly known, only the overall scaling factor a of the template would have to be determined. Minimization of the χ^2 given by

$$\chi^2 = \sum_n \frac{|\tilde{S}_n - a\tilde{A}_n|^2}{J_n} \tag{4.1}$$

directly yields

$$a = \frac{\sum_n \frac{\tilde{S}_n \tilde{A}_n^*}{J_n}}{\sum_n \frac{|\tilde{A}_n|^2}{J_n}}, \tag{4.2}$$

where * denotes complex conjugation. The linear dependence of the unknown parameter renders this problem trivial. However, apart from the pulse's amplitude characterized by the scaling factor its start time has to be determined as well. From the theory of Fourier transformations it follows that a translation in time by t_0 simply amounts to a multiplication by a phase factor given by $e^{-2\pi i t_0 f}$ in the frequency domain where f denotes the frequency. This modifies the original χ^2 (4.1) to

$$\chi^2 = \sum_n \frac{|\tilde{S}_n - a e^{-2\pi i t_0 f_n} \tilde{A}_n|^2}{J_n}, \tag{4.3}$$

where the parameters a and t_0 have to be estimated. Setting $\frac{\mathrm{d}\chi^2}{\mathrm{d}a} = 0$ and solving for a for fixed given t_0 yields

$$a = \frac{\sum_n e^{-2\pi i t_0 f_n} \frac{\tilde{S}_n \tilde{A}_n^*}{J_n}}{\sum_n \frac{|\tilde{A}_n|^2}{J_n}}, \tag{4.4}$$

similar to 4.2. Unfortunately $\frac{\mathrm{d}\chi^2}{\mathrm{d}t_0} = 0$ cannot be analytically solved for t_0. However, it can easily be shown that $\frac{\mathrm{d}\chi^2}{\mathrm{d}t_0} \propto \frac{\mathrm{d}a}{\mathrm{d}t_0}$. Calculating the second derivatives, it indeed turns out that the value of t_0, which minimizes χ^2, also maximizes a. Since the calculation of a for many values of t_0 is significantly faster than the corresponding calculation of χ^2, the pulse

fitting procedure employed by CDMS can be summarized as follows: Shift the template over the whole recorded event trace and take the values of t_0 and a, which maximize a. In our recent analysis it turned out that these mathematical calculations do not hold true for all events. It was observed, that in some rare cases for events at very low recoil energies the minimization of the full χ^2 did not yield the same result as the maximization of a. Implications of this possible misfitting are discussed in chapter 6.6. At this point, it should just be noted that this issue lead to a time consuming reprocessing of the data applying the full χ^2 minimization.

Three comments are of interest regarding the pulse fitting routine. First, the resolution of the scaling factor is independent of the actual value of a, while the resolution of the start time degrades as a^{-1}. Moreover, since the start time can only be estimated with an accuracy given by the time binning of the recorded traces, the actual χ^2 will always be slightly overestimated and the scaling factor will be underestimated. Finally, the approach of searching for the maximum value of a naturally induces a bias to higher values in cases, where no real pulse has been recorded.

Since the shape of the traces is nearly identical for all events, the minimum χ^2 turns out to be an excellent goodness-of-fit parameter, which is used to reject badly behaved pulses.

Figure 4.6 shows a typical charge pulse overlaid with the optimal-filter fit.

4.5.3.3 Charge calibration

The charge calibration is performed based on extensive exposure of the detectors to a ^{133}Ba source emitting gamma rays, whose primary line lies at 356 keV, which is clearly visible in the Ge detectors. This line is certainly high above the energy range CDMS is actually interested in. However, the calibration can easily be cross checked at low energies. In

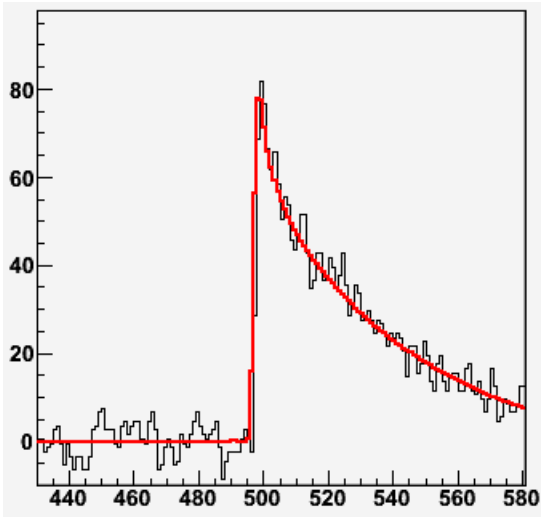

Figure 4.6: Cantle of a trace of a typical charge pulse and the corresponding fit.

addition to the barium calibrations the detectors are regularly exposed to neutrons from a ^{252}Cf source, particularly because WIMPs are expected to interact similarly to neutrons within the detectors. During these calibrations neutron capture on ^{70}Ge produces ^{71}Ge, which subsequently undergoes an electron-capture decay yielding a 10.36 keV line caused by x-rays and Auger electrons. This line is clearly visible at the expected energy in Fig. 4.7, which shows the coadded, efficiency corrected low-energy spectrum of the Ge detectors. Apart from this verification of the high-energy calibration at low energies this peak is also a good benchmark for estimating the resolution at low energies which is ∼0.3 keV.

Apart from the energy calibration itself, two corrections are applied during the calibration process. First, small correction factors <1% have to be introduced to correct for crosstalk between the inner and outer charge electrode related to their mutual capacitance. Moreover, the charge collection exhibits a significant position dependence. This effect is not understood quantitatively but is assumed to be due to the fact that the exposure from the flashing varies within the crystals related to the relative distance to the LEDs.

4.5.4 The phonon signal

4.5.4.1 Summary of phonon generation

Apart from ionization, CDMS also records the phonon signal inducted by a particle impact within the detectors. There are three contributions to the phonon signal. First, there are primary phonons, which are generated directly at the time of the scattering process. Their energy is simply given by $E_{\text{ph-primary}} = E_{\text{recoil}} - E_{\text{ionization}}$, where the subtracted term denotes the energy going into the electron-hole pair creation, as measured by the ionization channel, which in turn is given by $E_{\text{ionization}} = N_q \Delta$. N_q and Δ represent the

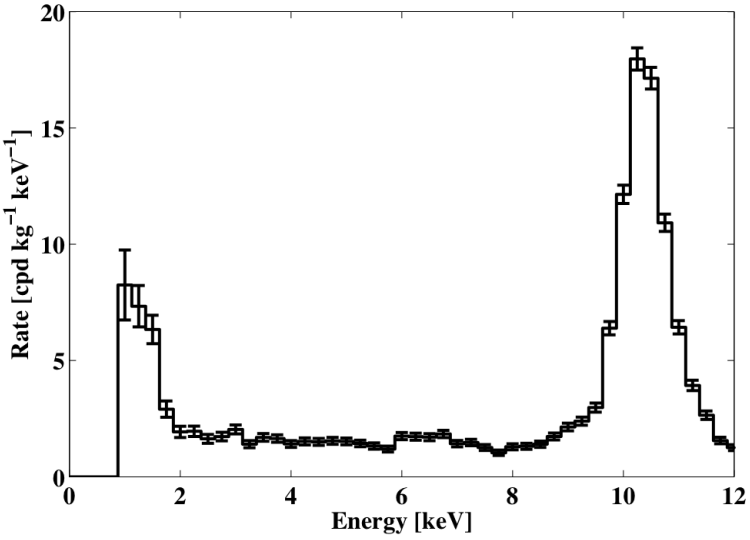

Figure 4.7: Coadded, efficiency corrected low-energy electron-recoil spectrum of the Ge detectors. Figure provided by T. Bruch.

number of generated charge carriers and the band gap respectively. The energy stored within the electron-hole system is not lost regarding the phonon signal. After the charge carriers are driven to the detector surfaces, they restore their energy to the phonon system. These recombination phonons have an energy of $E_{\text{ph-recomb.}} = N_q \Delta$, and thus it could be expected that simply $E_{\text{phonon}} = E_{\text{recoil}}$. However, there is an additional third contribution to the phonon energy, which arises from phonon radiation emerging from the charge carriers during their migration from the location of the interaction to the detector surfaces. These additional phonons are know as "Luke phonons" described by Neganov and Trofimov [82] and by Luke [83]. The energy $E_{\text{ph-Luke}}$ injected in this way into the phonon system is given by

$$E_{\text{ph-Luke}} = \sum_i q_i \int_{\vec{x}_i} \vec{E} \cdot \mathrm{d}\vec{x}\,, \tag{4.5}$$

where $q_i = e$ is the charge carried by each electron and hole, $\vec{x}_i$ is the path travelled by the i^{th} charge carrier and $\vec{E}$ denotes the electric field, which can be assumed to be uniform neglecting the detector edges, yielding $|\vec{E}| = U/d$. In the last equation U represents the applied bias voltage and d stands for the detector thickness. Further assuming that each electron-hole pair travels over the whole distance d, the expression can be simplified to give

$$E_{\text{ph-Luke}} = \sum_i e\,U = N_q\,e\,U = \frac{e\,U}{\Delta}\,E_{\text{ionization}}\,. \tag{4.6}$$

In order to obtain the original recoil energy this additional contribution has to be subtracted from the total phonon energy yielding

$$E_{\text{recoil}} = E_{\text{phonon}} - \frac{e\,U}{\Delta}\,E_{\text{ionization}}\,. \tag{4.7}$$

E_{phonon} and $E_{\text{ionization}}$ are the energies which are directly measured with the respective sensors. This generation of the phonon signal as well as the ionization signal are shown schematically in Fig. 4.8.

4.5.4.2 Phonon propagation

The phonon propagation within the crystal at temperatures of ∼10 mK is dominated by two processes, impurity scattering and anharmonic decays [84, 85]. Both mechanisms show a strong frequency dependence. The main part of the population of primary phonons originally have high energies with frequencies of several THz and mean free paths below 1 mm. In this regime, anharmonic decays dominate, in which a single phonon decays into two phonons of smaller energy. The lifetime τ of this process scales as $\tau \propto \nu^{-5}$, where ν denotes the frequency of the original phonon. At a frequency of around 1.6 THz, isotope scattering, which is elastic scattering of impurities within the crystal with a cross section σ scaling as $\sigma \propto \nu^{-4}$, starts to dominate the propagation process. The subsequent quasi-diffusive propagation, which typically lasts a few ms, yields phonons with mean free paths of ∼1 cm, which allows trapping of the phonons on the detector surfaces. These phonons

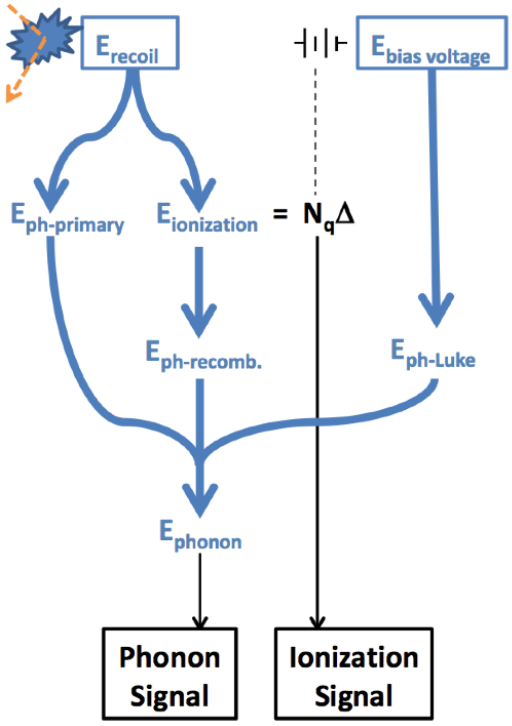

Figure 4.8: Sketch of the phonon and ionization signal generation. Figure provided by M. Fritts.

are denoted "ballistic" phonons. Luke phonons are expected to be directly generated at ballistic frequencies. The recombination phonons are typically of high frequency, however they are down-converted very quickly on the detector surfaces. There is no kind of quasi-diffusive propagation as in the case of the primary phonons.

4.5.4.3 Phonon detection

Phonon detection is achieved by four sensor arrays attached to the top sides of the detectors, each covering one quadrant. Each of these sensor arrays consists of 1036 quasiparticle-trap-assisted electrothermal-feedback transition-edge sensors (QET), which are wired in parallel, thus acting like one single sensor. These QETs in turn are made of a small superconducting tungsten transition-edge sensor (TES), which is surrounded by an absorber array of 350 μm long superconducting aluminium fins. It is their purpose to concentrate the phonon energy into the tiny TES. This layout is shown in Fig. 4.9.

The basic working principle of a TES can be described as follows: The TESs are voltage biased, so that self-heating sets them just below the edge of superconductivity, which occurs at a transition temperature of around ∼80 mK. Though the transition is broadened by wiring all TESs in parallel, it is still very sharp (transition width is around ∼10 mK), so that a small temperature increase induced by an energy deposition causes a significant increase of its resistance and corresponding lowering of the current. This change

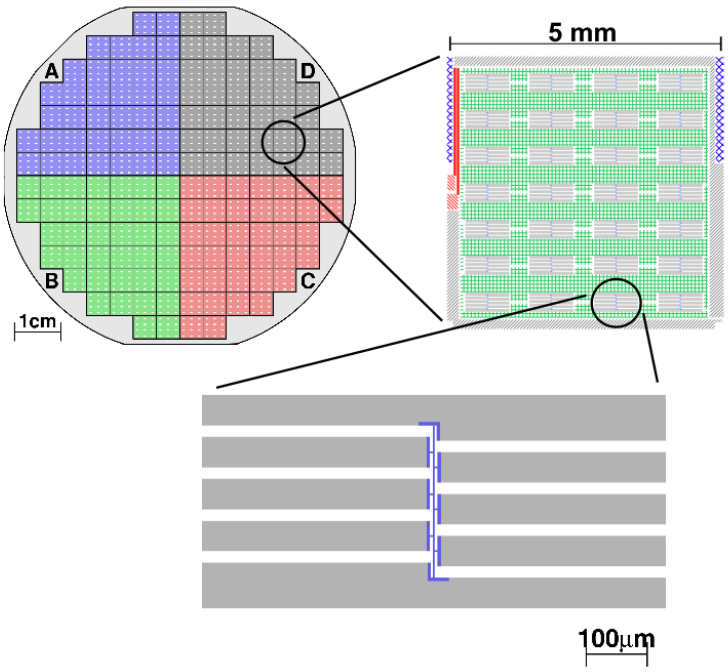

Figure 4.9: Phonon sensor layout. Segregation of the phonon readout system into four channels is shown in the upper left. A single QET is shown at the bottom.

of the current is read out using appropriate SQUID amplifiers. An important feature is the fact that in this configuration the sensors are operated in negative electrothermal feedback mode, which means that the just described lowering of the current after an energy deposition decreases the Joule power returning the TES back into its equilibrium state [86]. This provides a very stable operation of the phonon sensors.

The phonons do not directly deposit their energy into the tungsten TESs, it is rather collected within the aluminium fins. The energy gap of the Cooper pairs within these fins is $2\Delta_{\mathrm{Al}} = 0.36$ meV. If a phonon reaches the fins with a higher energy, it is capable of breaking a Cooper pair and generating quasiparticles. These quasiparticles migrate through the aluminium fins loosing energy by generating secondary quasiparticles and emitting sub-gap phonons until they come close to the TESs. As shown in Fig. 4.10 there is a slight overlap between the aluminium fins and the tungsten TESs, which causes the superconducting gap to be between the gap size in the fins and the TESs. Thus, quasiparticles entering this zone can easily be trapped since they cannot return into the fins after loosing enough energy. Subsequently, they are collected in the TESs inducing the aforementioned temperature increase. In summary, the aluminium fins work like antennas concentrating the phonon energy into the tungsten with the overlap region acting like a one-way road for the quasiparticles emerging from the broken Cooper pairs.

From this discussion it is not astonishing that the phonon collection process takes much longer than the charge collection. As mentioned before, charge pulses have risetimes of 1 μs and falltimes of 40 μs, while typical corresponding values for phonon pulses are 10 μs

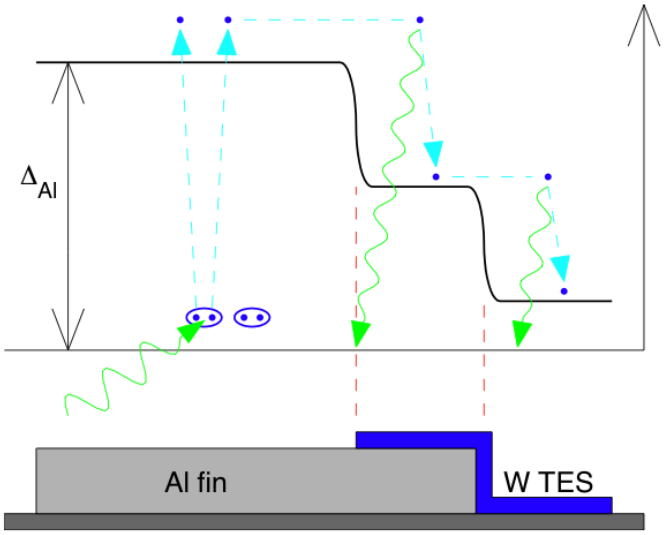

Figure 4.10: Process of phonon collection via generation and trapping of quasiparticles in the superconducting QETs. See text for details.

and 200 μs.

4.5.4.4 Phonon reconstruction

Because of the versatile phonon collection process, the shape of the phonon pulses varies substantially with energy and location of the interaction within the detectors. The energy dependence is dominated by nonlinearity of the TESs, while the position dependence is due to geometric effects, e.g. reflection of phonons at the crystals' edges. Thus, the corresponding reconstruction is much more ambitious than the charge pulse reconstruction. In particular it is performed in two steps, since no single algorithm is able to characterize the phonon response sufficiently.

Each event's energy is reconstructed applying the same optimal filter algorithm used for the charge pulses. The main problem is that the pulses do not have a fixed shape. Therefore, an appropriate template could not be obtained by averaging over some "well-behaved" pulses. Instead, a template based on a simple two exponential function given by $A(t) = A_0(1 - e^{-t/\tau_1})e^{-t/\tau_2}$ is used, which nevertheless cannot be expected to fit all pulses adequately. In particular, the corresponding minimum χ^2 returned by the fit routine cannot be used to reject badly behaved pulses accurately. Moreover, the obtained start times of the pulses are also questionable. Thus, they are determined applying a different algorithm.

The shape of the phonon pulses is not analyzed based on optimal-filter fits but on a time-domain walk algorithm, which is applied after smoothing the pulses with a 50 kHz Butterworth low-pass filter. The effect of this filtering is shown in Fig. 4.11. After the smoothing, the walk algorithm starts at the highest point of the pulse and subsequently walks down the rising edge in order to find certain points, e.g. the time where the trace reaches 10%

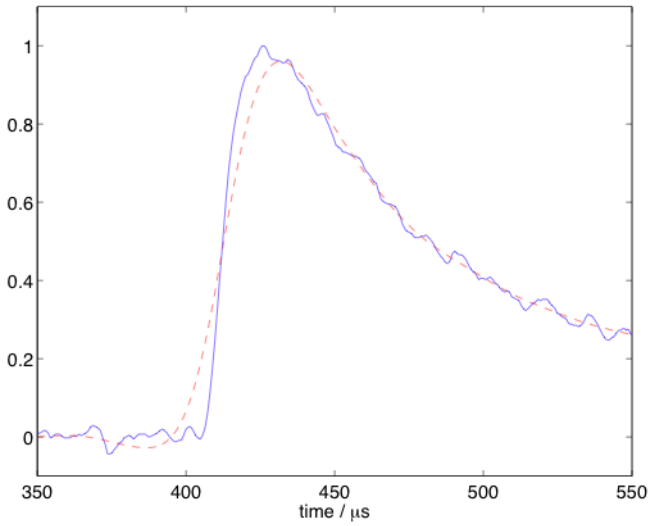

Figure 4.11: A typical phonon pulse before (blue/solid) and after (red/dashed) applying the butterworth filter to smooth the trace. Figure provided by R. W. Ogburn.

of its total amplitude. The main advantage is the independence of any knowledge of the actual shape of the pulse. A disadvantage is the poor noise discrimination especially at low energies. Two parameters are of special importance, since they are frequently used in the analysis, particularly regarding background rejection, which is illucidated in detail in later chapters. The first parameter is the risetime of the largest phonon pulse, which is defined as the difference between the times when the rising edge passes 40% and 10% of the total amplitude. The second parameter is the delay between the charge and the phonon signal defined as the difference between the start time of the charge pulse as estimated from the optimal-filter fit and the time when the primary phonon pulse reaches 20% of its total amplitude. These definitions are illustrated in Fig. 4.12.

4.5.4.5 Phonon calibration and signal correction

The phonon calibration is performed based on events from the barium calibrations, hence electron recoils. The first step of the calibration is to find factors which minimize the χ^2 between the uncalibrated summed phonon energy, as measured in the four phonon channels (p_A, p_B, p_C, p_D), and the total charge energy q_I+q_O (inner plus outer electrode), which has already been calibrated in the previous step. So for each detector the calibration factors a_A, a_B, a_C and a_D, with the subscripts denoting the phonon sensors are determined by minimizing

$$\left| \begin{pmatrix} p_{A1} & p_{B1} & p_{C1} & p_{D1} \\ p_{A2} & p_{B2} & p_{C2} & p_{D2} \\ \vdots & \vdots & \vdots & \vdots \\ p_{An} & p_{Bn} & p_{Cn} & p_{Dn} \end{pmatrix} \cdot \begin{pmatrix} a_A \\ a_B \\ a_C \\ a_D \end{pmatrix} - \begin{pmatrix} q_{I1}+q_{O1} \\ q_{I2}+q_{O2} \\ \vdots \\ q_{In}+q_{On} \end{pmatrix} \right|^2, \tag{4.8}$$

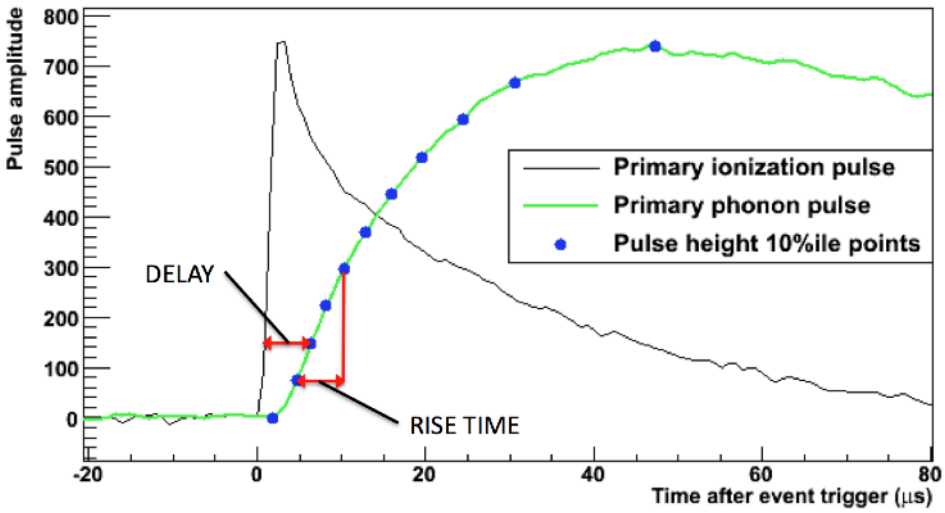

Figure 4.12: Visualization of the definitions of the risetime and delay parameters. Figure provided by M. Fritts.

where n denotes the total number of electron-recoil events within the calibration data. These correction factors set the total phonon energies to be of the same size as the charge energies. An additional factor of $1 + \frac{eU}{\Delta}$ (see formula (4.7)) is added to the calibration factors to set the ratio of the charge energy and the recoil energy to unity.

In a second step, the response of the four phonon channels is homogenized. This is necessary due to the aforementioned position dependence of the phonon signal, which can lead the sensors' sensitivities to differ by up to ∼10%. This is achieved by determining additional correction factors, which force the four phonon fraction distributions, defined by the ratio of each quadrant's energy to the total energy, to be aligned. In this step the overall calibration, achieved in the previous step, is maintained by imposing the additional constraint that they should sum to 4.

However, the detectors still exhibit a significant energy and position dependence. In order to reduce these dependencies, a technique based on additional correction factors, obtained for each event separately by averaging over "similar" events, is employed. At first a large sample from the barium calibration data is used to generate a "look-up" table containing the norm of vectors in a multidimensional parameter space for each event. The entries of these vectors contain each event's phonon energy and various quantities, based on timing parameters as discussed in the previous section. In a subsequent step, the corresponding vector norm is calculated for all events and compared to the values in the look-up table, assigning a set of nearest neighbors from the table to each event. The number of these nearest neighbors is crucial, since using too many of them would wash out local trends while using too few of them would render the approach unreliable. After this allocation, the actual correction is performed, which, for a parameter X, is of the form

$$X_{\text{corrected}} = X \cdot \frac{\overline{X}_{\text{all}}}{\overline{X}_{\text{NN}}} \,. \tag{4.9}$$

The enumerator denotes the mean over all events in the lookup table, while the denominator represents the mean only over the assigned nearest neighbors.

Chapter 5

Background

Since the WIMP-signal in dark matter search experiments like CDMS is expected to be very small, depending on the WIMP parameters it could be just a few events per year or less, it is of exceptional importance to reject the background as efficiently as possible. The first step regarding background rejection is a serious analysis of all possible contributions to this background, since only if they are sufficiently characterized it is possible to take counteractions, like employing appropriate shielding and optimizing background-rejection cuts.

The CDMS collaboration aims to have zero background, such that in case of observing any event it can be directly classified as a possible WIMP candidate. Since there is always a statistical chance of background events occurring due to fluctuations of the underlying distributions, this goal can never be perfectly achieved. Thus, it is necessary to estimate all contributions to the background very accurately to make sure that the total expected background is $\lesssim$1. After a general consideration regarding the impact of background on the sensitivity of the experiment, including two distinct possibilities to deal with this issue, the background categories, important for CDMS, are discussed.

5.1 Statistical considerations on background rejection

It is not astonishing that the presence of background diminishes the sensitivity and thus the possible reach in a given parameter space of an experiment. This argument can be nicely demonstrated following the reasoning of [87], which considers only simple counting statistics based on the Poisson distribution. In this context, a cut-based method, which is currently standard for most dark matter direct detection experiments is introduced. In the subsequent section a cut-free technique, based on a maximum-likelihood analysis, is discussed following [88]. Both of these methods, however in a much more ambitious way than presented here, are applied to the CDMS data. They constitute the main part of this thesis and are discussed in great detail in chapters 7 and 8 respectively.

5.1.1 Cut-based background rejection

We assume that apart from the expected signal there is another dominant background source, which however can be partly rejected based on a discrimination variable. As stated in the introduction, this discrimination is usually not perfect, so that both distributions, as determined from calibration data, have an overlap which is non-negligible. The "standard" way to deal with this issue is to impose a cut to define a signal region, with α representing the fraction of possible WIMPs, that pass the cut, and β denoting the fraction of background events, which leak into the acceptance region. A detector with perfect rejection capabilities would have $\alpha = 1$ and $\beta = 0$. It is the objective to obtain the number of signal (S) and background (B) events within the acceptance region. However, it is only possible to measure the number of events which pass (N_p) and fail (N_f) the rejection cut:

$$N_p = \alpha S + \beta B \tag{5.1}$$
$$N_f = (1-\alpha)S + (1-\beta)B \tag{5.2}$$

Solving for the parameter of interest S directly yields

$$S = \frac{(1-\beta)N_p - \beta N_f}{\alpha - \beta}\,. \tag{5.3}$$

Uncertainties regarding this estimate of the signal can be divided into two categories, statistical uncertainties, related to N_p and N_f, and systematic uncertainties, related to α and β, which must be determined from the calibration data together with the actual estimates of the signal and background distributions. Assuming simple Poisson errors regarding the number of observed events, e.g. $\delta N_p = \sqrt{N_p}$, the statistical error contribution can easily be calculated:

$$\delta S^2_{\text{stat.}} = \left(\frac{\partial S}{\partial N_p}\right)^2 \delta N_p^2 + \left(\frac{\partial S}{\partial N_f}\right)^2 \delta N_f^2 = \frac{\beta(1-\beta)}{(\alpha-\beta)^2} B + \frac{\beta^2 + \alpha(1-2\beta)}{(\alpha-\beta)^2} S \tag{5.4}$$

Setting $S = 0$ (or $S \ll B$), which is a common situation in current dark matter search experiments, and defining the background rejection quality factor

$$Q = \frac{\beta(1-\beta)}{(\alpha-\beta)^2} \tag{5.5}$$

yields the simple expression

$$\delta S_{\text{stat.}} = \sqrt{Q} \cdot \sqrt{N_t}\,, \tag{5.6}$$

which determines the statistical variance of a measurement with $S = 0$ and thus the statistical upper limit on the number of WIMP interactions. In the last equation $N_t = N_p + N_f = S + B = B$ for $S = 0$ is used. This result shows explicitly that background rejection is important regarding an experiment's sensitivity, since the quality factor Q becomes smaller, if better background rejection capabilities are achieved ($\beta \to 0$, $\alpha \to 1$).

However, systematic uncertainties should be taken into account. The corresponding contribution is given by

$$\delta S^2_{\text{syst.}} = \left(\frac{\partial S}{\partial \alpha}\right)^2 \delta\alpha^2 + \left(\frac{\partial S}{\partial \beta}\right)^2 \delta\beta^2 = \left(\frac{S}{\alpha-\beta}\right)^2 \delta\alpha^2 + \left(\frac{B}{\alpha-\beta}\right)^2 \delta\beta^2 \,. \tag{5.7}$$

The parameters α and β are determined using calibration data. Assume for example that N_α events with similar properties as WIMPs are taken. In the case of CDMS these would be nuclear recoils from the californium calibration data. If $N_{\alpha,p}$ denotes the number of these events, which pass the cut defining the acceptance region, the passage fraction $\alpha = N_{\alpha,p}/N_\alpha$ has statistical uncertainties given by

$$\delta\alpha^2_{\text{stat.}} = \left(\frac{\partial \alpha}{\partial N_{\alpha,p}}\right)^2 \delta N^2_{\alpha,p} + \left(\frac{\partial \alpha}{\partial N_\alpha}\right)^2 \delta N^2_\alpha = \frac{\alpha(1+\alpha)}{N_\alpha} \,, \tag{5.8}$$

calculated in a similar way as the result for S in equation (5.4). Note, that these are statistical errors of events in the calibration data employed, in order to estimate the passage fraction of dark matter particles, and that they are assigned to the category of systematic errors of S. A similar formula holds true for the passage fraction of background events $\beta = N_{\beta,p}/N_\beta$, which would be determined based on barium calibration data, inducing only electron recoils.

It is important to note that the systematic error scales differently with the number of acquired (background) events, or rather the exposure, than the statistical error. From (5.7) it can be inferred that for $S = 0$ the scaling is $\delta S_{\text{syst.}} \propto N_t$ while according to (5.6) $\delta S_{\text{stat.}} \propto \sqrt{N_t}$. Thus, the systematic errors dominate the result with increasing exposure, again emphasizing the need to decrease the background directly through improved shielding or material-handling techniques.

As an interesting annotation, the authors of [87] use a very simple reasoning to estimate the total number of calibration events necessary to render the contribution of these systematic errors (arising from statistical errors of the calibration data) to be negligible compared to the statistical errors (arising from statistical errors of the WIMP-search data). The results are given by:

$$N_\alpha > \frac{\alpha(1+\alpha)}{(\alpha-\beta)^2} \tag{5.9}$$

$$N_\beta > \frac{1+\beta}{1-\beta} N_t \tag{5.10}$$

The second condition is much more demanding than the first one, as it indicates that a number of background events larger than the number of total WIMP-search events needs to be acquired. However, since the counting rates during barium calibrations are much higher than during WIMP-search runs this condition can be satisfied running in calibration mode on an acceptable timescale.

Up to this point, systematic contributions to the uncertainties of α and β have not been discussed yet. They are related to possible differences of these passage fractions between

calibration and WIMP-search data and are particularly difficult to quantify. However, they should be included in the estimates if possible. Occurrence of such differences would not be unexpected at all. For example, the detectors might have a different response to high energetic gammas from a calibration source than to low-energy photons, which occur proportionately more often during WIMP-search runs. Moreover, a calibration source illuminates the detectors from a fixed location and thus might induce a position dependence in the detector response, while the actual background can be assumed to be distributed more uniformly.

The presented cut-based method is a powerful technique to reduce the background and has been established (in advanced forms) as the primary approach regarding background rejection in most dark matter direct detection experiments.

5.1.2 Maximum-likelihood method

Another technique to deal with background is based on a maximum-likelihood method. This approach has the advantage not to suffer from a reduction in WIMP acceptance, which becomes manifest in passage fractions $\alpha < 1$ and can be even below 0.5 depending on the detector's background rejection capabilities. Moreover, it uses the full power of the knowledge of the properties of background and signal distributions as obtained from calibration runs.

As in the previous section, it is assumed that the experimental outcome is determined by a possible signal and one dominant background contribution. Then, the maximum-likelihood method is based on the extended likelihood function:

$$\begin{aligned} L(\nu_s, \nu_b) &= \frac{\nu^n}{n!} e^{-\nu} \prod_{i=1}^{n} f(p_i) \\ &= \frac{(\nu_s + \nu_b)^n}{n!} e^{-(\nu_s+\nu_b)} \prod_{i=1}^{n} \left(\frac{\nu_s}{\nu_s + \nu_b} f_s(p_i) + \frac{\nu_b}{\nu_s + \nu_b} f_b(p_i) \right) \\ &= \frac{e^{-(\nu_s+\nu_b)}}{n!} \prod_{i=1}^{n} \Big(\nu_s f_s(p_i) + \nu_b f_b(p_i) \Big) , \end{aligned} \tag{5.11}$$

where ν_s and ν_b denote the expectation values of signal and background respectively, and should be regarded as equivalent to the parameters S and B from the cut-based method. The corresponding distributions are denoted f_s and f_b and might be the same distributions used for defining the cuts in the previous section. The parameter p represents the rejection variable and the index i runs over all acquired events from the WIMP-search runs passing miscellaneous selection cuts. The factor ouside the product is Poissonian and incorporates uncertainties related to the unknown numer of events. This is a standard approach for estimating the number of signal and background events from the experimental outcome by maximizing the likelihood function. Taking the logarithm and dropping the constant term

$-\log n!$, which does not affect the necessary maximization yields:

$$\log L(\nu_s, \nu_b) = -(\nu_s + \nu_b) + \sum_{i=1}^{n} \log\Big(\nu_s f_s(p_i) + \nu_b f_b(p_i)\Big)\,. \tag{5.12}$$

In order to perform an interesting comparison with the cut-based method, it is once again necessary to calculate the uncertainty of the signal. In a later chapter a confidence interval (or rather region) is constructed by finding the parameter values, which the log-likelihood function decreases at by $Q_{C,n}/2$, where $Q_{C,n}$ denotes the quantile of order C (equals the confidence level) of the χ^2 distribution with n degrees of freedom, from its maximum value:

$$\log L = \log L^{\max} - \frac{Q_{C,n}}{2}\,. \tag{5.13}$$

This approach is valid if the likelihood function is Gaussian or at least approximately Gaussian. For the moment however, we stick to an explicit calculation of the covariance matrix V:

$$\left(V^{-1}\right)_{kl} = E\left[-\frac{\partial^2 \log L}{\partial\nu_k \partial\nu_l}\right], \tag{5.14}$$

where k and l run over b and s or rather over background and signal. E denotes the expectation value. In the case of a sufficiently large WIMP-search data set this expression can be approximated by evaluating the second derivatives with the measured data and the maximum-likelihood estimates for ν_s and ν_b. Calculating the second derivatives of (5.12) is straightforward yielding:

$$V^{-1} = \begin{pmatrix} \displaystyle\sum_{i=1}^{n} \frac{\big(f_b(p_i)\big)^2}{\big(\nu_s f_s(p_i) + \nu_b f_b(p_i)\big)^2} & \displaystyle\sum_{i=1}^{n} \frac{f_s(p_i)\cdot f_b(p_i)}{\big(\nu_s f_s(p_i) + \nu_b f_b(p_i)\big)^2} \\ \displaystyle\sum_{i=1}^{n} \frac{f_s(p_i)\cdot f_b(p_i)}{\big(\nu_s f_s(p_i) + \nu_b f_b(p_i)\big)^2} & \displaystyle\sum_{i=1}^{n} \frac{\big(f_s(p_i)\big)^2}{\big(\nu_s f_s(p_i) + \nu_b f_b(p_i)\big)^2} \end{pmatrix}. \tag{5.15}$$

However, for the given example it is possible to calculate the expectation value explicitly

which is shown here in some detail:

$$
\begin{aligned}
\left(V^{-1}\right)_{kl} &= E\left[-\frac{\partial^2 \log L}{\partial\nu_k \partial\nu_l} \right] \\
&= \sum_{n=0}^{\infty} \int \left(\prod_{m=1}^{n} \mathrm{d}p_j \right) \left(-\frac{\partial^2 \log L}{\partial\nu_k \partial\nu_l} \right) L \\
&= \sum_{n=0}^{\infty} \int \left(\prod_{m=1}^{n} \mathrm{d}p_j \right) \left(-\frac{\partial^2}{\partial\nu_k \partial\nu_l} \sum_{i=1}^{n} \log\Big(\nu_s f_s(p_i) + \nu_b f_b(p_i)\Big) \right) \frac{\nu^n}{n!} e^{-\nu} \prod_{j=1}^{n} f(p_j) \\
&= \sum_{n=0}^{\infty} \frac{\nu^n}{n!} e^{-\nu} \sum_{i=1}^{n} \left[\left(\int \mathrm{d}p_i \left(-\frac{\partial^2}{\partial\nu_k \partial\nu_l} \log\Big(\nu_s f_s(p_i) + \nu_b f_b(p_i)\Big) \right) \cdot f(p_i) \right) \underbrace{\prod_{\substack{j=1 \\ j\neq i}}^{n} \int \mathrm{d}p_j f(p_j)}_{1} \right] \\
&= \underbrace{\sum_{n=0}^{\infty} \frac{\nu^n}{n!} e^{-\nu} \cdot n}_{\nu} \left(\int \mathrm{d}p \left(-\frac{\partial^2}{\partial\nu_k \partial\nu_l} \log\Big(\nu_s f_s(p) + \nu_b f_b(p)\Big) \right) \cdot f(p) \right) \\
&= -\int \mathrm{d}p \Big(\nu_s f_s(p) + \nu_b f_b(p)\Big) \cdot \frac{\partial^2}{\partial\nu_k \partial\nu_l} \log\Big(\nu_s f_s(p) + \nu_b f_b(p)\Big)
\end{aligned}
$$

Further evaluation of this expression yields:

$$
V^{-1} = \begin{pmatrix}
\displaystyle\int \mathrm{d}p \frac{\big(f_b(p)\big)^2}{\nu_s f_s(p) + \nu_b f_b(p)} & \displaystyle\int \mathrm{d}p \frac{f_s(p) \cdot f_b(p)}{\nu_s f_s(p) + \nu_b f_b(p)} \\[2ex]
\displaystyle\int \mathrm{d}p \frac{f_s(p) \cdot f_b(p)}{\nu_s f_s(p) + \nu_b f_b(p)} & \displaystyle\int \mathrm{d}p \frac{\big(f_s(p)\big)^2}{\nu_s f_s(p) + \nu_b f_b(p)}
\end{pmatrix} \tag{5.16}
$$

This is the exact result while (5.15) is just an approximation which converges to (5.16) in the large sample limit. Note, that the integrands in (5.16) have an additional factor of $\nu f(p)$ compared to the summands in (5.15), providing the correct weighting for the integrals, which is given intrinsically for the data.

As in the case of the cut-based method, assume that the signal contribution can be neglected, or rather set $\nu_s = 0$. In that case (5.16) simplifies to

$$
V^{-1} = \frac{1}{\nu_b} \begin{pmatrix}
1 & 1 \\[2ex]
1 & \displaystyle\int \mathrm{d}p \frac{\big(f_s(p)\big)^2}{f_b(p)}
\end{pmatrix} . \tag{5.17}
$$

Inversion of this matrix finally yields the covariance matrix

$$V = \frac{\nu_b}{\int \mathrm{d}p \frac{\left(f_s(p)\right)^2}{f_b(p)} - 1} \begin{pmatrix} \int \mathrm{d}p \frac{\left(f_s(p)\right)^2}{f_b(p)} & -1 \\ -1 & 1 \end{pmatrix} . \tag{5.18}$$

The uncertainty of the signal is $\sigma_{\nu_s} = \sqrt{V(2,2)}$. This result is valid independent of the actual shape of the signal and background distributions. For the comparison with the cut-based method it is however useful to assume a certain shape for these distributions. Taking both distributions to be Gaussian is a natural choice. Further assume that both have the same standard deviation σ and that the signal distribution is centered around 0, while the background distribution is centered around a mean μ, which is arbitrary for the moment. These distributions are thus given by:

$$f_s(p) = \frac{1}{\sqrt{2\pi}\sigma} e^{-\frac{p^2}{2\sigma^2}} \tag{5.19}$$

$$f_b(p) = \frac{1}{\sqrt{2\pi}\sigma} e^{-\frac{(p-\mu)^2}{2\sigma^2}} \tag{5.20}$$

Based on these distributions the uncertainty of the signal is calculated to be

$$\sigma_{\nu_s} = \frac{1}{\sqrt{e^{\mu^2/\sigma^2} - 1}} \cdot \sqrt{N_t}\,, \tag{5.21}$$

where it was additionally used, that the maximum-likelihood estimator for the number of background events equals the total number of observed events N_t if $\nu_s = 0$. This result can be directly compared to the corresponding formula (5.6) from the cut-based method. Obviously, in both cases the statistical uncertainty with which the experiment measures no signal scales with $\sqrt{N_t}$. The quality factors are

$$Q_{\mathrm{cut}} = \frac{\beta(1-\beta)}{(\alpha-\beta)^2} \tag{5.22}$$

for the cut-based method according to (5.5), which depends on the actual cut position, and

$$Q_{\mathrm{likelihood}} = \frac{1}{e^{\mu^2/\sigma^2} - 1} \tag{5.23}$$

for the likelihood method, which is constant for given background and signal distributions. A direct comparison assuming $\sigma = 1$ and $\mu = 1.5$ is given in Fig. 5.1. The probability distribution functions are shown in green while the cumulative distribution functions are shown in blue. The latter can be used to directly obtain the passage fractions α (for signal) and β (for background) and subsequently Q_{cut} for arbitrary cut positions. The minimum

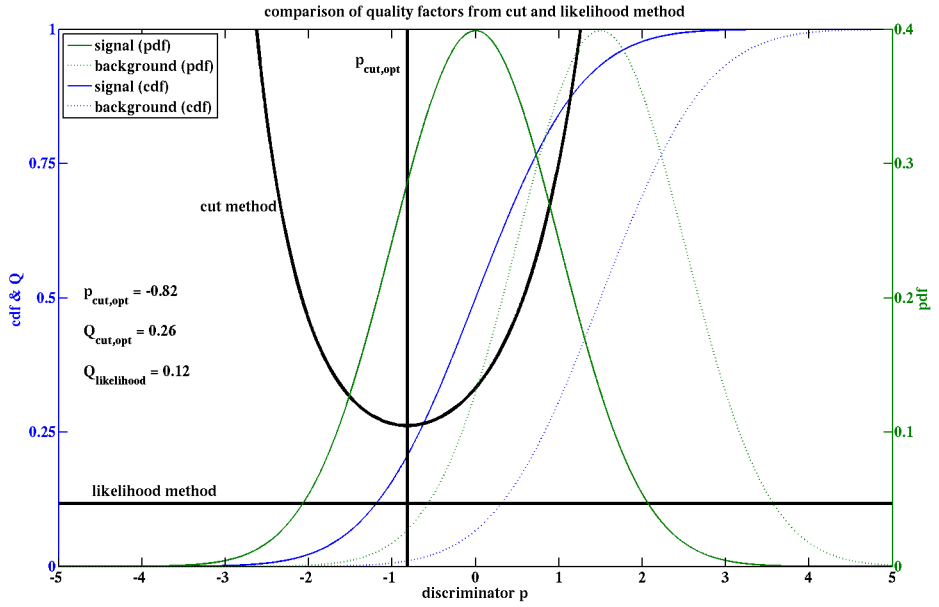

Figure 5.1: Comparison of cut-based and maximum-likelihood background rejection methods. The maximum-likelihood method achieves a lower quality factor and thus performs better independent of the actual cut position. See text for details.

of the corresponding curve (black parabola) determines the optimal cut position. However, it can be observed that even assuming this optimal cut the likelihood method provides a lower quality factor (black horizontal line) and would thus yield a more stringent upper limit on a possible signal. In other words, the likelihood function performs better than the cut-based method.

This result is independent of the assumed value of μ, which, in the given example, characterizes the distance between the signal and background distributions. This can be observed from Fig. 5.2, where the quality factors, in the case of the cut-based method the value of the quality factor at the optimal cut position, are plotted as a function of μ/σ.

In this section two methods were introduced to deal with the main issue of dark matter direct detection experiments: background rejection. Both of these approaches are applied to the CDMS data. However, it should be emphasized that the examples discussed here were extremely simplified with regard to the actual analysis. In particular, considering the cut-based method, the cut-optimization is performed applying a much more advanced technique. Moreover, the calculation of upper limits is accomplished employing an algorithm, which takes the expected energy-distribution of the signal into account, while the approach discussed here was based just on simple counting statistics. Regarding the likelihood method, multidimensional distributions including two rejection parameters are used and their energy-dependence is taken into account. Moreover, in this approach it is no longer possible to calculate the covariance matrix easily, since the distributions themselves depend on the model parameters. Given that the actual approaches applied to the data

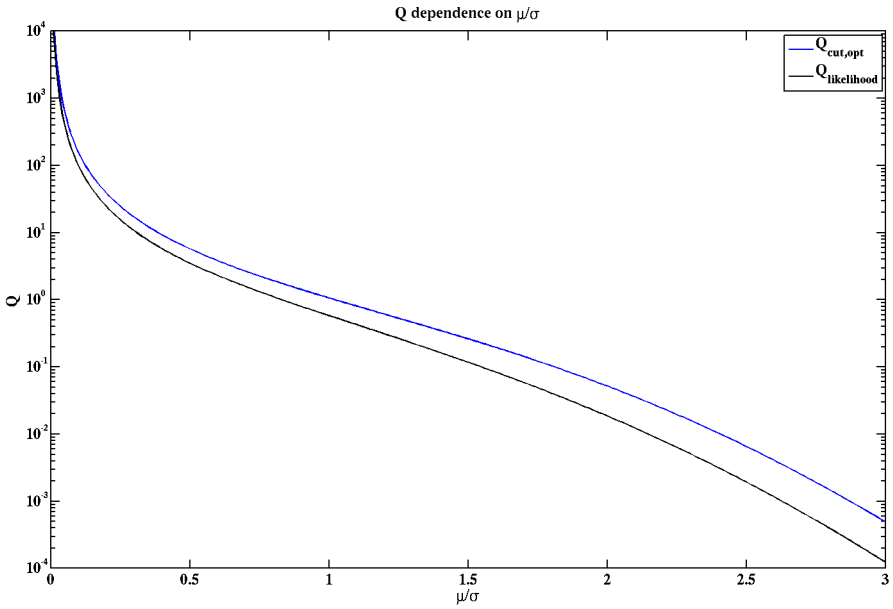

Figure 5.2: Comparison of quality factors for the cut-based and maximum-likelihood background rejection methods varying the distance between signal and background distributions. The value of Q_{cut} at the optimal cut position is always larger than $Q_{\text{likelihood}}$.

are in both cases much more advanced, it is unclear, whether the likelihood-based method indeed shows a better performance than the cut-based method. Nevertheless, it can be anticipated that leaving the standard route (the cut-based approach) might yield a great benefit regarding the interpretation of the data.

5.2 Nuclear-recoil background

As elucidated in the chapter on the detectors, neutrons scatter of the target nuclei, so their interaction and signature resemble those expected from WIMPs. Therefore, it is of utmost importance to prevent neutrons from interacting in the detectors. This can be achieved by operating the experiment in an underground location and installing a shielding surrounding the detectors as discussed before. The main problem regarding the neutron background is that it cannot be rejected on an event-by-event basis unless the neutrons scatter in more than one detector. Rejecting these multiple events is an efficient way to discriminate between a possible WIMP and a neutron interaction, due to the neutrons' high interaction rates. Nevertheless, special care is needed to diminish the remaining background. In particular, it is necessary to estimate the number of expected neutron interactions as accurately as possible. This section discusses the dominant types of neutron background, cosmogenic and radiogenic neutrons.

5.2.1 Cosmogenic neutrons

Cosmogenic neutrons were already shortly addressed in chapter 4 regarding the relocation from the Stanford Underground Facility to the Soudan Underground Laboratory and the active muon veto. The origin of this type of neutrons are cosmic ray particles interacting with atoms in the atmosphere and generating secondary particles. Due to the tremendous rock overburden electrons, photons and protons are efficiently absorbed leaving muons as the main hazard, whose flux is significantly reduced from its value at the surface, but still yields ∼1 event per minute in the muon veto. Recoils of the muons within the detectors themselves are of no concern regarding their high median kinetic energy of approximately 10 GeV [89]. However, they can generate neutrons within the shielding or other parts of the experimental hardware through spallation or various secondary processes within their hadronic and electromagnetic showers.

Extensive Monte Carlo simulations were performed in order to estimate this muon induced neutron background [90]. The starting point of these simulations was the generation of an initial muon sample with energies appropriate for the experimental location, taking into account the geological and geometrical circumstances as well as the observed angular distribution of the muons. This step was accomplished applying the MUSIC simulation package [91]. The two subsequent steps were performed employing the GEANT4 [92, 93] as well as the FLUKA [94, 95] simulation packages, whose results were in agreement and thus combined in order to increase the acquired statistics. The generated muons were propagated through a layer of rock to generate secondary particles, in particular neutrons. These particles could be assumed to resemble real particle showers induced by muons. In the third step of the simulation process these particles were injected into a simulation of the actual experimental apparatus, which included the detectors themselves as well as the passive shielding, active muon veto and hardware within the shielding, e.g. the ice box.

The adequacy of this approach could be tested by using the simulation to predict the number of neutron induced nuclear recoils, which were accompanied by a significant energy deposition within the active muon veto, taking into account the correct exposure and signal acceptance. This study could be performed for single scatters (events with significant energy deposition in only one detector) and multiple scatters. In both cases results from the actual data and the simulations were in agreement supporting the simulations' reliability. The final cosmogenic neutron background was the number of induced nuclear recoils, which were single scatters and *not* accompanied by a signal in the muon veto. This number was estimated by multiplying the neutron rate, as obtained from the data, with the ratio of non-vetoed to vetoed neutrons, as estimated from the simulations, and the acquired exposure of the WIMP-search runs, taking the detection efficiency into account. It was given by

$$n_{\mathrm{n,cosmo}} = 0.04^{+0.04}_{-0.03} \tag{5.24}$$

[89] for the standard analysis presented in chapter 6.

5.2.2 Radiogenic neutrons

Radiogenic neutrons are induced by radioactive contaminations within the experimental setup. The primary processes generating neutrons with kinetic energies up to 6 MeV, are (α,n) reactions and spontaneous fission. The dominant decay chains contributing to the former originate from uranium and thorium, while the latter is solely dominated by uranium. Both elements exist within the rock surrounding the experimental cavern, but the extensive polyethylene shielding renders this possible source of radiogenic neutrons to be negligible. Contaminations within the experimental setup are a more serious potential source, since there is no additional shielding.

As in the case of cosmogenic neutrons estimates of the expected radiogenic neutron background were based on Monte Carlo simulations [96, 97]. Accurate knowledge of the contamination levels of the materials within the experimental setup was mandatory for calculating a reliable estimate. They were obtained by screening samples of the shielding and detector materials with high-purity gamma counters. Since deriving the contamination levels based on measurements of gamma rates involved assumptions of equilibrium among various elements and isotopes in a decay chain, the estimates were kept very conservative. An independent test of these results was performed by fitting the electromagnetic spectrum, as obtained from the data to the spectrum from a Monte Carlo simulation [6]. Both results showed good agreement. With conservative uranium and thorium contamination levels of the experimental setup in hand, Monte Carlo simulations of the corresponding neutron background were performed, considering the hardware within the shielding, the inner polyethylene shield and both lead layers. The final background was calculated as the product of the background rate, as estimated from the simulations, and the exposure, again taking the efficiency into account. Since the error bars of the final result were extremely asymmetric, it is given in form of an interval:

$$n_{\mathrm{n,radio}} = 0.03 - 0.06\,. \tag{5.25}$$

Obviously both contributions to the neutron background were way below the aimed upper limit of 1 background event. In the next section it is elucidated that the neutron background was much less significant than the “surface-event background” which originates from electron-recoils.

5.3 Electron-recoil background

The main source of background for the CDMS experiment is related to electron recoils from photons produced by radioactive materials within the experimental setup. It is quite simple to reject these events, if the interactions occur within the bulk of the detectors, since electron recoils usually create much more electron-hole pairs and thus have a much higher charge signal than nuclear recoils. However, this rejection can fail for electron-recoil interactions occurring at the detector surfaces. Apart from photons related to radioactivity within the hardware surrounding the detectors, another source of these surface events

is ^{210}Pb contaminations on the detectors themselves. Due to incomplete charge collection, these events have a reduced ionization signal and occasionally the reduction is severe enough to mimic a WIMP-nucleus interaction. However, the phonon signals of these surface electron-recoil events have faster-rising pulses than bulk nuclear recoils and occur closer in time to the more prompt ionization pulses. As discussed in detail in chapter 7 a cut based on these timing parameters was employed to reject interactions at the detectors' surfaces. Alternatively, a likelihood-based method could be applied as discussed in chapter 8.

5.3.1 Bulk electron-recoil events

Bulk electron recoils constitute the main part of the CDMS background regarding the number of actually measured events, however they are rejected at a very high accuracy. As stated before, the charge energy of an event can be used to discriminate between the possibilities of it being a nuclear or an electron scatter. For practical reasons the ratio of ionization to recoil energy is used, rather than the charge energy itself. This ratio defines the ionization yield

$$y = \frac{E_{\text{ionization}}}{E_{\text{recoil}}} = \frac{E_{\text{ionization}}}{E_{\text{phonon}} - \frac{eU}{\Delta} E_{\text{ionization}}}\,, \tag{5.26}$$

which is the primary discrimination variable of the CDMS experiment. During the phonon calibration process the recoil energy of (bulk) electron recoils was set to have the same size as the ionization energy, so that these events have an ionization yield of ∼1. Nuclear recoils have an ionization yield of ∼0.3. Both populations can easily be identified in Fig. 5.3, which shows californium calibration data from a representative detector. The shown bands are defined as the 2σ regions around the respective means. More details on the exact definitions of these regions are given in chapter 6.4.3.3.

It should be noted that the observed nuclear-recoil band means in the Ge detectors are in excellent agreement with the theoretical predictions from Lindhard theory [1, 98] as shown in the Fig. 5.3. The parametrization of the model is given by

$$\epsilon(E_{\text{recoil}}) = 11.5\, E_{\text{recoil}}[\text{keV}] Z^{-7/3} \tag{5.27}$$

$$k = 0.133\, Z^{2/3}\, A^{-1/2} \tag{5.28}$$

$$g(\epsilon) = 3\,\epsilon^{0.15} + 0.7\,\epsilon^{0.6} + \epsilon \tag{5.29}$$

$$y(E_{\text{recoil}}) = \frac{k\, g(\epsilon)}{1 + k\, g(\epsilon)}\,, \tag{5.30}$$

where A and Z denote the atomic mass and charge number respectively. The silicon detectors are omited in the analyses presented here, however it should be mentioned, that in this case the agreement is not very good particularly at energies above ∼20 keV. At these energies, the theoretical prediction is much higher than the measured ionization yield, up to a factor of 1.25 at 100 keV. The reason for this discrepancy is not yet understood, but is not of too much concern, since the bands are fitted empirically to the calibration data.

Since the electron- and nuclear-recoil bands are well separated at energies as low as ∼5 keV in most detectors, the rejection of bulk electron recoils is very efficient. For each

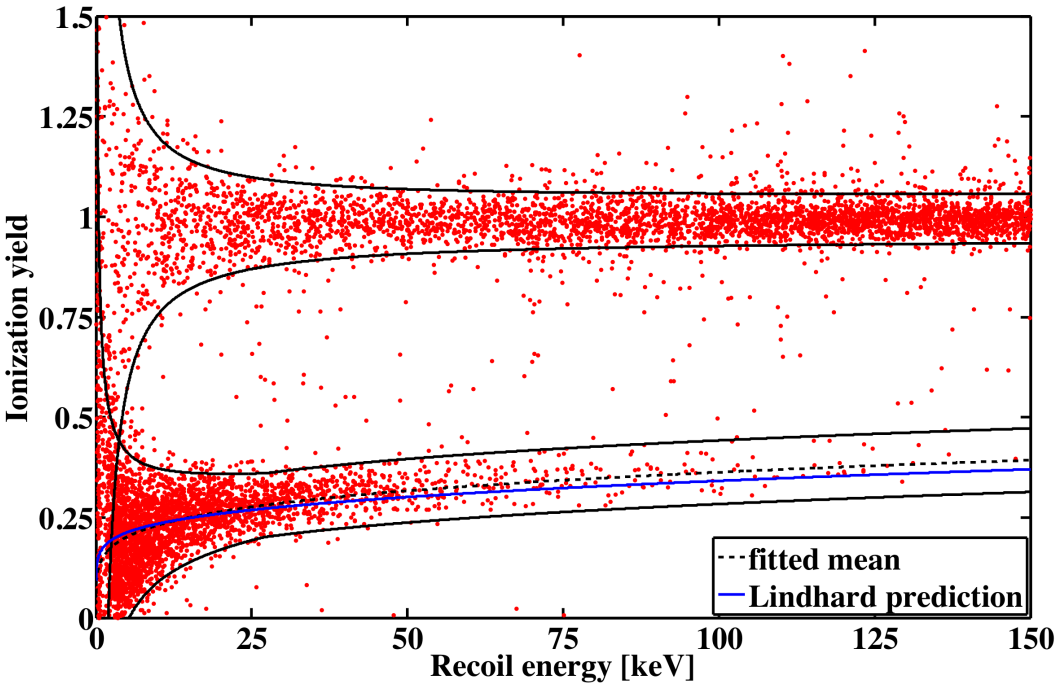

Figure 5.3: Ionization yield versus recoil energy of ^{252}Cf calibration data from a representative detector. The black/solid lines represent the electron-recoil band around a yield of 1 and the nuclear-recoil band around 0.3. The black/dashed line denotes the mean of the latter band, while the similar but blue/solid line is the corresponding prediction from Lindhard theory [1, 98].

detector the leakage fraction was estimated, based on a Monte Carlo simulation [6]. In this simulation, events with an ionization yield of 1, so bulk electron recoils, were generated and their charge and phonon energies smeared with the energy resolution given by the width of the 10.36 keV line shown in Fig. 4.7. The number of simulated events were subsequently scaled to match the energy spectrum of electron recoils. The low-energy range of this spectrum is shown in Fig. 4.7. Taking into account the electron-recoil rate and exposure of each detector, yielded the final expected bulk electron-recoil leakage above a 10 keV threshold of

$$n_{\mathrm{e,bulk}} < 5 \cdot 10^{-4} \,. \tag{5.31}$$

Since the estimate was extremely small, only an upper boundary was calculated. In any case, the contribution of bulk electron recoils to the total background estimate is negligible compared to the neutron background and surface electron-recoil background as discussed in the next section. The ionization yield parameter is obviously a very good rejection variable.

5.3.2 Surface electron-recoil events

Even combining the neutron background and the leakage from bulk electron recoils would yield a total number of background events well below 0.1, which would render CDMS to

be a background-free experiment. However, there is another type of background events, whose origin is electron scattering but which can have extremely reduced charge collection and subsequently very low ionization yield. Some of these events, leaking down to lower yield from the electron-recoil band, can be already observed in the californium calibration data shown in Fig. 5.3. However, the effect is much more obvious in Fig. 5.4, where surface events were taken from barium calibration data. The reduction of charge collection of low-yield events, denoted "betas", can be severe enough that they can populate the nuclear-recoil band, especially at low-recoil energies. Thus, these events constitute a dangerous background which cannot be rejected sufficiently based on the yield parameter alone.

The origin of these events with reduced charge collection is well understood [99]. They are due to electron-recoil events occuring within the first few μm of the detectors' surfaces. The main mechanism causing the reduced ionization collection is the back-diffusion of charge carriers into the "wrong" (with opposite sign) electrode. This can be understood from the cartoon in Fig. 5.5. As discussed before, an interaction within the crystal generates electron-hole pairs by liberating valence electrons from their bound states into the conduction band. These charge carriers are not separated immediately by the applied electric field because of self-shielding, which induces a short period of quasi-diffuse propagation. This short delay is insignificant for interactions occurring within the bulk of the detectors, so that electrons and holes are still separated very efficiently. However, charge carriers,

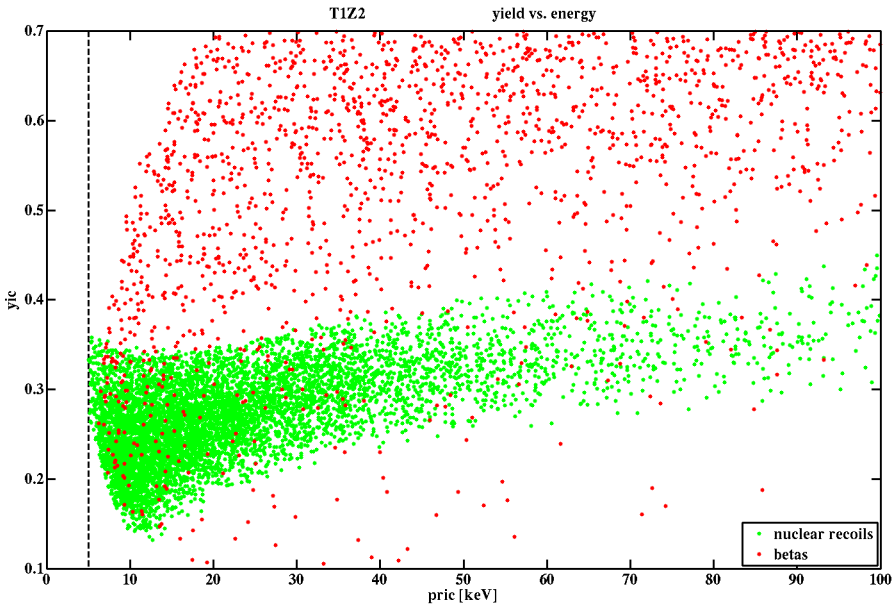

Figure 5.4: Ionization yield (yic) versus recoil energy (pric) for nuclear recoils from ^{252}Cf and surface events (betas) from ^{133}Ba calibration data in detector T1Z2. The cuts for the definitions of both populations are discussed in chapters 6 and 7. In particular the low-energy region of the nuclear-recoil band is subject to contaminations with surface events. The vertical line at 5 keV denotes the threshold for the likelihood analysis presented in chapter 8.

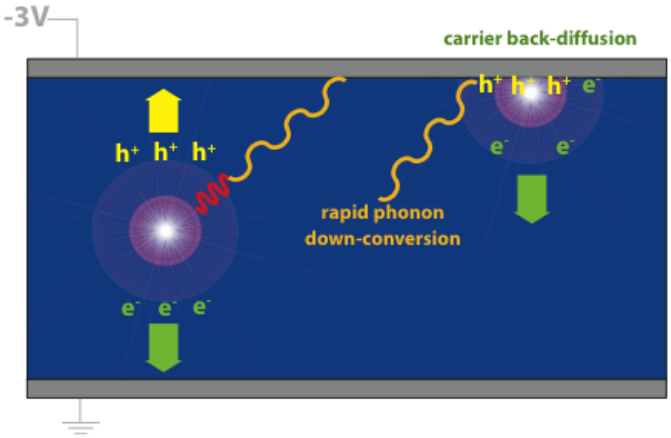

Figure 5.5: Cartoon illustrating the back-diffusion of charge carriers generated by surface events. The accompanying rapid down-conversion of phonons can be used to reject these events. See text for details.

generated very close to the surfaces, can be trapped on the "wrong" electrode during the regime dominated by diffuse propagation before the electric field is able to draw them apart and accelerate them towards the "correct" electrode. These charge carriers are lost regarding the ionization collection process and thus can mimic a nuclear-recoil like signature of the original scattering process. It has been shown that the deposition of an amorpheus Si layer with a large band gap between the electrodes and crystals themselves reduces the back-diffusion significantly [99]. After this improvement of the detectors the so-called "dead-layer", the region where interactions can suffer from reduced charge collection, has a thickness of $\sim$10 μm. It should be noted, that there might be additional mechanisms contributing to this surface effect, like the occurrence of an enhanced trap density due to damages during the fabrication or chemical reactions with air.

Two dominant sources for surface events have been identified, with extensive Monte Carlo simulations indicating that they approximately contribute equally to the total surface-event background. The first one is related to radioactive impurities within the experimental setup. The corresponding photon flux can induce low-energy electrons, e.g. by Compton scattering, which do not have sufficient kinetic energy to penetrate more than a few μm into the detectors. Moreover, the photons can interact directly within the detectors' surfaces via Compton scattering. The second source is related to contaminations of the detectors' surfaces themselves. During fabrication and testing they are exposed to environmental Rn. Thus, ^{210}Pb, which is a decay product of ^{222}Rn, can be deposited on the surfaces. The main issue with this radioactive isotope is its long half-life of 22.3 years. This was already mentioned in the discussion of the experiment's shielding (chapter 4.3), where it was noted that the inner lead layer was prepared from ancient lead to circumvent background from decay products of ^{210}Pb. Its decay chain is given by

$$^{210}\mathrm{Pb} \xrightarrow{\beta} {}^{210}\mathrm{Bi} \xrightarrow{\beta} {}^{210}\mathrm{Po} \xrightarrow{\alpha} {}^{206}\mathrm{Pb}\,. \tag{5.32}$$

As just mentioned the first β-decay has a long half-life of 22.3 years. In roughly 16% of the time the decay directly yields the ground state of ^{210}Bi with an energy level 63.6 keV below the mother isotope. However, in 84% of the time the decay goes into an excited state of ^{210}Bi, 46.5 keV above the ground state. The subsequent de-excitation can occur via a single photon but is usually accompanied by the emission of various particles, photons and Auger-electrons induced by internal conversion. The corresponding decay scheme is shown in Fig. 5.6. Since the detectors within the towers are very closely packed, with only approximately 2 mm space between them, some of these particles usually hit the adjacent detector, so that the total energy of 46.5 keV is partitioned into two detectors. This is a characteristic feature of the ^{210}Pb decay and can easily be observed when the energies of multiple hits in neighboring detectors are summed up. This is shown in the left panel of Fig. 5.7. The second β-decay with a short half-life of 5.0 days usually goes directly into the ground state of ^{210}Po and does not yield a significant feature. Finally, an α-decay generates the stable isotope ^{206}Pb. The half-life of this decay is 138 days. The emitted α has an energy of 5.3 MeV, which is a second characteristic feature pointing out the ^{210}Pb contamination of the surfaces. These αs can easily be identified due to their very high recoil energy and suppressed ionization yield, which is due to the fact, that they cannot penetrate the crystals deeply. An example is shown in the right panel of Fig. 5.7. The α-population can be distinguished clearly from the rest of the events. It should be noted that the rates, which both of the just discussed signatures occur at, are strongly correlated. Finally, as an annotation, Monte Carlo simulations indicate that the ^{210}Pb contamination is significantly lower in towers 3–5 compared to towers 1–2 [77]. This can be attributed to improved handling of the later detectors. In particular, they were not exposed to room air during longer storage but kept under a nitrogen atmosphere.

As discussed at the beginning of this section, it was not possible to reject surface

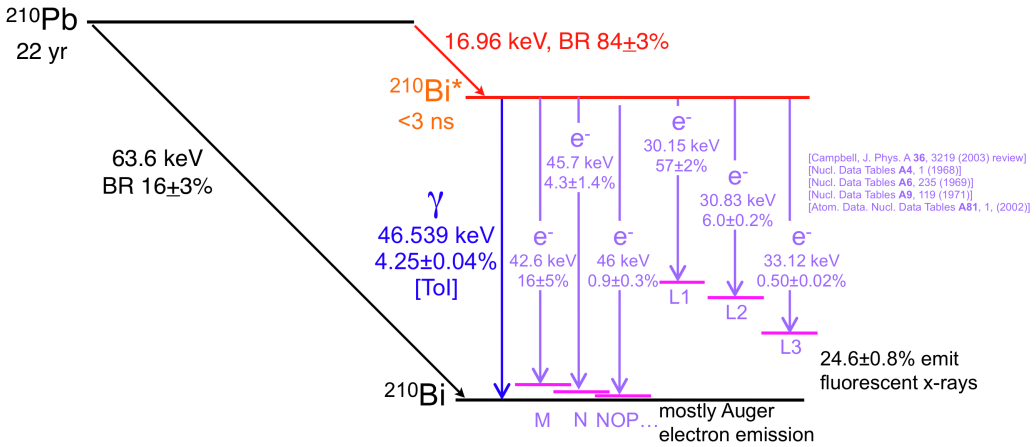

Figure 5.6: Decay scheme of ^{210}Pb. In 84% of the time the β-decay goes into an excited state of ^{210}Bi. The subsequent de-excitation yields a characteristic energy signal at 46.5 keV, which, however, is partitioned into two adjacent detectors.

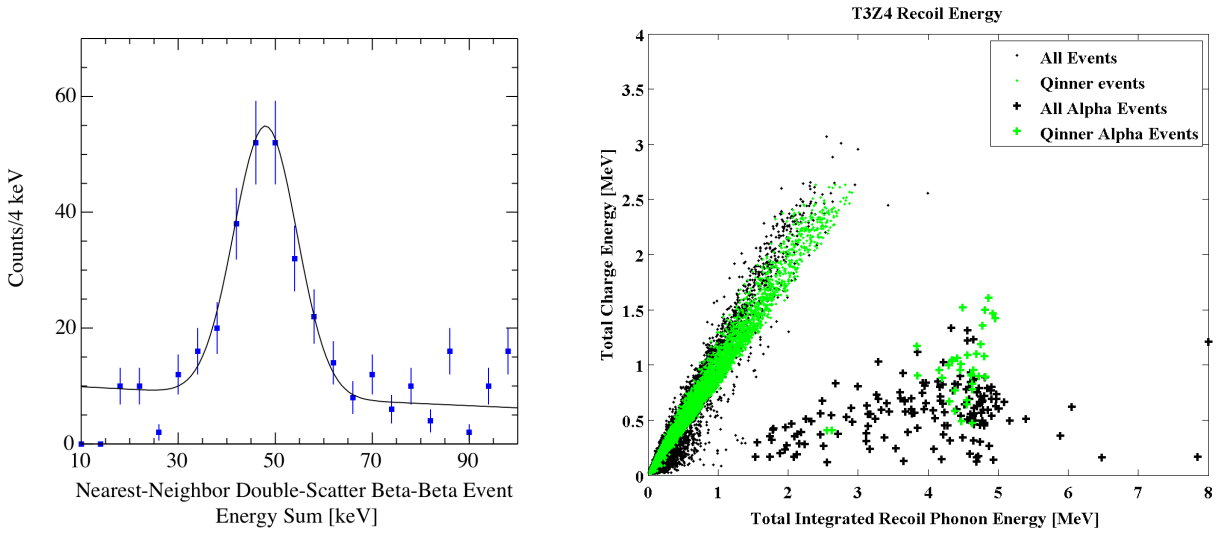

Figure 5.7: The two signatures of ^{210}Pb contamination of the detectors' surfaces. *Left*: Histogram of summed recoil energies of double scatters within adjacent detectors showing a clear peak just below 50 keV. *Right*: Scatter plot of charge energy versus recoil energy for detector T3Z4 showing a clear distinct population of α-induced interactions. Figure provided by R. Mahapatra.

events based on their ionization yield since they can directly populate the nuclear-recoil band. Thus, other parameters were investigated, which could be useful in this regard. For example, it sounds reasonable that an event, occurring very close to a detector's surface, deposits most of its energy within that quadrant of the phonon sensor, which is closest to the event location, while an interaction within the bulk of the crystal is very likely to yield significant signals in all four quadrants. Thus, a possible discrimination parameter could be the ratio of the phonon energy within the primary channel, the one with the largest pulse, and the opposite channel. This parameter has proven to have good discrimination characteristics. However, the signal in the opposite quadrant is usually very small so that this ratio suffers from poor noise behaviour. Fortunately, other characteristic differences between bulk nuclear recoils and surface electron recoils were observed, which are related to the pulse shape and timing characteristics of the phonon pulses. Since the interactions of surface events occur very close to the phonon channels, the propagation and down-conversion of the corresponding phonons are much faster compared to interactions within the bulk of the crystals. This is manifested particularly in two parameters introduced in chapter 4.5.4.4 on phonon reconstruction, the risetime of the primary (largest) phonon pulse and its delay relative to the more prompt ionization pulse. To illustrate the difference in risetime, Fig. 5.8 shows a comparison of primary phonon pulses of a typical surface electron recoil and a bulk nuclear recoil. Both events have similar recoil energies ($\sim$60 keV) but are additionally normalized to have the same amplitude. It can be observed that the rising edge of the surface event is much steeper. To keep the rejection of surface events simple, the collaboration decided to use the sum of both variables, rather than both independently or more complicated linear combinations of them, for discrimination.

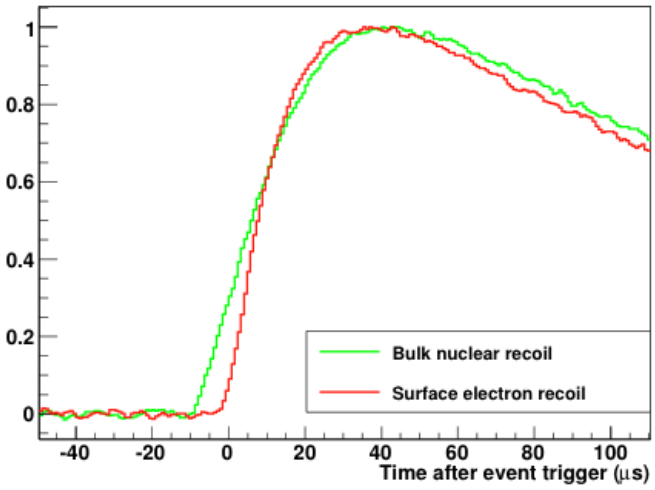

Figure 5.8: Comparison of typical pulse shapes of a surface electron recoil and a bulk nuclear recoil event. The rising edge of the surface event is much steeper. Figure provided by M. Fritts.

From Fig. 5.9, which shows the energy dependence of this timing parameter, it can be observed that there is a significant overlap between the populations of bulk nuclear recoils and surface electron recoils. In particular, it is clear that the rejection power is much worse than the ionization yield based discrimination of bulk electron recoils. Note the well-separated bands in Fig. 5.3. Therefore, the part of the analysis related to surface-event rejection was quite involved and demanded a significant employment of labour. The two statistical techniques dealing with background rejection discussed at the beginning of this chapter, the cut-based method and the likelihood approach, were of great importance in this regard. Their employment is elucidated later in this thesis. A comment regarding the cut-based method is in order: As the CDMS collaboration has the desire to keep the total expected background below 1 event, a significant part of the signal region has to be cut out, as can be seen from Fig. 5.9, decreasing the signal acceptance by up to a factor of $\sim$2. This illustrates that a proper treatment of the surface event background was a very important and delicate issue.

Before finishing this chapter and starting with the description of the actual analysis, it should be noted that there seems to be a difference in ionization yield as well as in timing behaviour between surface events occuring on the phonon and the charge side of a detector. These events can be identified by searching for double scatters in adjacent detectors, since at least the surface events, originating from the ^{210}Pb contamination, should yield a signal in both detectors as discussed before. A detailed analysis was performed at Berkeley, where a collimated ^{109}Cd source was mounted directly on the charge and phonon side one after another [75]. It was shown that charge-side events typically have higher yield compared to phonon-side events. This effect, which is is not understood yet, can also be observed in the barium calibration data taken at Soudan, for example in Fig. 5.10, which shows the ionization yield for surface electron recoils in a representative detector and run divided into events occurring on the charge side and phonon side. The events, which

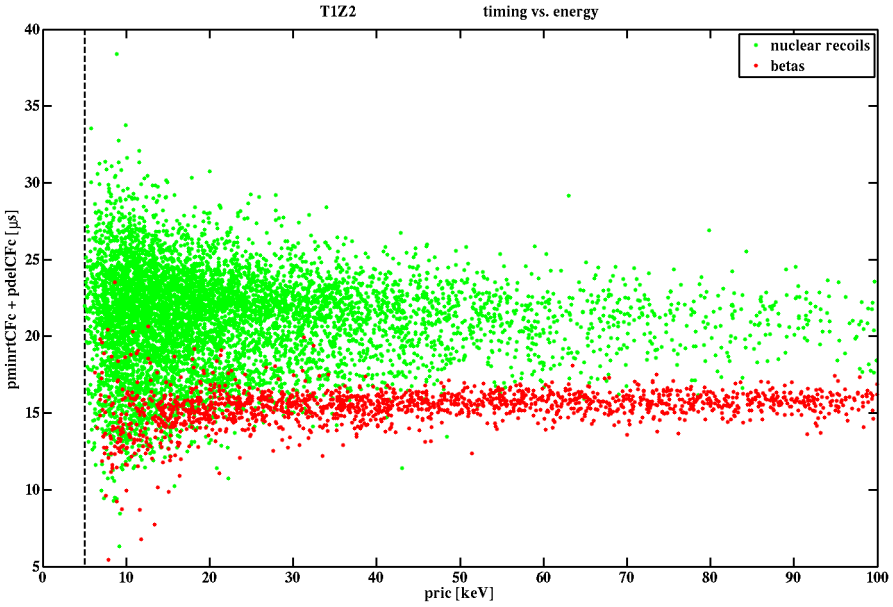

Figure 5.9: Timing parameter (pminrtCFc+pdelCFc) versus recoil energy (pric) for nuclear recoils from ^{252}Cf and surface events (betas) from ^{133}Ba calibration data in detector T1Z2. The cuts for the definitions of both populations will be discussed in a later chapter. The populations have a significant overlap thwarting the rejection of surface events. The vertical line at 5 keV denotes the threshold for the likelihood analysis presented in chapter 8.

cannot be assigned to either side, since there is no signal in any of the adjacent detectors, are denoted as untagged events. Thus, regarding ionization yield, phonon-side surface events are much more likely to mimic nuclear recoils than charge-side events. Moreover, it was observed in the Berkeley calibration runs that the phonon-side events typically have slightly lower timing parameters than charge-side events. This means that they are more likely to resemble WIMP interactions regarding ionization yield, but that they are at the same time also more likely to be rejected by a surface-event rejection cut, based on the timing parameter, compared to charge-side surface events. In contrast to the difference in ionization yield this behaviour cannot be definitely observed in the calibration data taken at Soudan. In some detectors, like the one used for Fig 5.11, there seems to be a slight trend of phonon-side events to lower timing parameters, but in some others it is just the other way around. This might be due to the lower statistics in the barium calibration data in Soudan compared to the Berkeley calibration run, where the source was positioned directly on the detector surfaces. For the "standard" WIMP analysis, presented in chapter 6, it was decided to take a possible difference between the timing response of charge- and phonon-side surface events into account. For the inelastic dark matter analysis, presented in chapter 7, such a correction was omitted, particularly because a separation amounts to neglecting all untagged events, which, as can be seen from the example in Fig. 5.10, is a quite large number of events. It should be directly noted that both approaches yielded

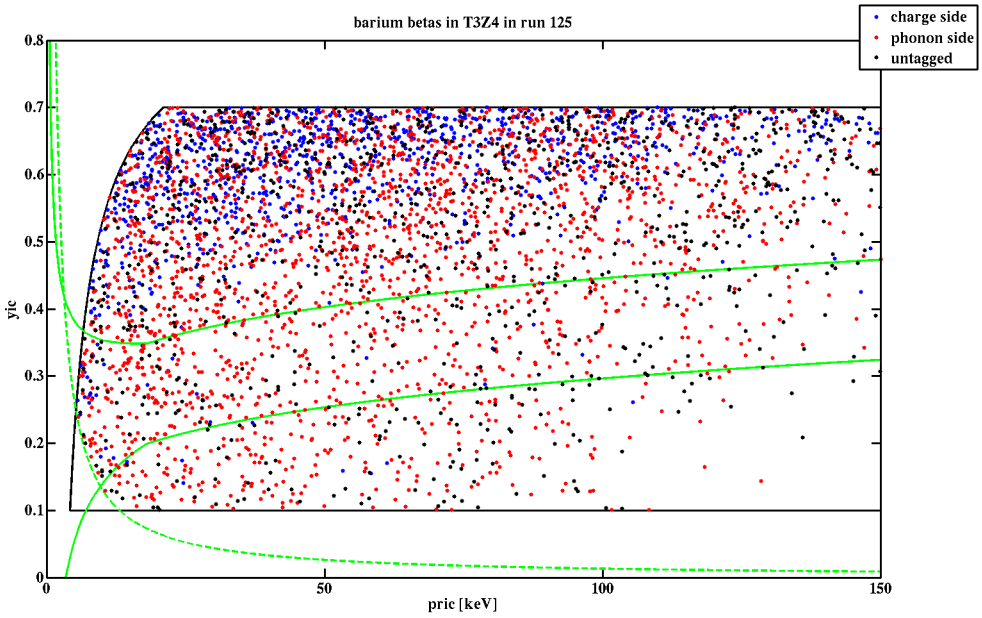

Figure 5.10: Ionization yield (yic) versus recoil energy (pric) for surface events (betas) from ^{133}Ba calibration data in detector T3Z4 in a representative run. Charge-side events (blue) typically have higher ionization yield than phonon-side events (red). The solid/green lines denote the nuclear-recoil band so the WIMP-acceptance region, and the dashed/green line denotes the charge-threshold cut as discussed in chapter 6.4.3.4. The surface event definition illustrated by the region bounded by the solid/black line is discussed in chapter 7.1.

appropriate results.

The expected number of surface-background events was significantly influenced by the actual surface event rejection cut. The estimated background for the standard analysis presented in the next chapter was given by

$$n_{\mathrm{e,surf}} = 0.82^{+0.12}_{-0.10}(\mathrm{stat.})^{+0.20}_{-0.19}(\mathrm{syst.}) \tag{5.33}$$

[89]. A detailed discussion of the definition of the surface event rejection cut as well as the estimate of the corresponding leakage is given in the context of the inelastic dark matter analysis in chapter 7. The corresponding elucidation for the standard analysis is omitted since the calculations were very similar.

5.4 Total background of the standard analysis

Combining the background estimates from cosmogenic neutrons, radiogenic neutrons, bulk electron recoils and surface electron recoils led to a total leakage estimate of

$$n_{\mathrm{tot}} = 0.9 \pm 0.2\,, \tag{5.34}$$

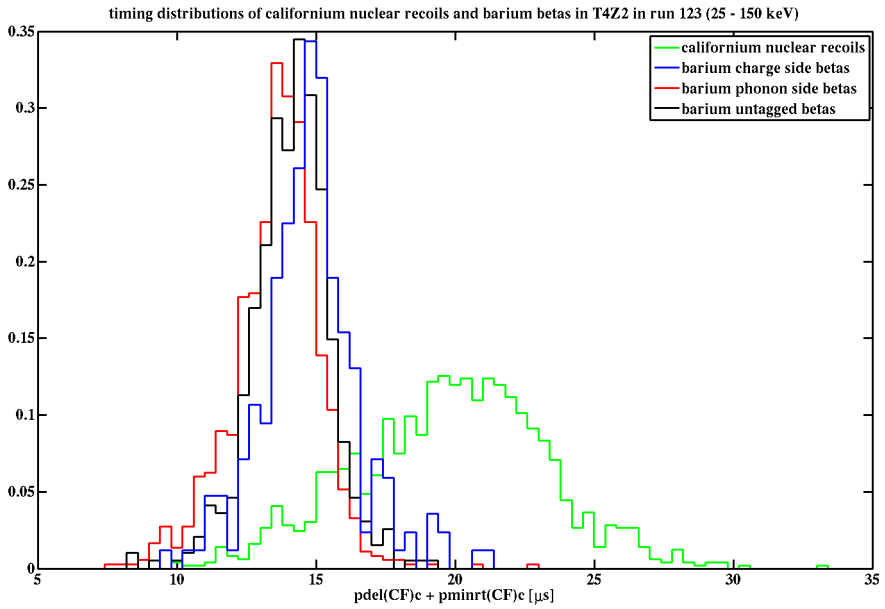

Figure 5.11: Histograms of the timing parameter (pdelCFc + pminrtCFc) for nuclear recoils from ^{252}Cf and the three types of surface events (betas) from ^{133}Ba calibration data as discussed in the text in detector T4Z2 in a representative run. In this case phonon-side surface events seem to have slightly lower timing parameter values than charge-side events. Besides, the plot again illustrates the large overlap between the distributions of nuclear recoils and surface events.

which was dominated by the surface events. The other three contributions were much less significant. The given result was valid for the exposure of the standard analysis and included cut acceptances as discussed in the next chapter. It was slightly below 1 event as desired, so that each possible event passing all WIMP criteria could be considered as a valid WIMP candidate, even though fluctuations of the background had to be considered.

Chapter 6

The "standard" WIMP search analysis

In this chapter the "standard" WIMP-search analysis is discussed. The additional denotation "standard" is used to distinguish this analysis from the inelastic dark matter analysis, discussed in the next chapter, which had a special emphasis on events with tens of keV recoil energy. Here, the focus is on the conventional WIMP scenario, characterized by an expected nearly exponential differential rate spectrum. In particular, WIMP candidates are expected at very low recoil energies, necessitating a low analysis threshold. Many parts of the analysis, especially quality cuts and basic energy-independent WIMP-selection cuts, could be used for the standard and the iDM analysis.

6.1 Outline of a WIMP analysis

Various ingredients, necessary to perform a direct detection WIMP-search analysis, were already discussed in previous chapters. First of all, a large amount of WIMP-search data has to be acquired. Moreover extensive calibrations, in the case of CDMS applying a ^{252}Cf source emitting neutrons and a ^{133}Ba source emitting gammas, are needed in order to calibrate the detectors' responses and define criteria for data quality and the WIMP-acceptance region. The signals/pulses of all gathered events have to be transformed into appropriate quantities like the discussed timing parameters and charge, phonon and recoil energies. This step already demands great caution, as will be seen at the end of this chapter, where the obtained WIMP candidates are examined in more detail. The actual analysis is completely based on these derived quantities. At the beginning, the WIMP search events "near" the expected signal region are removed from the data samples accessible to the analysis crew, in order to prevent a possible bias and fine-tuning of selection criteria. Subsequently, an enormeous labor input is needed to check the data for possible flaws, culminating in a large number of data-quality and data-reconstruction cuts. Traditionally, the CDMS collaboration is extremely conservative, regarding the quality of the final data to make sure that only true WIMP candidates survive the rigorous selection

process. Apart from these rather technical selection criteria, a few physics cuts have to be defined. Regarding its significance, the surface-event rejection, which is certainly the fanciest part of the analysis, is of particular interest. While defining these selection criteria, the reduction of WIMP acceptance has to be properly taken into account. Moreover, background estimates have to be calculated, which were already discussed in the previous chapter. In the next step, all cuts have to be applied to the WIMP-search data (of course including the events near the signal region which were removed at the beginning before the cuts were defined). The events surviving all cuts can be considered as possible WIMP candidates. Their number should be compared to the expected total background and their proximity to background and signal distributions should be analyzed if applicable. Finally, the result should be used to constrain a possible signal or set an upper limit on the strength of the WIMP-nucleon cross section.

6.2 Summary of data runs and used detectors

Before discussing the actual analysis it seems useful to summarize the data runs acquired by CDMS and the used detectors.

As mentioned in a previous chapter, the CDMS collaboration performed a WIMP search, based on data acquired at the shallow site at the Stanford Underground Facility (SUF) between April 2000 and July 2002. Since the shielding against muons was quite weak, only 17 m water equivalent, the background was dominated by cosmogenic neutrons rather than by surface events. In total, there were two runs with one tower. In October 2003, data taking at the Soudan Laboratory began using the tower from the previous SUF runs. Subsequently, additional towers were added, until the first data run with the final configuration with five towers, denoted run 123, was started in October 2006. Run 123 and the additional run 124 lasted until July 2007 and were jointly analyzed culminating in the world leading limit on spin-independent WIMP-nucleon interactions at the time of publication [61]. The discussion in this chapter is based on the combined analysis of the four subsequent runs, denoted 125–128 taken between July 2007 and September 2008. The results were published in Science [3]. Some of the following chapters also include analyses based on data from runs 123–124. A summary of all acquired data runs from the CDMS collaboration including some runs not explicitely mentioned in this paragraph is given in Table 6.1 for completeness. Each run consisted of a large number of "series" typically $\sim$12 hours long.

Not all of the 30 detectors were used for the analysis presented here. First of all, the Si detectors were omitted since except for low-mass WIMPs ($\lesssim$10 GeV/c^2) their sensitivity to spin-independent WIMP-nucleon scattering was much lower. Here they were only used to reject multiple-scatter events, which are expected to be due to neutron rather than WIMP interactions. From the remaining 19 Ge detectors a few were inoperative due to various issues. For example detector T1Z1 had three broken phonon channels and no working LEDs needed for the neutralization process. T1Z3 had a disconnected amplifier of the outer charge electrode and so forth. In total, five Ge detectors had to be omitted leaving

Run	Start of run	End of run	Location	Towers
20	April 2000	December 2000	Stanford	1
21	August 2001	July 2002	Stanford	1
118	October 2003	January 2004	Soudan	1
119	March 2004	August 2004	Soudan	1–2
123	October 2006	March 2007	Soudan	1–5
124	April 2007	July 2007	Soudan	1–5
125	July 2007	January 2008	Soudan	1–5
126	January 2008	April 2008	Soudan	1–5
127	May 2008	August 2008	Soudan	1–5
128	August 2008	September 2008	Soudan	1–5

Table 6.1: Summary of all CDMS data runs analyzed regarding the search for dark matter particles. Pure calibration runs are omitted. Data from grouped runs were combined and jointly analyzed.

14 remaining working detectors, whose data could be analyzed. A summary is shown in Table 6.2, where the working detectors are marked using bold font. All the others are either Si detectors or broken Ge detectors.

It should be noted that for previous analyses the CDMS collaboration had just used approximate standard weights of 250 g for Ge and 100 g for Si detectors. However, it turned out that these values were quite crude estimates. For the current analysis the masses were calculated based on the exact detector geometry shown in Fig. 4.4 and the measured thicknesses for each detector separately. The results are given in Table 6.2. The mean detector mass of 233 g for the used Ge detectors is much lower than the value used before.

	T1	T2	T3	T4	T5
Z1	Ge (230.5)	Si (101.4)	Si (104.6)	Si (101.4)	Ge (224.5)
Z2	**Ge** (227.6)	Si (104.6)	**Ge** (231.2)	**Ge** (238.9)	Ge (229.5)
Z3	Ge (219.3)	**Ge** (219.3)	Si (104.6)	Si (101.4)	Si (101.4)
Z4	Si (104.6)	Si (104.6)	**Ge** (238.9)	**Ge** (234.6)	**Ge** (224.5)
Z5	**Ge** (219.3)	**Ge** (238.9)	**Ge** (238.9)	**Ge** (231.9)	**Ge** (234.8)
Z6	Si (104.6)	Si (104.6)	**Ge** (231.7)	**Ge** (238.9)	Ge (223.6)

Table 6.2: Summary of all CDMS detectors. Those marked with bold fonts are working Ge detectors used for the analysis presented here, while all others are either Si detectors or broken Ge detectors. The values in brackets are the respective detector masses in g computed taking the exact detector geometry and measured substrate thicknesses into account.

6.3 Blinding of the data

As mentioned in the introduction of this chapter, the first step of the analysis consisted of the removal of all WIMP search events, which were "near" the expected signal region. This process called "blinding" was an important ingredient of the analysis procedure, since it ensured an unbiased analysis and made fine-tuning of the cuts essentially impossible. Without blinding it would have been possible that a few events were rejected or admitted by twisting a cut into the desired direction, which could also happen semi-unintentionally. This is of utmost importance regarding the interpretation of the data, since the final result depended significantly on the number and characteristics of the events passing all selection criteria. The blinding mask was not removed until all cuts were finalized and all background estimates were calculated.

In order to be more precise, some more details regarding the blinding cut are given here. First of all, the cut was defined and applied to the data at the very beginning before the position correction, discussed in chapter 4.5.4.5, was performed. This means, that possible changes regarding the quantities derived from the phonon signals had to be taken into account. Thus, the criteria for the blinding cut were set to be very conservative. In particular, a 3σ region around the mean of the nuclear-recoil band was blinded, even though only a 2σ band was intended to constitute the signal region regarding the ionization yield parameter. Moreover, a few additional criteria were added to the blinding cut. The phonon signal was expected to be within 6σ of the noise blob in all detectors, except of one, so the events had to be single scatters. Additionally, the location of the interactions had to be within the fiducial volume of the detectors. To be more precise, the charge energy in the outer electrode was supposed to be below 5 keV. In addition, the events should not be preceeded by a signal in the muon veto within a time window of 50 μs. Finally, the recoil energy was set to be within 5 keV and 130 keV. Only events obeying all five criteria were removed from the data sample available to the analysis crew. All other events were expected not to be possible WIMP candidates. However, after the position correction and definition of the actual bands it was observed that 14 events, which had not been removed, occurred within the 2σ nuclear-recoil band. Since this issue was discovered and a backup blinding cut was immediately defined before any of these events were studied in detail, especially regarding their timing properties, the collaboration was convinced that no bias for the analysis was possible.

6.4 Selection criteria - Cuts

The remainder of this chapter is mostly concerned with the discussion of cuts, needed in order to remove bad data or events, which cannot be good WIMP candidates. All cuts, including the less important ones, applied to the WIMP-search data are presented. Thus, this chapter gives a complete overview. It should be pointed out, that all the investigations presented here were based entirely on calibration data and WIMP-search data outside the acceptance region. These were events, which were not removed by applying the blindness

mask.

Apart from just defining and finally applying the cuts to the WIMP-search data, it is also necessary to calculate the corresponding loss of signal acceptance. This reduction can be accounted for in two ways, loss of detector lifetime or decrease in detection efficiency. There is a certain arbitrariness, which of these two categories the effect of a specific cut should be assigned to. The general procedure is to assign cuts, rejecting a certain period of time and a part or all of a detector, to a loss in lifetime. These cuts are typically energy-independent and fall into the category of data-quality and reconstruction-quality cuts. The selection criteria reducing the detection efficiency can be both energy-dependent and energy-independent. Most of these criteria are physics cuts like the nuclear-recoil cut based on the ionization yield. In the following, cuts having an impact on the lifetime and efficiency, are discussed separately.

6.4.1 Lifetime-reducing cuts

In this section all 19 cuts reducing the lifetime and subsequently the exposure of the CDMS experiment are elucidated. The cuts are loosely grouped into various classes, e.g. cuts related to neutralization or trigger information. Some of these criteria are just mentioned, while others are discussed in more detail. A summary of the impact of each of these cuts together with the calculation of the final exposure is given at the end of the section.

6.4.1.1 Issues directly observed via online diagnostics

Immediately after each series was taken, the scientist on shift at Soudan, responsible for data taking and keeping the experiment running, could mark a series as a bad data set. This might be due to incorrect DAQ settings when taking the data or to obvious misbehaviour of e.g. the noise spectra, which could be directly controlled by an online diagnostics system. The corresponding cut was named *cGoodSeries_c58*. The additional cut *cBadTimes_c58* was specifically defined to reject bad time periods after power outages.

6.4.1.2 Bad detectors and malfunctioning detector regions

As discussed at the beginning of this chapter, several Ge detectors could not be used for this analysis due to malfunctions. Even though the good detectors were usually selected manually, an explicit cut *cGoodDet_c58* was defined to omit the possibility of accidentally adding events from these detectors to the good data sample. Since malfunctioning detectors were usually neglected defining other cuts, these events might have survived the WIMP selection process.

Besides, it was observed, that a certain region of detector T3Z2 showed an unusual large population of low-yield events, which additionally had comparable low-timing parameters. This effect was assumed to be mainly due to reduced charge collection related to a disconnected part of the outer charge electrode. Since this region was localized on

one side of the detector, it was decided to remove this half from the analysis with the cut *cBadDetRegions_c58*, which reduces its exposure by about 50%.

6.4.1.3 Cuts on bias voltage

Two cuts were defined in order to reject periods with improper bias-voltage settings. The cut *cQnormbias_c58* rejected events, acquired when the bias voltage of the Ge detectors was not between 2.9 V and 3.1 V, 3.0 V being the nominal value. Besides, *cStabTuning_c58* was created to check for stable tuning of the same charge-bias voltage, but additionally and more important to check the stability of the bias voltages applied to the TES's to set them just below the edge of superconductivity.

6.4.1.4 Cuts based on trigger information

Several cuts were defined to check different criteria based on trigger information. First of all, *cErrMask_c58* removed all events with erroneous saved trigger information. Moreover, it was made sure by *cGlobTrig_Soudan*, that a global trigger actually occurred in at least one detector. As discussed in chapter 4.5.2, this global trigger was based on the phonon signal. It was found, that this trigger was accidentally disabled in some detectors over some short periods of time. All of the events acquired during these periods were removed by the cut *cPlo_Disabled_c58*.

If the experiment is in WIMP-search mode, in other words, if no calibration is performed, the trigger rate should be quite low, as mentioned in chapter 4.5.2 around 0.2 Hz. Thus, any occurrence of an increase in trigger rate is suspicious and such time periods were conservatively removed. The threshold for this cut denoted *cTrigBurst_c58* was set to 0.7 Hz. All series with a higher mean trigger rate were removed. Only four series were affected by this cut.

During some short periods of run 125 and run 127 a dramatic increase of the trigger rate was observed, related to events with a normal phonon but an extremely small charge signal. The reason for this behaviour is assumed to be related to scattering of Helium atoms on the detector's surfaces. These events would have extremely low ionization yield (<0.1), since they cannot penetrate deeply into the crystal. The origin of these Helium atoms is believed to be Helium used for the cooling of the dilution refrigerator, which reached the detectors through a possible small leak. Since the charge signal of these events was so small, the corresponding events actually were already removed by the charge-threshold cut discussed in the next chapter. However, to be conservative, all affected series were completely removed with a dedicated cut named *cHeFilm_c58*.

6.4.1.5 Uniformity of the data

An important prerequisite for an experiment, searching for rare events like CDMS, is the ability to gather uniform data over long periods of time. Since the performance of the detectors' responses can vary significantly over time, it is necessary to check this uniformity explicitly. Kolmogorov-Smirnov (KS) tests were applied to examine the similarity of

different series. These tests were based on a few representative parameters, like ionization yield, risetime and delay. For WIMP-search and barium calibration data, the distributions of these parameters from all series were compared with 30 different representative series from the same run. The corresponding KS-test values were calculated and averaged over all 30 comparisons. If these averaged KS-test values for any of the considered parameters were lower than the corresponding KS-test values, averaged over all series by more than 2σ or lower than 0.001, the series was removed. Extensive manual inspection of numerous plots was necessary to check the results, since small populations of outliers tended to have a significant impact on the actual cut setting. Thus, some tweaking of this cut was necessary, rendering its adequate definition a tedious labor. The final result was actually two cuts *cBadDet_bg_c58* and *cBadDet_Ba_c58* for WIMP-search data and barium-calibration data respectively. The number of californium-calibration series was too limited to allow a reliable application of KS-tests following the scheme just outlined.

6.4.1.6 Neutralization

As previously discussed, ionized trapping centers exist within the equilibrium state of the crystals. Their concentration is increased, if the detectors are voltage biased for a long time. Thus, the detectors are flashed every ∼12 hours. In particular, since this procedure failed occasionally due to problems with the DAQ software, it was necessary to check the neutralization state of the detectors explicitly. Because electron-recoil events with reduced charge collection due to trapped charge carriers can mimic nuclear-recoils, it is of great importance to remove all time periods with insufficient neutralization.

Investigating low-yield events provides good indication of proper neutralization. It is known from the discussion of surface events that a huge fraction of these events are due to electron-recoil interactions within thin layers at the detectors' surfaces. However, their contribution should be time-independent. Thus, periods within the data with particularly large fractions of low-yield events compared to the average over the whole runs indicate a loss of neutralization. A few criteria to quantify a fractional increase of low-yield events were used to define cuts removing these periods.

For this study low-yield events were defined to have ionization yield within 0 and 0.8. Considering barium data, all series were divided into chunks of 100000 events each. Subsequently, the means and standard deviations of the fractions of low-yield events were calculated separately for all of these chunks as well as for all data within a given run combined. A chunk was considered to be insufficiently neutralized, if its mean occurred more than 2σ above the combined mean. A second criterion was based on the Poisson probability to observe more low-yield events n_{low} within a given chunk of total events n_{tot} than expected regarding the average fraction of low-yield events over the whole run f:

$$p(n > n_{\mathrm{low}}) = \sum_{k=n_{\mathrm{low}}+1}^{\infty} \frac{(f \cdot n_{\mathrm{tot}})^k}{k!} e^{-(f \cdot n_{\mathrm{tot}})} = 1 - e^{-(f \cdot n_{\mathrm{tot}})} \cdot \sum_{k=0}^{n_{\mathrm{low}}} \frac{(f \cdot n_{\mathrm{tot}})^k}{k!} \overset{!}{<} 10^{-10} \quad (6.1)$$

If a chunk failed any of these two conditions, it was removed from the analysis. The

corresponding cut was denoted *cBadNeut_ba_c58_pre*. Since it only affected barium data, it had no impact on the obtained WIMP-search exposure.

Regarding WIMP-search data, it was impossible to divide a particular series into various chunks due to the low number of acquired events. Thus, each series had to be considered as a whole. The same two criteria, applied to the barium, were also used to characterize the neutralization state of WIMP-search series. However, it was observed that some obvious outliers still survived the cut. Thus, a third condition was added to the cut. A series was removed from the analysis, if its low-yield fraction was more than 5σ above the run's mean, with σ denoting the run-averaged standard deviation in this case:

$$\sigma = \sqrt{\frac{N}{\sum_{i=1}^{N} \frac{1}{\sigma_i^2}}} \tag{6.2}$$

Here N denotes the number of series in the run and σ_i the standard deviation in the i^{th} series. The cut arising from this investigation was *cBadNeut_bg_c58*.

Apart from these criteria, based on the search for abnormally high low-yield fractions, a different type of cut, based directly on the time elapsed after the last flash, was defined. For this analysis, every WIMP-search series was investigated using two criteria in order to be sure, that there were no problems with deneutralization in the detectors. If there was a WIMP-search run preceded by a barium or neutron calibration without a flash in-between, the detectors might not be properly neutralized. The same problem might occur, if the detectors were voltage biased for a very long time after the last flash. A quite conservative upper limit of 20 hours was chosen for this analysis. These criteria affected all detectors simultaneously, so that this cut was not defined on a detector-by-detector basis.

Regarding a missing flash between a calibration and a WIMP-search series it was found, that 22 series had to be considered as potentially insufficiently neutralized. However, most of the preceding calibration series were very short, with less than 1000 acquired events, while standard calibration series had ∼400000 events. Thus, the corresponding WIMP-search series were fine. Finally, only eight series were removed by this part of the cut. It should be noted, that WIMP-search series, after possibly deneutralized WIMP-search series with no flash in-between, were about to be checked, too. But it did not happen. Testing the second criterion of removing events acquired more than 20 hours after the last flash, if the detectors were voltage biased, removed only very few events at the ends of eight different WIMP-search series. Figure 6.1, for example, shows the time the detectors were biased after the last flash for all WIMP-search events acquired during run 125. In this case only three series at the end of the run extended to more than 20 hours after the last flash with an electric field applied.

The data removed by the corresponding cut denoted *cBadFlash_c58*, which combined both criteria, were compared to those tagged as potentially insufficiently neutralized by the criterion, based on the low-yield fraction (*cBadNeut_bg_c58*). Unexpectedly, only one series was removed by both cuts, and regarding *cBadNeut_bg_c58* it was only removed for one

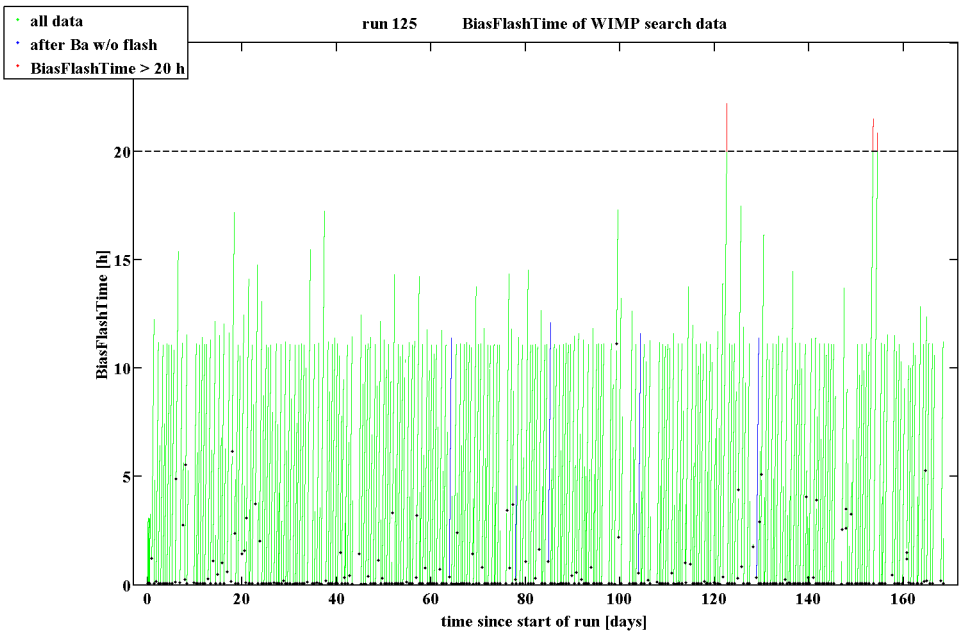

Figure 6.1: Times the detectors were voltage biased after the last flash for all acquired WIMP-search events of run 125. Typically, there was a new flash before the start of a WIMP-search series. Five series preceded a barium calibration run with no flash in-between (blue), e.g. due to DAQ issues. They were completely removed according to the first criterion discussed in the text. Additionally the last events of three series were removed according to the second criterion (red).

particular detector. In order to be conservative, and since *cBadFlash_c58* only removed a very small fraction of the total data, both cuts were used in the analysis.

6.4.1.7 Resolution of the fit parameters from optimum filtering

As discussed before the obtained pulses were fitted by applying an optimal filter algorithm with two free parameters, a scaling factor for the amplitude and the start time of the pulse. Approximate errors on these parameters could be estimated for all events within a given series together, since they were dominated by the power spectrum of the used template and the noise spectrum of each series. It should be noted, that a lower limit on the resolution of the start time existed due to the sampling bin size of the traces of 0.8 μs. The resolutions were calculated for all four phonon channels and the inner charge channel. A series was removed by the created cut *cBadResTight_c58*, if any of these 10 resolutions was more than 25% above the corresponding mean over the whole run. The plot in Fig. 6.2 shows the relative amplitude resolution of the phonon channel B for T5Z4 in run 125. Obviously, there were some periods of degraded resolution at the end of the run.

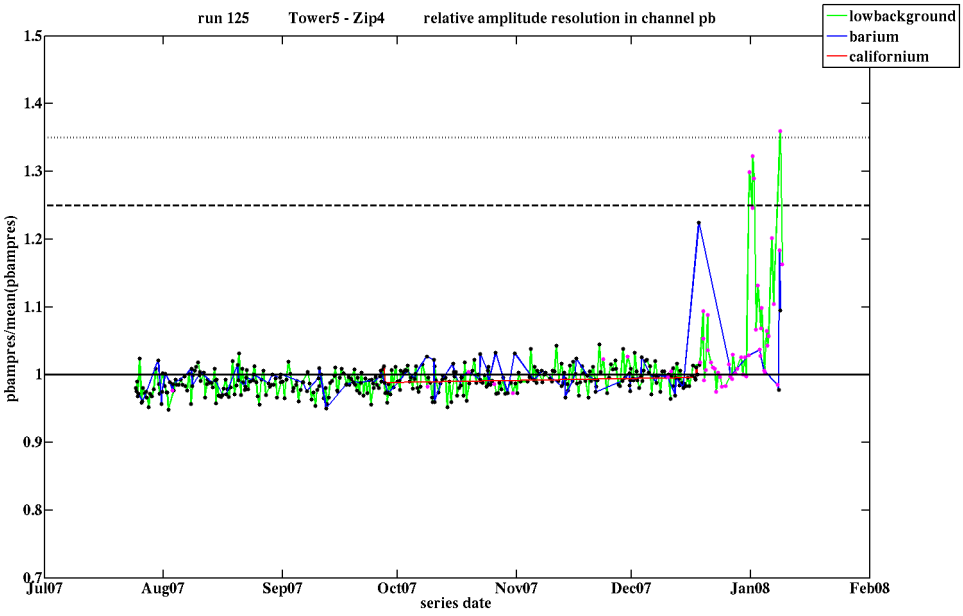

Figure 6.2: Relative amplitude resolution of phonon channel B for detector T5Z4 in run 125. At the end of the run, some WIMP-search series (lowbackground) had standard deviations of more than 25% above the run's mean (black/dashed) and were thus removed by the created cut *cBadResTight_c58*. A looser cut, used for different studies but not for the final analysis, was set at 35% (black/dotted). Series with magenta dots were also removed by other quality cuts discussed in this chapter, so regarding only the detector and channel shown here, the cut would be redundant. However, in general this was not the case.

6.4.1.8 Increased charge noise

It was of great importance to check the behaviour of the charge noise level, in particular considering its time dependence. Increased noise would lead to larger uncertainties regarding the determination of the charge pulse's start time, which would subsequently affect the rejection of surface events based partly on the delay parameter, as discussed in the previous chapter. In chapter 6.4.3.4 a cut rejecting events within the noise blob is discussed. However, the definition of this criterion is solely based on random triggers taken mostly at the beginning of each series with just a few additional random events taken throughout the remainder of the series. Thus, changes regarding the noise performance over the course of a series were not sufficiently accounted for by this cut. Therefore, additional rejection criteria for periods of elevated charge noise had to be introduced.

In order to define this cut, noise events had to be selected from the data. At first, Gaussian distributions were fitted to the noise blobs of the total phonon energy, summed over all four sensors, obtained from randomly triggered events series-by-series. Subsequently, all events below a series-dependent cut set at 4σ above the respective mean were considered as noise events. This population, containing events taken throughout each series and not just

at the beginning, was used for the analysis of the charge noise behaviour. The cut itself was based on the total charge energy summed over the inner and outer energies. This energy was first smoothed over 20 events by calculating the running average. These values were supposed to be below the mean plus $(6/\sqrt{20})\sigma$, calculated based on the noise distribution of the smoothed data, where the additional factor of $\sqrt{20}$ took the number of events used for the process of averaging into account. All time periods, identified as having a high noise level, were extended by additional time intervals of 5 minutes before and afterwards. The corresponding cut rejecting these time periods was denoted *cHighQNoise_c58*.

As discussed in chapter 4.5.2, each recorded trace contained a pre-pulse baseline of 409 μs. This baseline could be used to reject events with particular noisy traces. The main purpose of the corresponding cut was to reject time periods of elevated charge noise induced by the cryocooler, which was added to support the cooling system after towers 3–5 were added as elucidated in a previous chapter. During its duty cycle it induced mechanical vibrations into the detector assembly. The phonon channels and most of the charge channels were not affected by these vibrations, however, the charge channels in a few detectors, especially T3Z2 and T3Z5, showed a significant microphonic pickup near and below 10 kHz. It turned out that the corresponding noisy time periods could be efficiently removed from the data by defining a cut based on the deviations of the charge pre-pulse baseline. Therefore, the distributions of the standard deviations were fitted with a Gaussian for each series separately, and a cut denoted *cQstd_c58* was set at 4σ above the respective mean.

6.4.1.9 Summary

As mentioned in the introduction to this chapter, all of these 19 cuts reduced the acquired exposure. In order to check the severity of each cut, Fig. 6.3 shows the remaining exposure after applying the cuts given at the left side of the plot. The corrected detector masses, given in Table 6.2, were used for these calculations. The blue bar at the top (0) gives the raw exposure, considering only the used detectors (equivalent to directly applying *cGoodDet_c58*) and good series (equivalent to directly applying *cGoodSeries_c58*). It can be observed that the raw-exposure of runs 125–128 was ∼790 kg-days. All of the cuts, except for *cQstd_c58*, were merged into *cBad_c58*, so that the red bar denotes the total exposure after all cuts:

$$\mathrm{MT} = 612.1\,\text{kg-days} \tag{6.3}$$

Thus, ∼180 kg-days of exposure were omitted due to the imposition of basic quality criteria. This is not necessarily a sign of generally quite badly behaved data but reflects the great conservatism of the collaboration regarding the quality of its data manifested in very strict cut criteria.

Obviously, most of the discussed cuts had only a minor impact on the total exposure. This is clear for *cGoodDet_c58* and *cGoodSeries_c58*, since they actually were already imposed as preselection cuts, and *cBadNeut_ba_c58_pre* and *cBadDet_Ba_c58*, since they only removed series from barium calibrations. Regarding reduction of exposure, the dominant

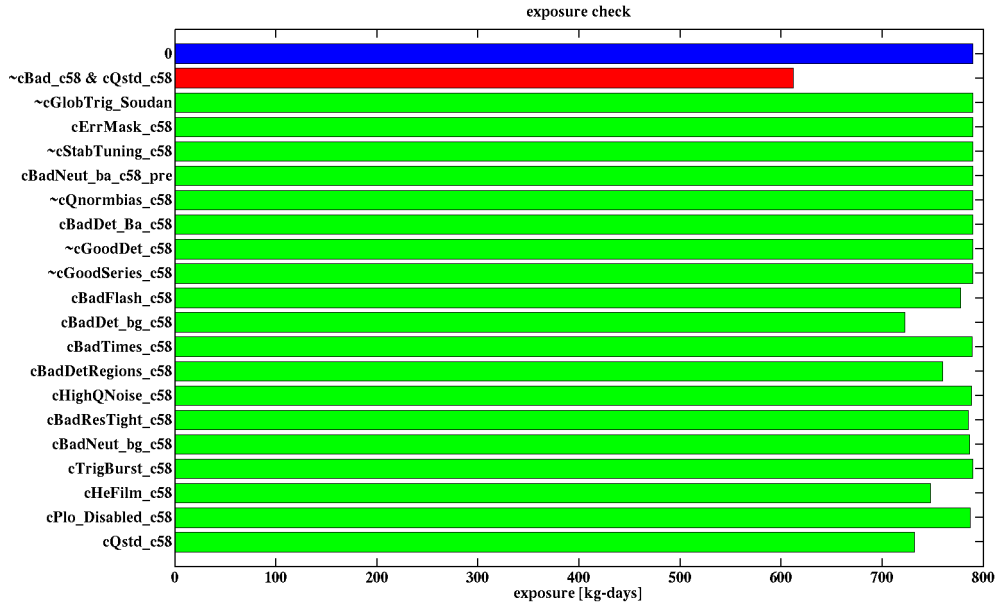

Figure 6.3: Summary of the loss of exposure for each cut discussed in this chapter. The blue bar gives the raw exposure, while the red bar shows the final exposure after all cuts. The main reductions are due to *cQstd_c58*, *cHeFilm_c58*, *cBadDet_bg_c58* and *cBadDetRegions_c58*. See text for more details.

cuts were *cQstd_c58*, *cHeFilm_c58*, *cBadDet_bg_c58* and *cBadDetRegions_c58* with the latter only affecting detector T3Z2. It should be noted that the sets of events, removed by theses cuts, were not disjoint, which means that loosening one of the cuts would not necessarily yield a large increase of the exposure. Therefore, it is not useful to show the reduction of exposure by imposing the cuts successively.

6.4.2 Energy-independent efficiency-reducing cuts

This chapter describes all cuts, which were attributed to a loss of efficiency rather than lifetime, and whose energy-dependence was either negligible or that were energy-independent by definition. In total, 11 cuts belonged to this category. Most, but not all of them, were related to quality issues.

Estimation of the cut efficiencies was essentially just the calculation of the ratio of a number of events n passing a certain cut that was examined, to the total number of considered events N. Usually, various preselection cuts were applied to obtain this test sample. Instead of considering Poisson errors on both of these numbers and applying error propagation to their ratio, the uncertainty of the efficiency estimate was based on the assumption of a binomial distribution: An event could either be accepted or rejected by a given cut. Thus the efficiency (f) and its lower (f_l) and upper boundaries (f_u) were

calculated by solving

$$f = \frac{n}{N} \tag{6.4}$$

$$\frac{\alpha}{2} \stackrel{!}{=} \sum_{k=n}^{N} \binom{N}{k} f_l^k \left(1 - f_l\right)^{N-k} \tag{6.5}$$

$$\frac{\alpha}{2} \stackrel{!}{=} \sum_{k=0}^{n} \binom{N}{k} f_u^k \left(1 - f_u\right)^{N-k}, \tag{6.6}$$

where 1-α denotes the confidence interval considered, usually taken to be 0.68 (1σ). The main difference to the application of simple Poisson errors is the occurrence of asymmetric error intervals. Moreover, these intervals could not extend to values below 0 or above 1, which would be unphysical.

6.4.2.1 Random triggers

Randomly triggered events, used for noise studies, were explicitly removed by *cRTrig*. Since these events typically had reconstructed energies well below the considered analysis threshold, this cut was essentially redundant and had an efficiency of 100%.

6.4.2.2 Pileup events

Similar to the cut *cQstd_c58* discussed previously, the pre-pulse baseline of the phonon channels was used to reject events with misbehaved signal traces. However, in this case, the cut was not intended to reject particular time periods as it was, regarding the charge pre-pulse baselines distorted by the cryocooler vibrations. Considering the phonon channels, it was more important to reject pileup events, which had pulses where two events, closely following each other, overlapped in a single digitizer trace. Such events occurred frequently taking calibration data but very rarely running in WIMP-search mode. Since the falltime of a typical phonon pulse (200 μs) was much larger than the falltime of a typical charge pulse (40 μs), the tail of a phonon pulse could be accidentally extended into the pre-pulse baseline of the subsequent phonon pulse, which could be examined by investigating the deviations of the baseline. The corresponding cut *cPstd_c58* was defined by fitting Gaussians to the standard deviations of the phonon pre-pulse baselines series-by-series and removing all events 5σ above the respective mean. The efficiencies were estimated based on random triggers, and they were generally larger than 99%. It should be noted that, as discussed in chapter 4.5.4.4, the minimum χ^2 from the optimal filter algorithm could not be used to examine the validity of the fits accurately and thus to reject pileup events.

Since negative phonon energies occurred for some events due to badly reconstructed traces, a cut was defined to remove such events. As shown in Fig 6.4, the distributions of the phonon noise blobs, based on random triggers, were fitted with Gaussian distribution functions. The cut *cNegPhononPulse_c58* removed all events 6σ below the respective mean. For simplicity, this criterion was not defined series-by-series but for all four runs as a

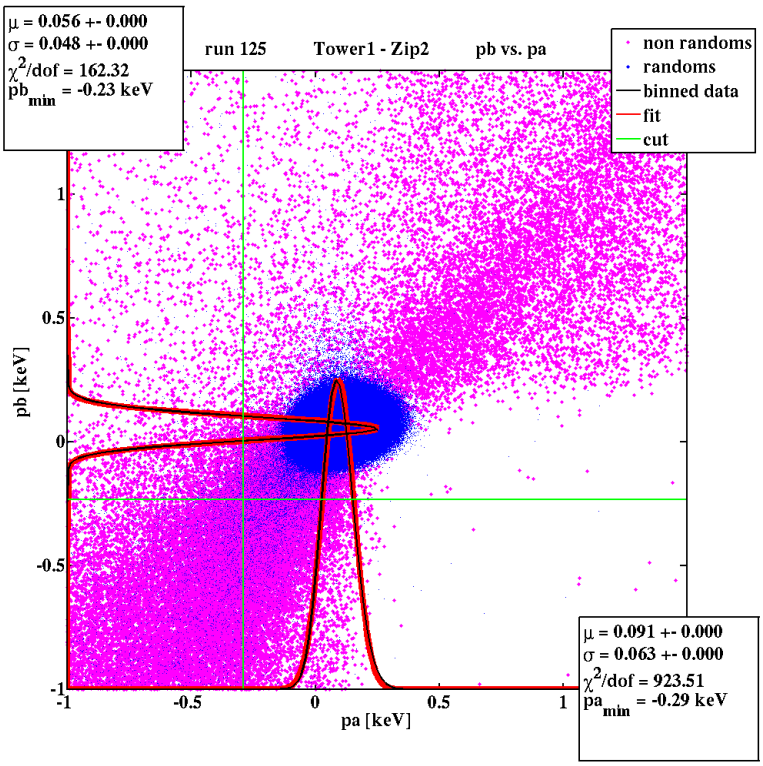

Figure 6.4: Phonon noise blob considering phonon channels A and B in T1Z2 in run 125. The noise events (blue) were based on random triggers. As discussed in chapter 4.5.3.2, the means of the Gaussians were slightly above zero. The thresholds for the cuts on both channels are indicated by the green lines.

whole. Since most erroneous events were already removed by other quality cuts discussed in the previous chapter, only 15 surviving events of the whole barium-calibration data were removed by *cNegPhononPulse_c58*. All of these events were misreconstructed due to pileup. Figure 6.5 shows the phonon traces of one of these events. Since the additional event distorting the trace of the event, which actually triggered, occurred after the trigger and not within the pre-pulse baseline, this event could not be rejected by *cPstd_c58*. The efficiency of the cut was estimated to be 100%.

There was an additional pathology related to pileup events. In calibration mode it frequently happened that a particle interacted in one detector issuing a trigger, and a second unrelated particle hit a different detector shortly afterwards. If the second interaction occurred close enough in time to induce a signal within the digitizer trace related to the first event, the pulses of both events were properly formed, but the pulse of the second (late) event often was not reconstructed correctly. Unlike pileup events occurring due to two events interacting within the same detector, this was not due to misbehaved pulse shapes but to an incorrect start time determination of the second pulse. This could happen, because the reconstruction algorithm of the optimal filter did not search for the correct

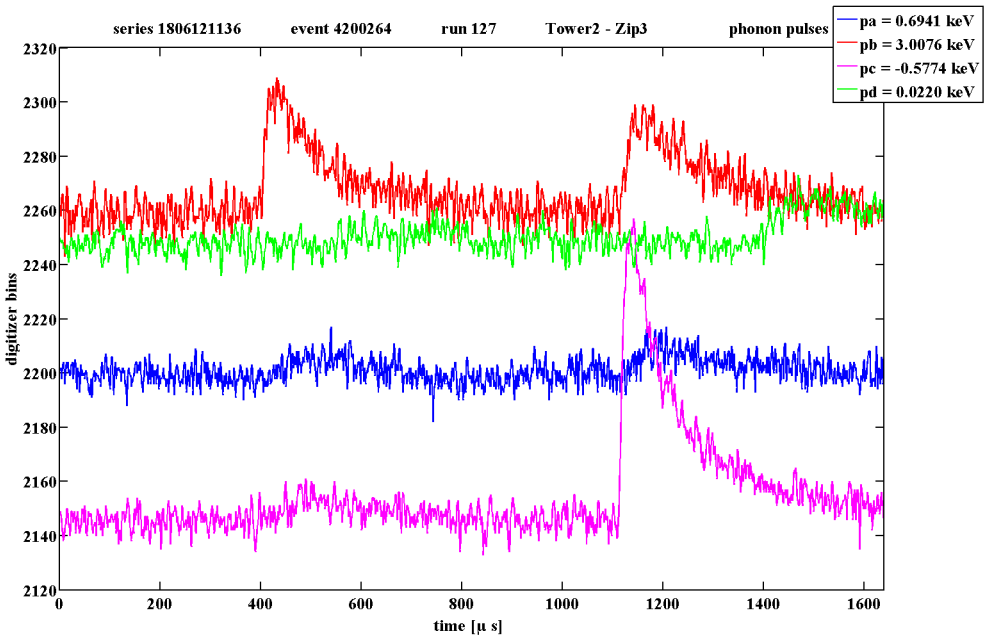

Figure 6.5: Phonon traces of a typical pileup event from barium calibration data removed only by *cNegPhononPulse_c58* but no other quality cut.

start time of the ionization pulses over the whole recorded digitizer window, but only within -100 μs and +10 μs around the trigger, in order to speed up the process. The corresponding time window for the phonon start time was [-50 μs, +200 μs]. Incorrect start times, assigned to pulses, led to very bad fits so that the events were usually rejected based on the charge χ^2-cut discussed in chapter 6.4.3.1. Nevertheless, it was observed that some events occasionally survived this criterion. This could be dangerous, since incorrectly determined start times would lead to optimal filter fits to the largest noise fluctuation within the search window leading to very low amplitudes, which mimic reduced charge collection. Therefore, these events could be misconsidered as nuclear recoils similar to surface events. Thus, an additional cut denoted *cGoodPStartTime* was defined removing pulses, where the start time of the primary phonon pulse, obtained by applying the time-domain walk algorithm, did not occur within a time window of [-50 μs, +10 μs] around the trigger. Note, that the time window mentioned before was related to the start time of the optimal filter algorithm. The pathology, discussed in this paragraph, was called cross-detector pileup. Since it occurred very rarely during WIMP-search runs due to the low data-acquisition rates, the efficiencies were 100% in all runs and detectors above the 10 keV recoil energy threshold discussed later.

6.4.2.3 Saturation of the channels

The cuts *cPsat* and *cQsat* were defined to make sure that the phonon and charge channels were not saturated for any acquired events. Since only events below 100 keV (150 keV for

the inelastic dark matter analysis) were considered, these cuts were essentially redundant and had an efficiency of 100%. A study, which these cuts were important for, was the search for α induced interactions in the context of finding evidence for a ^{210}Pb contamination on the detectors' surfaces, as discussed in chapter 5.3.2.

6.4.2.4 Electronic glitches

The complexity of the experiment's electronic system gave rise to electronic glitches, particularly since the system was upgraded from two to five towers. It was observed that these glitches usually led to triggers in many of the phonon sensors but not in the charge sensors. Thus, the difference between the number of phonon triggers and the number of charge triggers was used to reject such events. To be more precise, if this difference and the number of phonon triggers itself were larger than three, an event would be removed. Another condition was the occurrence of exactly three phonon triggers and no charge trigger. Since the corresponding cut *cGlitch_c58* should never reject a single scatter, the efficiency was 100% for all runs and detectors.

6.4.2.5 MINOS neutrino beam

An intense neutrino beam was directed to the MINOS neutrino oscillation experiment, which resides in the Soudan Underground Laboratory alongside CDMS, from Fermilab. These neutrinos could interact within the rock and shielding surrounding the detectors to induce muons and neutrons, which could subsequently scatter in the CDMS detectors constituting another possible contribution to the neutron background. Even though it seemed very unlikely to have a related unvetoed neutron interaction, it was decided to conservatively reject events within a 60 μs time window surrounding the on-time of the beam by a cut denoted *cNuMI_c58*. The efficiency was estimated to be 99.9984%.

6.4.2.6 Muon veto

In the chapters on the cosmogenic neutron background and shielding the importance of the muon veto, regarding rejection of muon induced neutrons, was discussed. It was mentioned that about one muon interacted within the veto panels per minute. The main issue was the much higher trigger rate induced by gammas from the ambient photon flux ($\sim$20000 per minute). Since the shielding surrounding the detectors provided sufficient protection against these gammas, and the loss of lifetime arising from removing all WIMP-search events coincident with activation in the veto would be unacceptable, a more involved cut had to be introduced. Given that muons typically deposited energies around 10 MeV, while the photon spectrum extended just up to 2.6 MeV, panel-dependent thresholds were defined to tag only high-energy interactions. At the end, two criteria were defined to reject WIMP-search events. Events were removed, if the aforementioned threshold was exceeded in any of the veto panels within a time window of [-185 μs, +20 μs] around the trigger, or the last veto hit occured less than 50 μs before the trigger independent of its actual

significance. The efficiency of the corresponding cut *cVTStrict_c58* was estimated to be 98%.

Moreover, *cVTrig* was specifically designed to reject events coincident with multiple triggers within the veto. Such interactions are typical for muon showers, while gammas usually induce just one trigger. Nearly all of these events were already removed by *cVTStrict_c58*, so that its efficiency was estimated to be 100%.

6.4.2.7 Rejection of multiple scatters

Since the WIMP-nucleon cross section must be extremely small, WIMPs were expected to interact in no more than just one single detector. Nuclear-recoil events with significant energy deposition in multiple detectors were very likely to be due to neutron scattering and were thus rejected as possible dark matter candidates. All 30 detectors were used to tag multiples, so this was in fact the only part of the analysis described in this thesis, which the Si detectors contributed to. The criterion was defined on the total collected phonon energy, which had superior rejection capabilities compared to the recoil energy, since it contained an additional contribution from the Luke phonons.

At first, the noise distributions of the phonon energies, based on randomly triggered events, were fitted with Gaussian distribution functions. Due to the aforementioned significant noise fluctuations these fits were performed series-by-series. An event was considered to be a single scatter, if the deposited energy in the triggered detector was more than 6σ above the mean of its noise distribution and below the anticoincidence thresholds of all other 29 detectors, which were set 4σ above the means of the respective noise distributions. In some detectors with particularly noisy phonon channels the ionization energy was used for the second criterion. The efficiency of this cut denoted *cSingle_c58* was estimated for each detector by calculating the fraction of random triggers, which exceeded the 4σ anticoincidence threshold in a different detector. The efficiencies typically were around 99%.

6.4.3 Energy-dependent efficiency-reducing cuts

The last chapter on selection criteria deals with energy-dependent efficiency-reducing cuts. In total 8 cuts fell into this category. In particular, two very important background rejection cuts, the nuclear-recoil cut, based on the ionization-yield parameter, and the surface-event rejection cut, based on the timing parameter, are discussed.

6.4.3.1 Ionization goodness-of-fit

Regarding the charge-pulse reconstruction via optimal filtering it was mentioned in chapter 4.5.3.2 that the minimum χ^2 was an excellent parameter to reject erroneous pulses, since normal pulses were of nearly fixed shape. It was also discussed that the corresponding values from the phonon pulse fits could not be used in a similar fashion. Again, the

main origin for such misbehaved pulses were pileup events, so events where another unrelated event occurred in the same detector close enough in time to induce a second pulse within the recorded digitizer trace of the first event. These pileup events were frequently found in calibration data but very rarely in WIMP-search data.

A cut was defined to reject events with a minimum χ^2 larger than a certain value. As can be seen from Fig. 6.6, which shows the minimum χ^2 as a function of the total charge energy for barium calibration data in a typical detector, the minimum χ^2 had a severe energy dependence. This was due to the inaccuracy of the pulses' start time determination related to the digitizer step size of 0.8 μs and the slight noise contributions of the templates, since they were obtained by averaging over several real pulses. The cut was defined separately for each detector and run applying barium calibration data. The means and standard deviations were calculated for the four intervals [20 keV, 40 keV], [60 keV, 100 keV], [120 keV, 160 keV] and [180 keV, 220 keV]. For low energies, the distributions could have also been fitted with Gaussians, however, the distributions became asymmetric at higher energies and a uniform procedure was intended. Subsequently, quadratic functions of the form

$$\chi^2 = a + b \cdot \mathrm{qsum}^2 \tag{6.7}$$

were fitted to the four points 3.5σ above the mean in each interval. The cut *cChisq_c58*

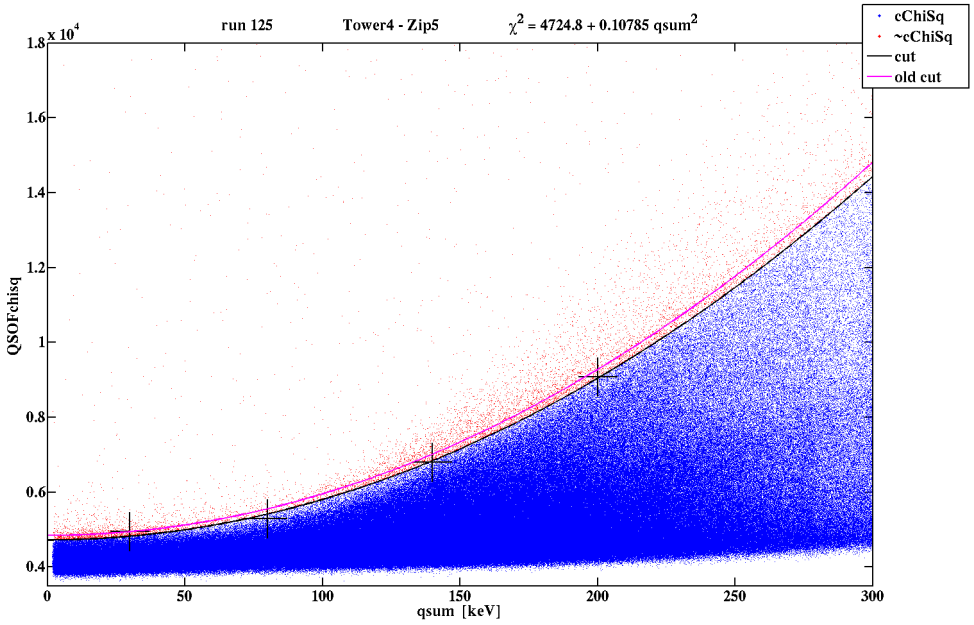

Figure 6.6: Minimum charge χ^2 returned from the optimal filter algorithm (QSOFchisq) as a function of the total charge energy (qsum) for T4Z5 in run 125. The broadening with increasing energy is accounted for by defining a cut, which is quadratic in energy. For comparison, the cut from this analysis (black) is shown together with the cut from the previous analysis of runs 123–124 (magenta).

removed all events with a minimum charge χ^2 above this line.

The efficiencies were calculated as the fraction of WIMP-search events (passing the blindness mask) passing the cut and fitted by the function

$$f(X) = a + \frac{b}{(X-c)^d} \,. \tag{6.8}$$

The efficiencies were typically larger than 98% except for low energies. An example of the result is shown in Fig. 6.7.

6.4.3.2 Efficiency of the phonon trigger

In order that the DAQ could record the signal from an interaction, it was necessary that the signal increased above a certain threshold and subsequently issued a trigger. The efficiency of this triggering process had to be estimated. Since WIMPs were expected to interact in not more than one detector, it seemed natural to consider all detectors separately for this investigation. However, the actual procedure had to take into account interactions in other detectors. This was due to the fact that only events, which were triggered by a different detector could be used for this analysis, since it was clear that considering events triggered by the detector that was investigated would introduce a severe bias: These events were recorded only because they triggered that particular detector. During the process of data acquisition CDMS saved some information about the trigger history. For each event the next five triggers, after the "global trigger" starting the recording process, were saved

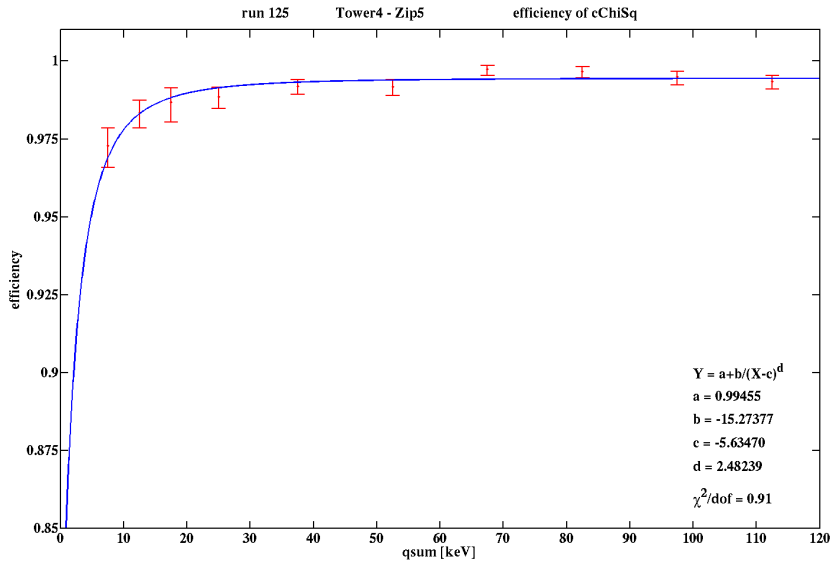

Figure 6.7: Efficiency of the charge χ^2 cut as a function of the ionization energy (qsum) for T4Z5 in run 125. The cut was defined based on barium calibration data, while the efficiency was estimated using WIMP-search events.

including the detectors, which they occurred in, and their time differences to the global trigger. The computation of the trigger efficiency was based on this information. All triggers within 50 μs after the global trigger were considered for this study. Thus, at first, all events with the last trigger of the trigger history, occurring less than 50 μs after the global trigger, were excluded by a pre-selection cut. This was necessary, since otherwise it would be possible to miss a trigger relevant for this analysis. In the next step, for a given detector, only events were considered, which had a trigger in at least one different detector in the trigger history, so either the global trigger of the event or any subsequent trigger. Finally, for various energy intervals, the fraction of these preselected events, which additionally issued a trigger (again an arbitrary trigger of the trigger history) in the detector of interest, was calculated.

Typically the efficencies, calculated applying WIMP-search data, were 100% down to recoil energies well below 10 keV and fell off quickly approaching 0 keV. They were fitted applying the functional form

$$f(X) = a + b \cdot \left(a + \mathrm{erf}\left(\frac{X - c}{d} \right) \right), \tag{6.9}$$

where erf denotes the error function, which is convenient to model the extreme decrease going to very low energies. An example is shown in Fig. 6.8.

6.4.3.3 Ionization yield discrimination

As discussed in great detail in the last chapter, ionization yield was the primary rejection parameter against bulk electron recoils. In Fig. 5.3 californium calibration data was shown,

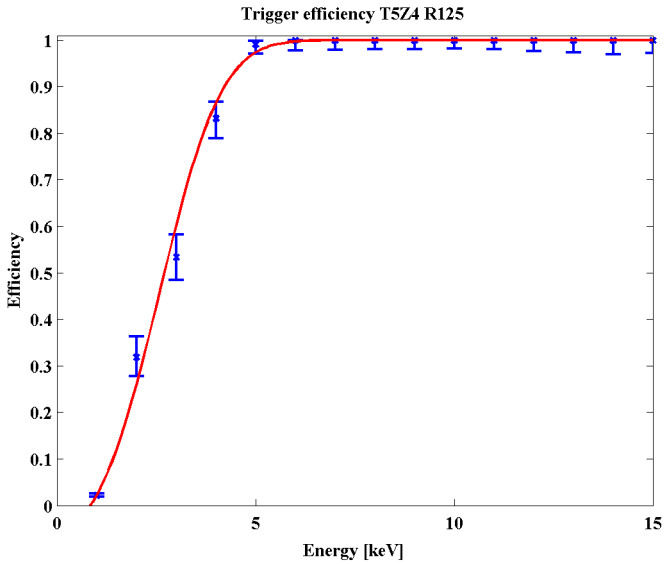

Figure 6.8: Energy dependence of the trigger efficiency for T4Z5 in run 125. It is 100% except for very low energies. Figure provided by T. Bruch.

and the typical separation of the bulk electron recoil and nuclear recoil populations was elucidated. In this chapter the specific cuts characterizing both populations are defined.

Since the ^{133}Ba source does not emit neutrons, the corresponding calibration data constituted a very large ensemble of electron-recoil events, which had an ionization yield of $\sim$1, as shown in Fig. 6.9. The population widens at low recoil energies due to increased noise, diminishing the energy resolution of the charge and phonon signals. In order to define a cut selecting only bulk electron recoils, the energy range between 5 keV and 120 keV was divided into 12 bins. Subsequently, the ionization-yield distributions in each of the bins were fitted with a Gaussian. Finally the obtained means and standard deviations were fitted with the following functions:

$$\mu(X) = \alpha \cdot X^{\beta} \tag{6.10}$$

$$\sigma(X) = \frac{\gamma^2 \cdot X^{\delta} + \eta^2}{X}\,, \tag{6.11}$$

which were empirically found to provide good estimates. These calculations were performed for each detector and run separately. The electron-recoil bands were defined to include all events located within 2σ around the fitted mean. The corresponding cut was named *cER_c58*. The band is shown for a particular detector in Fig. 6.9.

The definition of the nuclear-recoil bands was performed based on calibrations with a ^{252}Cf source, which predominantly emits neutrons so that it generates a large population of

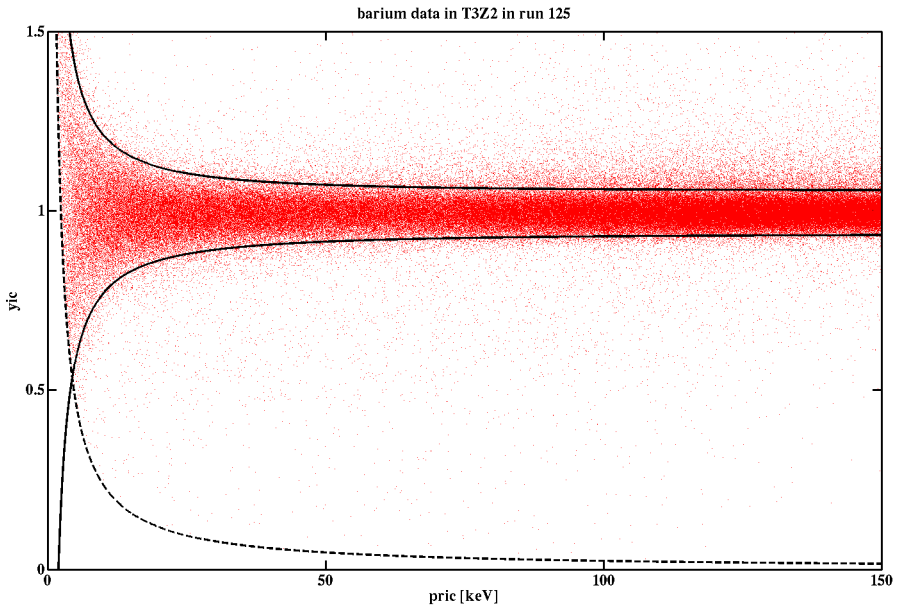

Figure 6.9: Ionization yield (yic) versus recoil energy (pric) of barium calibration data in T3Z2 in run 125. The black/solid lines represent the upper and lower boundary of the electron-recoil band discussed in the text. The black/dashed line denotes the series-independent charge-threshold cut discussed in the next section.

nuclear-recoil events, as shown in Fig. 5.3. Since the nuclear-recoil population was centered around an ionization yield of ∼0.3, only events between 0 and 0.6 were considered for the band definition. As in the case of the electron-recoil band, the data was divided into 12 energy bins between 5 keV and 120 keV. A logarithmic spacing was used, since the spectrum of the nuclear recoils was nearly exponential. Statistics above energies of ∼100 keV were quite limited, and thus it was difficult to obtain reliable estimates at high energies. This is discussed in more detail in chapter 7 on the inelastic dark matter analysis. Again, the yield distributions in each energy bin were fitted with Gaussians. The standard deviations were fitted with the same function as the means unlike in the case of the electron-recoil band. However, due to the mentioned low statistics at higher energies, the bands tended to broaden significantly. Thus, it was decided to introduce a certain energy cutoff X_{cut}, which typically was ∼30 keV, which the standard deviation was fixed above at its value at the cutoff. The final functions, again defined for each detector and run separately, were given by:

$$\mu(X) = \alpha \cdot X^{\beta} \tag{6.12}$$

$$\sigma(X) = \begin{cases} \gamma \cdot X^{\delta} & \text{if } X \leq X_{\mathrm{cut}} \\ \gamma \cdot X_{\mathrm{cut}}^{\delta} & \text{if } X > X_{\mathrm{cut}} \end{cases} . \tag{6.13}$$

As in the case of electron recoils, the nuclear-recoil acceptance region was defined to be the 2σ band around the mean and was determined for each detector and run separately. Events obeying this definition could be selected, applying the cut *cNR_c58*. Since the nuclear-recoil band also widened at low recoil energies, both bands overlapped below ∼5 keV, as can be observed from Fig. 5.3.

The efficiency of the nuclear-recoil cut was determined by calculating the fraction of events from californium calibration data 4σ around the mean of the nuclear-recoil band, which additionally passed the 2σ cut. The 4σ preselection cut was applied in order to allow only nuclear-recoils within the test sample. Since the width of the acceptance region was chosen to be 2σ, a more or less energy-independent efficiency of ∼95% was expected, which indeed was typically the case. The results were fitted with linear functions:

$$f(X) = a + b \cdot X . \tag{6.14}$$

An example is shown in Fig. 6.10.

6.4.3.4 Ionization threshold and bulk electron-recoil rejection cut

For an experiment searching for rare signals at low energies, it is important to impose cuts in order to reject noise events reliably. Thus, the CDMS collaboration defined two distinct threshold cuts, one on the recoil energy itself, which is discussed in chapter 6.5, and another one directly on the ionization signal from the inner charge electrode.

To establish such a cut, Gaussians were fitted to randomly triggered noise events for all detectors and runs separately. Due to significant changes of the noise behaviour in

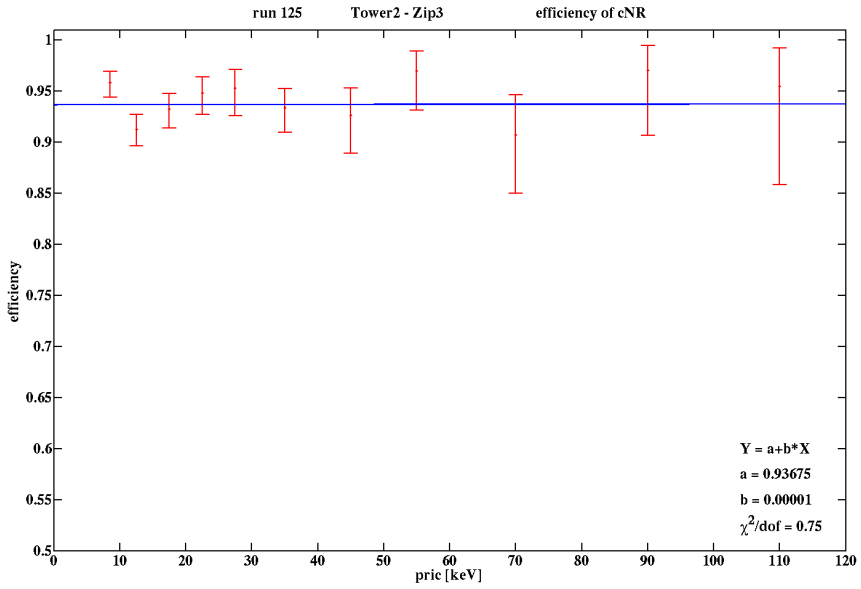

Figure 6.10: Recoil energy (pric) dependence of the nuclear-recoil cut efficiency in T2Z3 in run 125. As expected, the efficiency is nearly constant ∼95%.

certain detectors these fits were performed for all data sets together and also series-by-series. Figure 6.11 shows the results from the combined fits for all 30 detectors in run 125. The time dependence of the means and standard deviations of detector T1Z2 in the same run can be found in Fig. 6.12. An overall ionization threshold was defined by demanding the charge energy of each event to be more than $k\sigma$ above the mean of the noise blob, where the means and standard deviations from the combined fits were used. A similar criterion was imposed using the corresponding values for each series separately. Finally, the cut was set at the larger one of these two values to conservatively omit series-dependent downward fluctuations of the noise level.

Since ∼10 detectors were used for this analysis, it was decided to fix the parameter k, which determined, how many standard deviations above the noise blob's mean the cut was to be set, by allowing no more than $m = 0.01$ noise events above the threshold per detector. This estimate was performed as follows: At first, basic quality cuts were applied to the WIMP-search data, and the number of events below the mean of the noise blob n was calculated. Since events below the mean of the noise blob were expected to be only due to noise events, while events above included noise and real events, it was estimated that the total number of noise events in the sample was $2n$. Further assuming that the noise distribution was perfectly described by a Gaussian $f(x)$, which was a very good approximation, k could be estimated by solving

$$2n \cdot \int_{-\infty}^{\mu+k\sigma} \mathrm{d}x\, f(x) = 2n - m\,, \tag{6.15}$$

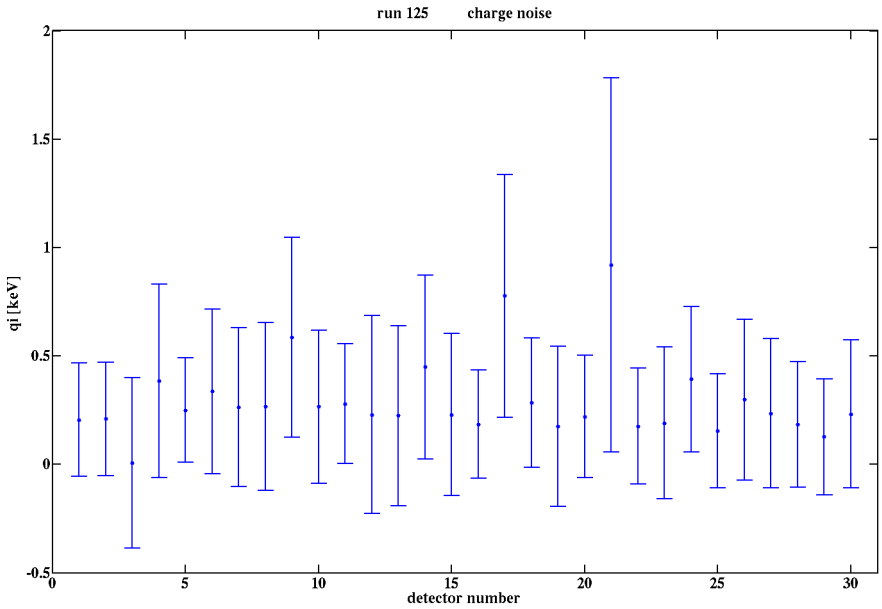

Figure 6.11: Means and standard deviations indicated by the error bars of the charge noise distributions for all 30 detectors in run 125.

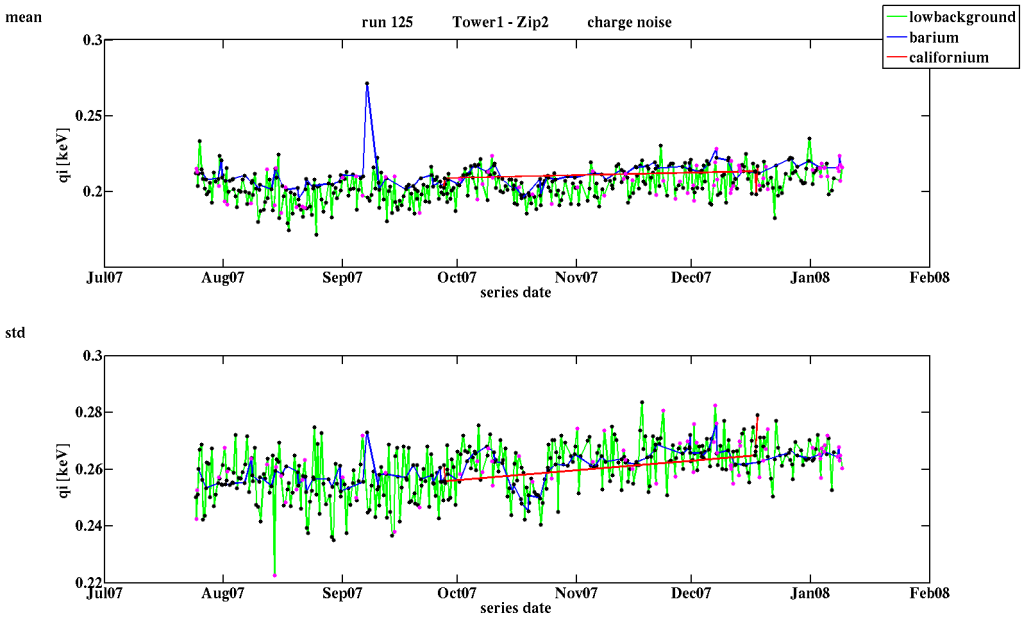

Figure 6.12: Time dependence of the means (top) and standard deviations (bottom) of the charge noise distributions for detector T1Z2 in run 125 obtained from fitting the distributions of each series separately. Series marked with magenta dots were removed by basic quality cuts as discussed in the previous chapter.

yielding

$$k = \sqrt{2} \cdot \mathrm{erfinv}\left(1 - \frac{m}{n}\right), \tag{6.16}$$

where erfinv denotes the inverse of the error function. It was found that $k = 4.5$ was an adequate value satisfying the imposed condition. The corresponding cut was denoted *cQThresh_c58*.

Application of the cut to californium calibration data, which was used to determine the efficiency, is shown in Fig. 6.13 for T1Z2 in run 125. Since ionization yield was defined as the charge energy divided by the recoil energy, a cut with threshold $\mathrm{qi_{th}}$ was given by the function $\mathrm{qi_{th}}/X$ in the yield versus recoil energy plane. The green/solid line denotes the series-independent charge-threshold cut. All events with charge energy below this curve were rejected independent of the data series. The green/dashed line shows the maximum run-dependent threshold cut. Note, that there were series with a lower threshold, which is the reason to have events between both lines passing the cut. The point of intersection of the lower edge of the nuclear-recoil band and the run-independent threshold cut was also computed. The corresponding recoil energy is marked with a vertical black line and is also given in the upper right corner of the plot. If the run-dependent cut was not added, the efficiency would be 100% above this energy, since it was calculated as the fraction of events

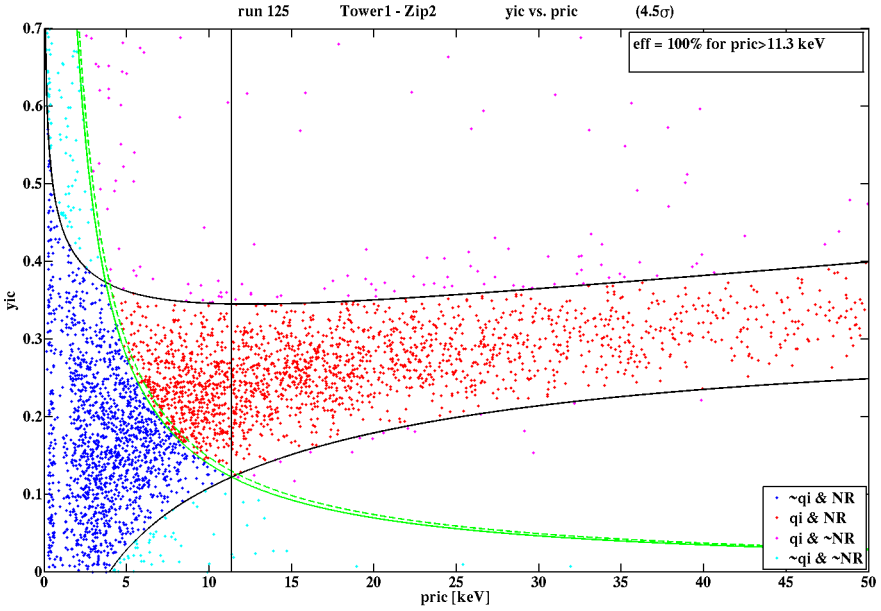

Figure 6.13: Application of the charge-threshold cut to californium calibration data in detector T1Z2 in run 125. Shown is the ionization yield (yic) versus recoil energy (pric) plane. The black lines denote the boundaries of the nuclear-recoil band, while the green/solid and green/dashed lines represent the series-independent and maximum series-dependent charge-threshold cut respectively. See text for more details.

within the nuclear-recoil band, which additionally passed the threshold cut. However, it was calculated combined with another cut.

As shown in Fig. 5.3 and discussed in the previous chapter on ionization yield discrimination, the electron- and nuclear-recoil bands overlapped at low recoil energies due to the widening of the bands. Thus, an additional criterion was defined to reject nuclear-recoil events, which occurred very close to the electron-recoil band. The cut *cBelowER_c58* only accepted events, which were more than 3σ below the mean of the electron-recoil band regarding their ionization yield. Setting this cut to 3σ and the recoil energy threshold to 10 keV, as discussed in chapter 6.5, led to the bulk-electron recoil leakage estimate of $n_{\mathrm{e,bulk}} < 5 \cdot 10^{-4}$, already given in chapter 5.3.1.

Since both of the cuts elucidated in this section cut into the nuclear-recoil band at low energies from low yield (*cQThresh_c58*) and high yield (*cBelowER_c58*), the efficiency was calculated applying both cuts combined. It was defined as the fraction of nuclear-recoil events within the 2σ band, which additionally passed both of the cuts. The result for detector T1Z2 in run 125 is shown as an example in Fig 6.14. Since the cuts only removed events at low recoil energies, the efficiency was 100% at all energies above ∼10 keV and quickly decreased to zero below. Thus, since the shape of the efficiency function was similar to the one of the trigger efficiency, a similar functional form, based on the error function, was used for the fit:

$$f(X) = \frac{1}{2} \cdot \left(1 + \mathrm{erf}\left(\frac{X-a}{b}\right)\right). \tag{6.17}$$

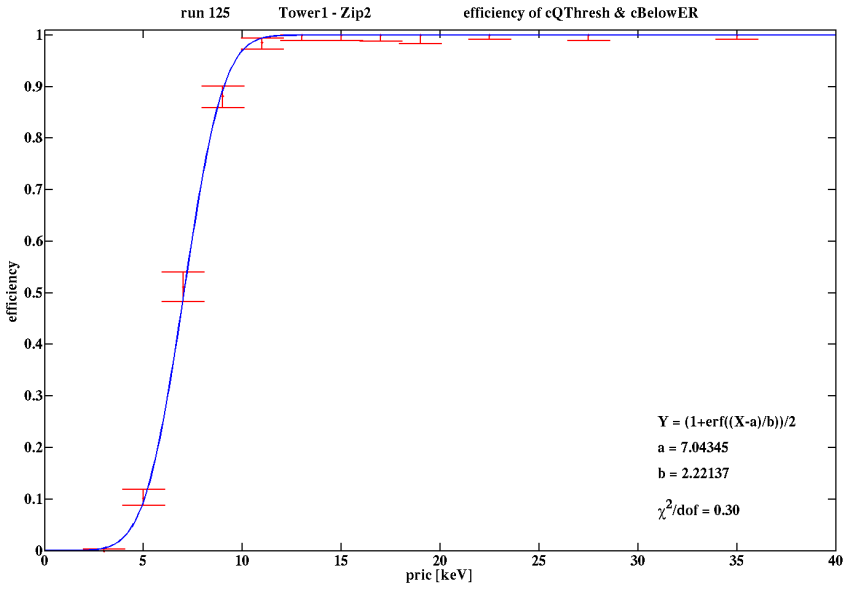

Figure 6.14: Recoil energy (pric) dependence of the combined efficiency of the charge-threshold and below electron-recoil band cut in T1Z2 in run 125. The efficiency is ∼100% except for low energies below ∼10 keV.

6.4.3.5 Fiducial volume cut

In a previous chapter on the detector layout it was discussed that a thin outer electrode served as a guard ring to identify and reject events at the edge of the detector, which was subject to higher background and reduced charge collection. In particular, the applied electric field suffered from non-homogeneity. The corresponding cut was defined in a very similar fashion as the electron- and nuclear-band cuts. For each detector and run, barium calibration data was divided into several energy bins of ionization energy between 4 keV and 300 keV, collected by the inner charge electrode, and subsequently the distributions of the ionization energy, collected by the outer charge electrode, were fitted with Gaussians in each of these bins. The obtained means and standard distributions were fitted with the following functions:

$$\mu(X) = \alpha + \beta \cdot X \tag{6.18}$$

$$\sigma(X) = \sqrt{\gamma + \delta \cdot X + \eta \cdot X^2}\,. \tag{6.19}$$

Finally, the cut *cQin_c58* was defined to accept only events within 2σ around the mean. An illustration of the cut is shown in Fig. 6.15. It was particularly strict at high energies and quite loose at low energies, since a high-energy event was only allowed to deposit a very

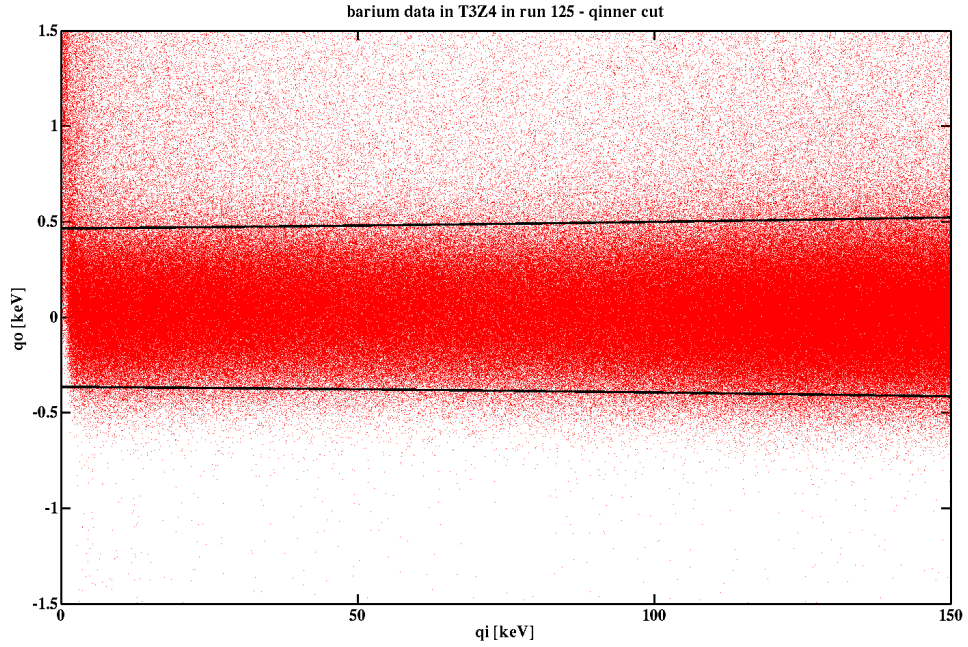

Figure 6.15: Illustration of the fiducial volume cut for detector T3Z4 in run 125 applying barium calibration data. Shown is the energy collected by the outer charge electrode (qo) as a function of the energy collected by the inner charge electrode (qi). The two black lines represent the cut boundaries 2σ around the outer charge signal.

low fraction of its energy within the outer electrode, while this fraction could be significant for low energies.

Due to the specific geometry of the detector layout, the efficiency was expected to be ∼85%. However, this expectation had to be checked based on a test sample, which was assumed to illuminate the detectors uniformly. Nuclear-recoil events from californium calibrations were used for this study. A possible issue with this sample was the fact that neutrons, which induced the nuclear recoils, were quite likely to scatter multiple times within a detector. It was estimated that ∼20% of the neutrons underwent multiple scattering. If at least one of the interactions of a multiple scatter event happened below the outer electrode, a significant amount of energy was deposited in the corresponding channel, and the event was rejected by the cut. Since WIMPs were expected to scatter only once, this led to a slight underestimate, which had to be corrected including results from a Monte Carlo simulation. It was found that the efficiency, obtained by applying nuclear recoils from the californium calibration data, had to be divided by a correction factor given by:

$$\eta = 0.9548 \pm 0.0082(\text{stat.})^{+0.0065}_{-0.0045}(\text{syst.}) \; . \tag{6.20}$$

A different sample, not suffering from multiple scatter pathologies, could be based on electron recoils emerging from ^{71}Ge decays yielding a characteristic line at 10.36 keV, as discussed in chapter 4.5.3.3. The events could be selected e.g. by fitting a Gaussian to the corresponding peak and taking all events within the 3σ interval. Since the ^{71}Ge production was based on neutron capture induced by the californium calibrations, these events were expected to be uniformly distributed within the detectors. However, the statistics of this sample were quite low and a possible energy dependence of the efficiency could not be tested. Thus, nuclear recoils were used at the end.

A simple estimate of the efficiency of the fiducial volume cut would be to calculate the fraction of nuclear-recoil events, which furthermore also passed the fiducial volume cut. However, since the californium calibration data did not just include nuclear recoils but also electron recoils, the nuclear-recoil band was subject to a population of surface events. As these events suffered from reduced charge collection and could thus distort the efficiency calculation based on the charge signal, it was decided to subtract the low-yield events statistically. Application of an event-by-event rejection based on the surface-event rejection cut, as discussed for the WIMP-search data in the next chapter, was not reliable, since this cut was specifically designed to discriminate between true nuclear-recoils and surface events within the fiducial volume.

In order to investigate the partition of charge energy into the inner and outer electrode, it was necessary to consider the total charge energy for this study. The aforementioned statistical rejection of low-yield electron recoils was based on correction factors calculated using barium calibration data. At first, the barium calibration data was divided into several recoil-energy bins between 7 keV and 100 keV. In each of these energy bins the ratio of the number of events within the nuclear-recoil band to the number of events between the electron and nuclear-recoil band was calculated. However, in fact three such ratios had to be calculated for each energy bin due to the occurrence of three distinct kinds of

populations with reduced charge collection, as shown in Fig. 6.16. The black/dotted events are bulk electron recoils with an ionization yield of ∼1. The three low-yield populations are separated by two black lines. All of these events are shown with two distinct colors for events within the nuclear-recoil band (green and blue) and between the nuclear- and electron-recoil band (cyan and red). The population within the lower right is the "standard" low-yield population of surface events occurring under the inner electrode, which is discussed in more detail in a subsequent chapter on surface-event rejection. Events under the outer electrode can be found within the upper left. Events from interactions between the electrodes with notable energy deposition in the inner and outer charge channel can be found in the middle. After calculating the three correction factors for each energy bin, the corresponding numbers of events (for the same energy intervals and considering the same three populations) between the electron- and the nuclear-recoil band in the californium calibration data were calculated. Multiplying these numbers with the corresponding correction factors yielded the numbers of low-yield events that had to be subtracted from the total numbers of events within the nuclear-recoil bands to obtain the numbers of true neutron scatters. Finally, the efficiency of the fiducial volume cut was calculated based on these numbers of true nuclear recoils instead of the total numbers of events within the nuclear-recoil band, which slightly increased the efficiency. A typical result is shown in

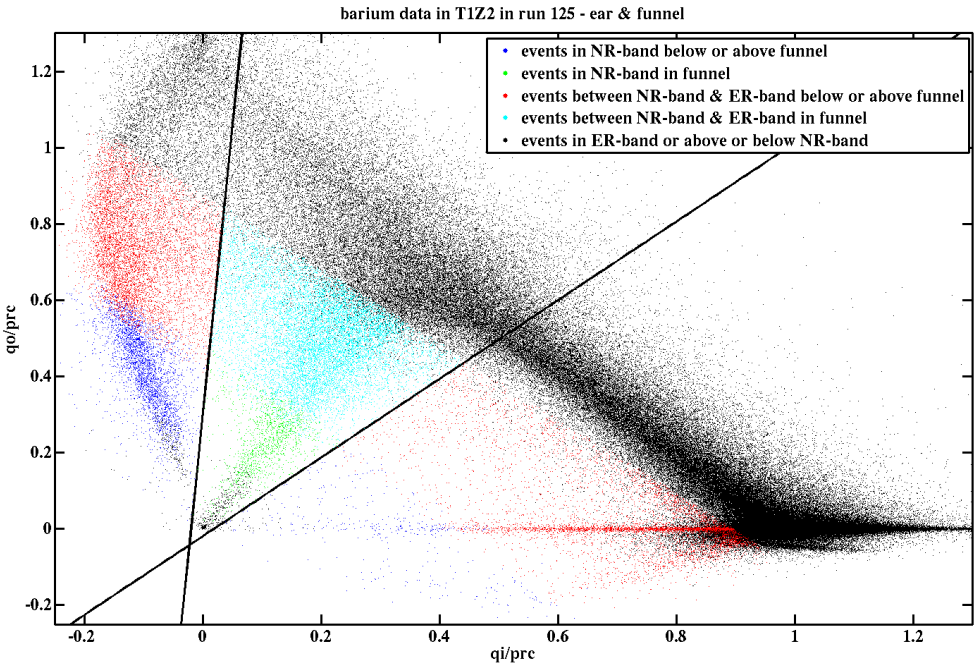

Figure 6.16: Definition of the three populations of low-yield events used for the calculation of the fiducial volume cut efficiency applying barium calibration data in detector T1Z2 in run 125. Shown is the ratio of "outer" charge energy (qo) and recoil energy (prc) versus the ratio of "inner" charge energy (qi) and recoil energy (prc). See text for a detailed discussion.

Fig. 6.17. The efficiencies were in general around 70%, so ∼15% lower than expected, and decreasing with energy. Fits applying linear functions were performed:

$$f(X) = a + b \cdot X \,. \tag{6.21}$$

A reason for the energy-dependence was the discussed fact that the cut was particularly tight at higher energies. However, further analyses are needed to gather a better understanding of the observed behaviour.

6.4.3.6 Manifold and surface-event rejection cut

In the chapter on phonon calibration and signal correction (4.5.4.5) a position correction, based on a look-up table, was introduced. It was mentioned that the correction was accomplished by deriving correction factors, based on a set of nearest neighbor events from the barium calibration data. However, if a certain event was particularly far away from its nearest neighbors, this correction was very likely to yield unreliable results. A cut denoted *cGoodRTFTManifold_c58* (manifold cut) was defined, which removed such outliers. The efficiency of the cut was calculated based on nuclear recoils from the californium calibration data and fitted with an analytic function together with the surface-event rejection cut.

Since the surface-event rejection cut is discussed in great detail in the context of the inelastic dark matter analysis in chapter 7 and the approaches were very similar, further elucidations regarding this cut in the standard analysis (*cRT_vanilla_c58*) are omitted. It should just be noted that it was the most elaborate cut as it was used to reject the dominant background and had a significant impact on the signal acceptance.

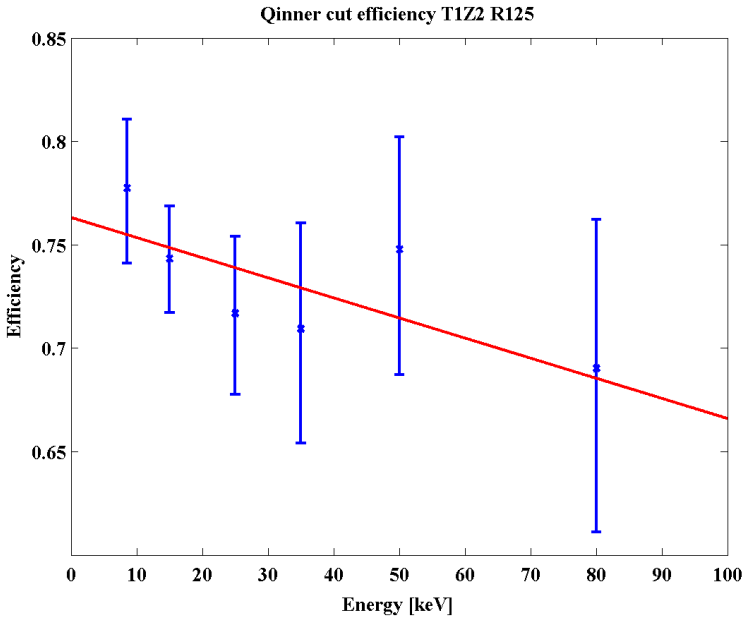

Figure 6.17: Energy dependence of the fiducial volume cut efficiency for T1Z2 in run 125. It is ∼70%, so ∼15% lower than expected, and decreasing with energy. Figure provided by T. Bruch.

6.4.4 The final efficiency

Finally, the exposure-weighted efficiency was calculated taking into account all cuts discussed in this chapter. Figure 6.18 shows the result from this computation in various steps, where the efficiencies from different cuts were added successively. The curve labeled quality cuts also contains the efficiencies from the muon-veto and singles cut. Obviously, the fiducial volume (qinner cut) and the surface-event rejection cut (timing cut) were by far the dominant cuts regarding reduction of signal acceptance, and thus deserve most of the attention regarding possible future improvements. Besides, adjustment of the surface-event rejection cut with respect to a particular dark matter model is discussed in great detail in the next chapter. The final efficiency including all cuts had a maximum of ∼34% near 20 keV and dropped down very steeply going to lower energies, dominated by the trigger efficiency and the combined efficiency of the charge-threshold and bulk electron-recoil rejection cut. The moderate decrease to ∼25% at 100 keV going to higher energies was due to the fiducial volume cut. For comparison, the final efficiency from the previous CDMS analysis [61], which is quite similar but rather constant at higher energies, is also shown (black/dashed).

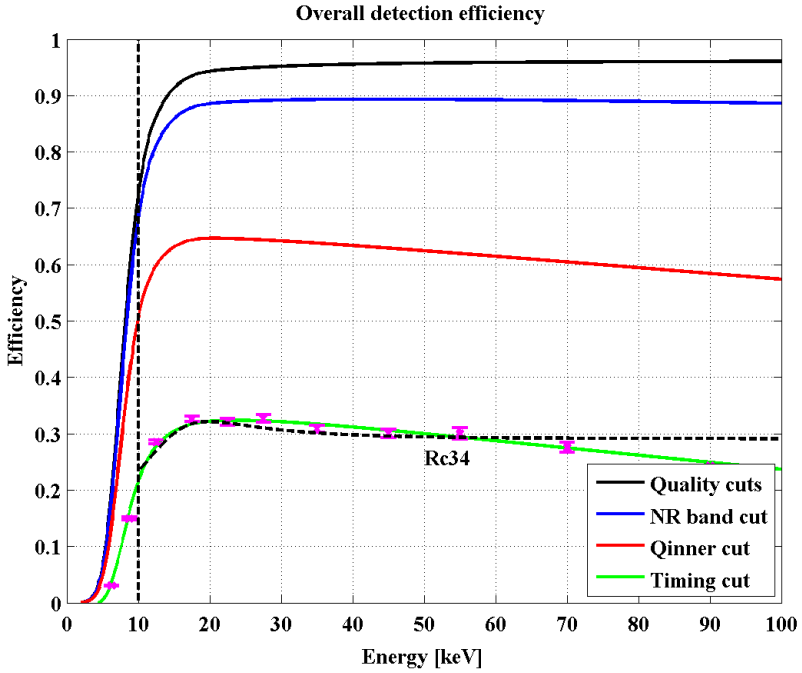

Figure 6.18: Efficiency of the standard analysis with successively added cuts. The green line represents the total nuclear-recoil acceptance including all cuts. The magenta errorbars were obtained by directly applying all cuts to the data and show a very good agreement. The result from the previous analysis [61] is also shown for comparison (black/dashed). Figure provided by T. Bruch.

6.5 Recoil-energy range

In addition to the threshold on the ionization energy, a threshold was set directly on the recoil energy. Its actual value was determined by analyzing two criteria, which were both related to the fact that the electron- and the nuclear-recoil bands widened and overlapped at low energies. First of all, it was demanded that the leakage of bulk-electron events from the electron-recoil band should be negligible. In chapter 5.3.1, it was mentioned that the calculated leakage was extremely low ($n_{\mathrm{e,bulk}} < 5 \cdot 10^{-4}$), given a 10 keV recoil-energy threshold as in the previous analysis [61]. A detailed analysis showed that the leakage was acceptably low even at 5 keV. Secondly, it was necessary to have a significant population (at least a few dozen) of surface events in the barium calibration data, in order to define the surface-event rejection cut. Since these events were defined to have ionization yield 5σ below the mean of the electron-recoil band, this criterion was much more demanding. Counting the events at low energies it was found that using a 10 keV threshold was reasonable and conservative.

The upper boundary of the analysis window was set to 100 keV, dominated by the difficulties to define the acceptance region due to low statistics in the californium calibration data at higher energies. This range was extended to 150 keV in a subsequent analysis, as discussed in the next chapter.

6.6 Unblinding and tests of the WIMP-candidates

After all cuts were fixed and the calculations of the exposure, efficiency and background estimates were finalized, the WIMP-search data was ready to be unblinded. Table 6.3 gives a summary of all important numbers characterizing the given analysis. Since the final exposure was just a factor of 1.6 larger than the exposure from the previous analysis [61], which did not yield the observation of any WIMP candidates, the number of events, obeying all selection criteria, was expected to be very small. Otherwise both runs would be inconsistent with each other.

The last step before the actual unblinding was to check the number of events, which passed all selection criteria *except* the surface-event rejection cut. It should be consistent with the expectation estimated by scaling the corresponding number from the previous analysis by the relative increase of the exposure. In total, 150 events were observed in acceptable accordance with 119.4 ± 15.3 expected events. The agreement on the individual detectors except for detector T3Z6, where 52 observed events were faced with an expectation of 19.3 ± 7.9, was also quite good. It was an endcap detector at the bottom of its tower, where there was less shielding from background and where there was no detector below it to help reject background by detecting multiple scatters. Despite of this disagreement, it was decided not to remove the detector from the analysis. It was also verified that these 150 events were uniformly distributed over time.

After finally applying all WIMP-search selection cuts to the WIMP-search data on November 5^{th} 2009, two candidates were found at low recoil energies passing all criteria.

Cosmogenic neutron background	$0.04^{+0.04}_{-0.03}$
Radiogenic neutron background	0.03–0.06
Bulk-electron background	$< 5 \cdot 10^{-4}$
Surface-electron background	$0.82^{+0.12}_{-0.10}(\text{stat.})^{+0.20}_{-0.19}(\text{syst.})$
total background	0.9 ± 0.2
exposure	612.1 kg-days
efficiency	∼30%
recoil-energy range	10–100 keV

Table 6.3: Summary of background estimates, exposure, efficiency and energy range for the standard analysis.

One event occurred at 12.3 keV in detector T1Z5 and the other one at 15.5 keV in T3Z4. A short summary is given in Table 6.4. These two detectors are examined in more detail in Fig. 6.19. The left panel shows ionization yield versus recoil energy for T1Z5 (top) and T3Z4 (bottom). The event in T1Z5 occurred near the upper boundary of the nuclear-recoil band, while the event in T3Z4 was located in the middle of the band. Except for these two candidates only events within the electron-recoil band passed the timing cut. From these plots it can only be seen which events pass or fail the surface-event rejection cut, however it cannot be inferred whether a particular event was very close to the timing-cut boundary or far away from it. Therefore, a different representation is shown in the right panel, where normalized ionization yield, defined as the distance from the nuclear-recoil band mean measured in units of standard deviations given by the width of the band, is plotted against the timing parameter relative to the actual cut position. The red/dashed line denotes the timing-cut boundary on the given detector, and the red/solid box indicates the acceptance region. It could be argued that, although it was a valid WIMP candidate, since it passed all of the selection criteria, the event in T1Z5 (top) might belong to the tail of the surface-event background distribution. On the other hand, the candidate in T3Z4 (bottom) was well separated from the background distribution. Nevertheless, none of the two events could be rejected as possible signal arising from WIMP-interactions in the detectors. However, due to the low number of candidates this result did not constitute a significant evidence for the discovery of dark matter. This was quantified by calculating the probability of observing two or more background events, given the background expectations summarized in Table 6.3, which yielded 23%. This estimate was solely based on counting statistics and did not take the proximity of the individual events to the signal and background

Energy (keV)	Detector	Run	Date
12.3	T1Z5	125	27.10.2007
15.5	T3Z4	125	05.08.2007

Table 6.4: Summary of the events passing all WIMP-search selection cuts from the standard analysis.

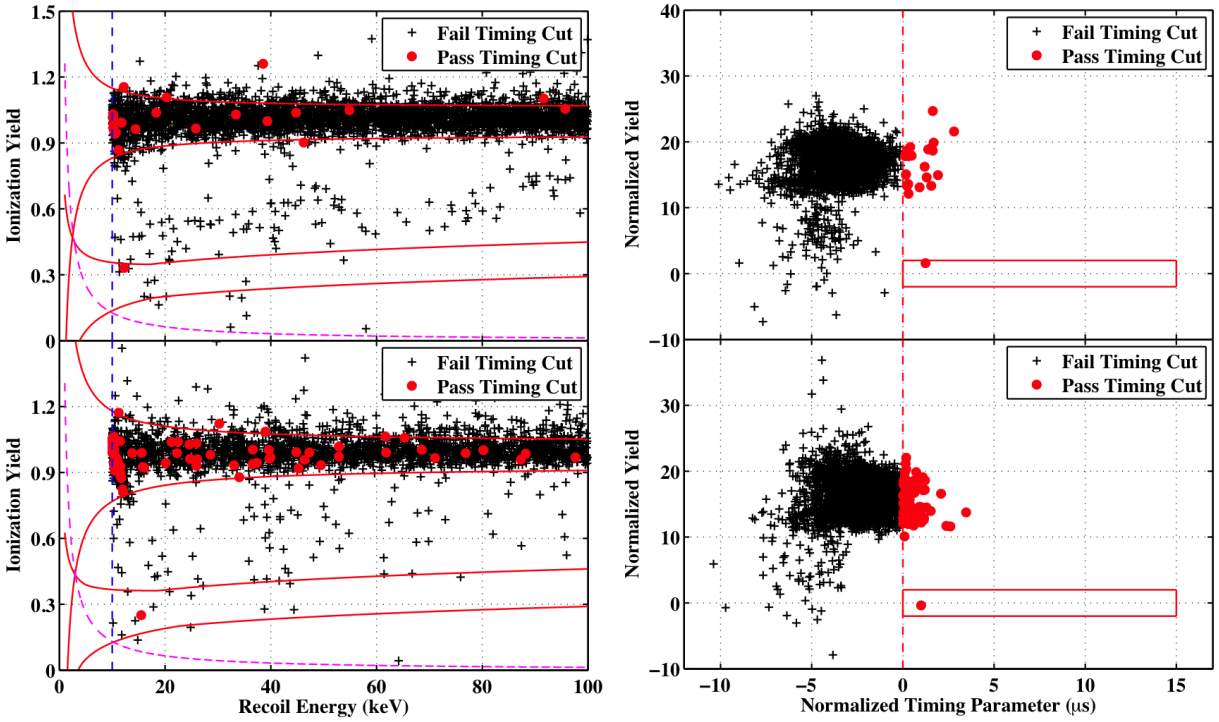

Figure 6.19: *Left*: Ionization yield versus recoil energy for T1Z5 (top) and T3Z4 (bottom) with WIMP candidates at 12.3 keV and 15.5 keV respectively. The red/solid lines represent the electron-recoil band around a yield of one and the nuclear-recoil band around 0.3. The series-independent ionization-energy threshold is given by the magenta/dashed line and the recoil-energy threshold is given by the vertical blue/dashed line at 10 keV. Only one event within the nuclear-recoil bands in each detector passes the timing cut. *Right*: Number of standard deviations each event is away from the mean of the nuclear-recoil band (normalized yield) versus timing parameter relative to the timing-cut position (normalized timing parameter) for the same detectors as on the left side. The red/dashed lines represent the timing cut boundaries and the red/solid boxes indicate the acceptance regions. The candidate in T1Z5 might be considered as an outlier of the background distribution, while the candidate in T3Z4 is very well separated from the background.

distributions in the respective detectors into account. Such advanced analyses based on likelihood-ratio tests were also accomplished and are discussed in the next section. Before proceeding, it should be noted that the low number of observed WIMP-candidates agreed with the expectation discussed at the beginning of this chapter.

Extensive checks were performed in order to make sure that none of the two candidates accidentally survived any of the cuts through a loophole. It was also investigated whether the events were particularly close to the boundaries of any cut, e.g. the charge threshold. Moreover, the whole series the events belonged to were investigated for unusual behaviour like increased noise. Both events successfully passed all the tests and it was observed that the performance of the experiment was stable at the times which the events occurred at.

However, one important issue related to the pulse reconstruction of the event in T3Z4

was found. As can be seen in Fig 6.20, which shows the raw trace of the ionization signal and the fit, obtained from the optimal filter algorithm, the start time of the pulse might not be properly found. It seems that the actual value should be slightly higher. Therefore, the reconstruction process was investigated in more detail. As elucidated in the chapter on the charge reconstruction (4.5.3.2), a fixed template was shifted along the digitized trace and the start time of the pulse was determined as the value, which maximized the amplitude of the fitted pulse. No proper χ^2-minimization was performed in order to increase the processing speed. For events with charge energies above ~6 keV the maximization worked perfectly fine and tests indicated that there was no difference between the obtained start times from both algorithms. However, it was observed that at lower energies there were disagreements in some rare cases. It turned out that the candidate in T3Z4 was such a problematic event. The bottom plot of Fig. 6.21 shows the maximum amplitude as a function of the digitizer bin reflecting the start time of the pulse. As mentioned before, each bin had a width of 0.8 μs. A similar plot for the minimum χ^2 can be found in the top panel of the same figure. Obviously, there were two local maxima regarding the amplitude, which coincided with the minima of χ^2. However, the absolute maximum of the amplitude denoted by the vertical red/dotted line did not match the absolute minimum of χ^2. The latter occurred 5 bins later corresponding to a time difference of 4 μs. This time shift would reduce the delay and subsequently the timing parameter by the same value, pushing the event below the timing cut boundary, as can be easily inferred from the lower right plot in Fig. 6.19. Consequently the event could not be regarded as a WIMP candidate

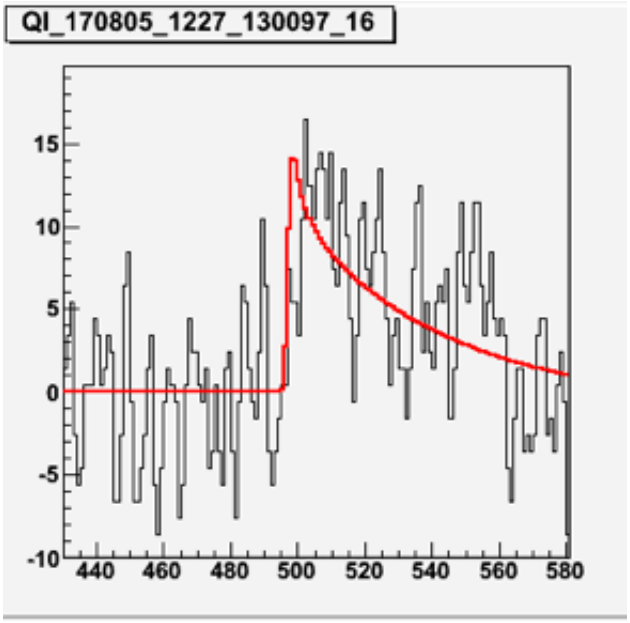

Figure 6.20: Trace of the ionization signal of the WIMP candidate in T3Z4. The pulse obtained from the optimal filter algorithm is overlaid. The reconstructed start time might be slightly to low. Figure provided by L. Hsu.

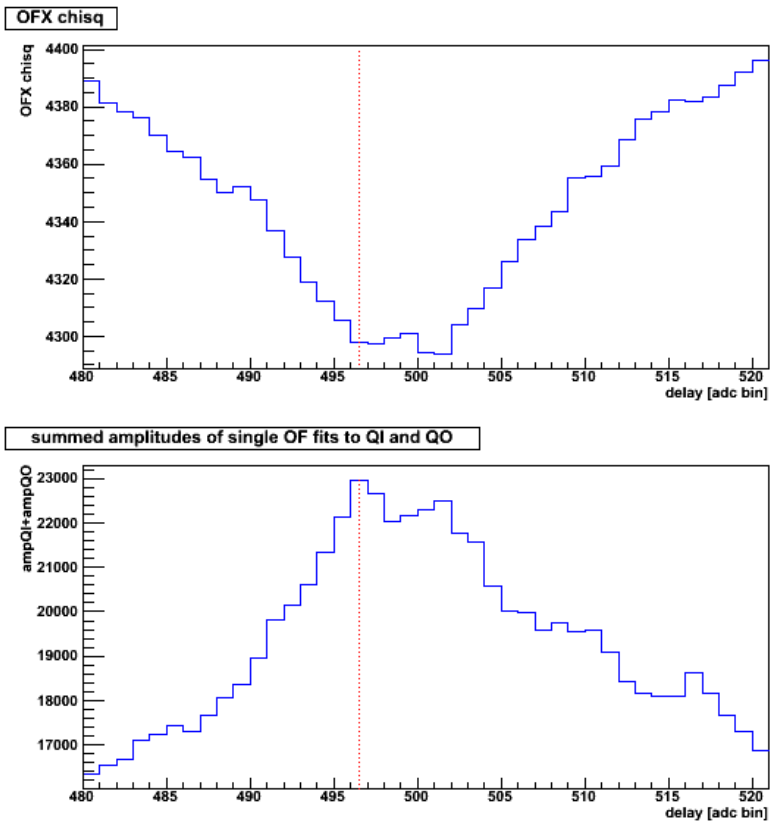

Figure 6.21: *Top*: Minimum χ^2 from fitting the charge template to the trace of the WIMP candidate in T3Z4 as a function of the pulse's start time. *Bottom*: Amplitude of the pulse obtained from the optimal filter algorithm as a function of the pulse's start time. The vertical red/dotted line indicates the start time yielding the maximum amplitude. Figure provided by L. Hsu.

anymore. However, it is certainly not valid to apply a modified reconstruction algorithm just to particular events, since a clear bias would be introduced. Even though this event would fail the timing cut, others might pass it, when they were reconstructed applying the proper χ^2-minimization. Therefore, the only valid approach is to reprocess the entire data set, based on the χ^2-algorithm and subsequently perform a reanalysis, which however cannot be considered as truly blind. Such an analysis is currently under way but still far from finalized. For the current analysis observation of this pathology was just accounted for by revising the surface-event leakage yielding the result given at the end of chapter 5.3.2. It should be noted that there was no ambiguity regarding the start time of the candidate in T1Z5.

6.7 Likelihood analysis of the two WIMP candidates

In the previous section a likelihood of 23% was given as the probability of observing two or more background events, given the background estimates summarized in Table 6.3. It was pointed out that this result was solely based on counting statistics and did not take the proximity of the two WIMP candidates to the signal and background distributions into account. In this chapter a more advanced analysis is presented. However, this is not a full likelihood analysis as discussed in chapter 5.1.2. Such an analysis is presented in chapter 8.

Surface events certainly constituted the dominant background contribution. As discussed before, the surface-event rejection parameters, used for this analysis, were the ionization yield and in particular the timing parameter, given by the sum of the phonon-pulse risetime and the delay between the charge and the phonon pulse. Thus, it had to be investigated, whether the ionization yield and timing parameters of the candidates seemed to be more like that expected from surface events or nuclear recoils. This was an important study, because, even though the cuts on both parameters were designed to make sure that any passing event had nuclear-recoil-like parameters, the distributions of both kinds of events had a significant overlap (see e.g. Fig. 5.4 and Fig. 5.9 regarding ionization yield and timing respectively). So the main reason for performing this study was to check how close the candidates were to the tails of the surface-event distributions in a sense that is discussed in more detail in the following.

As in chapter 5.1.2, f_s and f_b denote the signal (nuclear-recoil events) and background (surface events) distributions respectively. They depend on the ionization yield y and timing parameter t. Both parts were assumed to be independent for this study, so that e.g. $f_s(y,t) = f_s^y(y) \cdot f_s^t(t)$. Inclusion of a possible dependence of the parameters y and t, which in principle would not be unexpected, since both parameters depended on the depth within the crystal, which an interaction occurred at, is discussed in the overnext chapter on the full likelihood analysis. Moreover, any energy-dependence should be neglected for the moment.

Regarding the distributions of surface events and nuclear recoils, surface events were expected to have higher ionization yield and smaller timing parameters on average. Thus, an interesting question would be: What is the probability that $y < y_{\mathrm{cand}}$ and $t > t_{\mathrm{cand}}$ for surface events, were the subscript "cand" denotes the values of a WIMP candidate? The result represents the probability of a typical surface event to appear more signal-like than the candidate. Similarly, it would be interesting to calculate the probability for nuclear recoils that $y > y_{\mathrm{cand}}$ and $t < t_{\mathrm{cand}}$, which yields the likelihood of a typical nuclear recoil to look more background-like than the candidate. Given that y and t were assumed to be independent for this study, the conditions regarding both parameters could be separately investigated and subsequently combined in a second step. For the first mentioned example

this would amount to calculate:

$$p_y = \int_0^{y_{\mathrm{cand}}} \mathrm{d}y\, f_b^y(y) \tag{6.22}$$

$$p_t = \int_{t_{\mathrm{cand}}}^{\infty} \mathrm{d}t\, f_b^t(t) \tag{6.23}$$

$$p_{yt} = p_y\, p_t \left(1 - \log(p_y p_t)\right) \tag{6.24}$$

However, it is known that the most powerful discriminant between two hypothesis is the likelihood ratio, which moreover is applicable considering arbitrary distributions. Since its value typically varies over several orders of magnitude, it is more convenient to use its logarithm. Thus,

$$R(y,t) = \log\left(\frac{f_s(y,t)}{f_b(y,t)}\right) \tag{6.25}$$

was chosen as a measure of how much a candidate looks like signal or background. Regarding the first example again, the probability that $R(y,t) > R(y_{\mathrm{cand}}, t_{\mathrm{cand}})$, given that the event was actually a surface event, had to be computed. This probability can be calculated in two ways, applying Monte Carlo simulations or integration. The Monte Carlo method works as follows: Draw a large number N of random events from the distribution of surface events $f_b(y,t)$ and subsequently calculate $R(y,t)$ for each of these events. The probability, that a surface event looks more signal-like than a candidate, is thus given as the fraction of simulated events with $R(y,t) > R(y_{\mathrm{cand}}, t_{\mathrm{cand}})$:

$$p_{yt} = \frac{1}{N}\sum_{i=1}^{N} \Theta\Big(R(y_i,t_i) > R(y_{\mathrm{cand}}, t_{\mathrm{cand}})\Big)\,, \tag{6.26}$$

where Θ denotes the Heaviside step function. For the integration method the function $f_b(y,t)$ has to be integrated over all parts of the parameter space consisting of y and t, which obey the constraint $R(y,t) > R(y_{\mathrm{cand}}, t_{\mathrm{cand}})$:

$$p_{yt} = \iint_{R(y,t)>R(y_{\mathrm{cand}},t_{\mathrm{cand}})} \mathrm{d}y\,\mathrm{d}t\, f_b(y,t)\,. \tag{6.27}$$

Evaluation of this integral typically involves evaluation of f_s and f_b on a tiny grid. Depending on the complexity of the functions and the type of model, used for their estimation, both methods can be computationally intensive.

Up to this point, estimations of the actual distributions have not been discussed yet. Due to expected difficulties, e.g. regarding insufficient statistics in the tails of the distributions, systematic differences between WIMP-search and calibration data and systematic uncertainties related to the actual approach applied for the estimation of the distributions, three distinct methods were used. In all approaches ionization yield and timing parameter were assumed to be independent. A short summary is given here. One of these methods,

the one based on kernel density estimates (KDE), is discussed in much more detail in the chapter on the full likelihood method.

One approach was to construct two-dimensional probability distributions for nuclear recoils and surface events for the ionization yield and timing parameter, only considering events in fixed energy ranges around the candidates. This was basically the approach alluded to before. For the event at 12.3 keV in detector T1Z5 the interval [7 keV, 15 keV] and for the event at 15.5 keV in detector T3Z4 the interval [10 keV, 20 keV] were used. Since both parameters were assumed to be independent, the yield and timing distributions were fitted separately and subsequently multiplied. The function of choice for the fit was the generalized lambda distribution (GλD). The characteristics of this function are also discussed in more detail in the chapter on the full likelihood analysis. The yield and timing distributions of nuclear recoils were both based on events from the californium calibration data of the particular detector within the 2σ nuclear-recoil band. The timing distribution of surface events was obtained from betas within the barium calibration data, while the corresponding yield distribution was based on WIMP-search multiple-scatter events, obeying the beta definition (see chapter 7.1 for the beta definition). Thus, the estimate of the surface event yield distribution suffered from low statistics. However, an estimate based on barium calibration data seemed to be less reliable due to known systematic differences between WIMP-search and calibration data. It should be noted that for this approach the surface events were finally separated into charge- and phonon-side surface events, so that there were actually two kinds of background distributions. As discussed in chapter 5.3.2, charge-side events typically had higher ionization yield and slightly higher timing parameters. This separation was not performed for the other two approaches. The method described in this paragraph is referred to as GλD-2D.

In a second approach three-dimensional distributions were constructed. Here, apart from the ionization yield, risetime and delay were considered as two distinct parameters instead of just using the sum. As discussed before, both parameters were correlated. After removing this correlation with an orthogonal transformation, all three parameters were considered as independent. In this case energy ranges of 5–20 keV and 10–30 keV were used for the events at 12.3 keV and 15.5 keV respectively. Apart from the different energy intervals, the same data samples as in the previous method were used for estimating the distributions. Moreover, the fits were also based on GλDs. This method is referred to as GλD-3D.

The third method was based on KDEs rather than GλDs. In this case, three-dimensional distributions were determined based on ionization yield, the summed timing parameter and recoil energy. This was the only approach fully taking the energy dependence of yield and timing into account. The data samples, which the estimates were based upon, were the same as in the previous two approaches. This method is referred to as KDE-3D. As an example for the results of this approach the distributions of $R(y,t)$ regarding nuclear recoils and surface events are shown for T1Z5 in Fig. 6.22. The probability for a surface event to have a likelihood ratio larger than the candidate was given by $0.44^{+0.58}_{-0.29}$. However, the shown distributions were evaluated based on the actual data, while they were estimated for the final results based on the aforementioned Monte Carlo method to reduce statistical

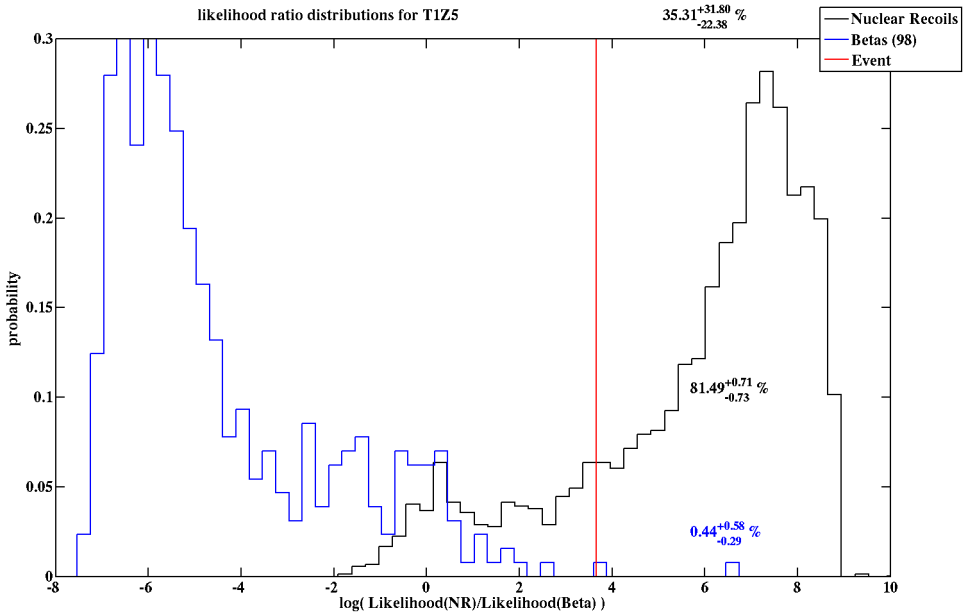

Figure 6.22: Likelihood-ratio test for the candidate in T1Z5 applying the KDE-3D method. The distribution of nuclear recoils (black) was evaluated based on nuclear recoils from the californium calibration data and the distribution of surface events (blue) was evaluated using WIMP-search data. The likelihood ratio of the candidate is denoted by the vertical red line. The values given in the plot denote the probabilities of nuclear recoils (black) and surface events (blue) to have likelihood ratios larger than the candidate. The final results for this analysis were obtained based on Monte Carlo simulations.

uncertainties.

Subsequently, the aforementioned probability of a surface event to look more like signal than a WIMP candidate was computed for all three approaches and both WIMP candidates applying the Monte Carlo approach. The results are given in Table 6.5.

However, it can be argued that these results only determine the probabilities of a *single* surface event to look more signal-like than the candidates but do not take the actual number of events into account. Therefore, an even more interesting result is the probability P to

	GλD-2D		GλD-3D	KDE-3D
	charge side	phonon side		
T1Z5	0.37 ± 0.06	0.23 ± 0.05	0.36 ± 0.01	0.28 ± 0.04
T3Z4	0.07 ± 0.03	0.20 ± 0.05	0.21 ± 0.01	0.07 ± 0.02

Table 6.5: Probabilities (in %) of single surface events to look more like nuclear recoils than the WIMP candidates in the respective detectors. The given errors reflect the uncertainties related to the limited statistics of the Monte Carlo simulations and do not contain any systematic effects. See text for details.

have *at least one* surface event within the WIMP-search data in the given detector that looks more like a nuclear recoil than the candidate. Since an event can either have a lower or a larger likelihood ratio than a candidate, this can be regarded as a Bernoulli process. Given the probabilities p_{yt} just discussed and a sample size of N events these probabilities can be easily calculated:

$$P = 1 - (1 - p_{yt})^N \,. \tag{6.28}$$

This is certainly formally correct. However, one could argue about possible changes regarding the used cut definitions, e.g. for surface events. As previously mentioned in this chapter, the standard beta definition was used for this event population. In particular, the upper boundary regarding ionization yield was given by the minimum of 0.7 and the lower boundary of the 5σ electron-recoil band at the events' recoil energies. However, even though this is a reasonable definition, it is arbitrary to some extent. One could think about extending the yield range to an upper boundary of just 4σ below the mean of the electron-recoil band. This would increase the number of events N within the sample but at the same time it would decrease the probability p_{yt}, since a larger part of the surface-event distribution was further away from the signal region. Figure 6.23 shows an illustration of this situation. The two axis denote the ionization yield and timing parameter. Region A represents surface events obeying the standard beta definition with the smaller region a_r, being that part of region A, which lies further out in the tail of the population than a particular candidate located at x_0, e.g. based on a likelihood-ratio test. The signal region is not explicitly shown, though it is indicated by the equipotential lines of the distribution f_1. (Note that f_s is used throughout the text.) So regarding Fig. 6.22, region A is represented by the whole surface-event distribution shown in blue, while the region a_r is represented by that part of the distribution, which lies to the right of the vertical red line denoting the likelihood ratio of the candidate. As just discussed, the cuts could be loosened, e.g. to

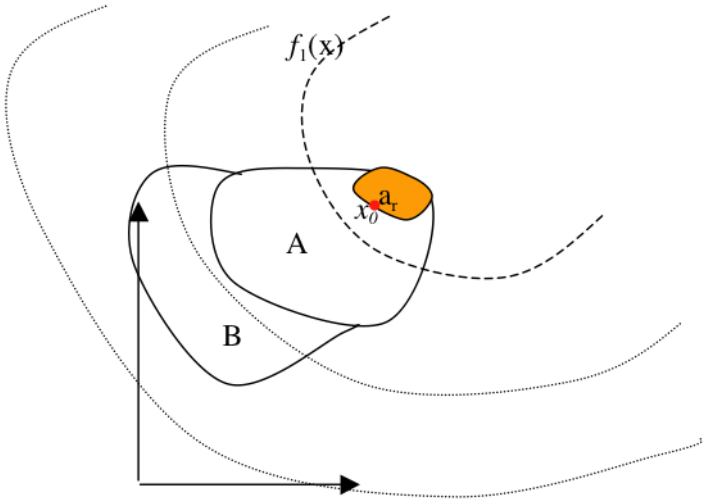

Figure 6.23: Illustration regarding the inclusion of additional events to the background sample "far away" from the signal region. Figure provided by B. Sadoulet. See text for details.

include more events at higher ionization yield represented by the region B. If this population only contained events with likelihood ratios lower than that of the candidate, which means that the corresponding distribution of likelihood ratios does not extend to values above the vertical red line in Fig. 6.22, it can be shown that the value of the propability P given in (6.28) does not change, though N and p_{yt} surely change. The reasoning, which is a simplified version of a proof given by B. Sadoulet, is as follows: The distributions of the background are respectively denoted f_b^{A} and f_b^{B} within the regions A and B. They are zero outside the respective regions. The corresponding numbers of events are N_{A} and N_{B}. Thus, the background probability distribution over the combined region A∪B is given by

$$f_b^{\mathrm{A}\cup\mathrm{B}} = \frac{N_{\mathrm{A}}}{N_{\mathrm{A}}+N_{\mathrm{B}}} f_b^{\mathrm{A}} + \frac{N_{\mathrm{B}}}{N_{\mathrm{A}}+N_{\mathrm{B}}} f_b^{\mathrm{B}}\,, \tag{6.29}$$

and subsequently

$$\begin{aligned} p_{yt}^{\mathrm{A}\cup\mathrm{B}} &= \iint_{R(y,t)>R(y_{\mathrm{cand}},t_{\mathrm{cand}})} \mathrm{d}y\,\mathrm{d}t\; f_b^{\mathrm{A}\cup\mathrm{B}}(y,t) && (6.30)\\ &= \iint_{R(y,t)>R(y_{\mathrm{cand}},t_{\mathrm{cand}})} \mathrm{d}y\,\mathrm{d}t\; \frac{N_{\mathrm{A}}}{N_{\mathrm{A}}+N_{\mathrm{B}}} f_b^{\mathrm{A}}(y,t) && (6.31)\\ &= \frac{N_{\mathrm{A}}}{N_{\mathrm{A}}+N_{\mathrm{B}}} p_{yt}^{\mathrm{A}}\,. && (6.32) \end{aligned}$$

Finally, the probability P is given by:

$$\begin{aligned} P^{\mathrm{A}\cup\mathrm{B}} &= 1-\left(1-p_{yt}^{\mathrm{A}\cup\mathrm{B}}\right)^{N_{\mathrm{A}}+N_{\mathrm{B}}} = 1-\left(1-\frac{N_{\mathrm{A}}}{N_{\mathrm{A}}+N_{\mathrm{B}}}\,p_{yt}^{\mathrm{A}}\right)^{N_{\mathrm{A}}+N_{\mathrm{B}}} && (6.33)\\ &\approx 1-e^{-N_{\mathrm{A}}\,p_{yt}^{\mathrm{A}}} \approx 1-\left(1-p_{yt}^{\mathrm{A}}\right)^{N_{\mathrm{A}}} = P^{\mathrm{A}}\,, && (6.34) \end{aligned}$$

where $\approx$ becomes exact for large N_{A} and small p_{yt}^{A}, which typically holds true. In other words, the exact definition of selection cuts "far away" from the signal region (defined by the likelihood ratio) is of no concern regarding the calculation of the probability to observe at least one surface event looking more like a nuclear recoil than a WIMP candidate.

Finally, the probabilities P could be calculated by evaluating equation (6.28). The results can be found in Table 6.6, where the probabilities regarding charge- and phonon-side

	GλD-2D	GλD-3D	KDE-3D
T1Z5	11.9 ± 2.2	12.2 ± 1.9	$24.2^{+5.5}_{-4.8}$
T3Z4	4.6 ± 1.3	5.1 ± 1.0	$4.2^{+2.4}_{-1.6}$

Table 6.6: Probabilities (in %) of observing at least one surface event looking more like nuclear recoils than the WIMP candidates in the respective detectors. The given errors reflect the uncertainties related to the limited statistics of the Monte Carlo simulations as well as the Poisson errors on the numbers of observed events, but they do not contain any systematic effects. See text for details.

events for method GλD-2D have been combined. All three probabilities for the candidate in T3Z4 agree reasonably well. Regarding the candidate in T1Z5, the results from the two methods based on GλDs also show a very good agreement. However, the value obtained from the KDE approach is significantly higher. These discrepancies are most likely to be attributed to difficulties regarding the estimates of the extreme tails of the surface-event distributions. Nevertheless, it can be observed that the probability to have a surface event with timing and ionization yield parameters, looking more like a nuclear recoil than the candidate in T3Z4, is quite low (∼5%), while it is moderate for the candidate in T1Z5. That is exactly what was expected from the discussion of Fig 6.19. However, as discussed in the previous section, the candidate in T3Z4 showed issues regarding the proper determination of its charge pulse's start time. Therefore, especially considering the low statistical significance of observing only two candidates, it is not possible to draw a final conclusion regarding the nature of these events. It is hoped that a reanalysis of the data, reprocessed with the updated χ^2-minimization algorithm, gives further insight regarding a possible WIMP discovery. In particular, a full likelihood analysis, as introduced in chapter 5.1.2 and further discussed in a later chapter, seems very promising.

Before continuing with the calculation of cross section limits, it should be noted that the CDMS collaboration also investigated, whether the candidates surprisingly had ionization yield and timing like those expected from surface events, which leak into the acceptance region. Thus, the probabilities of random nuclear recoils with the same recoil energies as the candidates and within the timing versus yield acceptance region, to look more like surface events than the candidates, were computed by integration of the probability density functions for the KDE-3D method and via Monte Carlo evaluation for the GλD-3D approach. The results are given in Table 6.7. These probabilities should be uniformly distributed between 0% and 100% for true nuclear recoils, which was verified using californium calibration data. Thus, the low probabilities encourage suspicion that the candidates are not nuclear recoils. Moreover, the probabilities of surface events, again with the same energies as the candidates and within the acceptance regions, to resemble nuclear recoils better than the candidates, were calculated. These probabilities are given in Table 6.8. In this case, the rather high probabilities again indicate that the two candidates seem to look more like background events. However, it should be noted that in this section only events *within* the acceptance regions were considered, while the full distributions were used

	GλD-3D	KDE-3D
T1Z5	3.21±0.06	1.18
T3Z4	1.88±0.04	11.50

Table 6.7: Probabilities (in %) of nuclear recoils, with the same recoil energies as the candidates and within the timing versus yield acceptance region, to look more like surface events than the candidates in the respective detectors. Errors given in the case of the GλD-3D method reflect the uncertainties related to the limited statistics of the Monte Carlo simulations. The values from the KDE-3D method were computed by integration of the likelihood function. See text for details.

	GλD-3D	KDE-3D
T1Z5	27.68±0.6	83.17
T3Z4	33.92±0.7	54.52

Table 6.8: Probabilities (in %) of surface events with the same recoil energies as the candidates and within the timing versus yield acceptance region, to look more like nuclear recoils than the candidates in the respective detectors. Errors given in the case of the GλD-3D method reflect the uncertainties related to the limited statistics of the Monte Carlo simulations. The values from the KDE-3D method were computed by integration of the likelihood function. See text for details.

in the likelihood-ratio analysis described in the previous parts of this section. Thus, the computed probabilities naturally indicate an electron recoil origin of the candidates, since they both occurred close to the timing-cut boundary (and in the case of T1Z5 also close to the yield-cut boundary).

6.8 Constraining the WIMP-parameter space

Since only a hint for WIMP interactions but no clear signal was found, the next step was to calculate an upper limit on the WIMP-nucleon interaction strength. In a first step, the limits are usually placed on the expected number of observed WIMP interactions μ, which are subsequently used to constrain the WIMP parameters by investigating

$$\mu = \mathrm{MT} \cdot \int_{E_{\mathrm{lower}}}^{E_{\mathrm{upper}}} \mathrm{d}E \, \frac{\mathrm{d}R}{\mathrm{d}E} \cdot \mathrm{eff}(E) \,, \tag{6.35}$$

where $[E_{\mathrm{lower}}, E_{\mathrm{upper}}]$ is the considered recoil-energy interval, MT is the exposure and $\mathrm{eff}(E)$ is the energy-dependent efficiency. The differential rate $\frac{\mathrm{d}R}{\mathrm{d}E}$ is given in (2.21). It depends on the WIMP parameters, so regarding pure spin-independent scattering the WIMP-nucleon cross section and the WIMP mass. There are several methods to compute an upper limit on μ, but regarding the blinding paradigm, it was desirable to decide on a particular method beforehand, in order to remove any possible bias by applying the method, which is assumed to give the most stringent results.

Regarding its application, the simplest method is to use only counting statistics based on the Poisson distribution. In that case, the upper limit is obtained from

$$1 - \gamma = \sum_{n=0}^{n_{\mathrm{obs}}} \frac{\mu^n}{n!} e^{-\mu} = 1 - F_{\chi^2, 2(n_{\mathrm{obs}}+1)}(2\mu) \,, \tag{6.36}$$

where n_{obs} denotes the number of observed events and $1 - \gamma$ equals the desired confidence level, e.g. 0.9. $F_{\chi^2, 2(n_{\mathrm{obs}}+1)}$ is the cdf of the χ^2-distribution, where the index denotes the number of degrees of freedom. Finally the limit is given by

$$\mu = \frac{1}{2} F^{-1}_{\chi^2, 2(n_{\mathrm{obs}}+1)}(\gamma) \,. \tag{6.37}$$

This result greatly simplifies in the case of no observed WIMP candidates. Setting $n_{\text{obs}} = 0$ directly yields

$$\mu = -\log \gamma \,. \tag{6.38}$$

Regarding a 90% confidence level $\mu \approx 2.30$ is obtained.

However, since this method only takes the number of events into account, different more advanced approaches were developed, which incorporate the expected distribution of the WIMP spectrum. The maximum gap and the optimum interval methods developed by Steven Yellin [100], a member of the CDMS collaboration, are of particular importance. Both approaches received great acceptance within the dark matter direct detection community, and within the last few years nearly all collaborations applied one of these methods to derive their upper limit. As just mentioned, these approaches take the signal's spectral shape into account but do not require any knowledge about possible background contributions. In particular, no background subtraction is performed, and all WIMP candidates are assumed to be signal. This is very convenient, since, even though great care is taken to characterize the background as accurately as possible, an additional contribution might have been missed or systematic errors might have been underestimated. In short, the maximum gap method is based on the probability of observing zero events between any two adjacent WIMP candidates or analysis window boundaries given the signal expectation. Regarding the standard analysis, there were three of those intervals: [10 keV, 12.3 keV], [12.3 keV, 15.5 keV] and [15.5 keV, 100 keV]. The final limit is based on the interval, which yields the most stringent constraint. The optimum interval method is a generalization of the maximum gap method in the sense that it does not only consider intervals with zero events. In addition to the three intervals just mentioned, the probabilities to have one event in the intervals [10 keV, 15.5 keV] and [12.3 keV, 100 keV] as well as two events in the interval [10 keV, 100 keV] are included in the limit calculation. It should be noted that the optimum interval limits are typically stronger than the maximum gap limits, which seems reasonable since there are more additional intervals to obtain constraints from. However, the additional options to "choose" the interval yielding the strongest limit impose a statistical penalty. A typical analogon is the binned Poisson method. If only binned data is available, the confidence levels from the combined bins $1 - \gamma$ and the confidence levels from the individual bins $1 - \gamma_{\text{bin}}$ are related by

$$1 - \gamma = (1 - \gamma_{\text{bin}})^{N_{\text{bin}}} \,, \tag{6.39}$$

where N_{bin} denotes the number of bins. Given two bins for example, a 90% C.L. would require 94.9% C.L.s in the individual bins. Nevertheless, the optimum interval method is usually preferred, since it principally is more powerful. It should be noted that both approaches give more stringent constraints than the simple Poisson method, discussed in the previous section in the presence of WIMPs, and give exactly the same result (6.38), when no events survive the selection process. A general drawback of both methods is the fact that they only yield one-sided confidence intervals, so that they can only be used to derive upper limits. Thus, they are unfeasible in the case of a detection and cannot be used to characterize a preferred region of the parameter space.

Another possibility is the application of maximum-likelihood methods. These methods are capable of characterizing the preferred region from a possible detection. The main drawback is the necessity to have accurate models of the background distributions, which are usually difficult to obtain. If the detector's response is not perfectly understood, modeling of the background distributions is only possible based on calibration data. Since systematic differences to the WIMP-search data may exist, which is indeed the case as discussed in great detail in the next chapter, this approach is quite involved. Nevertheless, a likelihood-based method was developed and is discussed in chapter 8.

For the current analysis it was chosen to place upper limits based on the optimum interval method, which was decided well before unblinding.

Upper limits on the spin-independent WIMP-nucleon cross section were calculated for WIMP masses between 10 GeV/c^2 and 1000 GeV/c^2. The result is shown as the red/solid line in Fig. 6.24. The most striking feature of this curve is the step near its minimum at ∼60 GeV/c^2, which is a special feature arising from the use of the optimum interval method. Above that particular mass only intervals with zero events can yield the upper limit. The

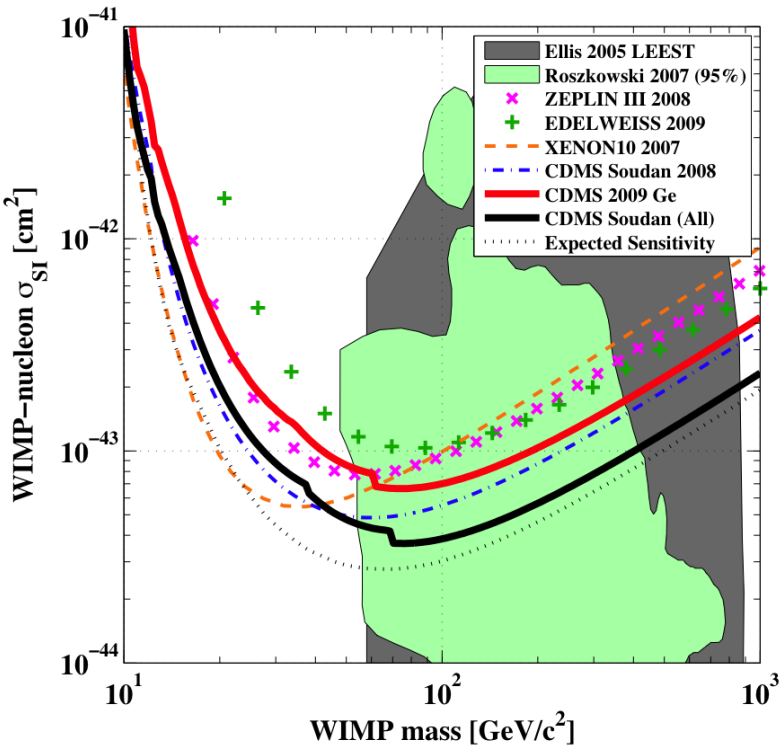

Figure 6.24: Constraints on the spin-independent WIMP-nucleon cross section. The red/solid line marks the limit from the analysis discussed in this chapter, the blue/dashed-dotted line marks the results from the previous analysis [61] and the black/solid line represents the combined limit. The expected sensitivity of the combined analysis is also shown (black/dotted). The constraints from other leading experiments are also shown. The colored regions represent the WIMP parameters preferred by supersymmetric dark matter models. See text for more details.

expectation value μ is very small, so intervals with more events cannot contribute. At the kink, intervals containing one event enter the calculation. The observed feature is due to this threshold-crossing. The constraints from the previous analysis are also shown [61] (blue/dashed-dotted). However, they were corrected by incorporating the updated detector masses, which slightly decreased the exposure from the value stated in that paper. Even though the exposure, analyzed here, is a factor of 1.6 larger than the one from the previous analysis, the limits are weaker, especially at low WIMP masses. This is due to the occurrence of the two candidates at low recoil energies. A combination of the total exposure yielded the upper limit shown as the black/solid curve. The black/dotted line marks the corresponding expected sensitivity based on the total estimated background for the combined exposure. The limit is compared to the constraints from three other leading experiments, XENON10 [101], ZEPLIN-III [46] and EDELWEISS [102]. The combined CDMS limit was the leading constraint for WIMP masses above $\sim$44 GeV/c^2 at the time of the publication. However, the XENON100 collaboration has published more stringent limits in the meantime [103], which are not shown on this plot. The colored regions show preferred parts of the supersymmetric parameter space. The models regarded in [104] (dark/gray) are quite general, while the analysis presented in [105] (green) considered a variety of experimental constraints. It can be observed that current experiments already probe a significant part of the theoretically preferred parameter space.

The obtained results can also be interpreted considering spin-dependent interactions. In that case, limits are usually computed by assuming that the WIMPs couple either only to protons ($a_n = 0$) or neutrons ($a_p = 0$). Since only one coupling is left, the results can be directly interpreted as constraints on the WIMP-proton or WIMP-neutron cross section. It should be noted that it is not necessarily an adequate assumption that one of the couplings dominates, especially since theoretical models usually suggest that both should be of similar size. Nevertheless, attributing the interactions to only one coupling yields a conservative constraint on this parameter and is thus a valid approach. Ge has only one naturally occurring isotope with an odd number of nucleons, ^{73}Ge, which has an unpaired neutron and a quite low abundance of 7.73%. Thus, competitive constraints can only be set on the spin-dependent WIMP-neutron cross section. They are shown in Fig. 6.25. As in Fig. 6.24 the red/solid line marks the limit from the analysis discussed in this chapter, the blue/dashed-dotted line marks the results from the previous analysis [61], and the black/solid line represents the combined limit. Moreover, limits from two other leading experiments are shown, XENON10 [43] and Zeplin-III [106], which provide stronger constraints particularly at low recoil energies. They profit from the use of Xe targets, which have two odd-neutron isotopes, ^{129}Xe and ^{131}Xe, which additionally have much higher abundances of 26.44% and 21.18% respectively. Theoretical predictions, e.g. from [105], are not shown in this plot, since they do not extend significantly to cross sections above 10^{-39} cm^2. Unlike the spin-independent case, current spin-dependent constraints do not yet constrain theoretically favored regions of the parameter space.

In addition, the data was used to constrain the inelastic dark matter interpretation of the DAMA/LIBRA results. DAMA/LIBRA allowed cross-section intervals at the 90% C.L. were calculated for given WIMP mass and mass splitting, as presented in chapter 2.3,

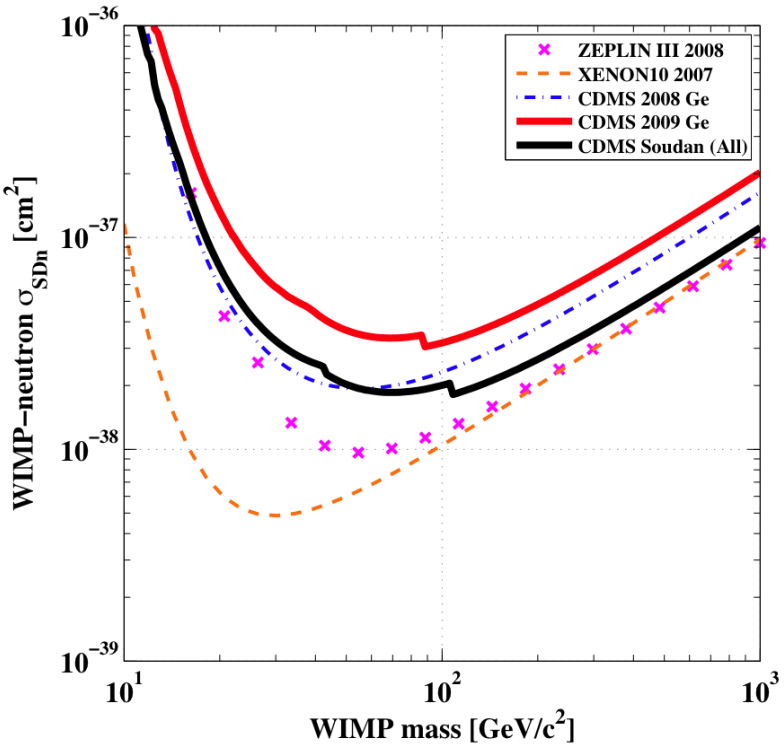

Figure 6.25: Constraints on the spin-dependent WIMP-neutron cross section. As in Fig. 6.24, the red/solid line marks the limit from the analysis discussed in this chapter, the blue/dashed-dotted line marks the results from the previous analysis [61] and the black/solid line represents the combined limit. Limits from other experiments, which are more constraining, are also shown. See text for details.

based on a χ^2 goodness-of-fit technique. Limits emerging from the analysis discussed in this chapter and those from XENON10 [107] were computed using the optimum interval method. It should be noted that the XENON10 limits were recalculated with a different method than in [107], since for that publication the so-called $p_{\max}$ method [100] was used, and a uniform treatment, so in particular the application of the same limit calculation procedure, was desired. For this recalculation a constant value of 0.19 was assumed for the light collection efficiency $\mathcal{L}_{\text{eff}}$, which is comparable to the ionization yield from CDMS. This parameter, in particular regarding its energy-dependence, is the subject of controversial debates [108]. Thus, the energy-dependence presented in [109], which was expected to be more accurate, was also investigated. This led to slighty more stringent constraints below WIMP mass of $\sim$100 GeV/c^2 and slightly less stringent limits above. Nevertheless, here $\mathcal{L}_{\text{eff}} = 0.19$ was applied as just stated. Regions excluded by CDMS and XENON10 were defined by demanding the 90% C.L. upper limit to completely rule out the DAMA/LIBRA allowed cross section intervals for allowed WIMP masses and mass splittings. The results are shown in Fig. 6.26. The CDMS data disfavor all but a narrow region of the parameter space allowed by DAMA/LIBRA, that resides at a WIMP mass of $\sim$100 GeV/c^2 and mass

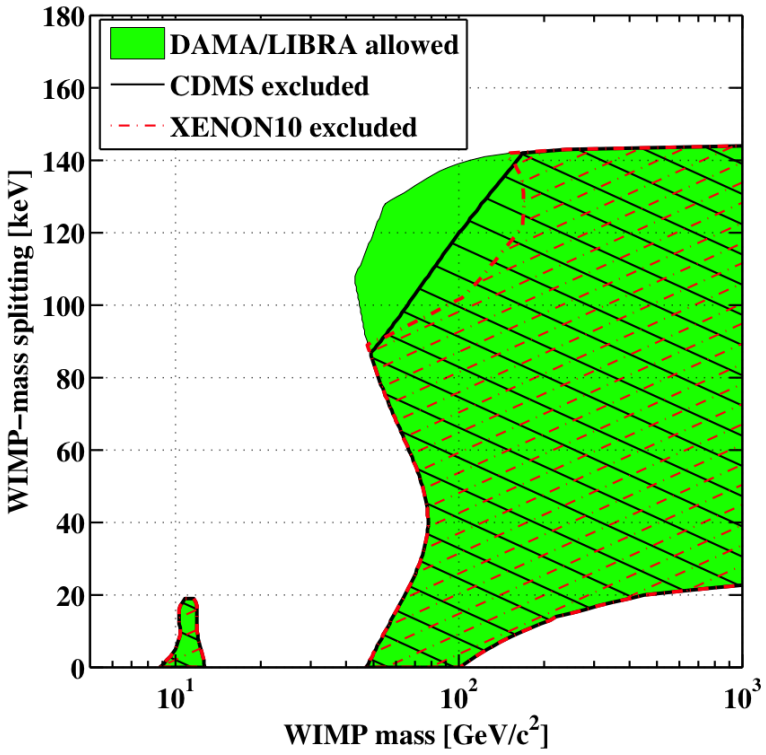

Figure 6.26: The shaded green region represents WIMP masses and mass splittings, which a cross section, compatible with the DAMA/LIBRA modulation spectrum at 90% C.L. under the inelastic dark matter interpretation, exists for. Excluded regions from the analysis presented in this chapter combined with the results from the previous analysis [61] (black hatched) and XENON10 (red-dashed hatched) were calculated using the optimum interval method.

splittings of 85–140 keV. A reanalysis of the CDMS data, performed in order to increase the sensitivity to the iDM model, is discussed in the next chapter. In that context, more recent constraints from other experiments are discussed as well. However, it should already be pointed out that in the meantime this model has been excluded by the XENON100 collaboration at 90% C.L. [110].

Chapter 7

The search for inelastic dark matter

Initial constraints from CDMS on the iDM model interpretation of the DAMA claim were set using a recoil-energy range of 10–100 keV and presented at the end of the previous chapter. In this chapter, a dedicated iDM analysis of the entire CDMS five-tower data set, including runs 123–124 (see Table 6.1), is presented. Note, that the constraints on the WIMP-parameter space shown in Fig. 6.26 were a combination of the final results from all data sets taken at the Soudan Underground Laboratory, which, however, were analyzed separately. In particular, the surface-event rejection cuts, as discussed below, were set at fixed backgrounds for runs 123–124 and runs 125–128 separately. For the analysis presented here, the whole acquired data were combined in advance and surface-event rejection was based on the entire data set. There were two main reasons for performing this reanalysis. The iDM parameter space allowed by the previous analysis (see Fig. 6.26) includes WIMP masses $m_W \sim 100\,\mathrm{GeV/c^2}$ and mass splittings $\delta \sim 120\,\mathrm{keV}$. As shown in Fig. 7.1, these parameters result in a significant expected rate above the previous analysis upper limit of 100 keV, so a simple extension to 150 keV increases the expected sensitivity. Moreover, the expected rate drops to zero for low recoil energies, in contrast to the elastic-scattering case, obviating the need for a low threshold. Since most of the dominant surface-event background occurred at energies just above the 10 keV threshold [61], where no iDM signal is expected, the sensitivity could be further improved by redefining a looser surface-event rejection cut based upon the estimated background with recoil energy between 25 keV and 150 keV, while leaving the lower boundary for the analysis at 10 keV. Thus, a significant number of surface-background events was expected in the 10–25 keV range, which, however, had only a minor effect on the results in the parameter-space region of interest ($m_W \sim 100\,\mathrm{GeV/c^2}$, $\delta \sim 120\,\mathrm{keV}$).

The same data-quality selection cuts used in previous analyses for ensuring detector stability and removing periods of poor detector performance, e.g. due to insufficient neutralization, causing incomplete charge collection owing to impurities in the detector crystal, resulted in a total Ge exposure of 969.4 kg-days for this reanalysis, a factor of 1.6 larger than the 612.1 kg-days the analysis presented in the previous chapter was based on. It should be noted that the same 14 detectors used in runs 125–128 could also be used in runs 123–124. The Si detectors were again omitted due to their lower sensitivity to inelastic scattering.

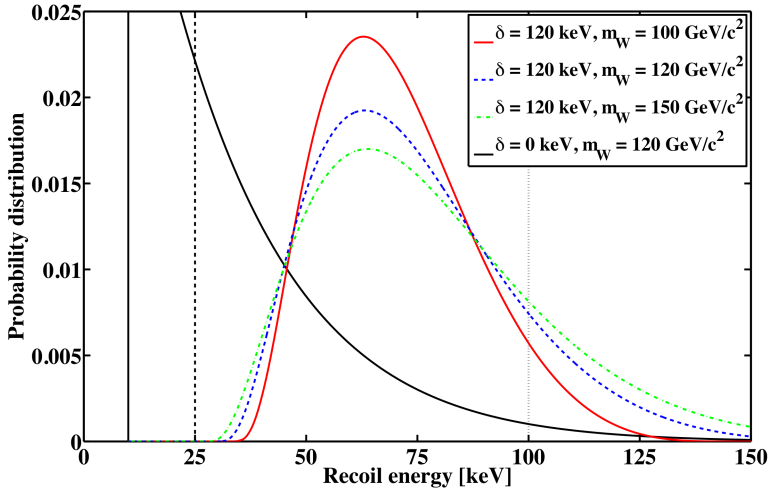

Figure 7.1: Differential recoil spectra in a Ge target for a WIMP-mass splitting δ of 120 keV and a few representative WIMP masses m_W. For comparison the spectrum for a WIMP with a mass of 120 GeV/c^2 assuming elastic scattering ($\delta = 0$ keV) is also shown (black/solid). The spectra are normalized to unity in the 10–150 keV recoil-energy range. The vertical lines denote the analysis threshold at 10 keV, the lower boundary for the setting of the surface-event rejection cut at 25 keV and the upper analysis limit from the previous analysis at 100 keV. See text for details.

Because both data sets had already been analyzed, this analysis was not "blind". However, the analysis was performed in a similar manner to minimize bias: selection criteria and background estimates were defined and evaluated using only WIMP-search data outside the signal region and calibration data.

In addition to the quality cuts, most of the selection criteria for WIMP-nucleon interactions remained unchanged from the previous analyses. This included the single-scatter cut, requiring there to be no signal exceeding the phonon-noise level by more than 4σ in any of the other 29 detectors; the ionization-based fiducial-volume cut, rejecting events near the edges of the detectors; and the muon-veto cut, demanding negligible coincident energy deposited in the active muon veto surrounding the apparatus.

Extending the analysis window to 150 keV was hindered by the fact that statistics from the ^{252}Cf neutron source were low above ∼100 keV, which can be seen in Fig. 5.3. Thus, the nuclear-recoil bands at higher energies were extrapolated from the fits below 100 keV. The extrapolation showed good agreement with Lindhard theory [1, 98], when statistics from all six runs were combined for each detector, and both the band locations and the nuclear-recoil cut efficiencies had only a minor energy dependence above ∼25 keV. To quantify the last statement, the slope of the bands above 25 keV was typically of the order of ∼1‰, while the final efficiency was conservative at high energies and expected to underestimate the true efficiency by ∼2–3% (see also the next paragraph).

As discussed in the previous sections, all cuts except for the surface-event rejection cut could be inherited from the previous analysis, though, in the case of the nuclear-recoil

band, extrapolations were necessary. However, the efficiencies of the energy-dependent cuts, already discussed in the previous chapter, had to be recalculated including the energy range from 100 keV to 150 keV. Since the trigger efficiency in one particular detector and run (T3Z4, run 123) was known to be abnormally low (∼80%), this efficiency had to be recalculated as well, even though it was 100% in all other detectors above 10 keV. Only the combined efficiency of the ionization threshold and bulk-electron rejection cut could be left out, since it was 100% in all detectors above ∼10 keV without any exceptions. Since these calculations are not very illuminative, only the final exposure-weighted overall efficiency without the efficiency of the timing cut is shown in Fig. 7.2. The dashed/dotted lines represent the results from the standard analysis discussed in the previous chapter and shown in Fig. 6.18. It can be observed that inclusion of runs 123–124 and the energy range of 100–150 keV led to a slight decrease of the efficiency at higher energies. In the next step, the timing cut was defined and its efficiency was calculated. Following the reasoning of the first section of this chapter, it could be anticipated that the corresponding efficiency would turn out to be much higher than the efficiency of the standard analysis. So considering the plot in Fig. 7.2 it was expected to be somewhere between the red and the green curves.

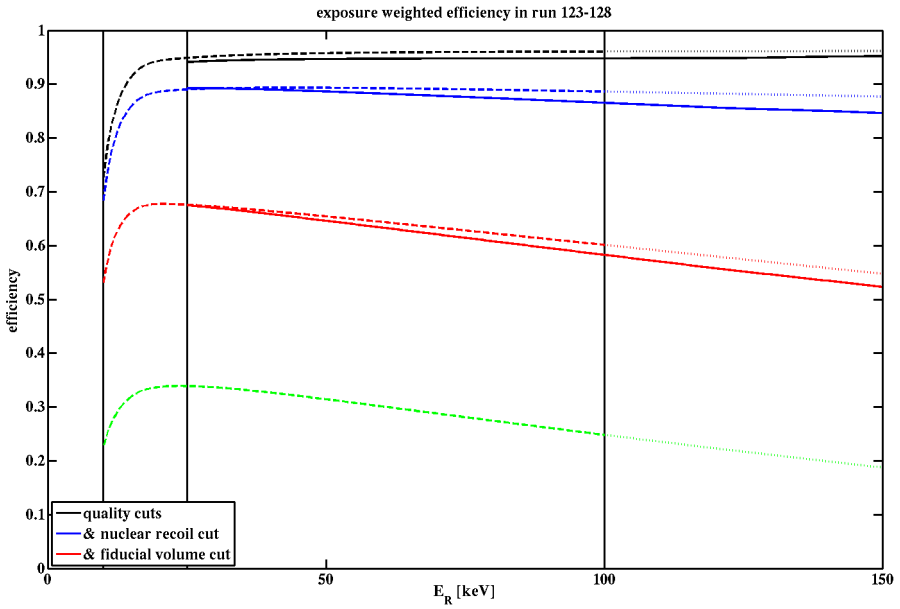

Figure 7.2: Exposure-weighted overall efficiency of the inelastic dark matter analysis without the efficiency of the timing cut (solid). The cuts denoted in the legend were successively added in the same way as in Fig. 6.18. The efficiencies from that figure, representing the results from the standard analysis, are also shown (dashed). The green/dashed line denotes the final efficiency from that analysis including the timing cut. These efficiencies were only defined up to 100 keV, so the dotted lines up to 150 keV are simple extrapolations.

7.1 Definition of the surface-event rejection cut

As already mentioned in previous chapters, the surface-event rejection was based upon a timing parameter consisting of the sum of the rise time of the largest phonon pulse and its delay relative to the ionization pulse. This timing cut was set in the 25–150 keV energy range using barium and californium calibration data. Since surface events in WIMP-search data did not have the same recoil-energy and ionization-yield distributions as in barium calibration data, this cut was not expected to be optimal, although corrections, based on WIMP-search multiple scatters, were applied to the distributions to diminish these differences. Thus, the cut performance had to be tested on WIMP-search data before "unblinding". The cut setting and testing are discussed in more detail in this chapter and in the following one respectively.

At first the exact definition of surface events is given. Since they are characterized by a reduced charge collection, they also suffer from reduced ionization yield, which, as discussed in the chapter on the surface-event background, is the actual reason why these events can mimic nuclear recoils and thus constitute such a dangerous background. The definition of these events is therefore based on the ionization yield parameter. All events with an ionization yield above 0.1 and below the minimum of 0.7 and the lower boundary of the 5σ electron-recoil band at the events' recoil energies are considered surface events (also called "betas" among members of the CDMS collaboration). This definition is illustrated in Fig. 5.10, where the boundaries of the corresponding region are shown as black/solid lines. It was chosen to set the upper boundary of that region particularly far below the population of bulk electron recoils, in order to avoid contamination of the sample with events, which interacted in the bulk of the detectors.

A few important observations can be made regarding the event populations in Fig. 5.9. First, it can be seen that the population of surface events is quite constant regarding a possible energy dependence. It only widens at lower energies due to worse signal-to-noise behaviour: Low energy events have smaller pulses, and thus it is more difficult to determine the exact timing parameters, broadening the timing distribution. Note, that this issue was manifested regarding the start time determination of the charge pulse of the WIMP candidate in T3Z4, which was elucidated in great detail in the last chapter. However, this energy-independence over large parts of the energy range is very convenient, since it allows a reliable definition of an energy-independent timing cut. This cut will nevertheless be dominated by the outliers at low-energies. For example, an event just above the timing cut boundary at low energies is likely to be very close to the surface-event distribution and thus an outlier of that distribution, while an event with the same timing parameters at higher energies might be well separated from the background. Attempts to define an energy-dependent timing cut have not shown superior performance than energy-independent cuts in the past, however, the collaboration still works actively on such improvements. A cut-free analysis, based on the maximum-likelihood approach introduced in chapter 5.1.2, which takes into account the energy dependence of the timing parameters, is discussed in the next chapter. Neglecting this slight energy-dependence greatly simplifies the cut setting, which can be understood as follows: As mentioned in chapter 5, the CDMS collaboration

has the desire to keep the total background below 1 event, since in this case all events, which satisfy all WIMP selection criteria, can be directly regarded as possible WIMP candidates, even though fluctuations of the background have to be considered. Thus, as will be discussed in more detail in this chapter, it is necessary to set the timing cut in the tails of the surface-event distributions, where statistics are limited and it is very difficult to accurately model the distributions. Therefore, it is at least convenient that all events regardless of their energies can be used for these estimates. On the other hand, it can be observed from Fig. 5.9 that the fraction of true nuclear recoils passing the cut can be obtained without too many problems: The cut will be set in the bulk of the distribution. This is convenient regarding the calculation of the efficiency, however, at the same time it is also very unfortunate since ∼50% of all WIMP candidates have to be neglected in order to make sure that the background is reduced to an acceptable level. In that sense, the surface-event rejection, based on the timing parameter, is much less powerful than the rejection of bulk-electron recoils based on ionization yield. The harsh reduction of WIMP acceptance rendered the proper treatment of the surface-event background the most involved part of the analysis.

To understand the complicated machinery of the rejection of surface events developed by the CDMS collaboration, it is illuminating to start with a very simple possible ansatz and subsequently discuss the numerous improvements. The main part of these calculations was based on surface events from the barium calibration data, as defined at the beginning of this chapter, and on nuclear recoils from the californium calibration data within the standard 2σ band. Usage of the timing parameters from WIMP-search single scatters within the nuclear-recoil band was not permitted due to the quasi-blind policy of this reanalysis. Models of the detectors' responses, e.g. regarding the phonon propagation, are under development, but currently only calibration data can be applied for these calculations.

Regarding the low statistics issue, it would be desirable to combine the surface events from all detectors and runs to set just one single timing cut boundary. However, all detectors showed a quite different performance regarding the timing response and distributions, so that it was impossible to combine the detectors. Even worse, for each detector two different cuts had to be defined for runs 123–124 and runs 125–128, since the corresponding distributions were separated as shown in Fig. 7.3 for detector T4Z4. This was mainly due to different position correction schemes applied to the two data sets (cf. chapter 4.5.4.5). The distributions of nuclear recoils were separated as well, but typically with a different offset. Thus, since timing-cut boundaries had to be defined for two data sets in each of the 14 detectors, the total number of parameters, which was to be estimated was 28.

Assuming, that the distributions of surface events from barium calibration and WIMP-search data were identical, a simple approach to start this analysis could be as follows: Denote N_{ij} the estimated total number of events within the WIMP-search data of detector i and run data set j, that obey all constraints for WIMPs (of course except for the timing cut). In particular, these events should be single scatters within the nuclear-recoil band. The index i runs over all detectors, so from 1 to 14 and j can be 1 or 2 for data from runs 123–124 and runs 125–128 respectively. Moreover, l_{ij} denotes the corresponding fraction of surface events above the timing parameter value t_{ij}. The function $l_{ij}(t_{ij})$ can be easily

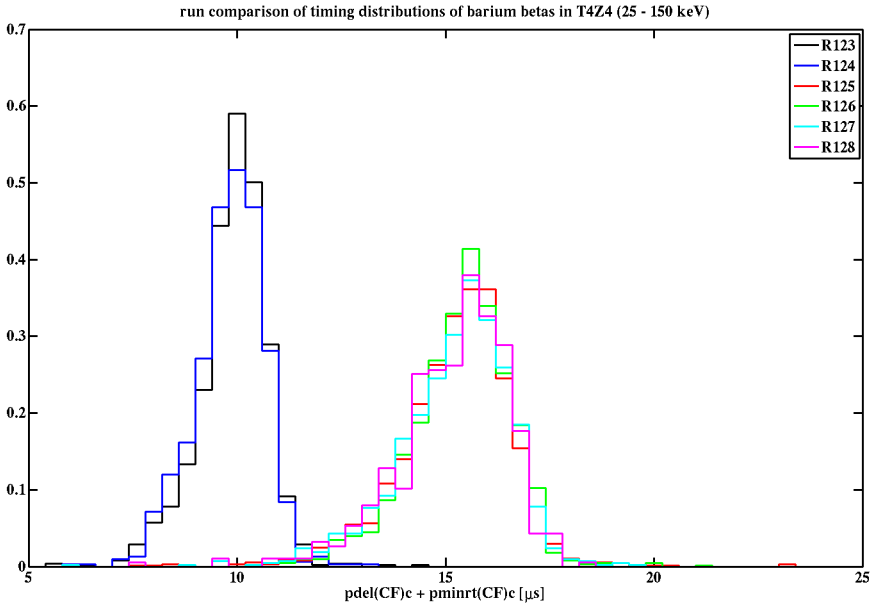

Figure 7.3: Run comparison of the timing (pdel(CF)c + pminrt(CF)c) distributions of surface events (betas). The distributions of runs 123–124 and runs 125–128 are significantly separated. Thus, it was not possible to just combine all runs for a chosen detector. Instead, timing cuts were set for runs 123–124 combined and for runs 125–128 combined.

obtained by plotting the survivor function of the corresponding distribution, which is just 1 minus the cumulative distribution function. Further assuming that the pass-to-all ratios of surface events from barium calibration and WIMP-search data were identical, the number of surface events in the WIMP-search data, passing a cut set at the timing parameter value t_{ij}, is given by:

$$n_{ij}(t_{ij}) = N_{ij} \cdot l_{ij}(t_{ij})\,. \tag{7.1}$$

However, as stated at the beginning of this chapter, surface events in barium calibration and WIMP-search data had different ionization-yield and recoil-energy distributions. Regarding ionization yield, this was mainly related to different fractions of surface events on the phonon and charge sides. In chapter 5.3.2 it was shown that phonon-side events typically have lower ionization yield than charge-side events. Moreover, it was observed that the fraction of surface events on the charge side in WIMP-search data was typically a factor of ∼3 higher than in barium calibration data. This was predominantly caused by different locations of the sources inducing surface events in both kinds of data sets. While the sources were contaminations of the detector assembly and the detectors' surfaces themselves in the WIMP-search runs, they were predominantly localized single sources in the calibration runs. However, as also discussed in chapter 5.3.2, the distributions of timing parameters of surface events on the phonon and charge sides were quite similar, so that no correction was applied for the iDM analysis. Nevertheless, a possible difference in timing performance was included for the standard analysis discussed in the previous chapter.

This caused the disadvantage of dividing the surface-event sample, which already suffered from low statistics, into even smaller data samples, and neglecting the large population of events, which were not tagged by any of the two sides.

The difference regarding the energy spectrum can be observed from the plot in Fig. 7.4, which shows a comparison of the distributions of surface events from barium calibration data in T4Z4 in run 125 and WIMP-search multiple-scatter events within the nuclear-recoil band. Due to the low number of acquired WIMP-search events, all detectors of runs 125–128 were combined for this plot. It should be noted that it was observed in previous analyses, that the energy spectra of WIMP-search multiple and single scatters were very similar. The spectrum of surface events is almost uniform and falls off very moderately at higher energies, while the shape of the WIMP-search spectrum could be described as nearly exponential. Thus, the most striking difference is to be found at low energies with a much higher fraction of WIMP-search events. The reason for this difference is related to the selection cuts used for both populations. Since the upper boundary of the surface-event selection cut was set to 5σ below the mean of the electron-recoil band, a large fraction of events was removed at low energies due to the widening of the band, while the population of WIMP-search events within the nuclear-recoil band typically was only slightly affected by the charge-threshold cut. This behavior can be observed in Fig. 5.4 and Fig. 5.10. The surface-event spectrum would be much more similar to the WIMP

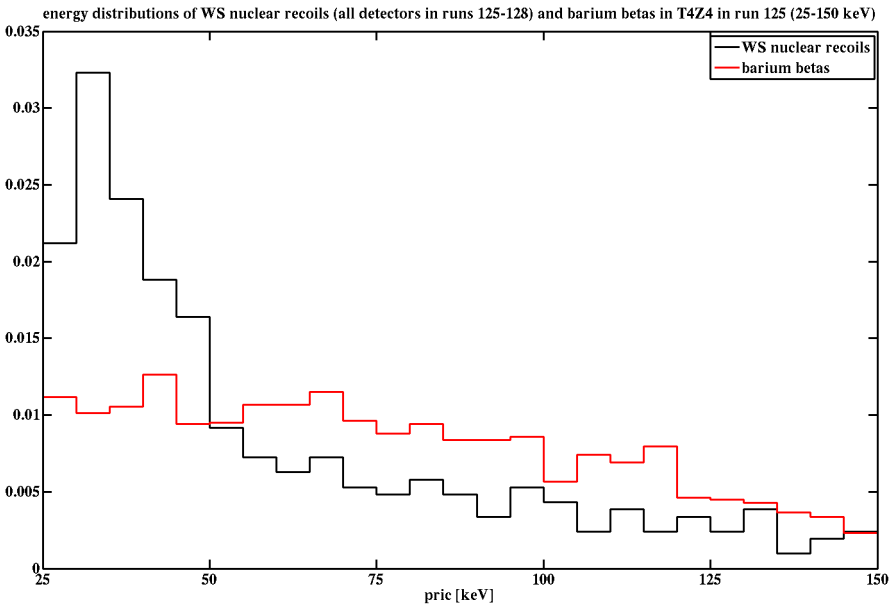

Figure 7.4: Comparison of energy (pric) spectra of surface events from barium calibration data in T4Z4 in run 125 and WIMP-search multiple-scatter events within the nuclear-recoil band. Regarding the WIMP-search events, all detectors and runs 125–128 were combined because of low statistics. The fraction of low-energy events is significantly higher for WIMP-search events.

spectrum, if only surface events within the nuclear-recoil band were considered. However, this would reduce the statistics by a factor of ∼10 and therefore render the cut setting almost impossible. Thus, increased systematic differences were accepted in order to reduce the statistical uncertainties. However, it was necessary to introduce correction factors to account for these systematic errors. This was due to the fact that the population of timing outliers, dominating the actual leakage, predominantly occurred at low recoil energies, and it was just shown that usage of barium surface events would underestimate this fraction of events. Therefore, the leakage, calculated using surface events from barium calibration data, would also underestimate the leakage in the WIMP-search data yielding a cut, which would be too loose. Finally, it was decided to incorporate an energy correction using two energy intervals, 25–45 keV and 45–150 keV. Hence, the simple estimate for the number of surface events in the WIMP-search data, passing the timing cut set at t_{ij} given in (7.1), was updated to

$$n_{ij}(t_{ij}) = N_{ij} \cdot \left(\left(f_{ij}^{1} \cdot l_{ij}^{1}(t_{ij}) \right) + \left(f_{ij}^{2} \cdot l_{ij}^{2}(t_{ij}) \right) \right), \tag{7.2}$$

where the upper indices 1 and 2 denote the two just mentioned energy intervals. The leakage fractions $l_{ij}^{1/2}$ were defined as before but with the additional constraint that only events within the corresponding energy ranges should be used for the estimates of the distributions. The scaling factors $f_{ij}^{1/2}$ were given as the fractions of WIMP-search events within the nuclear-recoil bands in the respective intervals. The results can be found in Fig. 7.5. They were based on WIMP-search multiple scatters, but it was known from previous analyses that the fractions from singles scatters were similar. There were only small differences in runs 123–124. This was different for runs 125–128. Unlike for the standard analysis presented in the previous chapter, the scaling factors were not averaged over various groups of detectors (interior and endcap detectors). It should also be noted that for the correction for the standard analysis three different energy intervals were used: 10–20 keV, 20–30 keV and 30–100 keV. The fine binning was necessary to take the broadening of the timing distributions at very low energies, which were omitted for the cut setting of the iDM analysis, into account. Moreover, the surface events were divided into charge- and phonon-side events, so that for the standard analysis the data was divided into six categories instead of two, rendering the estimates even more involved. In that sense, the cut setting of the iDM analysis was less complicated. Finally, it should be noted that the actual cut was about to be fixed at one single value t_{ij} for all of the 2 (6 in the case of the standard analysis) categories.

An estimate of the numbers of WIMP-search single scatters within the nuclear-recoil bands in the energy range 25–150 keV N_{ij} was needed for the cut setting. Actually, it was not permitted to take them directly from the data, since this would contradict the blinding paradigm. Therefore, for the standard analysis of runs 125–128, presented in the previous chapter, the numbers from runs 123–124 were used, rescaled by the gain in exposure. However, this was obviously not possible for this reanalysis of the combined data. Therefore, for the iDM analysis, the numbers were directly taken from the WIMP-

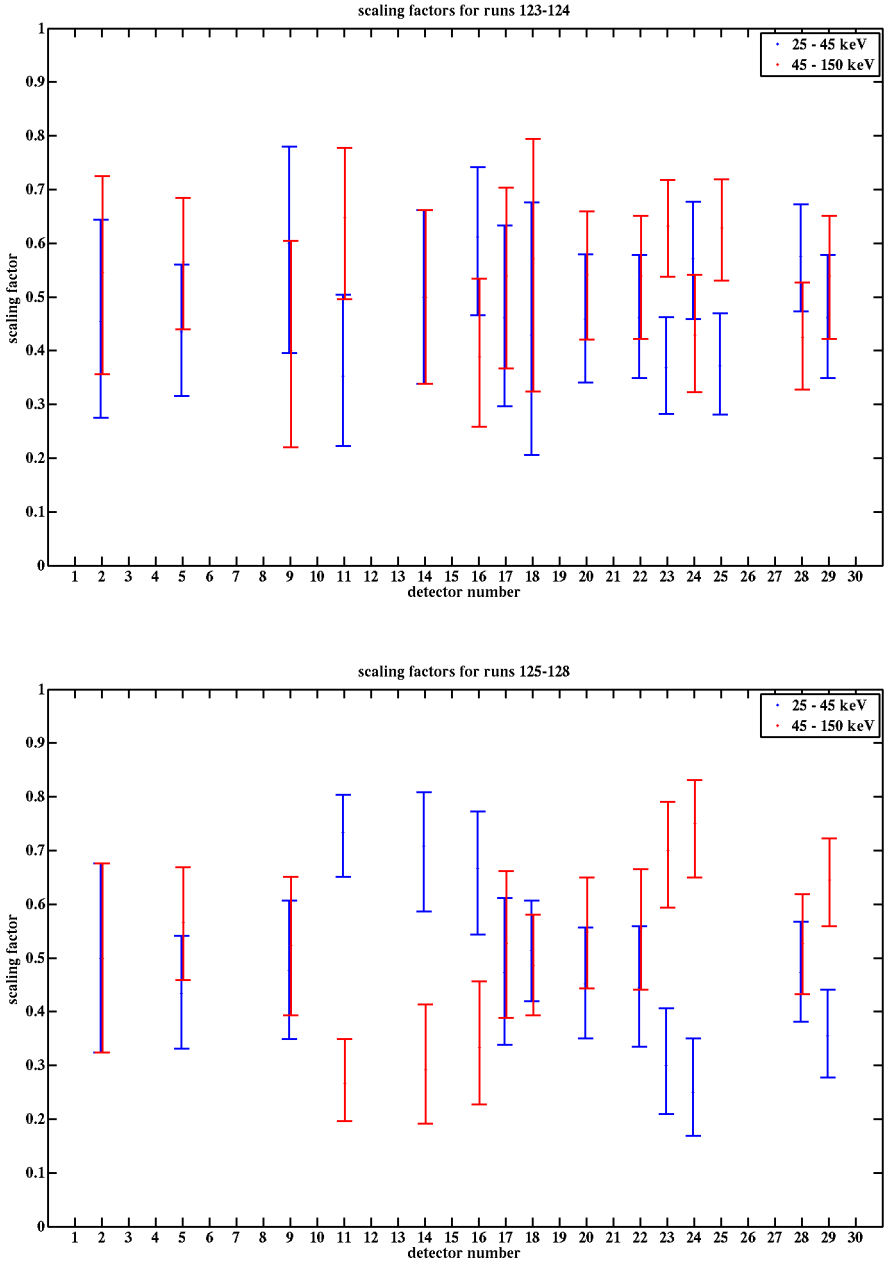

Figure 7.5: Fractions of WIMP-search events within the nuclear-recoil bands in the energy intervals 25–45 keV (blue) and 45–150 keV (red) for each detector. These factors were incorporated into the procedure for setting the timing cut. The top plot is for runs 123–124 and the bottom plot for runs 125–128. Note that T5Z1 (detector 25) was removed from the analysis due to detector issues.

search data. The results are shown in Fig. 7.6 together with the corresponding numbers of multiple scatters, which were needed for later checks. For the further analysis numbers of events were applied to each detector/data-set category ij by adding the event numbers (in the particular detector) from both data sets (runs 123–124 and runs 125–128) and weighting them with the respective exposure from the data sets. It should be emphasized that no parameters, in particular not the timing values of the singles, were investigated before the cut was fixed.

After applying corrections for differences of surface events in the barium calibration and WIMP-search data, the next question would be, how the cut should actually be set. Given a desired total leakage of n_{tot}, which, as discussed above, should be $\lesssim 1$, and the total number of 28 detector/data-set categories, a possible first choice would be to demand

$$n_{ij}(t_{ij}) \leq \frac{n_{\mathrm{tot}}}{28}\,, \tag{7.3}$$

with $n_{ij}(t_{ij})$ given in (7.2). This would allow equal leakage in all 28 categories and would render the determination of t_{ij} comparably simple, since they could be directly read off from plots of each $n_{ij}(t_{ij})$ separately. However, this would disregard the individual timing performance of each detector. Some of them show very good background rejection capabilities, manifested by a comparably small overlap of the timing distributions of surface events from the barium calibration data and nuclear recoils from the californium calibration data, while others were worse. Apart from the detector's phonon response, another factor in this regard was the fact that some detectors suffered e.g. from a larger surface event contamination. Moreover, the expected leakage should not be the only criterion regarding the cut definition. Instead, the cut setting should be regarded as a tradeoff between background rejection and WIMP acceptance, which again is due to the overlap of both distributions. In some detectors a tight cut might hurt the overall efficiency much more than in others. Thus, the final procedure was based on the minimization of the following function:

$$f(\underline{t}) = \left(1 - \frac{1}{\mathrm{SAE}_{\mathrm{max}}} \sum_{i=1}^{14} \sum_{j=1}^{2} \mathrm{SAE}_{ij}(t_{ij})\right)^2 + 10\left(1 - \frac{1}{n_{\mathrm{tot}}} \sum_{i=1}^{14} \sum_{j=1}^{2} n_{ij}(t_{ij})\right)^2\,, \tag{7.4}$$

where $\mathrm{SAE}_{ij}(t_{ij})$ denotes the spectrum averaged exposure of each category given by

$$\mathrm{SAE}_{ij}(t_{ij}) = \mathrm{MT}_{ij} \cdot \frac{\displaystyle\int_{E_{\mathrm{lower}}}^{E_{\mathrm{upper}}} \mathrm{d}E\, \frac{\mathrm{d}R}{\mathrm{d}E} \cdot \mathrm{eff}_{ij}(E, t_{ij})}{\displaystyle\int_{E_{\mathrm{lower}}}^{E_{\mathrm{upper}}} \mathrm{d}E\, \frac{\mathrm{d}R}{\mathrm{d}E}}\,. \tag{7.5}$$

As in (6.35) MT_{ij} denotes the exposure and $\mathrm{eff}_{ij}(E, t_{ij})$ denotes the energy-dependent efficiency. The index ij indicates that in this case the exposure only represents the total exposure in the respective category and also that the efficiency (without the timing-cut efficiency) was not taken from Fig. 7.2. Instead, e.g. for $i = 1$ and $j = 1$ the efficiency (without the timing-cut efficiency) of the first used detector (T1Z2) was exposure-weighted over

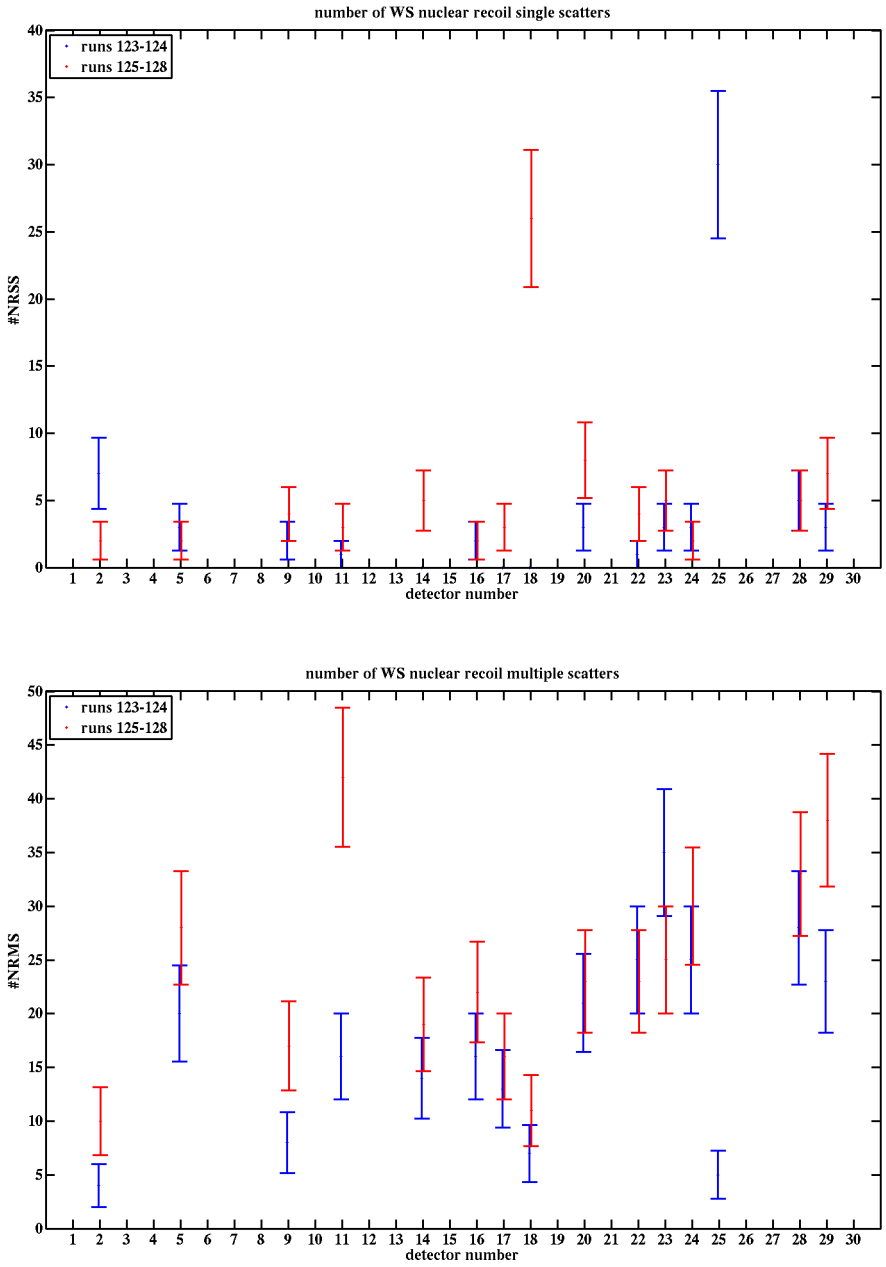

Figure 7.6: Numbers of nuclear-recoil single (top) and multiple (bottom) scatters in the WIMP-search data passing all cuts except for the surface-event rejection criteria within 25 keV and 150 keV. The shown error bars are simple Poisson errors. Note that T5Z1 (detector 25) was removed from the analysis due to detector issues.

runs 123–124. Since the total efficiency was needed for the computation of the spectrum averaged exposure the efficiency of the timing cut itself had to be added to get $\mathrm{eff}_{ij}(E, t_{ij})$. It was obtained similar to the leakage fraction from the surface events by plotting the survivor function of the timing distribution of the nuclear recoils from the californium calibration data. Thus, the spectrum averaged exposure depended on the actual timing-cut position. Besides, it depended on the WIMP parameters through the differential rate. Since the WIMP-nucleon cross section entered the rate as simple factor it canceled in the ratio and thus, regarding the iDM model, it only depended on the WIMP mass m_W and the WIMP-mass splitting δ. Since, as discussed at the beginning of this chapter, the parameter space region of interest was around $m_W \sim 100\,\mathrm{GeV/c^2}$ and $\delta \sim 120\,\mathrm{keV}$, these values were chosen for the calculation of the rate. The corresponding spectrum is shown as the red/solid line in Fig. 7.1. It should be noted, that for the standard analysis, which was mainly concerned with spin-independent scattering, only a value for the WIMP mass had to be chosen for the optimization, which was fixed at 60 $\mathrm{GeV/c^2}$. $\mathrm{SAE_{max}}$ is defined as the maximum possible spectrum averaged exposure summed over all detector/data-set categories. It is obtained by setting the timing cut efficiencies to 1. In short, the function (7.4) optimizes the nuclear-recoil efficiency (first term) for a fixed surface-event leakage (second term). The factor of 10 in front of the second term is included to allow only tiny variations of the leakage. This optimization scheme was applied for the setting of the timing cut. The results from the simple approach, where equal leakage was allowed in all detectors (7.3), were calculated to obtain start parameters for the optimization and for comparative reasons.

Before investigating the actual timing cut, a consistency cut was defined, based on the timing parameters of the nuclear recoils from the californium calibration data, to directly remove extreme outliers, which were likely to suffer from incorrectly reconstructed timing parameters. Gaussians were fitted to the sum of the risetime and the delay, so the standard timing parameter, and to their difference. Subsequently, all events more than $\pm 4\sigma$ away from the means of the fitted Gaussians were removed. For a typical detector an illustration of the cut in the delay versus risetime plane is shown in Fig. 7.7. The lower boundary on the sum of the risetime and delay (line with negative slope in the lower left) was in fact redundant with regard to the actual timing cut, which was about to be defined in the next step.

Finally, the timing cut could be defined. As mentioned before, the survivor functions of the timing distributions of surface events from barium calibration data and nuclear recoils from californium calibration data had to be determined for all 28 detector/data-set categories. In the latter case, they were needed in order to compute $\mathrm{eff}_{ij}(E, t_{ij})$, which was also considered to be a function of the timing parameter t_{ij} as indicated for this part of the analysis. Figure 7.8 shows this dependence for several energy intervals for a typical detector. It includes the impact of the timing consistency cut, discussed in the previous section, and of the manifold cut, elucidated in chapter 6.4.3.6. Since the final cut was about to be set in the bulk of the distribution, no special care was needed to obtain the shown curve: Simple KDEs based on Gaussian kernels were used. As only the time dependence was considered for this analysis, this was just a one-dimensional estimate and thus much

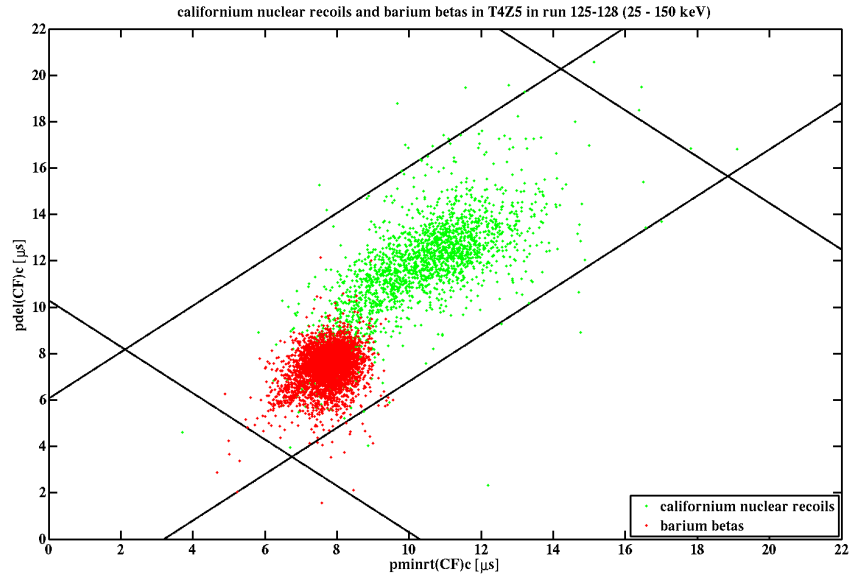

Figure 7.7: Illustration of the timing-consistency cut in the delay (pdel(CF)c) versus risetime (pminrt(CF)c) plane for T4Z5 in runs 125–128. All outliers outside of the rectangular region were removed from the analysis.

less involved than the multi-dimensional estimates needed for the full likelihood analysis (cf. chapter 8). Therefore, uncertainties emerging from these calculations were neglected.

The corresponding estimates regarding surface events were much more involved, since the cuts were about to be set in the tails of the distributions. Depending on the desired leakage, it was even possible that it had to be set at a value higher than those from any event of the surface-event population, so that extrapolations were inevitable. Thus, it was at least desirable to have a functional form for the tails. Generalized pareto functions of the form

$$p(t) = \frac{1}{\sigma}\left(1 + \frac{\eta\,(t-\mu)}{\sigma}\right)^{-\frac{1}{\eta}-1} \tag{7.6}$$

were empirically determined to describe these tails well and were fitted to the 12 events with the highest timing parameters. The bulks of the distributions were modeled with the same KDE estimates already applied to the nuclear recoils. Both parts were connected with cubic splines to obtain a smooth transition. The uncertainties from these estimates were expected to be much more significant than those regarding the nuclear-recoil distributions. In the bulk, error bands were calculated based on Greenwood's formula [111], which is a common estimator, and subsequently smoothed, using a Gaussian kernel with the bandwidth obtained from the KDE estimate of the actual distribution. In the tails, the errors were determined from the covariance matrix of the pareto-tail fit. Similar to the distributions themselves, the error bands were connected with cubic splines. Examples for the results of this procedure can be found in Fig 7.9, 7.10 and 7.11, which show

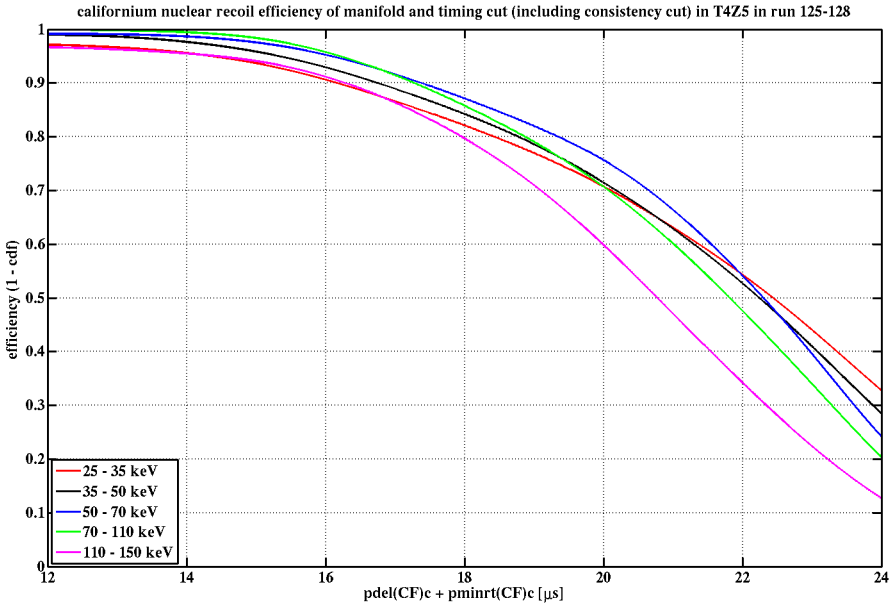

Figure 7.8: Nuclear-recoil acceptance as a function of the timing parameter (pdel(CF)c + pminrt(CF)c) for T4Z5 in runs 125–128 for several energy ranges. The effects of the timing consistency and manifold cuts are included. For example, if the timing cut was set at 20 μs, 60% of the nuclear recoils in the recoil-energy range of 110–150 keV would pass the cut.

the pareto-tail fit, the smoothed matching region of the bulk and the tail and the full survivor function respectively for the 25–45 keV energy range of T3Z4 in runs 123–124. The red/solid and red/dotted lines respectively denote the empirical cumulative survivor distribution functions and the corresponding errors. The blue lines represent the smoothed estimates, which were used for the optimization.

The last issue before determining the actual cut position was the number of desired, or rather tolerable, leakage events n_{tot}. At first sight, it might seem advantageous to set this number to an extremely low value $\ll$1, so that the occurrence of even 1 background event was nearly impossible. However, this would also reduce the signal acceptance tremendously. Thus, as mentioned before, a value $\lesssim$1 was preferable. For this analysis values between 0.1 and 1.5 were tested in steps of 0.1. A further analysis of the experimental sensitivity for each resulting cut was conducted in order to make the final choice. Below, this procedure is outlined in more detail. Additionally, values between 2 and 20 in steps of 1 were investigated. As discussed before and as will be shown below, the cuts for low values of the leakage ($\lesssim$1) had to be set far out in the tails of the surface-event distributions where statistics were low. For higher leakages, the cuts were set in the bulks of the distributions, and thus the predictions regarding the leakage were much more reliable. Hence, leakage events between 2 and 20 were not considered as options for the final cut setting but for general tests.

In the next step, the expected surface-event leakage and the spectrum averaged expo-

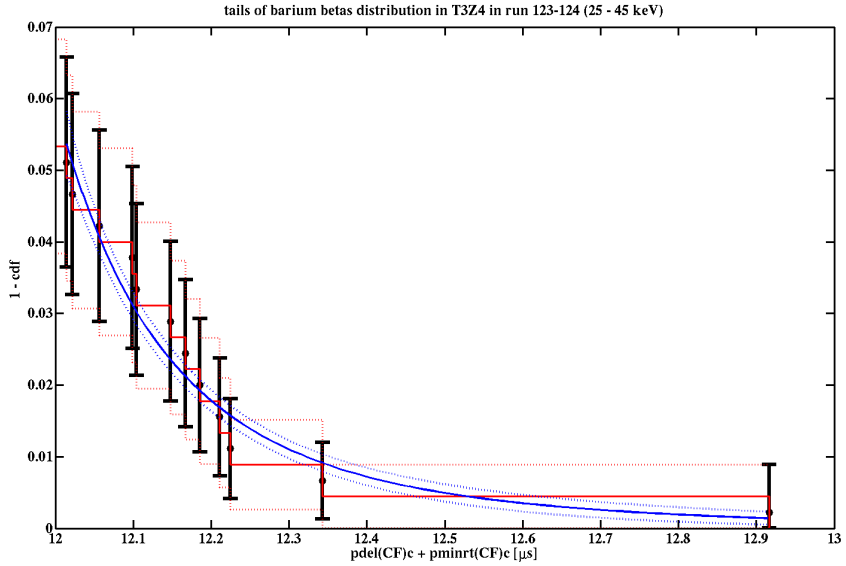

Figure 7.9: Pareto-tail fit to the 12 surface events with the highest timing parameters (pdel(CF)c + pminrt(CF)c) in the 25–45 keV energy range of T3Z4 in runs 123–124. The red/solid and red/dotted lines denote the empirical cumulative survivor distribution functions and the corresponding errors respectively. The blue lines represent the smoothed estimates, which were used for the optimization. See text for details.

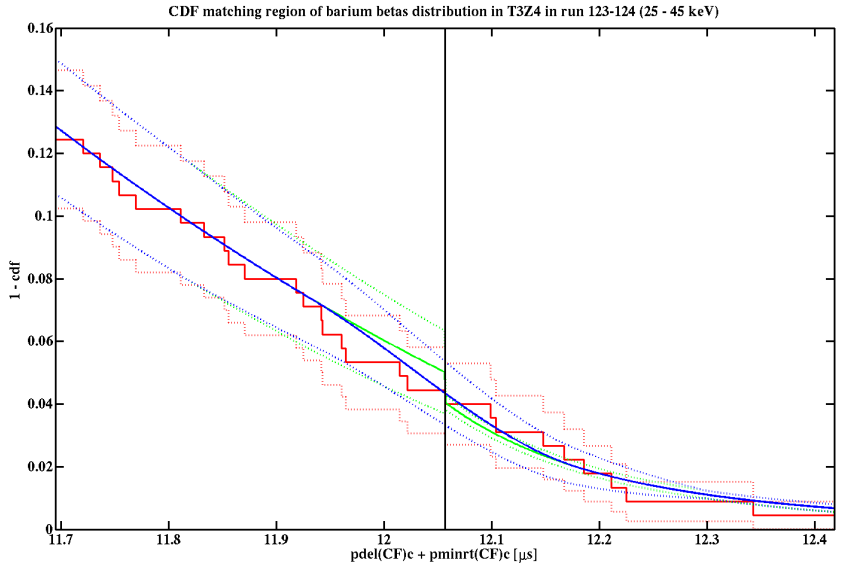

Figure 7.10: Matching region of the bulk distribution based on KDEs and the tail distribution based on the pareto-tail fit shown in Fig. 7.9. The green lines represent the KDE and the generalized pareto function within the matching region in the bulk and the tail. Cubic splines were used to provide a smooth transition (blue). See caption of Fig. 7.9 for more details.

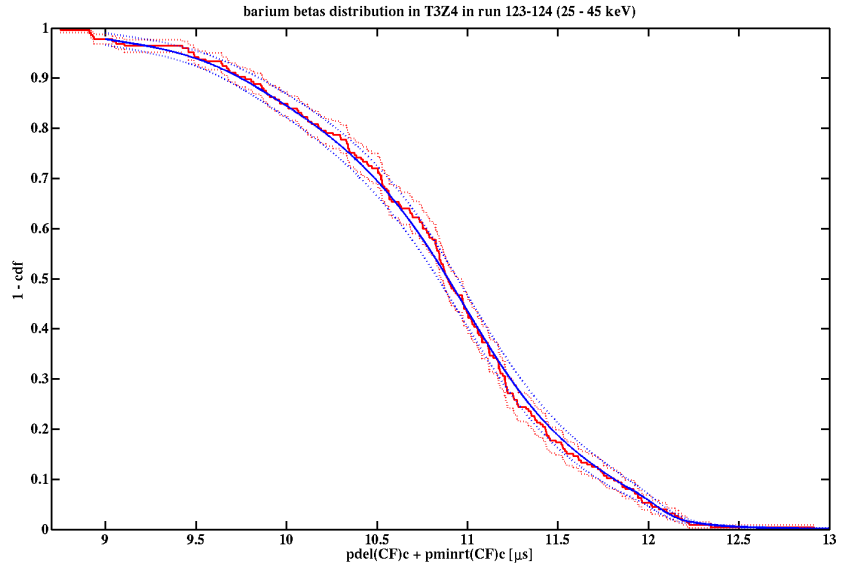

Figure 7.11: Full survivor distribution function for the example already used for Fig. 7.9 and 7.10.

sure could be calculated for each detector/data-set category according to (7.2) and (7.5) respectively. Subsequently, timing cuts were defined for all values of n_{tot} just given by minimizing (7.4) and for comparison by requiring (7.3). In fact, the results from the latter approach were also used as the starting values for the minimization, which was non-trivial, since it had 28 free parameters as discussed before. The estimated uncertainties of the leakage did not enter these calculations. The results can be found in Fig. 7.12 for $n_{\mathrm{tot}} = 0.6$ (top) and $n_{\mathrm{tot}} = 10$ (bottom) regarding detector T3Z4 in runs 123–124. As discussed below, the timing cut corresponding to the first value yielded the best sensitivity. Thus, it was chosen as the final timing cut for the analysis. It can be observed that the cuts for the shown example, the one obtained from the optimization and the one demanding equal leakage on all detectors, were set in the bulk of the $\mathrm{SAE}_{ij}(t_{ij})$ function (blue) and in the tail of the $n_{ij}(t_{ij})$ function (green) as predicted before. The result for $n_{\mathrm{tot}} = 10$ is included in the figure to show that, for a high leakage, the cut is set in the bulk of the $n_{ij}(t_{ij})$ function and is thus much more reliable. In both cases ($n_{\mathrm{tot}} = 0.6$ and $n_{\mathrm{tot}} = 10$), the cut from the optimization was set at a higher timing parameter than the one obtained by demanding equal leakage in all detector/data-set categories. This indicates that this particular detector/data-set had comparably bad background rejection capabilities.

A comparison of the cut positions for $n_{\mathrm{tot}} = 0.6$ is shown in Fig. 7.13 for each detector for runs 123–124 (top) and runs 125–128 (bottom). It also contains the values from the original used cuts in the standard analyses. Those from runs 123–124 were defined for the analysis presented in [61], while those from runs 125–128 correspond to the analysis discussed in the previous chapter. Note, that the new cuts, defined with equal leakage on all detectors and the optimized ones, were much looser, as expected because of the higher

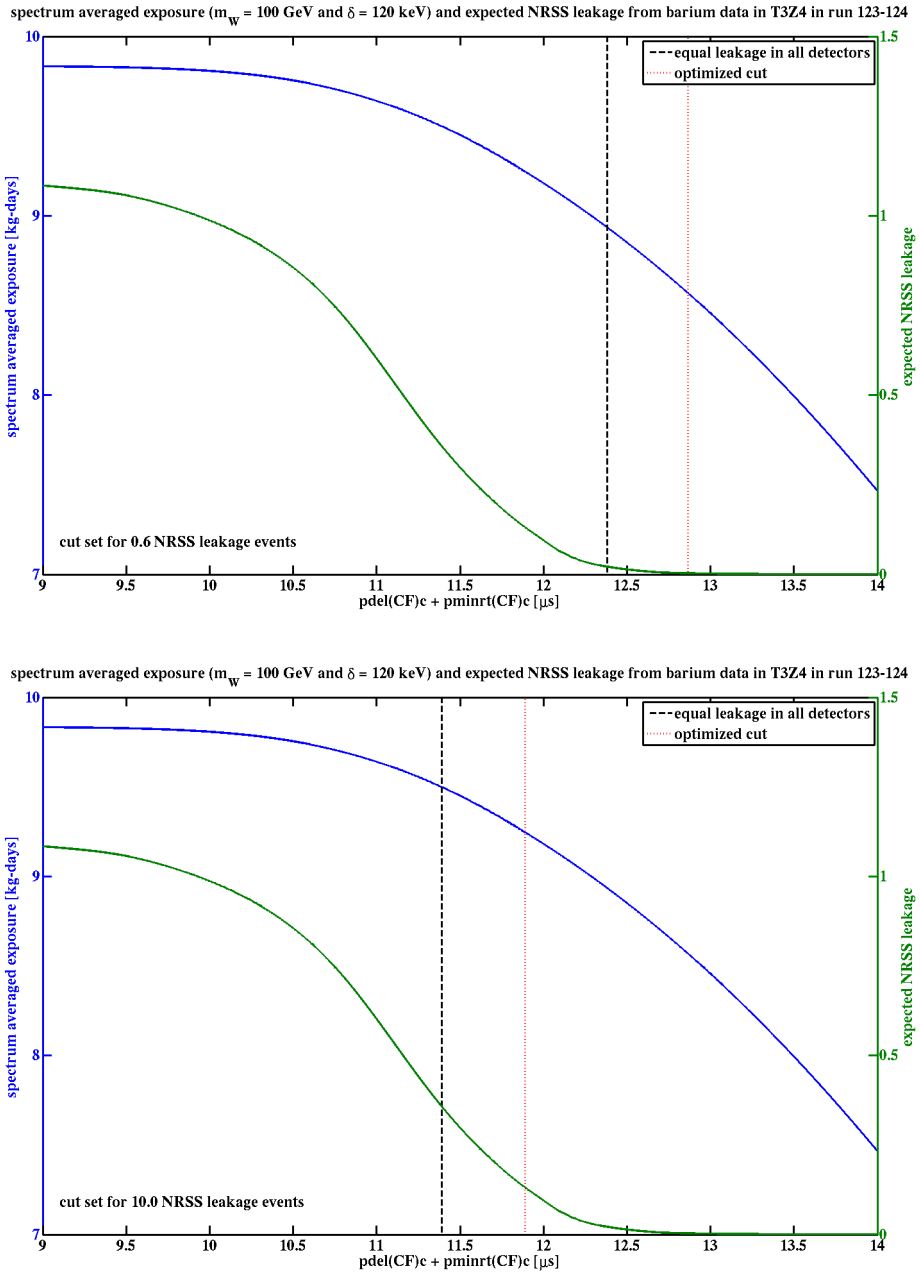

Figure 7.12: Spectrum averaged exposure (blue) and expected surface-event leakage (green) as a function of the timing parameter for T3Z4 in runs 123–124. The positions of the cuts from the optimization (red/dotted) as well as from requiring equal leakage on all detectors (black/dashed) are shown demanding a total leakage of 0.6 (top) and 10 (bottom) events.

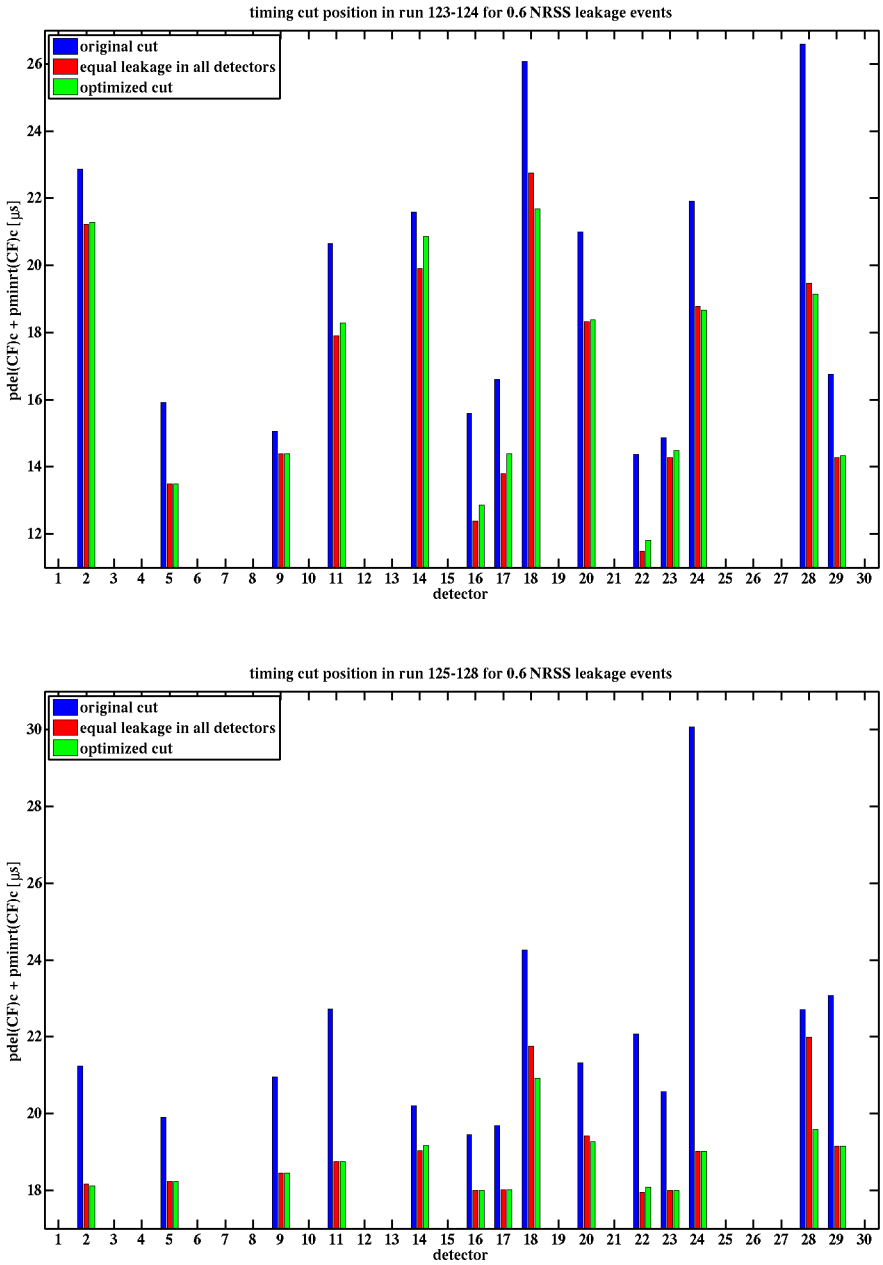

Figure 7.13: Comparison of the cut positions for each detector for runs 123–124 (top) and runs 125–128 (bottom) considering a total leakage of 0.6 events. As expected, the new cuts, defined applying both discussed schemes, were much looser than those from the standard analyses.

threshold of 25 keV for the setting of the timing cut. This was especially pronounced in endcap detector T4Z6 (detector 24) in runs 125–128. That was due to the fact that this detector had a large number of estimated WIMP-search events passing all cuts (except for the timing cut) N_{ij} between 10 keV and 25 keV, so that the timing cut from the standard analysis was particularly strict, while there were only a few events above, yielding a much looser cut for the iDM analysis.

After defining timing cuts for various expected numbers of leakage events, they were tested on a population of events, which was expected to have the least systematic differences to potential WIMP candidates: WIMP-search multiple scatters within the nuclear-recoil band. Therefore, it was necessary to calculate predictions for the number of such events, which pass the timing cuts. These could be easily obtained by evaluating (7.2) at the respective cut positions replacing the expected number of single scatters, passing all criteria except for the timing cut N_{ij}, by the corresponding expected number of multiple scatters and finally summing over all detector/data-set categories. So the numbers shown in the top plot of Fig. 7.6 had to be interchanged by the corresponding numbers in the bottom plot of the same figure. The uncertainty of the final result included Poisson errors on the number of these multiple scatters (bottom plot of Fig. 7.6), errors on the scaling factors (Fig. 7.5) and errors from the uncertainty of the surface events' survivor functions at the position of the timing cut, given e.g. by the blue belts in Fig. 7.9, 7.10 and 7.11). A comparison of these numbers to the actually observed leakage with Poisson errors is shown in Fig. 7.14 for the results from the optimization scheme (top) and requiring equal leakage on all detectors (bottom). It can be seen that the predictions (blue) were slightly above the values measured on WIMP-search data (red) for all assumed numbers of predefined leakage events. Thus, the cut could be considered to be conservative, and in the range of 0.2–1.0 predefined leakage events the results agreed within error bars. This ensured confidence in the cut setting procedure. Nevertheless, it should be noted that this conclusion was subject to possible systematic differences regarding the timing cut passage fractions of single and multiple scatters.

Figure 7.15 shows the combined spectrum averaged exposure as a function of the expected number of single-scatter leakage events. The errors on the latter were calculated in the same way as discussed in the previous paragraph for multiples. The actual cut should be set somewhere between 0.3 and 1 events. In this range, the spectrum averaged exposure lies roughly between 400 kg-days and 450 kg-days. Considering that the combined exposure was 969.4 kg-days this corresponded to an average efficiency of ∼40–45%, so significantly higher than the ∼30% achieved in the standard analysis (see Fig 6.18). This indicated, that raising the threshold for the cut setting to 25 keV, in order to get rid of leakage events at low recoil energies, was successful. It should be further noted that the optimization yielded additional ∼10 kg-days of spectrum averaged exposure in this range compared to the cut with equal leakage on all detectors.

Finally, the question remained, which leakage n_{tot} the cut should be fixed at. A very simple approximation of the expected sensitivity for each defined timing cut was to calculate a 90% upper limit on the counting rate for the chosen WIMP parameters ($m_W \sim 100\,\mathrm{GeV/c^2}$ and $\delta \sim 120\,\mathrm{keV}$), considering only simple counting statistics. Since

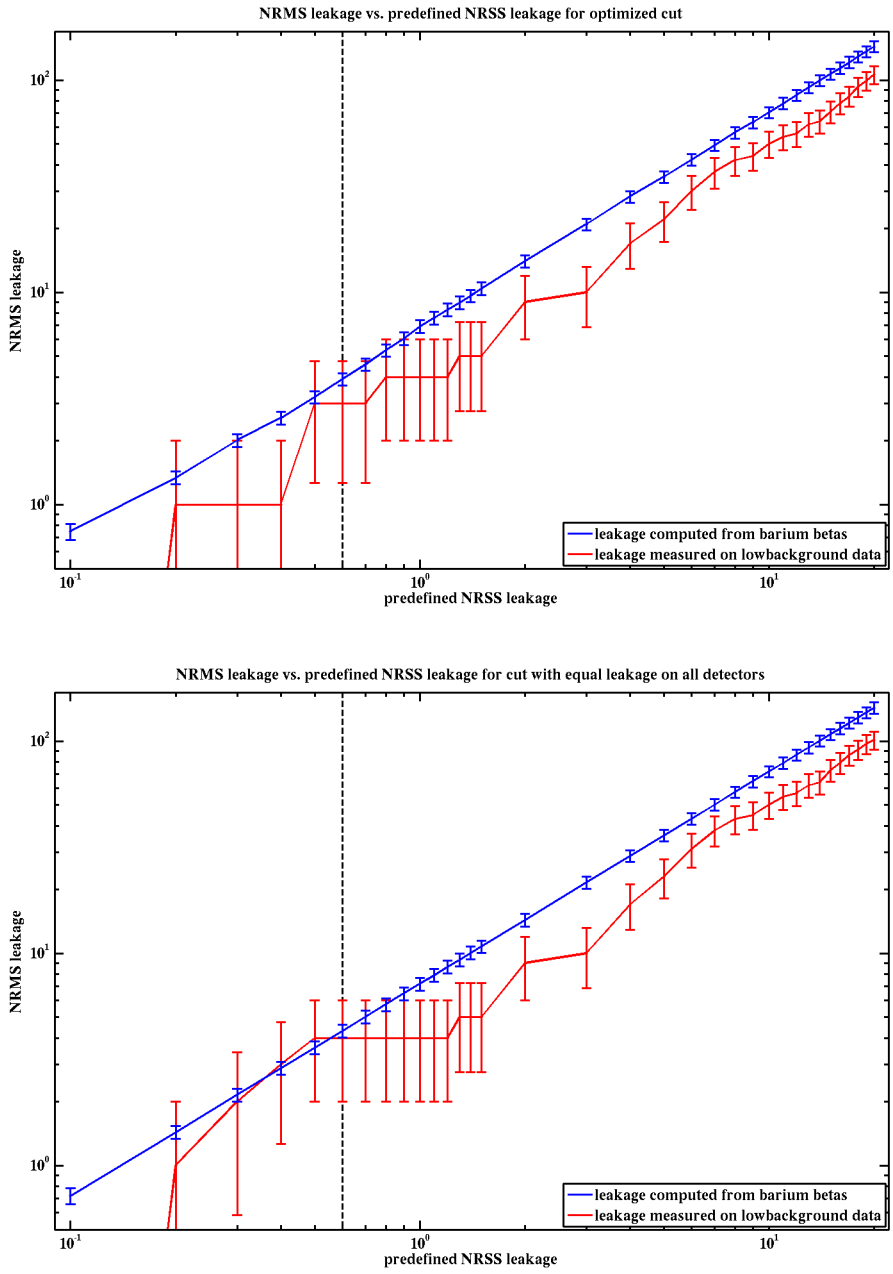

Figure 7.14: Comparison of the predicted numbers of WIMP-search multiple scatters passing the timing cuts (blue) and the actually observed numbers (red) for various numbers of predefined WIMP-search single scatter leakage events. The top plot shows the comparison for the optimized cuts and the bottom plot shows the comparison for the cuts demanding equal leakage on each detector. The expected numbers are always higher indicating that the cut setting procedure is conservative. The finally used cut, defined for a total of 0.6 leakage events, is indicated by the vertical black/dashed lines.

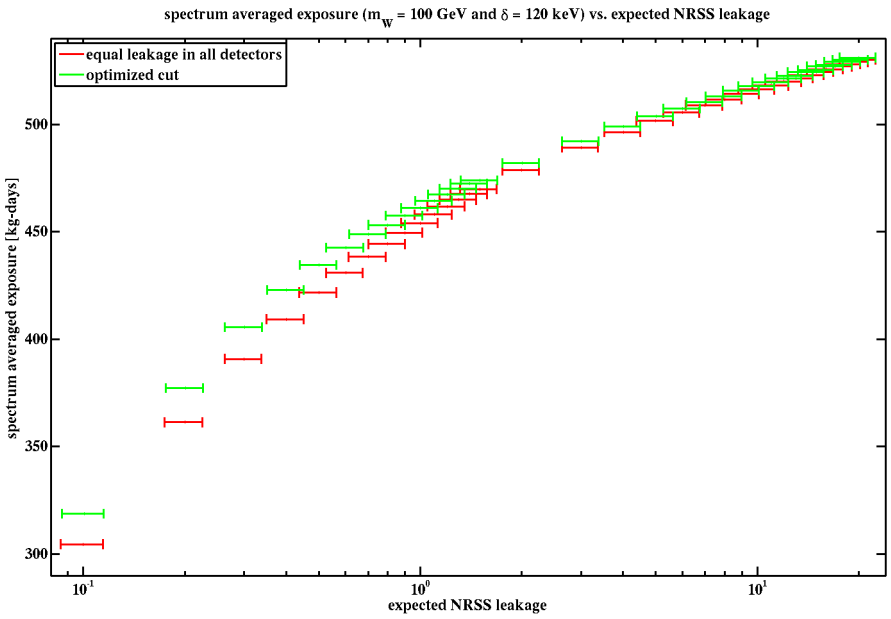

Figure 7.15: Total spectrum averaged exposure as a function of the expected leakage for both cut setting schemes discussed in the text. The optimization yielded additional ∼10 kg-days of spectrum averaged exposure in the region of interest for the actual cut setting (∼0.3–1 events).

the number of candidates, that were about to be observed, was of course not known a priori, a Poisson-weighted average upper limit at 90% C.L. on the number of observed events, given by

$$\overline{\mu} = \sum_{n_{\mathrm{obs}}=0}^{\infty} \frac{n_{\mathrm{tot}}^{n_{\mathrm{obs}}}}{n_{\mathrm{obs}}!} e^{-n_{\mathrm{tot}}} \cdot \mu(n_{\mathrm{obs}}) = \frac{1}{2} \sum_{n_{\mathrm{obs}}=0}^{\infty} \frac{n_{\mathrm{tot}}^{n_{\mathrm{obs}}}}{n_{\mathrm{obs}}!} e^{-n_{\mathrm{tot}}} \cdot F^{-1}_{\chi^2,2(n_{\mathrm{obs}}+1)}(\gamma)\,, \tag{7.7}$$

was calculated in a first step. $\mu(n_{\mathrm{obs}})$ was taken from equation (6.37). With

$$\mu = \mathrm{MT} \cdot \int_{E_{\mathrm{lower}}}^{E_{\mathrm{upper}}} \mathrm{d}E\, \frac{\mathrm{d}R}{\mathrm{d}E} \cdot \mathrm{eff}(E) \approx \sum_{i=1}^{14} \sum_{j=1}^{2} \mathrm{MT}_{ij} \cdot \int_{E_{\mathrm{lower}}}^{E_{\mathrm{upper}}} \mathrm{d}E\, \frac{\mathrm{d}R}{\mathrm{d}E} \cdot \mathrm{eff}_{ij}(E, t_{ij}) = \mathrm{SAE}_{\mathrm{tot}} \cdot R\,, \tag{7.8}$$

where $\mathrm{SAE}_{\mathrm{tot}}$ denotes the total spectrum averaged exposure as shown in Fig. 7.15 and R denotes the differential rate integrated over the considered energy interval. Thus, an approximate average upper limit on the counting rate was given by

$$\overline{R} = \frac{\overline{\mu}}{\mathrm{SAE}_{\mathrm{tot}}}\,. \tag{7.9}$$

The results of this calculation are shown in Fig. 7.16. According to these upper limits on the counting rate, the timing cut set to $n_{\mathrm{tot}} = 0.3$, where the minimum was found, should

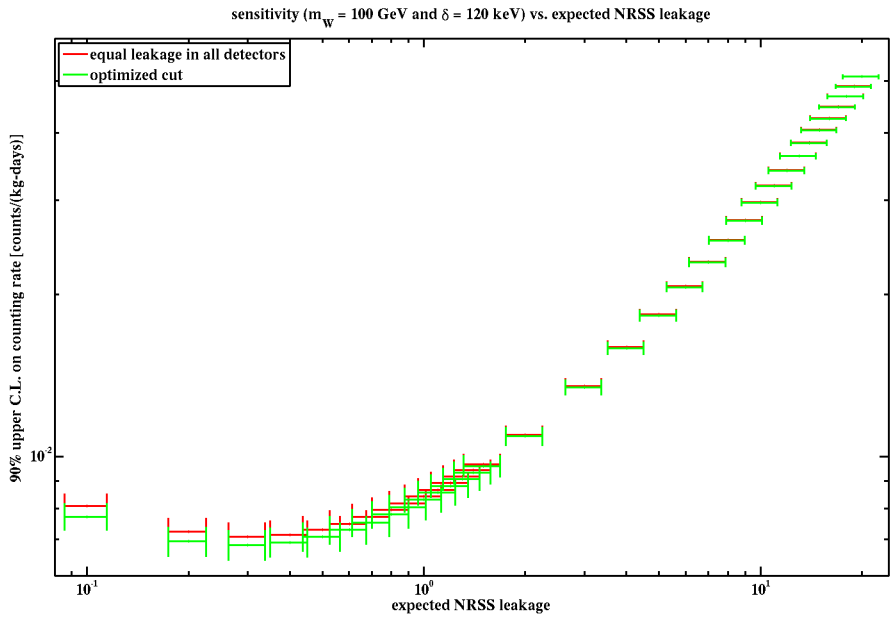

Figure 7.16: Approximate average upper limit on the counting rate as a function of the expected leakage for both cut setting schemes discussed in the text. Regarding this simplified approach the timing cut should have been finalized at the values obtained for a leakage of $n_{\mathrm{tot}} = 0.3$, where the minimum was reached.

have been chosen as the final cut for the analysis. However, apart from the approximation made in (7.8), this computation only took the number of events and not the energy distributions of the signal and background into account. In particular, it also did not consider the actual limit calculation approach, which was foreseen to be applied to the final result, the optimum interval method. This procedure is quite appropriate in the case where signal and background distributions are similar, so considering elastic scattering for example, since then both are more or less exponential. Compare the predicted WIMP spectrum assuming elastic scattering and $m_W \sim 120\,\mathrm{GeV/c^2}$, shown in Fig. 7.1 (black/solid) and the (approximate) expected background spectrum shown in Fig. 7.17. In fact, the determination of the final cut for the standard analysis was based on this simple reasoning. However, focussing on the inelastic dark matter scenario the recoil spectrum is completely different peaking at tens of keV recoil energy as shown in Fig. 7.1. Thus, a better estimate of the sensitivity, taking the respective energy distributions and the correct limit-computation procedure into account, was implemented as discussed in the following paragraph.

For each given expected leakage, using only the values between 0.1 and 1.5 (in steps of 0.1), Monte Carlo simulations were run to find the average upper limit based on the optimum interval method that could be obtained, if there were no true WIMP signal. For each expected leakage, 10^5 surface-event mock data sets were generated, each with number and energies of background events chosen randomly according to the given expected leakage and the expected energy distribution. The numbers of events for each mock data set were

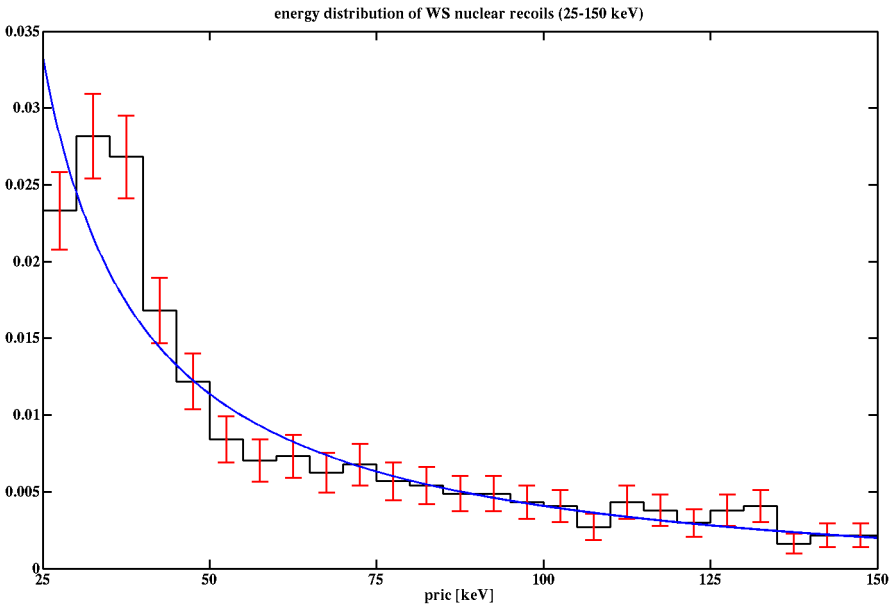

Figure 7.17: Energy distribution of WIMP-search multiple scatters within the nuclear-recoil band from all detectors and runs. From previous analyses it was known that it was very similar to the corresponding spectrum of single scatters. The blue line represents a fit to the spectrum.

obtained by simply drawing random numbers from a Poisson distribution with the corresponding mean. Energies were assigned to these events by generating uniformly distributed random numbers between 0 and 1 and subsequently inverting the cumulative distribution function of the energy distribution at these values numerically. This procedure was much faster than the acceptance-rejection method, which is the standard approach for generating random numbers from arbitrary distributions. The energy distribution of the background was estimated in two steps: Since it was known from previous analyses that the energy distributions of singles and multiples were quite similar, the distribution of WIMP-search multiple scatters within the nuclear-recoil band could be used. It is shown in Fig. 7.17 together with a fit to the spectrum. All detectors and all runs were combined because of low statistics. Note, that only runs 125–128 were included for the similar spectrum shown in Fig. 7.4. However, this was an estimate of the energy distribution of WIMP-search single scatters within the nuclear-recoil band, while, in fact, the distribution of WIMP-search surface events within the nuclear-recoil band, which additionally passed the timing cut, was needed. From previous analyses it was known that the timing cut passage fraction had only a minor energy dependence above 25 keV. Due to low statistics it had to be determined based on barium calibration data instead of WIMP-search data. Fortunately, such estimates, including corrections for the differences between both kinds of data, were already calculated and used for the setting of the timing cut: The passage fractions in the energy intervals 25–45 keV and 45–150 keV are given by the two terms in the large bracket on the right side of equation (7.2). Evaluating these terms at the respective cut positions

and calculating the exposure-weighted means over all detector/data-set categories yielded the results shown in Fig. 7.18. As expected, the passage fractions in both energy bins were quite similar. Simple linear estimates yielded negative slopes of order 10^{-5}, which nevertheless introduced a slight energy dependence. The energy distribution shown in Fig. 7.17 was multiplied by these linear functions for each tested cut. The results were renormalized to obtain estimates of the energy distributions of surface events passing the respective timing cuts. As was to be done with the actual data, a 90% C.L. upper limit on the spin-independent WIMP-nucleon cross section was calculated for each mock data set, using the optimum interval method with the WIMP recoil-energy distribution for the chosen parameters $m_W = 100\,\mathrm{GeV/c^2}$ and $\delta = 120$ keV. Thus, the timing cut efficiencies were needed for each of the corresponding cuts. They were already estimated for the timing-cut setting, too. The respective exposure-weighted timing cut efficiencies were added to the overall efficiency without the timing cut, which is shown as the red/solid curve in Fig. 7.2. Finally, the efficiencies shown in Fig. 7.19 were obtained. For all considered leakages they were significantly higher than the efficiency from the standard analysis, where the cut was fixed in the energy range of 10–100 keV, which is included in the plot for comparison. It should be noted that simple polynomial fits were used to model the energy-dependence of the timing-cut efficiencies, which should be sufficient for this sensitivity study. For the timing-cut efficiency of the cut that was eventually used, fits with more appropriate

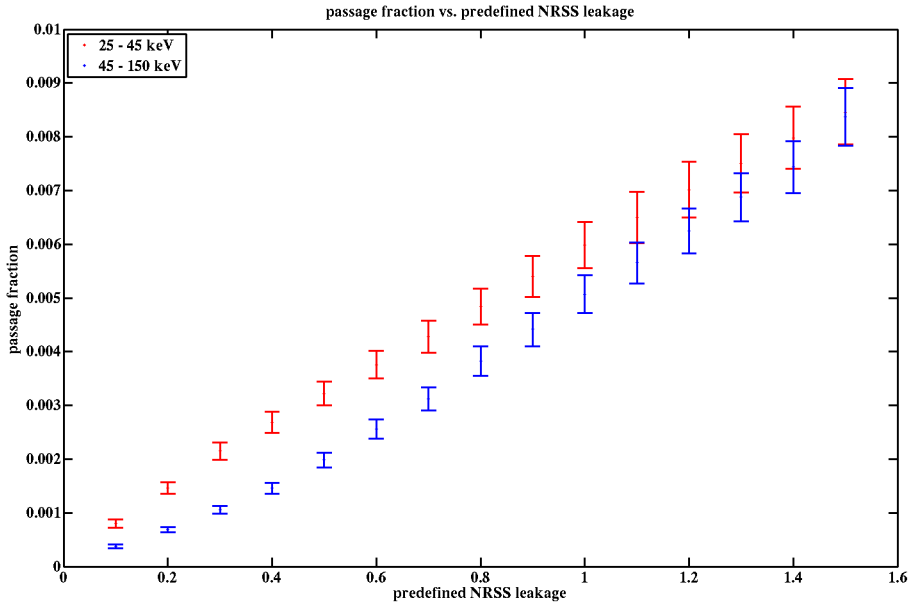

Figure 7.18: Expected timing cut passage fractions of surface events within the nuclear-recoil band from WIMP-search data for the two energy intervals used for the cut setting, as discussed in the text. The estimates were based on surface events from barium calibration data but corrected for systematic differences between calibration and WIMP-search data.

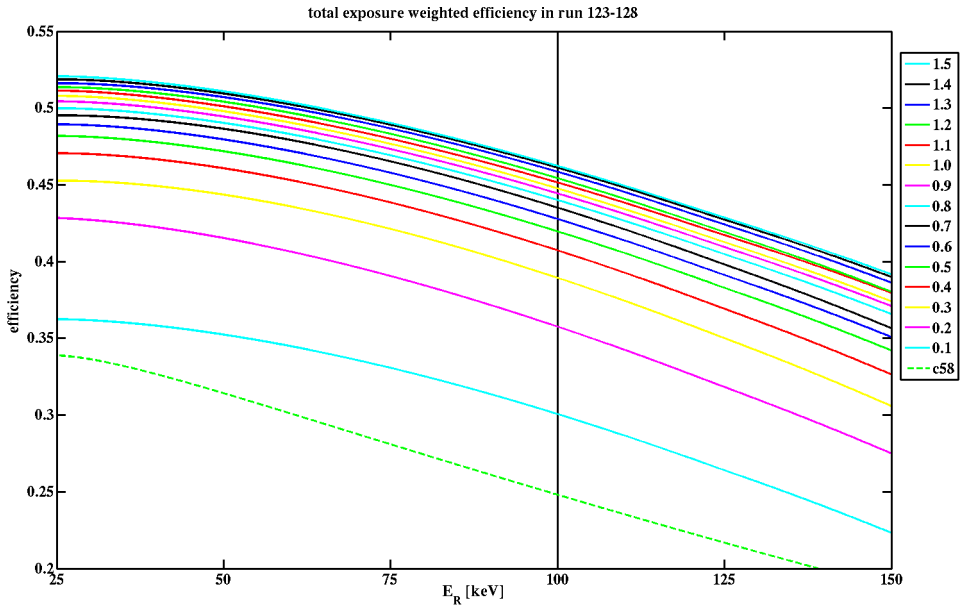

Figure 7.19: Exposure-weighted overall efficiencies for timing cuts corresponding to various considered surface event leakages between 0.1 and 1.5 events. The lines in the plot are in the same order (from top to bottom) as the numbers in the legend. The final efficiency from the standard analysis is shown for comparison (green/dashed). The vertical black line at 100 keV denotes the upper boundary of the energy range considered in that analysis.

functions were performed separately for every detector/data-set category, as discussed below. Finally, Fig. 7.20 shows the mean upper limit obtained as a function of the expected leakage used for selecting the set of timing-parameter cuts. The timing-parameter cuts were finalized at the values obtained for a fixed expected leakage of 0.6 events, where the minimum was reached. This value was twice as large as the one obtained from the simple estimate discussed before, which was just based on counting statistics.

In Fig. 7.21 the distributions of surface events from barium calibration data and nuclear recoils from californium calibration data are shown for detector T4Z5 in runs 125–128. This is the same data already used for Fig. 7.7. The upper plot shows histograms with the vertical black/dashed line marking the final timing-cut position. The bottom plot simply is a repetition of the just mentioned figure but it includes the timing cut and uses square axis, in order to emphasize the orthogonality of the cuts. All events within the yellow region pass the timing consistency and the actual timing cut.

In the process of setting the cut, the timing-cut efficiencies had already been computed for all leakages. However, they were only computed in the energy range 25–150 keV and it was decided to set the threshold to 10 keV, even though the timing cut was fixed to a leakage in the aforementioned energy interval. Moreover, simple polynomial fits were used previously. Thus, they were recalculated for all detector/data-set categories as the fraction of events from the californium calibration data within the 2σ nuclear-recoil band, which

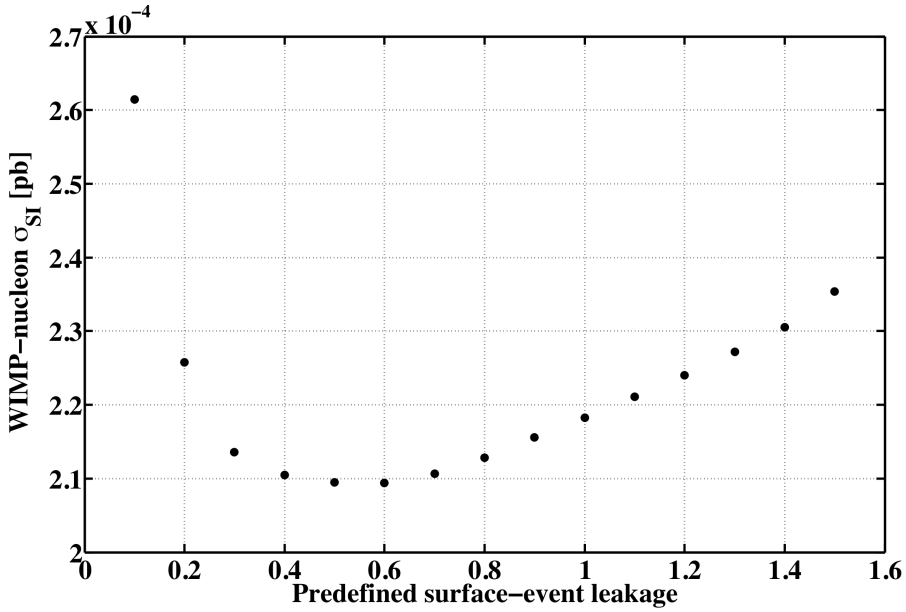

Figure 7.20: Expected sensitivity of the iDM analysis for a WIMP of mass 100 GeV/c^2 and mass splitting 120 keV for different predefined surface-event leakages at which the timing cut could be fixed. The cut corresponding to the minimum of 0.6 events was chosen as the final cut for this analysis before looking at the WIMP-search signal region.

passed the cut. As previously indicated, the timing-cut efficiencies were combined with the timing consistency-cut and manifold-cut efficiencies. The result for detector T4Z5 in runs 125–128 is shown in Fig. 7.22. The efficiencies were fitted with the function

$$f(X) = a + \frac{b}{(X-c)^d} \tag{7.10}$$

and in some rare cases with

$$f(X) = a \cdot \left(1 - \frac{b}{(X-c)^d}\right) \cdot \left(1 + e \cdot X\right). \tag{7.11}$$

Figure 7.23 compares the final efficiency from the iDM analysis, based on runs 123–128, with the efficiency from the standard analysis. In both analyses the surface-event rejection cuts had roughly the same expected leakage in the energy range the cut was defined on (10–100 keV for the standard analysis and 25–150 keV for the iDM analysis) [1]. Even though an exposure, which was larger by a factor of 1.6, was considered for the setting of the timing cut, the final efficiency increased by a factor of ∼1.5. This improvement in efficiency was possible because background at energies below where a signal was expected from iDM was neglected.

[1]Note, that the value of 0.6 leakage events, which the cut was fixed at was not considered as the final surface-event background estimate. The lengthy calculations, based on WIMP-search data leading to an improved estimate, are discussed in great detail in the next chapter.

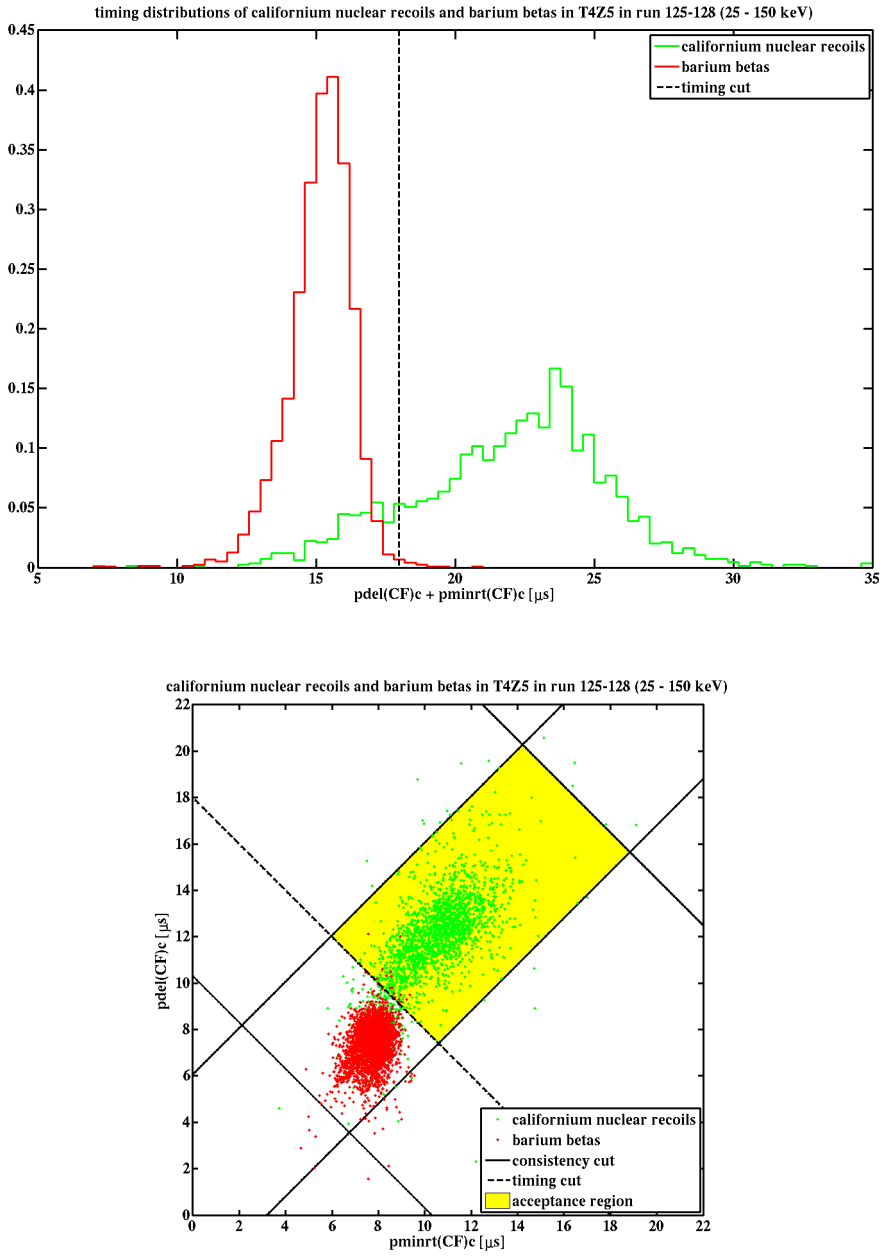

Figure 7.21: Timing parameter distributions of surface events from barium calibration data and nuclear recoils from californium calibration data for detector T4Z5 in runs 125–128. The bottom plot is a repetition of Fig. 7.7 but including the timing cut (black/dashed) and using square axis in order to emphasize the orthogonality of the cuts.

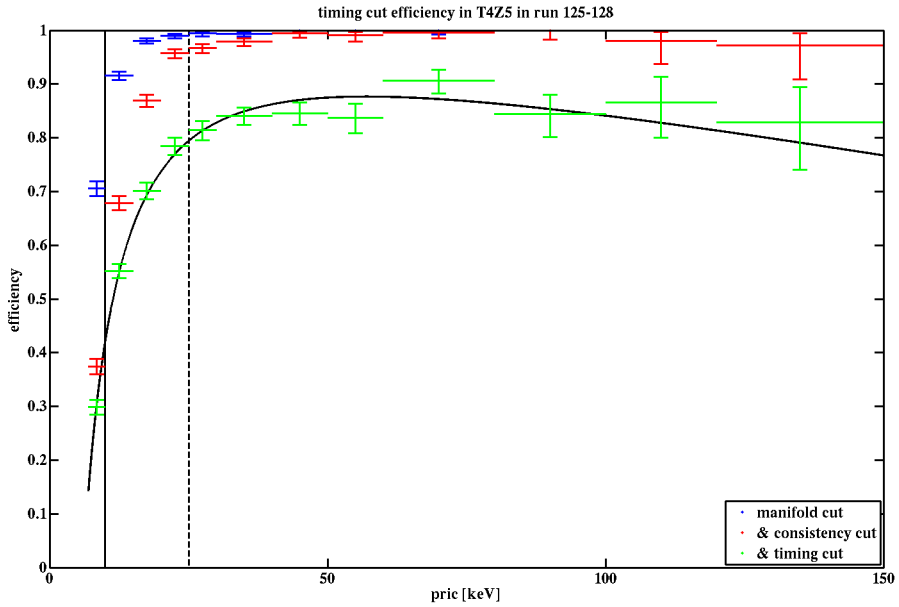

Figure 7.22: Recoil energy (pric) dependence of the efficiency of the timing cut for detector T4Z5 in runs 125–128. The cuts denoted in the legend were successively added.

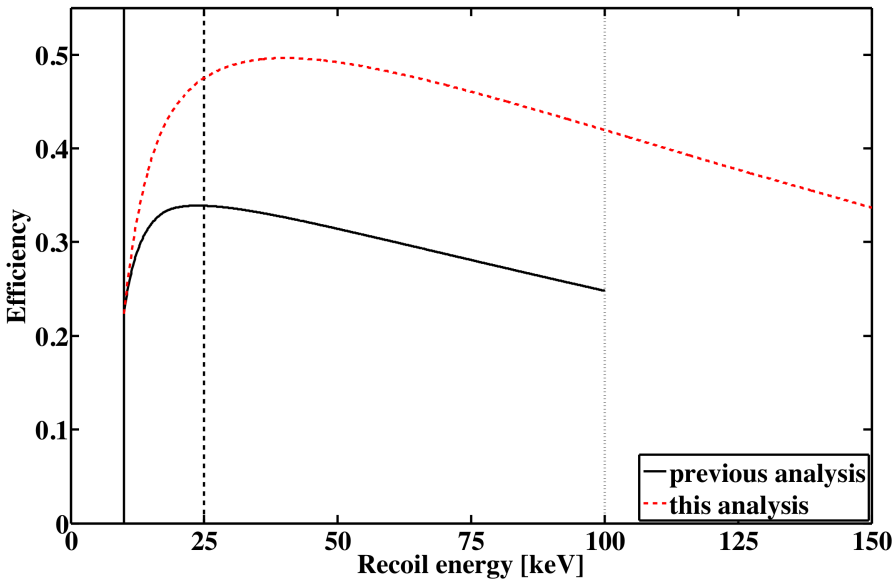

Figure 7.23: Comparison of the total exposure-weighted nuclear-recoil efficiency obtained in the iDM analysis (red/dashed) and from the standard analysis based only on runs 125–128 (black/solid). The latter is only defined up to 100 keV. Redefining the timing cut achieved an increase in efficiency by a factor of ∼1.5. As in Fig. 7.1, the vertical lines denote the analysis threshold at 10 keV, the lower boundary for the setting of the surface-event rejection cut at 25 keV and the upper analysis limit from the standard analysis at 100 keV.

7.2 Calculation of the surface-event background estimate

As explained at the beginning of the previous chapter, the leakage value chosen for optimizing cuts was not a sufficiently accurate estimate of the expected background. Thus, WIMP-search data was used to improve the estimate of the expected leakage. This was accomplished by multiplying the number of WIMP-search nuclear-recoil single scatters [2] failing the timing cut by pass-fail ratios, deduced from event samples, which were assumed to resemble the population of background events. This approach suffered from various subtleties, which are discussed in great detail in this chapter. It is very similar to the method oulined in J. P. Filippini's thesis [77]. Due to the different tagging efficiencies of single-scatter events of detectors, that were not located at the top or bottom of their towers (interior detectors), and two used detectors at the bottom of their towers (endcap detectors), it was necessary to investigate both classes of detectors separately, which is discussed in the two subsequent sections. The first one also includes a detailed description of the actual method, which is based on Bayesian reasoning.

7.2.1 Interior detectors

As mentioned in the introductory paragraph of this chapter, the total leakage was about to be estimated by multiplying the number of WIMP-search nuclear-recoil single scatters failing the timing cut by pass-fail ratios obtained from event samples, which were assumed to resemble the population of background events. The class of events with the least systematic differences to the event population of interest, which is the class of WIMP-search nuclear-recoil single scatters, is WIMP-search nuclear-recoil multiple scatters. The latter class was already used to perform preliminary tests of the timing cut, as shown in Fig. 7.14. Problems might possibly arise from different timing cut performances of singles and multiples. Thus, a naive estimate of the total predicted leakage would be

$$n_{\mathrm{tot}} = \sum_{i=1}^{12} n_i = \sum_{i=1}^{12} N_i \cdot \frac{n_i}{N_i} \approx \sum_{i=1}^{12} N_i \cdot \frac{b_i}{B_i}\,, \tag{7.12}$$

where n_i and N_i denote the numbers of nuclear-recoil single scatters passing and failing the timing cut in detector i respectively. b_i and B_i represent the corresponding numbers for multiple scatters. Regarding this formula a few annotations are appropriate. First of all, the sum goes over all 12 internal detectors with no separation into the two run categories (runs 123–124 and runs 125–128), as was done for the actual cut setting, which would render the calculations, described in the following, much more complicated. This was based on the assumption that even though the timing parameter distributions between

[2] Note, that this denotation should just indicate that the events are within the nuclear-recoil band, which, however, does not mean that they are indeed due to interactions with the target nuclei. They can also be surface events. This denotation is used for brevity throughout the chapter and its actual meaning should be kept in mind.

both run categories were different, the intrinsic background rejection capabilities were quite similar. It will turn out below that the advanced leakage estimate, emerging from the procedure described in this section, is in quite good agreement with the predefined value of 0.6 events from the cut setting, which approved confidence in the used method. Moreover, the terms for the individual detectors $N_i \cdot b_i/B_i$ are very similar to the approach proposed in the chapter regarding the cut setting given in equation (7.1). However, there are also important differences. First of all, in the previous chapter the total number of expected passing singles was multiplied by a leakage fraction, which represents a pass-total ratio. This was a useful approach, since the leakage fraction was obtained from barium calibration data. The current improved estimate was based on WIMP-search data. Since it was desirable not to use the total number of WIMP-search singles for the leakage estimate, which, to a certain extent, would violate the blinding policy, the current estimate was based on the product of the singles failing the timing cut and pass-fail ratios. Because WIMP-search data was used here, no correction similar to the one leading from equation (7.1) to equation (7.2) was necessary. Finally, it should be noted that the pass-fail ratios b_i/B_i were indeed considered to be the ratios of the actually observed numbers, while the similar leakage fractions from the cut setting procedure were obtained from the survivor functions of the corresponding timing-parameter distributions. This was possible, since the latter were based on calibration data with comparably high statistics. The number of WIMP-search events was way too small to consider reasonable estimates of their timing parameter distributions. This issue of particularly low statistics regarding the WIMP-search data rendered the background estimation extremely difficult, as discussed in the remainder of this section.

Anyway, the formula given in (7.12) is considered to be an appropriate ansatz for calculating the surface-event leakage in the interior detectors. As discussed before, systematic uncertainties could arise only from differences between the pass-fail ratios of nuclear-recoil single and multiple scatters. The simplest estimate would be to just plug the actually obtained numbers into the formula to get the leakage and assume Poisson errors (the square roots of these numbers) in order to obtain the corresponding errors via standard error propagation. However, this obvious scheme was not expected to work properly due to the very low statistics, particularly regarding the values of the multiples passing the timing cut b_i, which were very small and even 0 for some detectors. Regardless of the concatenated difficulties this was of course aspired since the leakage (of single scatters) was demanded to be very low. In order to approach this problem it is illuminating to realize that what was about to be estimated was actually the *expected* leakage. The difference between the actually observed number of events and the corresponding expectation value is clear from considering the simple Poisson distribution:

$$p(m|\mu) = \frac{\mu^m \, e^{-\mu}}{m!} \, . \tag{7.13}$$

The notation of the arguments is used to indicate that $p(m|\mu)$ is actually the conditional probability of observing m events given the expectation value μ. In that sense, each of the 36 numbers in formula (7.12) should be considered as a possible outcome of a ran-

dom experiment with random numbers drawn from 36 Poisson distributions with different, unknown expectation values. Thus, the naive estimate (7.12) should be updated to

$$\mu_{n_{\text{tot}}} \approx \sum_{i=1}^{12} \mu_{N_i} \cdot \frac{\mu_{b_i}}{\mu_{B_i}} \,. \tag{7.14}$$

Therefore, regarding the notation from (7.13), it was necessary to draw conclusions about the expectation value μ given the number of observed events m. This interchange of the meaning of the two variables can be obtained by applying Bayes' theorem:

$$p(\mu|m) = \frac{p(m|\mu)\, p(\mu)}{p(m)} = \frac{\dfrac{\mu^m\, e^{-\mu}}{m!} \cdot p(\mu)}{\displaystyle\int_0^\infty \mathrm{d}\mu\, \frac{\mu^m\, e^{-\mu}}{m!} \cdot p(\mu)} = \frac{\mu^m\, e^{-\mu}\, p(\mu)}{\displaystyle\int_0^\infty \mathrm{d}\mu\, \mu^m\, e^{-\mu}\, p(\mu)} \,, \tag{7.15}$$

where $p(m)$ merely serves as a factor ensuring proper normalization. In contrast to (7.13), which constitutes the probability distribution of m given μ, this is the probability distribution of μ given m. It is denoted the *posterior distribution* of μ. The main issue with this Bayesian approach concerns the choice of the function $p(\mu)$, which is called the *prior distribution* of the parameter μ. In principle, it should include all prior knowledge regarding μ available before performing the experiment. However, useful information about the prior is rare in many cases, so that it is difficult to specify a reasonable function. Given high statistics this is not really a problem, because in this case the factor $p(m|\mu)$, regarded as a function of μ, will be very narrowly distributed around the most likely value of μ. Thus, for any reasonable (not extremely peaked) prior $p(\mu)$ the posterior distribution will still be very narrowly distributed around the same value. In other words, the final result is not very sensitive to the choice of the prior. Unfortunately, as already mentioned numerous times, this was not the case regarding the current leakage estimate. Thus, the choice of prior was expected to have a significant impact on the outcome of the calculation, and it was necessary to find a reasonable way to deal with this arbitrariness. In particular, it was necessary to find a prior, which did not bias the result.

An appropriate way to deal with such a difficult case is to find a prior with "beneficial" properties, which depends on some parameters, that can finally be tweaked to obtain "reasonable" results. This sounds like a very ambiguous endeavour, but in fact there were certain guidelines that could be followed. At first, it was necessary to find an appropriate parameterized family of priors suitable for this leakage estimate. Given that the only ingredients were Poisson distributions the appropriate prior family was the gamma distribution:

$$p_\Gamma(\mu|a,b) = \frac{\mu^{a-1}\, e^{-\frac{\mu}{b}}}{b^a\, \Gamma(a)} \,, \tag{7.16}$$

which depends on the two parameters a and b. It was found by searching for the so-called conjugate prior of the Poisson distribution. The conjugate prior of a certain probability distribution has the useful property that the corresponding posterior distribution is of the

same family. Only the parameters of the function undergo a change. The possibility to draw random numbers from the obtained posterior distribution very fast and easily was also an important aspect regarding the choice of the prior distribution. The fact, that the gamma distribution is the conjugate prior of the Poisson distribution, can easily be shown by plugging (7.16) into (7.15):

$$p(\mu|m,a,b) = \frac{\mu^m\, e^{-\mu}\, p_\Gamma(\mu|a,b)}{\int_0^\infty \mathrm{d}\mu\, \mu^m\, e^{-\mu}\, p_\Gamma(\mu|a,b)} = \frac{\mu^{a+m-1}\, e^{-\mu(1+\frac{1}{b})}}{\left(\frac{1}{1+\frac{1}{b}}\right)^{a+m}\Gamma(a+m)} = p_\Gamma\left(\mu\middle|a+m, \frac{1}{1+\frac{1}{b}}\right) \tag{7.17}$$

Thus, the posterior of a Poisson distribution with m obtained events, regarding the gamma distribution with parameters a and b as the prior, is simply a gamma distribution with shifted parameters:

$$a \;\rightarrow\; a+m \tag{7.18}$$

$$b \;\rightarrow\; \frac{1}{1+\frac{1}{b}}\,. \tag{7.19}$$

However, it was desirable to remove one of the two parameters of the gamma distribution to simplify the following calculations. A particular simple case of the gamma distribution is given by demanding $a = c+1$, where c is just a different convenient parameter, and $b \rightarrow \infty$, since then $p_\Gamma \propto \mu^c$, which is the so-called Jaynes prior for $c = -1$. It has the property to be scale invariant, i.e. it is uniform in log-space. Together with a constant prior, which is uniform in linear space, it is one of the most commonly used choices in Bayesian statistics, if no detailed prior knowledge about the distribution of μ is available. The subsequently obtained posterior distribution is thus given by

$$p(\mu|m,c) = p_\Gamma(\mu|c+1+m,1) = \frac{\mu^{c+m}e^{-\mu}}{\Gamma(c+1+m)}\,. \tag{7.20}$$

It is illuminating to calculate the expectation value and standard deviation of this posterior distribution, since they indicate the values of c, which are most likely to yield reasonable results:

$$\mu_\mu \;=\; \int_0^\infty \mathrm{d}\mu\; \mu\, p(\mu|m,c) = \frac{\Gamma(c+m+2)}{\Gamma(c+m+1)} = c+m+1 \tag{7.21}$$

$$\sigma_\mu^2 \;=\; \mu_{\mu^2} - \mu_\mu^2 = (c+m+2)(c+m+1) - (c+m+1)^2 = c+m+1\,. \tag{7.22}$$

Obviously $c = -1$ is a very reasonable choice, since it leads to the result that the expectation value is equal to the actually observed number of events $\mu_\mu = m$. The problem of this choice is the fact that the posterior distribution cannot be normalized in the case that no events are observed, $(m = 0)$. Therefore, it seems like a valid assumption that in general c should be close to -1 but usually a little higher. In the following, values between -1 and -0.5 are considered as possible choices.

An additional difficulty regarding the evaluation of formula (7.14) is the fact, that the 36 μs do not have fixed values due to the application of the Bayesian framework. As just discussed, each of these numbers rather obeys a probability distribution as given in (7.20). Therefore, instead of just plugging fixed values into (7.14), it is rather necessary to calculate the probability distribution of $\mu_{n_{\text{tot}}}$, which is a quite complicated integral:

$$\begin{aligned} p(\mu_{n_{\text{tot}}}|N_i, b_i, B_i, c) \;\approx\; & \left(\prod_{i=1}^{12}\int_0^\infty \mathrm{d}\mu_{N_i}\, p(\mu_{N_i}|N_i, c)\right)\left(\prod_{i=1}^{12}\int_0^\infty \mathrm{d}\mu_{b_i}\, p(\mu_{b_i}|b_i, c)\right) \\ & \cdot\left(\prod_{i=1}^{12}\int_0^\infty \mathrm{d}\mu_{B_i}\, p(\mu_{B_i}|B_i, c)\right)\delta\left(\mu_{n_{\text{tot}}} - \left(\sum_{i=1}^{12}\mu_{N_i}\frac{\mu_{b_i}}{\mu_{B_i}}\right)\right) \end{aligned} \tag{7.23}$$

where δ denotes Dirac's delta distribution. It was chosen to use only one value of c for all 36 prior distributions. Thus, in the considered framework and given the numbers of observed events N_i, b_i and B_i, which are certainly fixed, the probability distribution of $\mu_{n_{\text{tot}}}$ only depends on one additional parameter. Below, it will be shown that it was possible to find an appropriate estimate for the distribution with this approach. If this method had not been successful, it would have been necessary to introduce different parameters for the different distributions. It should be noted that in this framework the 36 parameters μ_{N_i}, μ_{b_i} and μ_{B_i} can be considered as nuisance parameters, which are removed from the total background estimate by integration, since they are not of interest themselves. The parameter of interest $\mu_{n_{\text{tot}}}$ is a function of these nuisance parameters given by (7.14). In many applications, where maximum-likelihood techniques, as introduced in chapter 5.1.2, are used, the likelihood function directly depends on the parameter(s) of interest and additionally on some nuisance parameters. A case like this is discussed in great detail in the next chapter, which also includes a comparison of Bayesian and Frequentist treatments of nuisance parameters. The use of the delta function indicates that it is assumed, that (7.14) holds exactly. In principle, it would be possible to include systematic uncertainties by replacing this function e.g. by a Gaussian with a peak at (7.14) and width representing these uncertainties. A very similar approach was indeed applied and is discussed below.

The complicated formula (7.23) can be simplified by using the following decomposition of the delta distribution:

$$\begin{aligned} & \delta\left(\mu_{n_{\text{tot}}} - \left(\sum_{i=1}^{12}\mu_{N_i}\frac{\mu_{b_i}}{\mu_{B_i}}\right)\right) \\ = \;& \left(\prod_{i=1}^{12}\int_0^\infty \mathrm{d}\rho_i\,\delta\left(\rho_i - \mu_{N_i}\frac{\mu_{b_i}}{\mu_{B_i}}\right)\right)\delta\left(\mu_{n_{\text{tot}}} - \sum_{i=1}^{12}\rho_i\right) \\ = \;& \left(\prod_{i=1}^{12}\int_0^\infty \mathrm{d}r_i\,\delta\left(r_i - \frac{\mu_{b_i}}{\mu_{B_i}}\right)\right)\left(\prod_{i=1}^{12}\int_0^\infty \mathrm{d}\rho_i\,\delta\left(\rho_i - \mu_{N_i}\,r_i\right)\right)\delta\left(\mu_{n_{\text{tot}}} - \sum_{i=1}^{12}\rho_i\right), \end{aligned}$$

which yields

$$
\begin{aligned}
p(\mu_{n_{\text{tot}}}|N_i, b_i, B_i, c) \;\approx\; & \left(\prod_{i=1}^{12}\int_0^\infty \mathrm{d}\rho_i\right)\delta\left(\mu_{n_{\text{tot}}} - \sum_{i=1}^{12}\rho_i\right)\left(\prod_{i=1}^{12}\int_0^\infty \mathrm{d}r_i\right) \\
& \cdot\left(\prod_{i=1}^{12}\int_0^\infty \mathrm{d}\mu_{N_i}\, p(\mu_{N_i}|N_i, c)\,\delta\big(\rho_i - \mu_{N_i}\, r_i\big)\right) \\
& \cdot\left(\prod_{i=1}^{12}\int_0^\infty \mathrm{d}\mu_{b_i}\int_0^\infty \mathrm{d}\mu_{B_i}\, p(\mu_{b_i}|b_i, c)\, p(\mu_{B_i}|B_i, c)\,\delta\left(r_i - \frac{\mu_{b_i}}{\mu_{B_i}}\right)\right),
\end{aligned}
$$

after rearrangement of some terms. The integrals in the second and third line can be easily evaluated:

$$
\begin{aligned}
p(\mu_{n_{\text{tot}}}|N_i, b_i, B_i, c) \;\approx\; & \left(\prod_{i=1}^{12}\int_0^\infty \mathrm{d}\rho_i\right)\delta\left(\mu_{n_{\text{tot}}} - \sum_{i=1}^{12}\rho_i\right)\left(\prod_{i=1}^{12}\int_0^\infty \mathrm{d}r_i\right) \\
& \cdot\left(\prod_{i=1}^{12}\frac{1}{r_i}\frac{\left(\frac{\rho_i}{r_i}\right)^{N_i+c} e^{-\frac{\rho_i}{r_i}}}{\Gamma(N_i+c+1)}\right) \\
& \cdot\left(\prod_{i=1}^{12}\frac{\Gamma(b_i+B_i+2c+2)}{\Gamma(b_i+c+1)\Gamma(B_i+c+1)}\frac{r_i^{b_i+c}}{(1+r_i)^{b_i+B_i+2c+1}}\right) \\
= \;& \left(\prod_{i=1}^{12}\frac{\Gamma(b_i+B_i+2c+2)}{\Gamma(N_i+c+1)\Gamma(b_i+c+1)\Gamma(B_i+c+1)}\int_0^\infty \mathrm{d}\rho_i\,\rho_i^{N_i+c}\right) \\
& \cdot\left(\prod_{i=1}^{12}\int_0^\infty \mathrm{d}r_i\frac{r_i^{b_i-N_i-1}\, e^{-\frac{\rho_i}{r_i}}}{(1+r_i)^{b_i+B_i+2c+1}}\right)\delta\left(\mu_{n_{\text{tot}}} - \sum_{i=1}^{12}\rho_i\right).
\end{aligned}
$$

Unfortunately, it is not possible do perform the r_i-integration analytically. Moreover, since $b_i = 0$ on many detectors, the integrand has a singularity at its lower boundary $r_i = 0$. In order to perform the integration numerically it was much more convenient to go back to (7.23) and use a simple Monte Carlo approach.

This Monte Carlo method works as follows: Draw a large amount (e.g. 10^6) of randomly generated numbers from each of the 36 distributions, corresponding to the observed events N_i, b_i and B_i for a chosen value of c. This was a very simple and fast calculation, since all of these distributions were gamma distributions, each having different parameters. Subsequently, use these numbers to calculate $\mu_{n_{\text{tot}}}$ by evaluating (7.14) for each trial. The histogram of the results represents the distribution of $\mu_{n_{\text{tot}}}$. It was decided to use its median as the leakage estimate and the quantiles at 15.87% and 84.13% as the boundaries of the 68.27% (1σ) credibility interval. The results are shown in Fig. 7.24 for a few representative values of the parameter c given in the legend. As expected, the dependence of its actual value is striking due to the low statistics.

Regarding this particular estimate, the final problem was the determination of an accurate value for the parameter c. First, it was desirable to have an unbiased leakage

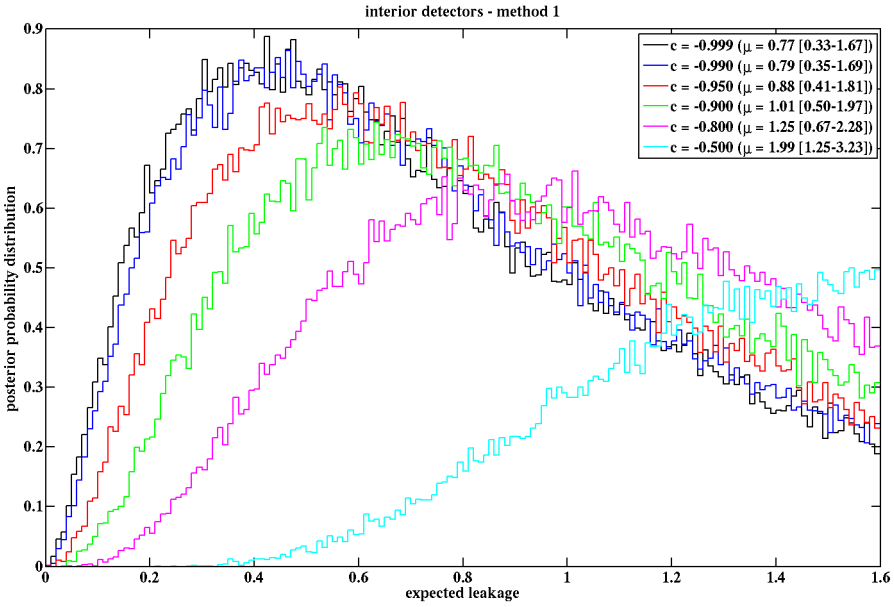

Figure 7.24: Probability distributions of the expected leakage for various values of the parameter c, using WIMP-search multiple scatters within the nuclear-recoil band to determine the pass-fail ratios for the timing cut. The shown result is for the combination of all 12 used interior detectors. The final leakage estimates, given by the medians of the distributions, and the corresponding credibility intervals are given in the legend for each tested value of c. See text for details.

estimator. Moreover, proper coverage of the applied method was an important feature. Extensive Monte Carlo simulations were performed to check both of these prerequisites and determine an optimal value for c. At first, representative values for all 36 numbers μ_{N_i}, μ_{b_i} and μ_{B_i} entering the leakage estimate (7.14) were chosen by hand. As indicated by the notation, they should represent the true expectation values rather than the actual numbers, as obtained from the experimental data. In order to check the adequate performance of the algorithm, it was important to use values, which were close to the measured values, but some variation was mandatory. To account for possible fluctuations, four different scenarios were considered:

1. All detectors were assumed to be identical, and therefore all three kinds of parameters μ_{N_i}, μ_{b_i} and μ_{B_i} were set to the mean observed values of N_i, b_i and B_i respectively, yielding a total leakage of 0.45.

2. All detectors were assumed to be identical. The mean values of N_i and B_i were used for the numbers of failing singles μ_{N_i} and failing multiples μ_{B_i}, but the expectation value for the number of passing multiples μ_{b_i} was scaled to give an overall leakage of 0.6.

3. Same as before, but here the number of passing multiples μ_{b_i} was scaled to give an

overall leakage of 1.0.

4. All numbers of passing multiples were set to 0 except for one detector. On this detector the number of passing multiples was scaled to give the total leakage, using mean values for all numbers, so 0.45, as given in the context of the first case. This possibility represented a rather extreme, less likely case.

Subsequently, 20000 mock data sets were generated for each of the four cases by drawing random numbers from Poisson distributions with the given respective expectation values. In the next step, the leakage estimates and credibility intervals were calculated for various values of c. For each scenario, the bias was defined as the mean difference between the 20000 estimated values of $\mu_{n_{\mathrm{tot}}}$ and the given value, e.g. 0.45 for the first case. The coverage was defined as the fraction of mock data sets, for which the given value resided within the constructed credibility interval. The results are shown in Fig. 7.25. It was decided to use $c = -0.97$, since this value minimized the bias. As expected, the most appropriate value was slightly higher than -1. Given the deviations of the bias, a systematic error of 0.02 on the leakage was adopted. The coverage at $c = -0.97$ was quite close to the nominal value of 68.27% for all four cases, which indicated a satisfactory performance of the algorithm.

Apart from the systematic uncertainty arising from the choice of the parameter c, fully determining the used prior distributions, additional systematic uncertainties were due to possible differences regarding the pass-fail ratios of nuclear-recoil single and multiple scatters. In order to estimate this uncertainty, the ratio of the pass-fail ratio of singles to the pass-fail ratio of multiples within the beta region but outside the nuclear-recoil band was calculated. Events within the nuclear-recoil band had to be omitted, since the singles constituted a possible signal. An illustration of this region is shown in Fig 5.10. Due to the low numbers of events passing the timing cut, it was necessary to directly sum over all interior detectors:

$$r = \frac{\left(\sum_{i=1}^{12} \mu_{s_i}\right) / \left(\sum_{i=1}^{12} \mu_{S_i}\right)}{\left(\sum_{i=1}^{12} \mu_{m_i}\right) / \left(\sum_{i=1}^{12} \mu_{M_i}\right)} \,. \tag{7.24}$$

s_i and S_i denote the single scatters in the aforementioned region, which pass and fail the timing cut respectively. m_i and M_i represent the corresponding numbers regarding multiples. This ratio was estimated in the same way as the leakage itself. Results for various values of the prior exponent c are shown in Fig. 7.26. It can be observed that the dependence on c is rather weak. Considering that the main concern was about upward fluctuations and that the intervals, given in the legend, were for once set at 90% C.L., a systematic error of 10% was certainly a conservative estimate.

To sum up, it was decided to use a prior exponent of $c = -0.97$. Statistical errors, related to the low number of observed events, were intrinsically included in the Monte Carlo approach. Additional systematic errors of 0.02 from the choice of the prior parameter c and 10% from possible differences of the timing cut passage fractions of singles and multiples

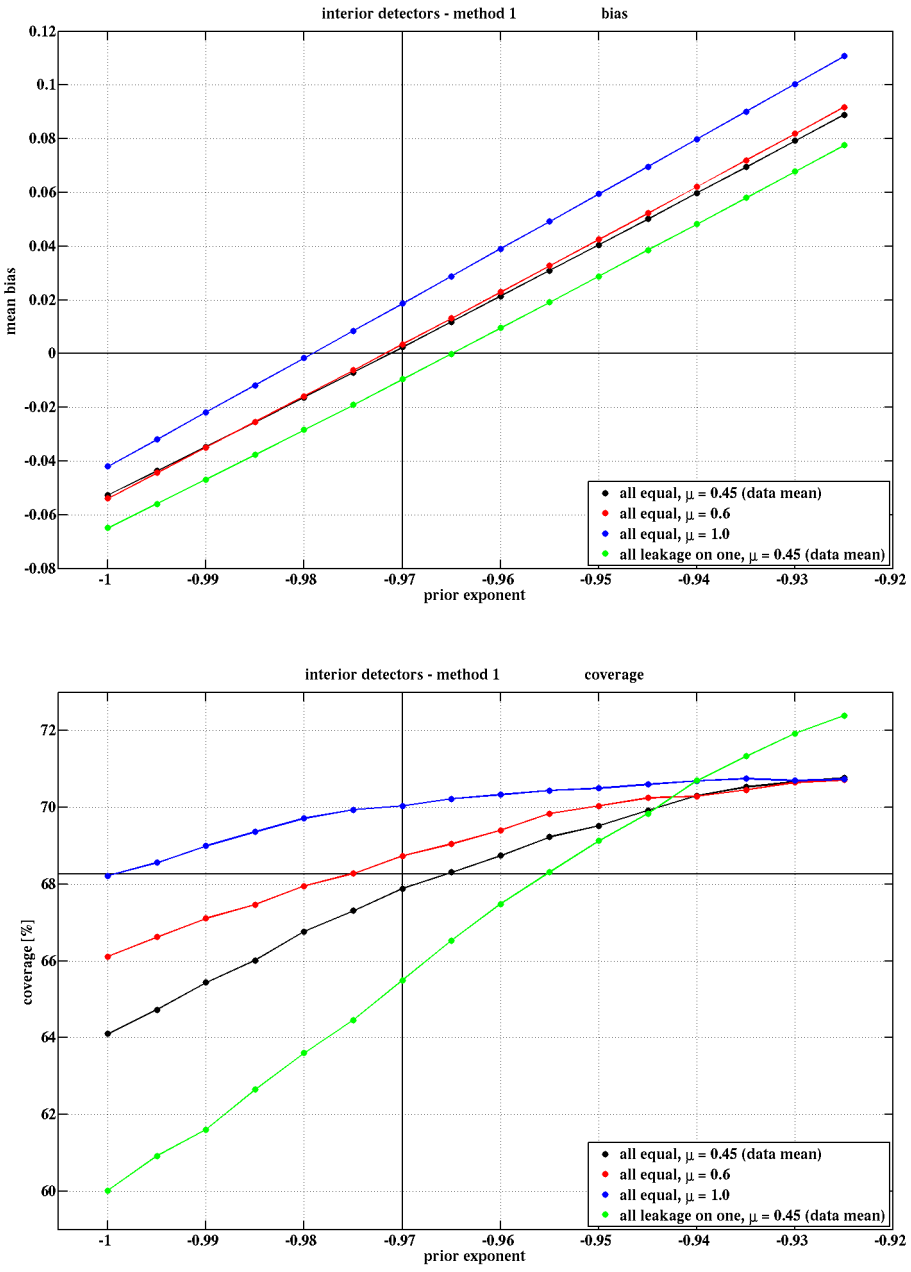

Figure 7.25: Bias (top) and coverage (bottom) of the algorithm for calculating the total leakage of the interior detectors, using WIMP-search multiple scatters within the nuclear-recoil band to determine the pass-fail ratios for the timing cut, as a function of the parameter c. The four tested scenarios are described in the text. The final choice of $c = -0.97$, which minimized the bias, is indicated by the vertical black line. A systematic error of 0.02 was assigned to the leakage estimate.

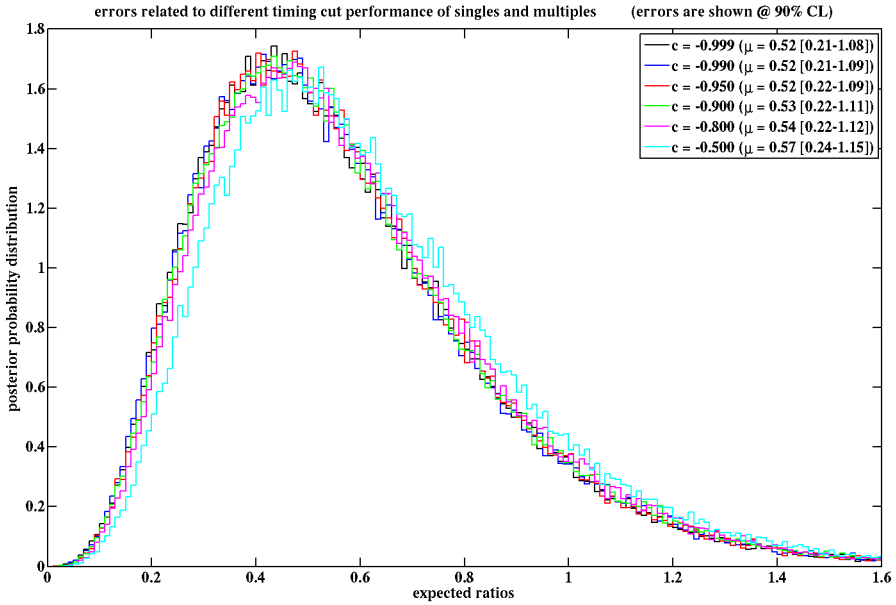

Figure 7.26: Ratio of the pass-fail ratio of singles to the pass-fail ratio of multiples within the beta region but outside the nuclear-recoil band. The intervals given in the legend represent 90% C.L. The dependence on the parameter c is extremely weak. A systematic error of 10% was assigned to the ratio.

had to be included in the final estimate. The systematic errors were included in the Monte Carlo simulation by adding two random numbers from Gaussian distributions with widths corresponding to the aforementioned errors to each of the 10^6 trials. To be more specific

$$\mu_{n_{\mathrm{tot}}}^{\mathrm{syst.}} = \mu_{n_{\mathrm{tot}}} + 0.1\,\overline{\mu}_{n_{\mathrm{tot}}}\,R_1 + 0.02\,R_2 \tag{7.25}$$

was calculated, where $\mu_{n_{\mathrm{tot}}}$ denotes the 10^6 values obtained directly from the Monte Carlo, so considering only statistical errors, and $\overline{\mu}_{n_{\mathrm{tot}}}$ the corresponding median, which would represent the leakage estimate, if systematic uncertainties were neglected. R_1 and R_2 represent 10^6-tupel of random numbers drawn from the standard Gaussian distribution with mean 0 and standard deviation 1. Unphysical negative values were avoided by "throwing the dice" again for all values that were negative, which was equal to a cutoff at zero and a reweighting in the allowed positive physical range. However, the exact treatment was not of great concern. A few different approaches were tested, for example including the unphysical negative values or just setting them to zero. In each case the change of the final leakage estimate was much smaller than the systematic errors, which were already included. The results are shown in Fig. 7.27, where the red curve represents the distribution without systematic errors (the histogram of $\mu_{n_{\mathrm{tot}}}$), while the blue curve represents the distribution including systematic uncertainties (the histogram of $\mu_{n_{\mathrm{tot}}}^{\mathrm{syst.}}$). Inclusion of the systematic uncertainties led to a slightly wider distribution corresponding to replacing the delta function in (7.23) by a wider distribution as mentioned before. Nevertheless, it is obvious that

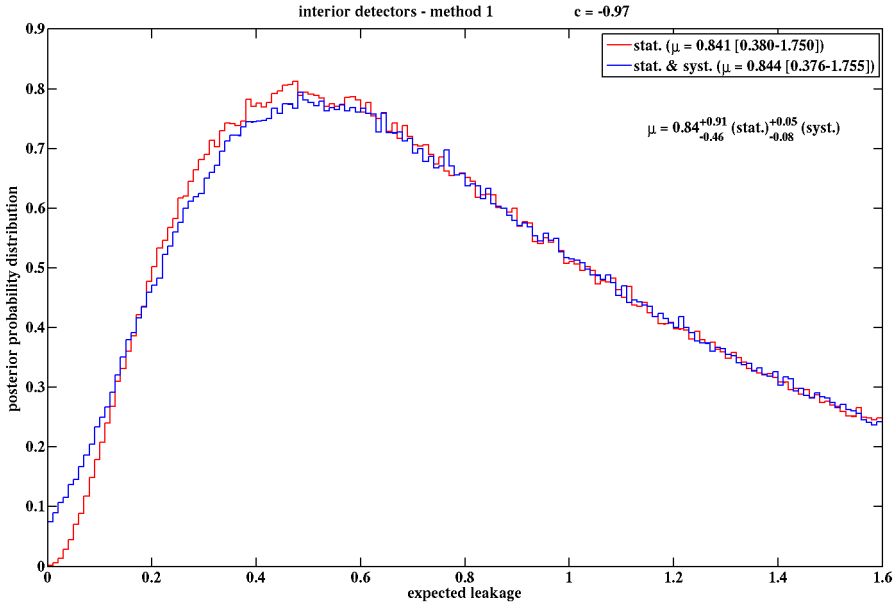

Figure 7.27: Final probability distribution of the expected leakage, using WIMP-search multiple scatters within the nuclear-recoil band to determine the pass-fail ratios for the timing cut. The shown result is for the combination of all 12 used interior detectors. The distribution shown in red represents the result including only statistical uncertainties, while systematic uncertainties were included for the distribution shown in blue. The final leakage estimate, given by the median of the distribution, and the corresponding credibility interval are given below the legend.

the statistical uncertainties dominate the width of the final distribution as expected. The obtained leakage is given below the legend. The systematic errors alone were obtained by taking the errors from the distributions including systematic errors and subtracting the errors from the distributions including just statistical errors in quadrature. Due to the fact that the statistical uncertainties led to a very wide distribution, it was desirable to base the used pass-fail ratios on another kind of event population than multiple scatters within the nuclear-recoil band, which has higher statistics. Since no other population has more similar properties than single scatters within the nuclear-recoil band, any other class of events was expected to have larger systematic errors. Therefore, it seems advantageous to finally combine both estimates. This procedure is discussed in the remainder of this section.

The next, most appropriate population to estimate the pass-fail ratios were multiple scatters within the beta region but outside the nuclear-recoil region. These events were already used before to study systematic differences in timing-cut performance between singles and multiples. The calculations were performed in a very similar way as before,

only replacing formula (7.14) with

$$\mu_{n_{\text{tot}}} \approx \alpha \sum_{i=1}^{12} \mu_{N_i} \cdot \frac{\mu_{m_i}}{\mu_{M_i}} \,, \tag{7.26}$$

where an explicit correction factor, given by

$$\alpha = \frac{\left(\sum_{i=1}^{12} \mu^*_{b_i}\right) / \left(\sum_{i=1}^{12} \mu^*_{B_i}\right)}{\left(\sum_{i=1}^{12} \mu^*_{m_i}\right) / \left(\sum_{i=1}^{12} \mu^*_{M_i}\right)} \,, \tag{7.27}$$

was introduced to correct for systematic differences in timing-cut performance of multiple scatters within and outside the nuclear-recoil band. As before, m_i and M_i denote the multiple scatters in the aforementioned region, which pass and fail the timing cut respectively, while b_i and B_i represent the corresponding numbers regarding multiples within the nuclear-recoil band. As for the study of systematic differences between singles and multiples, the statistics of all interior detectors were combined to calculate the correction factor α. Additionally, a slightly looser version of the timing cut, the cut set to 1.0 rather than 0.6 leakage events, was used in order to increase statistics, which is indicated by adding the index *. The results of the calculations are shown in Fig. 7.28 for various values of the parameter c as given in the legend. It can be observed that the dependence on its actual value is much less significant than regarding the previously studied case shown in Fig. 7.24, where the pass-fail ratios were calculated based on multiples within the nuclear-recoil band. This was expected, since only in the case of very low statistics the final result should depend significantly on the prior.

As in the previous case, extensive Monte Carlo studies were performed to investigate the bias and coverage as a function of the parameter c. The same four scenarios as before, given on page 172, were considered. Note, however, that the total leakage obtained using formula (7.26) yielded 0.43 instead of 0.45 for scenarios 1 and 4. The results are shown in Fig. 7.29. It was decided to use a value of $c = -0.885$ with a systematic error of 0.02 on the total leakage. It can be observed that the coverage seems to be systematically too low. However, since this was only a $\sim$2% effect, neglecting the rather artificial method where all leakage is lumped onto one detector, it should not be of too much concern.

Some effort was made in order to estimate the systematic uncertainties of the correction factor α. Systematic errors could arise from using a slightly looser version of the timing cut and from summing over all detectors to calculate an average value. At first, it was verified that usage of the standard timing cut, set to 0.6 leakage events, in the definition of α had almost no impact on the best estimate (the median of the distribution, the width certainly increased due to decreased statistics), indicating that usage of the loosened timing cut introduced only small systematic errors, which could be safely neglected. Computing a posterior distribution for all detectors separately led to very large variations between them.

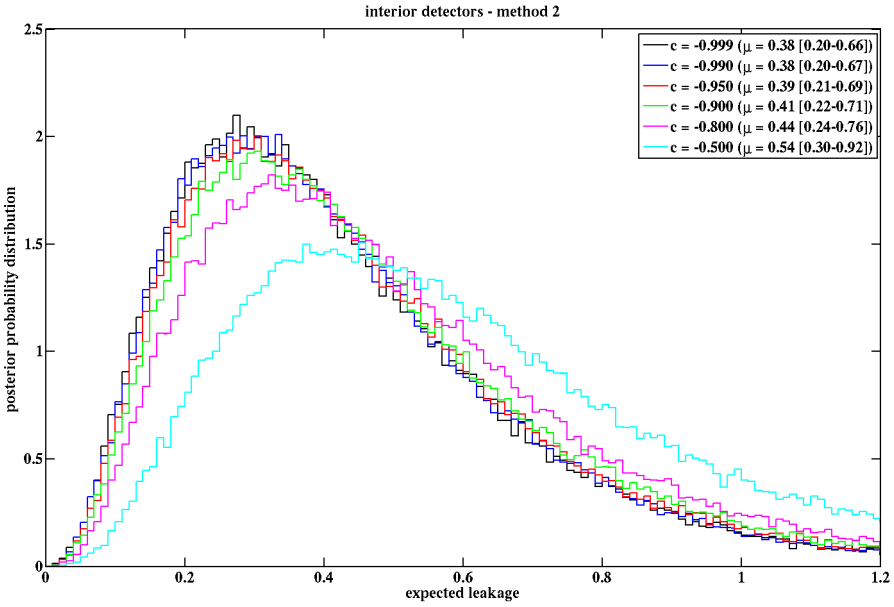

Figure 7.28: Probability distributions of the expected leakage for various values of the parameter c, using WIMP-search multiple scatters within the beta region but outside the nuclear-recoil band to determine the pass-fail ratios for the timing cut. The shown result is for the combination of all 12 used interior detectors. The final leakage estimate, given by the median of the distribution, and the corresponding credibility interval are given in the legend for each tested value of c. See text for details.

This implied that statistics on only one single detector were much too low to compute a reliable estimate. Thus, there was no real handle to characterize the systematic differences between detectors. Lacking a more appropriate approach, large systematic errors, equal in size to the mean statistical errors, regarding upward and downward fluctuations, and assuming a Gaussian distribution, reweighted to omit negative values, were assigned. The results for $c = -0.885$ are shown in Fig. 7.30. The comparably low value of the best estimate, given below the legend, indicates that the passage fraction of multiples within the beta region but outside the nuclear-recoil band is significantly higher than the passage fraction of multiples within the nuclear-recoil band. It should be noted that the dependence on the prior exponent c was very weak.

In summary, a prior exponent of $c = -0.885$ was used. Statistical errors were intrinsically included in the Monte Carlo approach. Three kinds of systematic errors were included for this leakage estimate. Those were the error of 0.02 related to the choice of prior exponent c, the same 10% uncertainty from possible differences of the timing cut passage fraction of singles and multiples already included for the approach discussed previously and the systematic error on the correction factor α. The result calculated in a similar way, as discussed for the previous method, is shown in Fig. 7.31. As expected, including systematic errors has a bigger effect in this case than in the previous method (see Fig. 7.27),

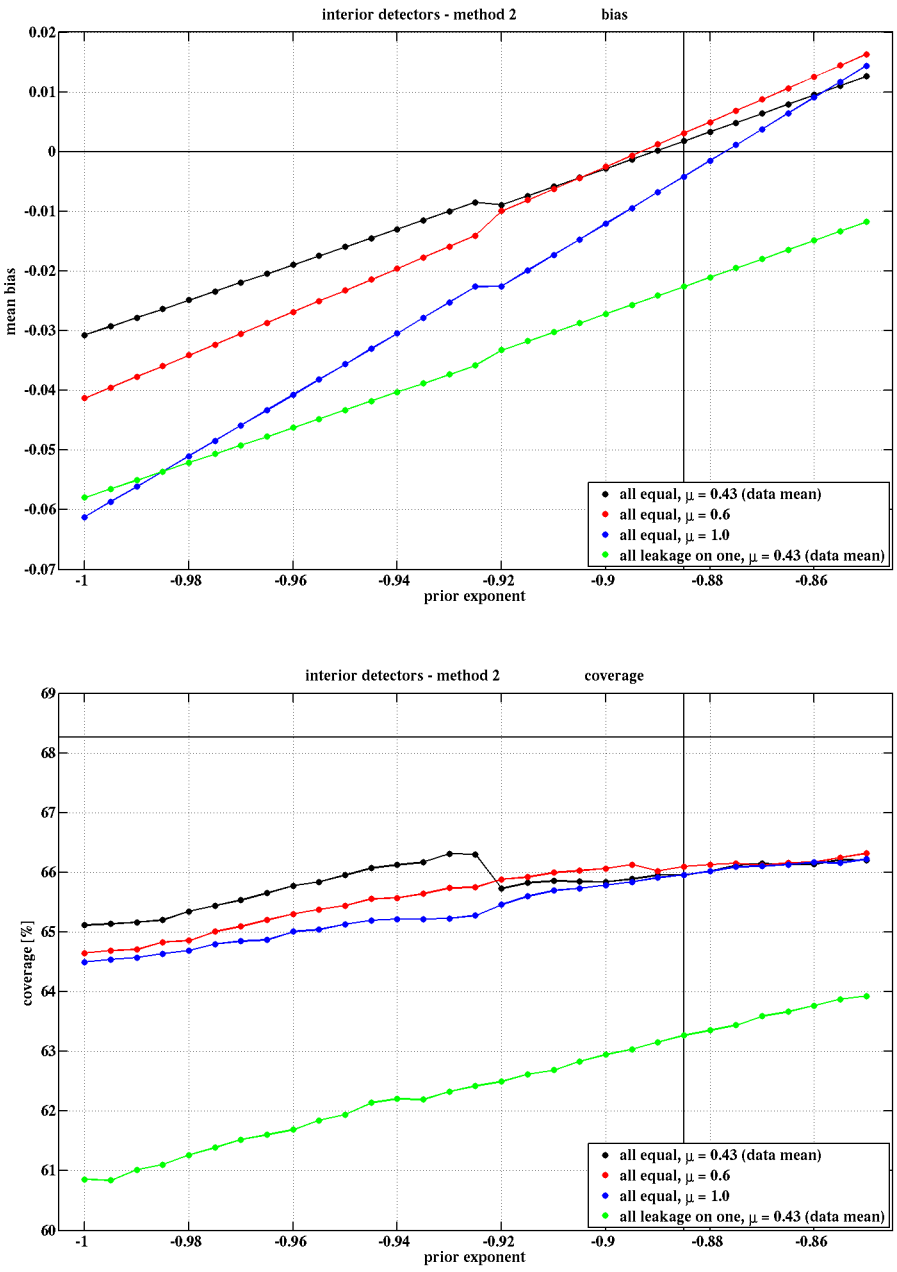

Figure 7.29: Bias (top) and coverage (bottom) of the algorithm for calculating the total leakage of the interior detectors, using WIMP-search multiple scatters within the beta region but outside the nuclear-recoil band to determine the pass-fail ratios for the timing cut, as a function of the parameter c. The four tested scenarios are described in the text. The final choice of $c = -0.885$, which minimizes the bias, is indicated by the vertical black line. A systematic error of 0.02 was assigned to the leakage estimate.

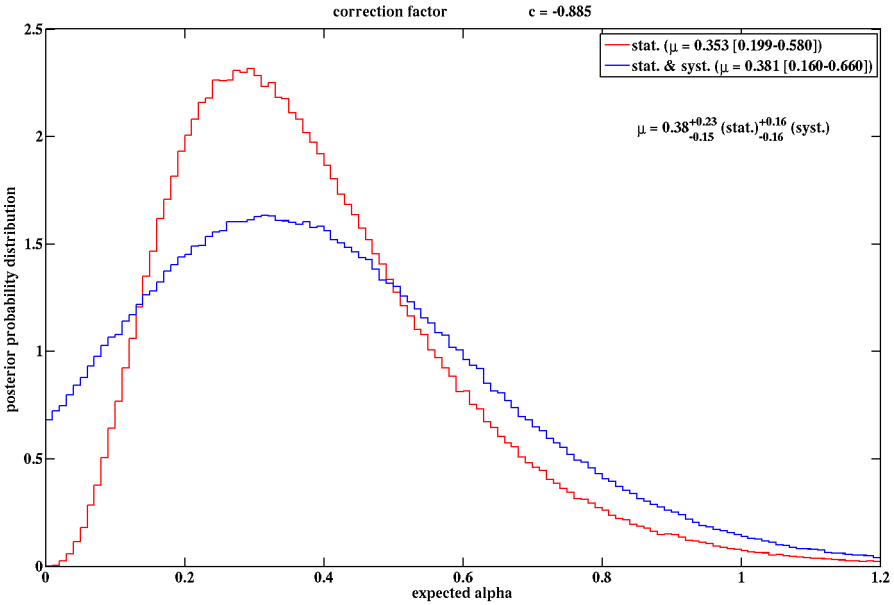

Figure 7.30: Distribution of the factor α used to correct for systematic differences of the timing-cut performance of multiple scatters within and outside the nuclear-recoil band. Results with (blue) and without (red) inclusion of systematic errors are shown. The parameter c was fixed at the value, which minimized the bias of the leakage estimate. The values given below the legend denote the expectation value of α and the corresponding errors.

simply because a third systematic error had to be introduced, since multiples outside the nuclear-recoil band were used to estimate the pass-fail ratios. The advantage of the second method was higher statistics and therefore significantly smaller statistical errors.

The final step regarding the leakage estimate for the interior detectors was the combination of the two discussed estimates. The most elegant way to do this would certainly be the usage of the posterior distribution of one of these estimates as the prior distribution of the other estimate. However, this would be very difficult to achieve, since, as previously discussed, only the individual gamma distributions constituting the distribution of the total leakage could be handled appropriately. Therefore, a different approach was applied. For its discussion, it is appropriate to combine in two lists all numbers and all corresponding expectation values, entering the calculation of the leakage estimate. Regarding the first discussed method, these two lists, denoted $\underline{k}_1$ (N_i, b_i, B_i) and $\underline{\nu}_1$ (μ_{N_i}, μ_{b_i}, μ_{B_i}) respectively, would contain 36 values each. Thus, the corresponding leakage estimate given in (7.23) can be written as:

$$p_1(\mu_{n_{\mathrm{tot}}}|\underline{k}_1, c_1) \approx \int_0^\infty \mathrm{d}\underline{\nu}_1\, p(\underline{\nu}_1|\underline{k}_1, c_1)\, \delta\big(\mu_{n_{\mathrm{tot}}} - f_1(\underline{\nu}_1)\big)\,, \tag{7.28}$$

where the distribution $p(\underline{\nu}_1|\underline{k}_1, c_1)$ represents the product of the individual posterior distributions, since they were uncorrelated. Besides, the integral is meant to go over all 36

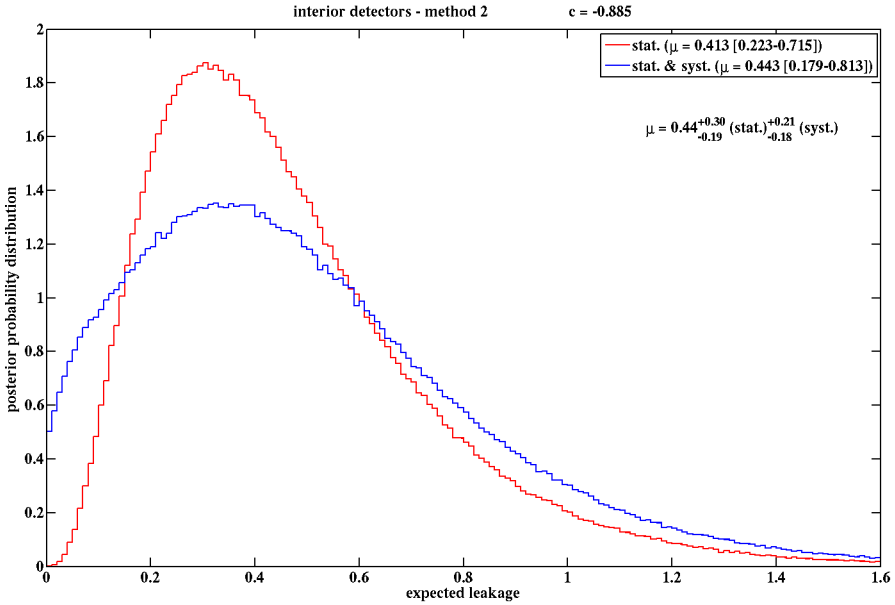

Figure 7.31: Final probability distribution of the expected leakage, using WIMP-search multiple scatters within the beta region but outside the nuclear-recoil band to determine the pass-fail ratios for the timing cut. The shown result is for the combination of all 12 used interior detectors. The distribution shown in red represents the result including only statistical uncertainties, while systematic uncertainties were included for the distribution shown in blue. The final leakage estimate, given by the median of the distribution, and the corresponding credibility interval are given below the legend.

dimensions of $\underline{\nu}_1$ and $f_1(\underline{\nu}_1)$ denotes formula (7.14). A formula of the same kind holds for the second method. Assuming that both methods were uncorrelated, a combined estimate would be given by:

$$\begin{aligned} p_{12}(\mu_{n_{\text{tot}}}|\underline{k}_1, \underline{k}_2, c_1, c_2) &\approx \int_0^\infty \mathrm{d}\underline{\nu}_1 \int_0^\infty \mathrm{d}\underline{\nu}_2 \; p(\underline{\nu}_1|\underline{k}_1, c_1)\, p(\underline{\nu}_2|\underline{k}_2, c_2) \\ &\quad \cdot\delta\big(\mu_{n_{\text{tot}}} - f_1(\underline{\nu}_1)\big)\delta\big(\mu_{n_{\text{tot}}} - f_2(\underline{\nu}_2)\big) \\ &= p_1(\mu_{n_{\text{tot}}}|\underline{k}_1, c_1) \cdot p_2(\mu_{n_{\text{tot}}}|\underline{k}_2, c_2)\,, \end{aligned} \tag{7.29}$$

where the integrals could be simply factorized into two parts corresponding to the respective methods. In short, for uncorrelated methods a combined estimate is obtained by multiplying both distributions as anticipated. However, both approaches depend on the 12 numbers of single scatters within the nuclear-recoil band failing the timing cut N_i, which prevents a simple multiplication of the distributions. Denoting the corresponding measured values and expectation values $\underline{k}_{12}$ and $\underline{\nu}_{12}$ respectively, while keeping the notations of the

remaining variables unchanged, yields:

$$
\begin{aligned}
p_{12}(\mu_{n_{\text{tot}}}|\underline{k}_1,\underline{k}_2,c_1,c_2,c_{12}) \;\approx\; & \int_0^\infty \mathrm{d}\underline{\nu}_1 \int_0^\infty \mathrm{d}\underline{\nu}_2 \int_0^\infty \mathrm{d}\underline{\nu}_{12}\, p(\underline{\nu}_1|\underline{k}_1,c_1)p(\underline{\nu}_2|\underline{k}_2,c_2)p(\underline{\nu}_{12}|\underline{k}_{12},c_{12}) \\
& \cdot\delta\big(\mu_{n_{\text{tot}}} - f_1(\underline{\nu}_1,\underline{\nu}_{12})\big)\delta\big(\mu_{n_{\text{tot}}} - f_2(\underline{\nu}_2,\underline{\nu}_{12})\big) \\
= \; & \int_0^\infty \mathrm{d}\underline{\nu}_{12}\, p(\underline{\nu}_{12}|\underline{k}_{12},c_{12}) \\
& \cdot\left(\int_0^\infty \mathrm{d}\underline{\nu}_1\, p(\underline{\nu}_1|\underline{k}_1,c_1)\,\delta\big(\mu_{n_{\text{tot}}} - f_1(\underline{\nu}_1,\underline{\nu}_{12})\big)\right) \\
& \cdot\left(\int_0^\infty \mathrm{d}\underline{\nu}_2\, p(\underline{\nu}_2|\underline{k}_2,c_2)\,\delta\big(\mu_{n_{\text{tot}}} - f_2(\underline{\nu}_2,\underline{\nu}_{12})\big)\right)
\end{aligned}
\tag{7.30}
$$

From Fig. 7.24 and Fig. 7.28 it can be observed that the result from the first method significantly depended on the value of the prior exponent, while the result from the second method was much more robust. Therefore, it was decided to simply set the prior exponent of the variables contained in both approaches to $c_{12} = c_1$. Equation (7.30) can be evaluated with a Monte Carlo approach, which, however, is more involved than for the individual methods. Draw a large number (e.g. 10^6) of randomly generated numbers from the distributions corresponding to the 12 correlating variables $\underline{\nu}_{12}$. For each of these trials, the distributions of the leakage can be separately calculated for both methods as before. They can subsequently be multiplied and normalized to get the combined estimate. This step corresponds to performing the two integrations over $\underline{\nu}_1$ and $\underline{\nu}_2$ and multiplying the results. Note, that the simple multiplication is only possible for fixed values of the correlating variables. In the second step, the integral over $\underline{\nu}_{12}$ is evaluated, which simply amounts to summing over the joint distributions, obtained for each trial, and dividing by the number of trials. It is important to include all systematic errors in the calculations of the individual methods *before* combining them. As an annotation, values for the variables $\underline{\nu}_1$ and $\underline{\nu}_2$ were generated via Monte Carlo only once and they were subsequently used for all trials of $\underline{\nu}_{12}$ to speed up the calculation. For a large number of generated events (e.g. 10^6) the whole distribution is sampled with a very high accuracy. The result of this calculation can be found in Fig 7.32. It can be observed that the distribution from the second method dominates the final result, due to the fact that the first method had much lower statistics and, correspondingly, a much wider distribution.

7.2.2 Endcap detectors

As mentioned before, two detectors at the bottom of their respective towers were included in the WIMP-search analysis. In this case, the surface events on the top (internal) and bottom (external) sides had to be treated separately, since tagging of multiple scatters was not possible for events on the external sides. The corresponding formula was given by

$$
\mu_{n_{\text{tot}}} \approx \sum_{i=1}^{2} \mu_{N_i} \cdot \left(\Phi\,\frac{\mu_{b_i^p}}{\mu_{B_i^p}} + (1-\Phi)\,\frac{\alpha^q}{1-\phi}\,\frac{\mu_{s_i}}{\mu_{S_i}}\right), \tag{7.31}
$$

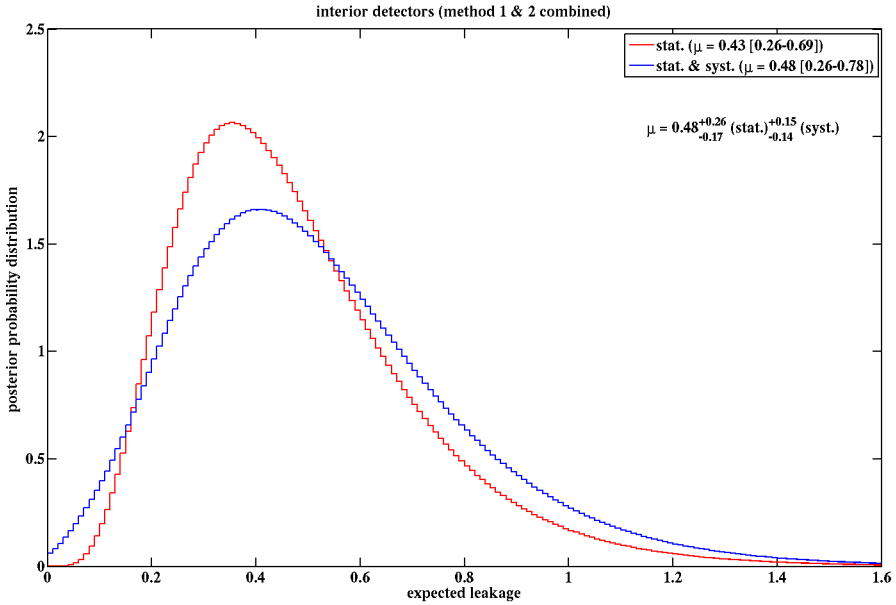

Figure 7.32: Final probability distribution of the expected leakage for the 12 used interior detectors. The distribution shown in red represents the result including only statistical uncertainties, while systematic uncertainties were included for the distribution shown in blue. The final leakage estimate, given by the median of the distribution, and the corresponding credibility interval are given below the legend.

where the top and the bottom sides were represented by the first and second summand respectively. Regarding the top side, multiple scatters within the nuclear-recoil band were used to estimate the pass-fail ratios. A similar population of events was used for the first method regarding the interior detectors (see formula (7.14)), but here the multiples were additionally demanded to occur on the phonon (internal) side, requiring a signal in the detector directly above the considered endcap detector. This is indicated by the additional index p. Single scatters outside the nuclear-recoil band, as used in (7.24) for estimating the differences regarding the pass-fail ratios of singles and multiples, were used to estimate the pass-fail ratios of charge-side events. As mentioned on page 86 charge-side surface events were subject to slightly higher timing parameters than phonon-side surface events.[3] In particular, it could not be definitely expected that the passage fractions, obtained from all single scatters, were a conservative estimate of the passage fractions of charge-side events. Therefore, the factor $1/(1-\phi)$ was added with ϕ representing the fraction of phonon-side events outside the nuclear-recoil band. For interior detectors it could be obtained from the

[3]Note, that since this effect was not clearly visible in the calibration data taken at Souden, it was not considered for the setting of the timing cut.

class of multiple scatters outside the nuclear-recoil band failing the timing cut:

$$\phi_i = \frac{\mu_{M_i^p}}{\mu_{M_i^p} + \mu_{M_i^q}} \,. \tag{7.32}$$

The similar factor Φ, representing the same fraction for events within the nuclear-recoil band, given by

$$\Phi_i = \frac{\mu_{B_i^p}}{\mu_{B_i^p} + \mu_{B_i^q}} \tag{7.33}$$

for interior detectors, was added to preserve the proper weighting between both contributions. Note, that these two formulae were valid only for interior detectors, but could not be applied to the case of endcap detectors, which was actually needed. However, the interior detectors could be used to estimate corresponding average values for the two endcap detectors at the bottom of their towers [77]:

$$\begin{aligned} \phi &= \frac{\sigma^m \phi^m}{\sigma^m + \gamma^m(1-\phi^m)} \\ \Phi &= \frac{\Sigma^m \Phi^m}{\Sigma^m + \Gamma^m(1-\Phi^m)} \,, \end{aligned} \tag{7.34}$$

where ϕ^m and Φ^m denote average values over all interior detectors of (7.32) and (7.33) respectively. Moreover, σ^m and Σ^m denote the average values of the ratios of single- to multiple scatters outside and within the nuclear-recoil band respectively, over all interior detectors, which were given by:

$$\begin{aligned} \sigma_i &= \frac{\mu_{S_i}}{\mu_{M_i}} \\ \Sigma_i &= \frac{\mu_{N_i}}{\mu_{B_i}} \,. \end{aligned} \tag{7.35}$$

Similarly, γ^m and Γ^m denote the average values of the fractions of multiple scatters tagged as charge- or bottom side events outside and within the nuclear-recoil band respectively, summed over all interior detectors, which were given by:

$$\begin{aligned} \gamma_i &= \frac{\mu_{M_i^p} + \mu_{M_i^q}}{\mu_{M_i}} \\ \Gamma_i &= \frac{\mu_{B_i^p} + \mu_{B_i^q}}{\mu_{B_i}} \,. \end{aligned} \tag{7.36}$$

Finally, the factor α^q, defined by

$$\alpha^q = \frac{\left(\sum_{i=1}^{12} \mu^*_{b_i^q}\right) \Big/ \left(\sum_{i=1}^{12} \mu^*_{B_i^q}\right)}{\left(\sum_{i=1}^{12} \mu^*_{m_i^q}\right) \Big/ \left(\sum_{i=1}^{12} \mu^*_{M_i^q}\right)} \,, \tag{7.37}$$

was introduced to correct for systematic differences in timing-cut performance of charge-side events within and outside the nuclear-recoil band. It is similar to the factor α, used for the second method regarding interior detectors defined in (7.27), with the additional constraint that only charge-side events were considered. It was based on the numbers of events observed in the interior detectors as indicated by the upper limit of the sum (12). Thus, all three correction factors Φ, ϕ and α^q were calculated solely based on the observed event counts in the interior detectors.

Apart from these necessary corrections, the evaluation of the leakage was performed in the same way as for the interior detectors. The results for various values of the prior exponent c are shown in Fig. 7.33. In the next step Monte Carlo simulations were performed to investigate the bias and coverage as a function of c. The three following scenarios were considered for the endcap detectors.

1. All detectors were assumed to be identical, and therefore all parameters were set to the mean observed values yielding a total leakage of 0.62.

2. All detectors were assumed to be identical. The expectation value for the number of passing phonon-side multiples was scaled to give an overall leakage of 1.0.

3. All detectors were assumed to be identical. The expectation value for the number of passing singles was halved and the number of passing phonon-side multiples was

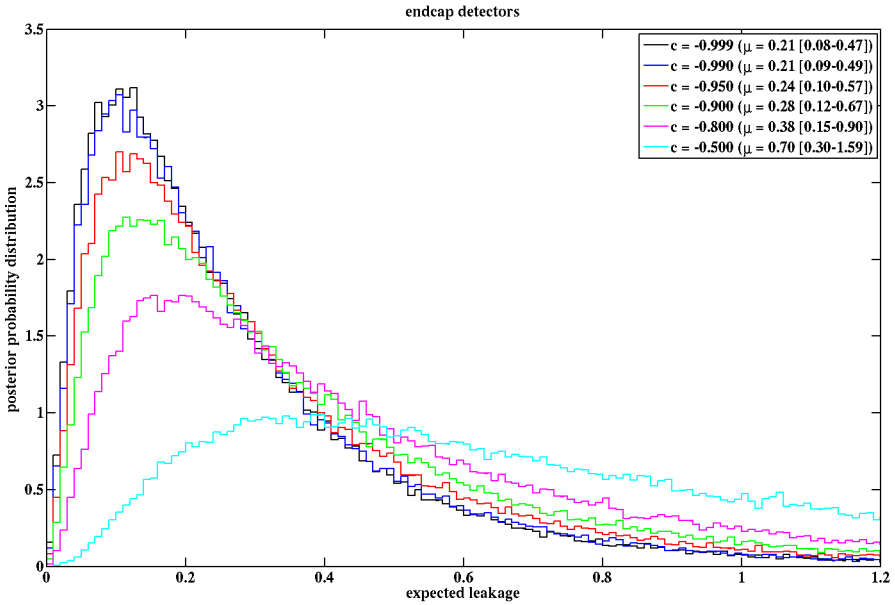

Figure 7.33: Probability distributions of the expected leakage for various values of the parameter c. The shown result is for the combination of both used endcap detectors. The final leakage estimate, given by the median of the distribution, and the corresponding credibility interval are given in the legend for each tested value of c. See text for details.

subsequently scaled to give the total leakage using mean values for all numbers, so 0.62.

Based on the results shown in Fig. 7.34, it was decided to use a value of $c = -0.92$ with a systematic error of 0.02 on the total leakage. As in the case of the second method for the interior detectors, the coverage seems to be systematically too low by a few percent for the chosen prior exponent.

Systematic uncertainties, related to the correction factor α^q, were treated in exactly the same way as for the similar factor α from the second estimate of the interior detectors. Thus, the systematic errors were conservatively assumed to be of the same size as the statistical errors emerging directly from the Monte Carlo. The distribution of α^q for $c = -0.92$ is shown in Fig. 7.35. The comparably high value of the best estimate, given below the legend, indicates that the passage fraction of charge-side multiples within the beta region but outside the nuclear-recoil band is significantly lower than the passage fraction of charge-side multiples within the nuclear recoil band. Note, that it was just the other way around, when all surface events were considered for the estimation of α as shown in Fig. 7.30.

Additionally, systematic errors of 0.1 and 0.2 were assigned to the fractions ϕ and Φ respectively. These values were based on the deviations regarding the 12 interior detectors separately.

To sum up, a prior exponent of $c = -0.92$ was used. Statistical errors were intrinsically included in the Monte Carlo. Five kinds of systematic errors were included for the endcaps. Those were the error of 0.02 related to the choice of prior exponent c, a 10% uncertainty related to possible differences of the timing-cut passage fraction of singles and multiples, an error of 0.1 on ϕ, an error of 0.2 on Φ and the systematic uncertainty on the correction factor α^q. The final result is shown in Fig. 7.36. A comparison with Fig. 7.32, which shows the distribution of the leakage estimate from the interior detectors, indicates that the leakage in the endcap detectors is roughly half as big as the leakage in the interior detectors. This is quite high, considering that 12 interior detectors but only two endcap detectors were included in this analysis, which underpins the difficulties of surface-event background rejection regarding endcap detectors.

7.2.3 Combined leakage estimate

Finally, the distributions for interior and endcap detectors were convoluted to obtain the distribution of the total leakage. The result without and with inclusion of systematic errors, with the latter representing the final leakage estimate, is shown in Fig. 7.37. It has a maximum at around 0.6 events, where the leakage had been fixed for the setting of the cut, while the median, which was used as the final background estimate, was slightly higher but agreed with this value within error bars:

$$\mu_{25-150\,\mathrm{keV}} = 0.8^{+0.5}_{-0.3}(\mathrm{stat.})^{+0.3}_{-0.2}(\mathrm{syst.})\ . \tag{7.38}$$

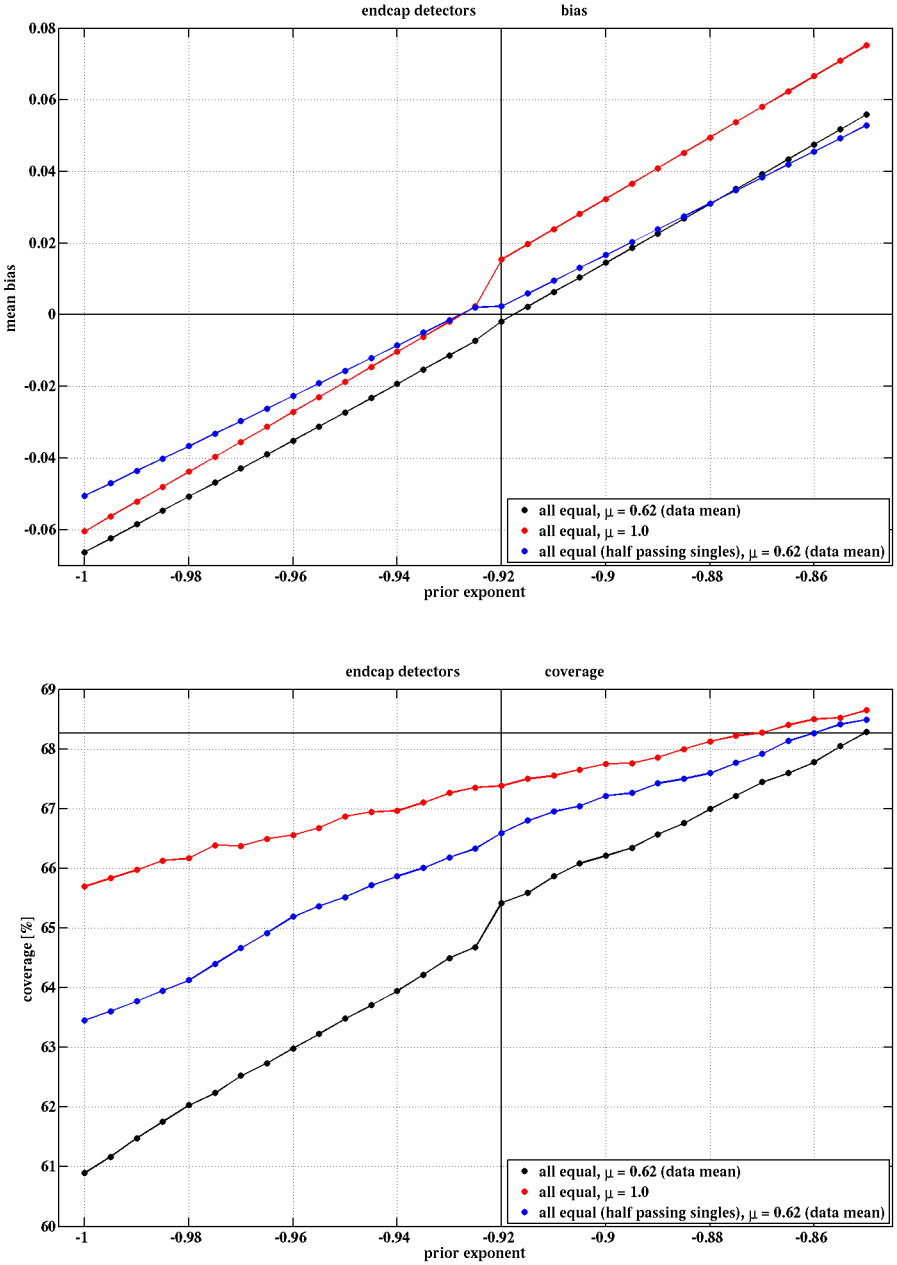

Figure 7.34: Bias (top) and coverage (bottom) of the algorithm for calculating the total leakage of the endcap detectors as a function of the parameter c. The three tested scenarios are described in the text. The final choice of $c = -0.92$, which minimizes the bias, is indicated by the vertical black line. A systematic error of 0.02 was assigned to the leakage estimate.

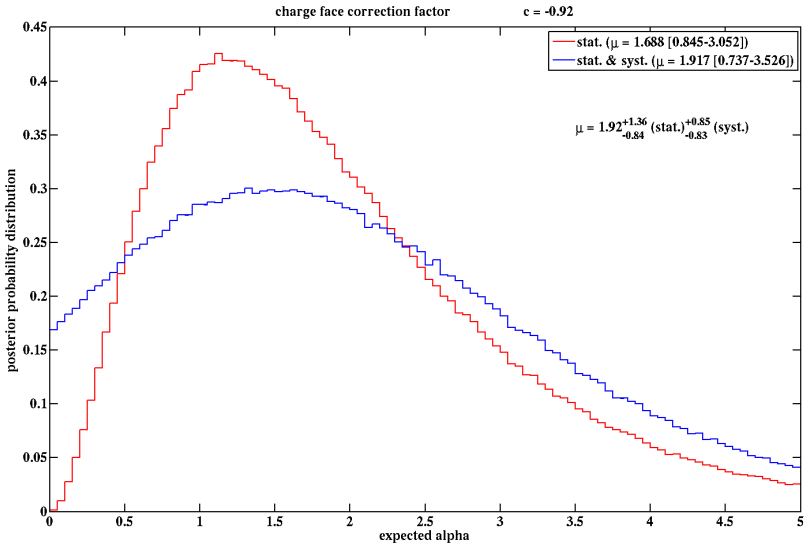

Figure 7.35: Distribution of the factor α^q used to correct for systematic differences of the timing-cut performance of charge-side multiple scatters within and outside the nuclear-recoil band. Results with (blue) and without (red) inclusion of systematic errors are shown. The parameter c was fixed at the value, which minimized the bias of the leakage estimate. The values given below the legend denote the expectation value of α^q and the corresponding errors.

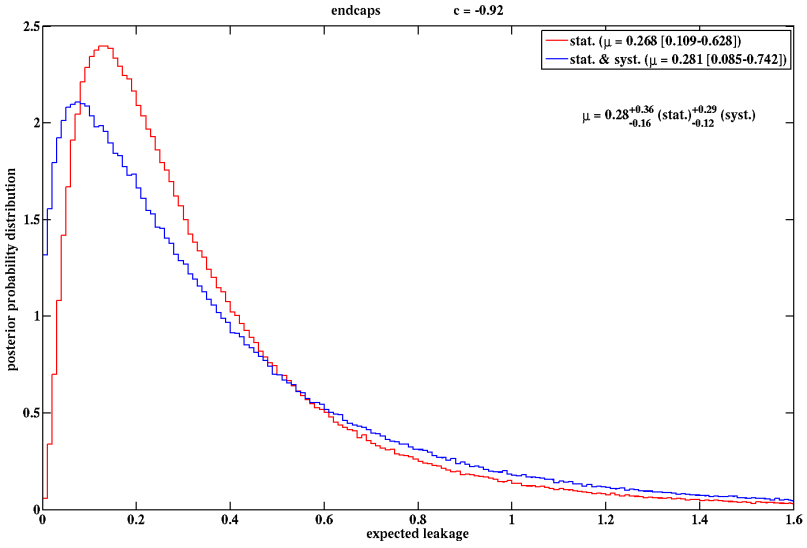

Figure 7.36: Final probability distribution of the expected leakage for the two used endcap detectors. The distribution shown in red represents the result including only statistical uncertainties while systematic uncertainties were included for the distribution shown in blue. The final leakage estimate, given by the median of the distribution, and the corresponding credibility interval are given below the legend.

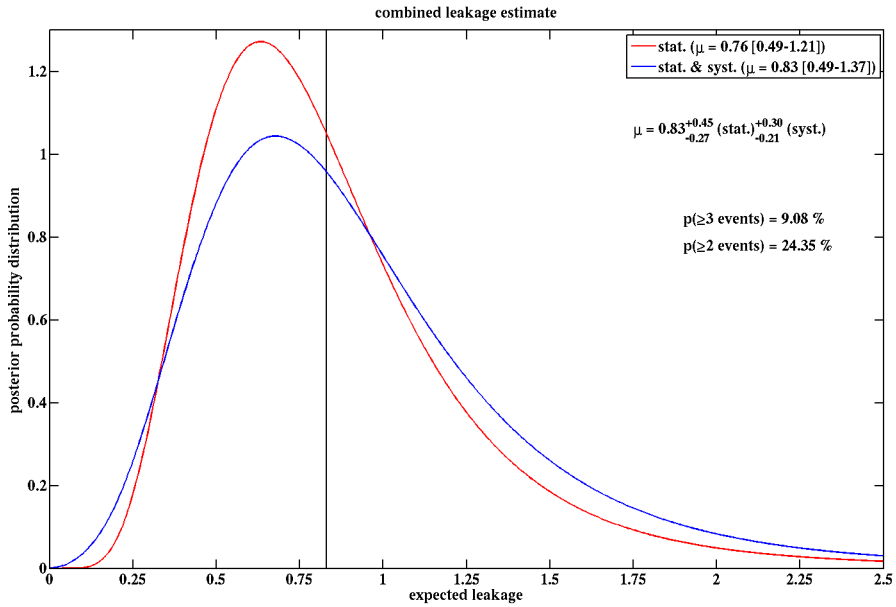

Figure 7.37: Distribution of the total surface-event leakage estimate in the 25–150 keV energy range with (blue) and without (red) inclusion of systematic errors. The vertical black line marks the median of the distribution, which was used as the final background estimate. See text for details.

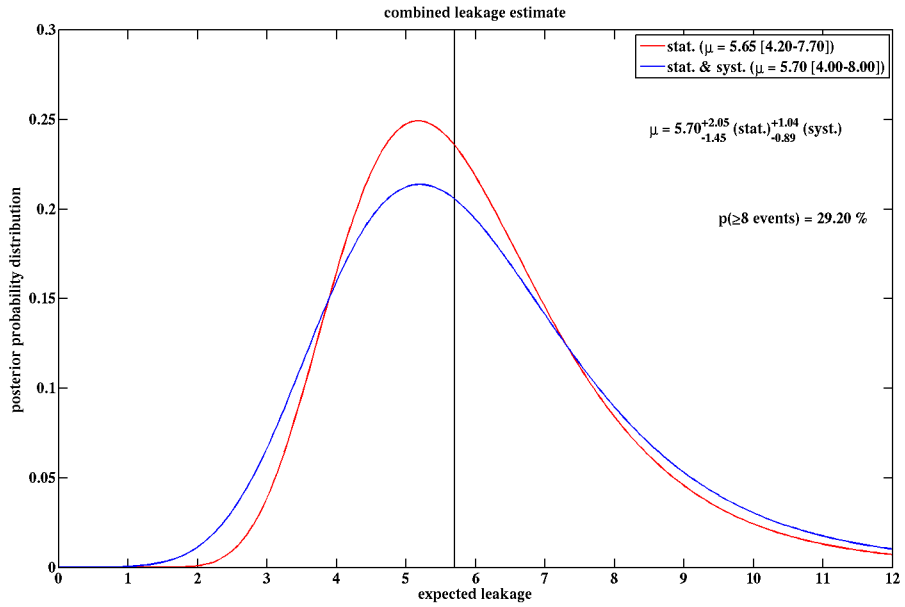

Figure 7.38: Distribution of the total surface-event leakage estimate in the 10–25 keV energy range with (blue) and without (red) inclusion of systematic errors. See text for details.

The median is indicated in the plot by the vertical black line. The subscript is used to indicate that the whole procedure was only performed including events between 25 keV and 150 keV, the energy range the timing cut was defined on.

A complete analog estimate was performed for the low-energy range from 10–25 keV. The result is shown in Fig. 7.38. As anticipated, it resulted in a much higher number of expected leakage events:

$$\mu_{10-25\,\mathrm{keV}} = 5.7^{+2.1}_{-1.5}(\mathrm{stat.})^{+1.0}_{-0.9}(\mathrm{syst.})\ . \tag{7.39}$$

The probabilities, given in the two figures below the leakage estimate, denote the likelihoods to observe more than the given number of events, for the shown background distributions (including systematic errors). These results are discussed in more detail in the next chapter.

7.3 Unblinding and tests of the WIMP-candidates

In the previous chapter the surface-event cut was discussed in great detail. Apart from that, it was also necessary to calculate neutron-background estimates. This analysis was based on the Monte Carlo simulations already performed for the standard analysis, but taking the increase in exposure and efficiency, as well as the different energy range, into account. As for the surface-event leakage, these estimates were calculated for the 10–25 keV and 25–150 keV separately. No estimate of the bulk-electron recoil background was calculated, since it was particularly negligible at energies above 25 keV. A summary of all important numbers for the iDM analysis is given in Table 7.1.

After "unblinding", eleven events were observed within the acceptance region passing the surface-event rejection cut, three within the 25–150 keV range and eight between 10 keV and 25 keV. Figure 7.39 shows these candidates, along with all other WIMP-search events in or close to the signal region, which pass all constraints except for cuts on the ionization yield and timing parameter. As can be seen in Table 7.2, the candidates are well distributed over the whole data-taking period and are spread over various detectors; though, six of

	10–25 keV	25–150 keV
Cosmogenic neutron background	$0.06^{+0.07}_{-0.04}$	$0.04^{+0.05}_{-0.03}$
Radiogenic neutron background	0.04–0.08	0.03–0.06
Surface-electron background	$5.7^{+2.1}_{-1.5}(\mathrm{stat.})^{+1.0}_{-0.9}(\mathrm{syst.})$	$0.8^{+0.5}_{-0.3}(\mathrm{stat.})^{+0.3}_{-0.2}(\mathrm{syst.})$
exposure	969.4 kg-days	
efficiency	∼45%	
recoil-energy range	10–150 keV	

Table 7.1: Summary of background estimates, exposure, efficiency and energy range for the iDM analysis. The numbers for the background on the left are for the 10–25 keV energy range and those on the right are for the 25–150 keV energy range. A similar summary for the standard analysis can be found in Table 6.3.

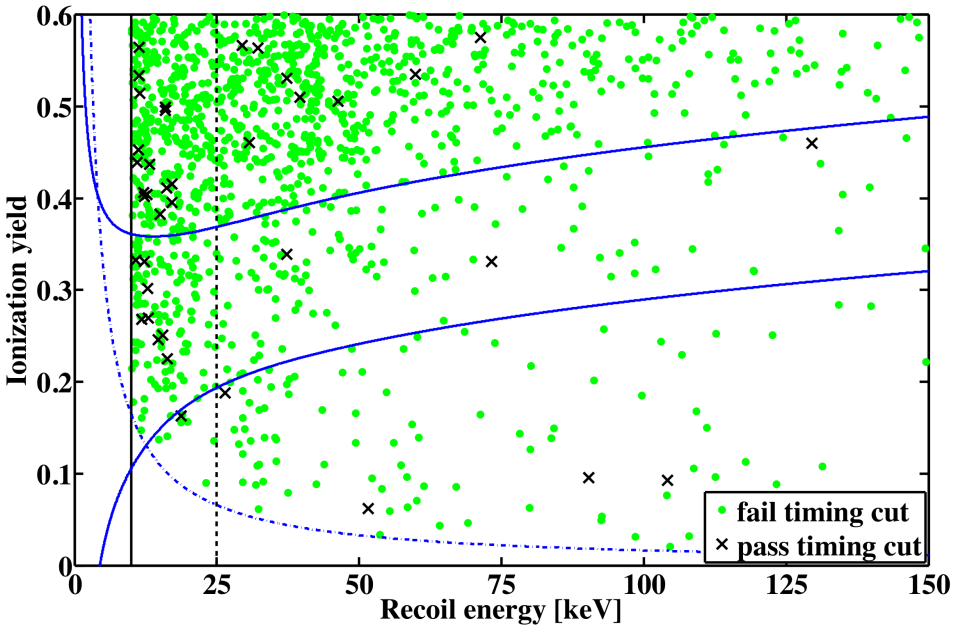

Figure 7.39: Ionization yield versus recoil energy for all low-yield WIMP-search single scatters from the combined five-tower data set (runs 123–128) passing all constraints except for cuts on the ionization yield and timing parameter. Most events fail the timing cut (green dots), while most of the few dozen that pass the timing cut (×) fall outside the nuclear-recoil band (blue/solid lines). Eleven events pass all the selection criteria, with three occurring within the 25–150 keV range upon which the surface-event rejection cut was defined, and eight between the 10 keV recoil-energy threshold and 25 keV. The ionization-energy threshold is also shown (blue/dashed-dotted). This threshold and the shown nuclear-recoil band represent the exposure-weighted means over all runs and detectors.

Energy (keV)	Detector	Run	Date
10.8	T2Z3	127	31.05.2008
11.8	T4Z6	124	31.05.2007
12.3*	T1Z5	125	27.10.2007
12.8	T3Z6	127	01.06.2008
13.0	T4Z6	125	05.10.2007
14.7	T3Z6	123	10.12.2006
15.5*	T3Z4	125	05.08.2007
16.4	T4Z6	123	30.10.2006
37.3	T4Z6	126	02.02.2008
73.3	T4Z2	126	04.02.2008
129.5	T1Z2	123	24.12.2006

Table 7.2: Distribution of the eleven event candidates over detectors and time. The two marked events (*) are the candidates already found in the standard analysis (see Table 6.4).

the eleven candidates occurred in the two endcap detectors (T3Z6 and T4Z6), where there was less shielding from background, and where there was no detector below it to help reject background by detecting multiple scatters. It was verified that the performance of the experiment was stable at the times during which the events occurred. The detectors in which the three candidates above 25 keV occurred are examined in more detail in Fig. 7.40, where normalized ionization yield, defined as the distance from the nuclear-recoil band mean measured in units of standard deviations given by the width of the band, is plotted against the timing parameter relative to the actual cut position. Note, that for these plots, the events from both data-set categories (runs 123–124 and runs 125–128) with two different timing cuts were combined for each detector. The vertical black/solid line denotes the timing-cut boundary on the given detector, and the shaded box indicates the acceptance region. The top plot is for T4Z6, with a WIMP candidate at 37.3 keV and three additional candidates below 25 keV. T4Z6 was a detector at the bottom of its tower with reduced background rejection capability. The middle plot shows events in T4Z2, where an event occurred just above the timing-cut boundary with a recoil energy of 73.3 keV. Finally, events from T1Z2 are shown in the bottom plot with a candidate above the analysis range from previous analyses at 129.5 keV. This event is far above the timing-cut boundary and would be rejected neither by the surface-event cut from the standard analysis, nor by a tighter timing cut tuned to a leakage as low as 0.1 (instead of 0.6) events, which was the most stringent timing cut that was tested. No additional events appear in the signal region above 25 keV until the timing cut is loosened to an estimated surface-event leakage of more than 2.0 events. A detailed comparison of the predicted numbers of WIMP-search nuclear-recoil single scatters within the nuclear-recoil band, passing the optimized cuts for various numbers of the predefined leakage, and the actually observed numbers can be found in Fig. 7.41. The calculations were performed in the same way as the similar test on multiple scatters, discussed in the previous chapter with the results shown in Fig. 7.14. Based on that analysis it was assumed that the cut setting procedure was conservative, since the predicted number of multiple scatters passing the cut was always larger than the actually observed number. Regarding single scatters the situation looks different. Above leakages of $\sim$2 events the predictions and observations agree very well, while the latter are larger at lower leakages. First of all, it can be concluded that the timing-cut passage fractions of single scatters seem to be larger than the passage fractions of multiple scatters. Moreover, the shown results could indicate one of three things. Since the cuts regarding higher leakages are set in the bulk of the distributions, the corresponding predictions are much more reliable than those regarding lower leakages, where the cuts have to be set in the tails of the distributions. Therefore, the agreement for high leakages is very good, while the disagreement at lower leakages reflects the uncertainties regarding the reconstruction of the tails of the surface events' timing-parameter distributions. Thus, it might be that the cut setting in the tails is just not very reliable. Some of the candidates could also be due to neutron background even though it is estimated to be extremely small (cf. Table 7.1). However, it could also be possible that some of the candidates, or even all of them, are indeed due to WIMP interactions.

The probability to observe three or more surface-leakage events between 25 keV and

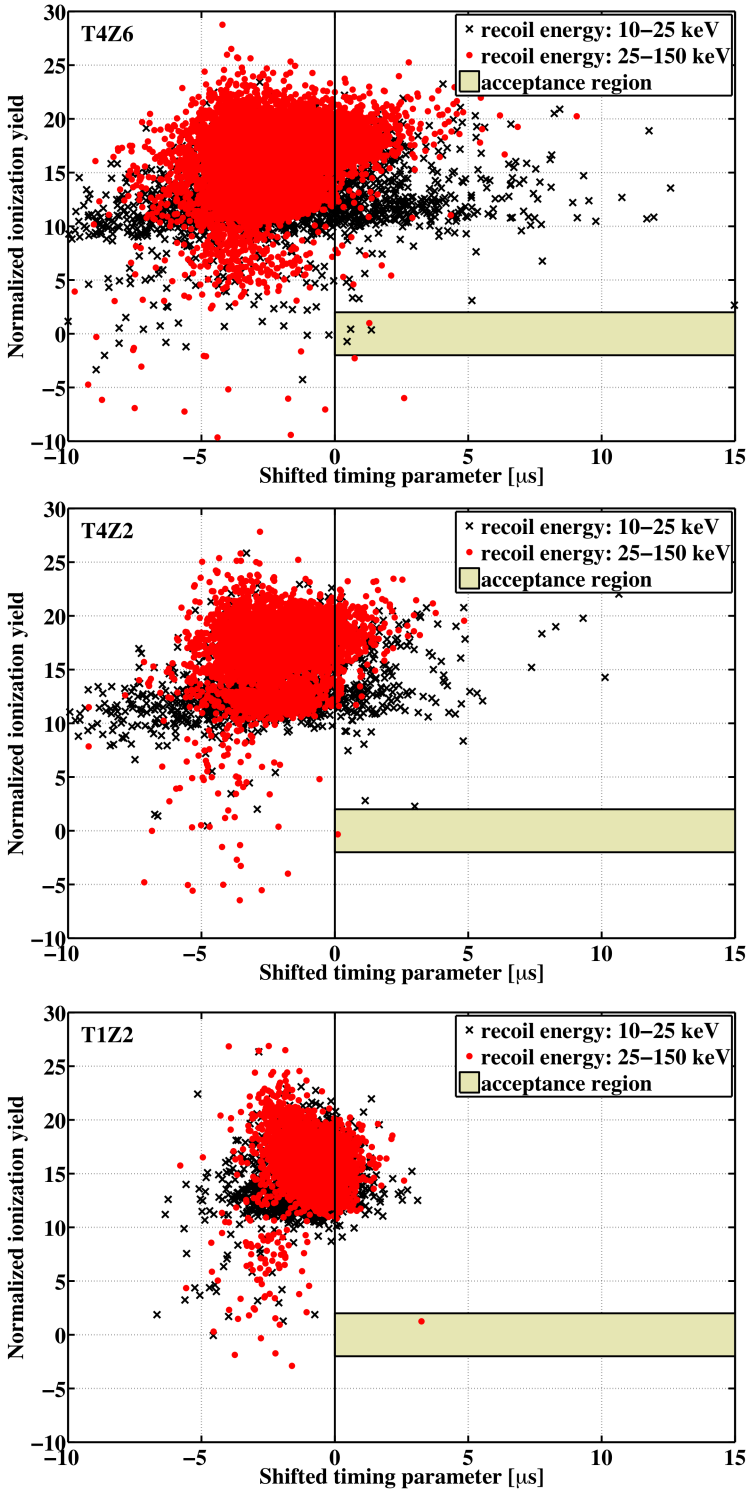

Figure 7.40: Number of standard deviations each event is away from the mean of the nuclear-recoil band (normalized ionization yield) versus timing parameter relative to the timing-cut position (shifted timing parameter) for the three detectors with WIMP candidates above 25 keV. The detectors are (from top to bottom) T4Z6, T4Z2 and T1Z2 with candidate events at 37.3 keV, 73.3 keV and 129.5 keV, respectively. In detector T4Z6 three additional candidates occurred in the 10–25 keV range. The acceptance regions are indicated by the shaded boxes. It can be observed that the candidate in T1Z2 is well separated from the background distribution.

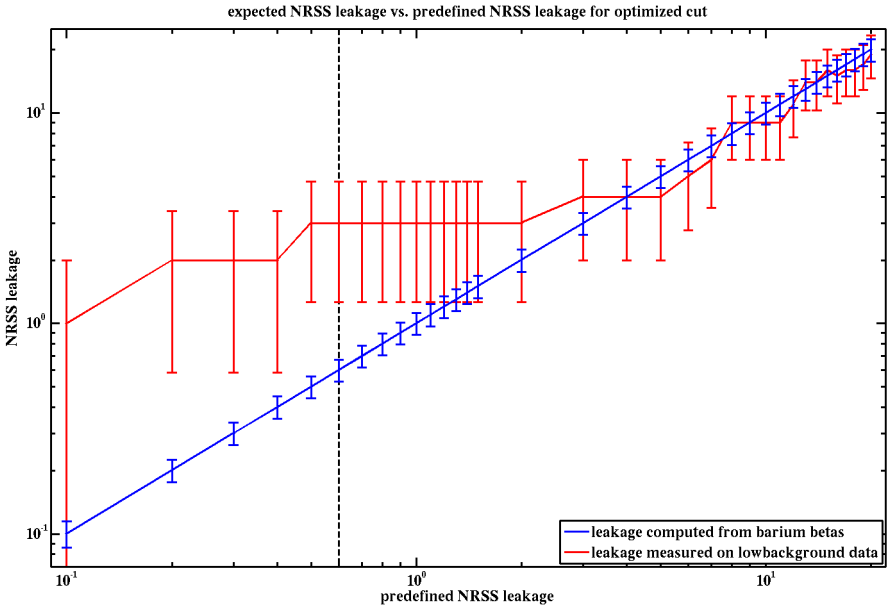

Figure 7.41: Comparison of the predicted numbers of WIMP-search single scatters passing the optimized timing cuts (blue) and the actually observed numbers (red) for various numbers of predefined WIMP-search single scatter leakage events. The used cut, defined for a total of 0.6 leakage events, is indicated by the vertical back/dashed line. Similar plots considering multiple scatters are shown in Fig. 7.14 (for the optimized cuts and also for the cuts demanding equal leakage on all detectors). Unlike the case of multiple scatters the observed number of passing events is higher than the prediction for cuts set to have $\lesssim$2 leakage events.

150 keV, given the background distribution $f(\mu)$ shown in Fig. 7.37, was calculated as

$$p = \int_0^\infty \mathrm{d}\mu \, f(\mu) \cdot \sum_{k=3}^{\infty} \frac{e^{-\mu}\mu^k}{k!} \tag{7.40}$$

and yields 9%. Inclusion of the estimated neutron background increases this probability to 11%, which is low but not negligible. Thus, this analysis does not constitute a significant detection of WIMP scattering. The probability for eight or more surface-background events between the 10 keV threshold and 25 keV was calculated based on the background distribution, shown in Fig. 7.38, and is 29%, which indicates compatibility of our result with the background expectation. The inclusion of the neutron background has a negligible effect on the low-energy range due to the dominant surface-event background. Finally, it should be mentioned that no detailed likelihood analysis, as for the candidates of the standard analysis, was performed.

7.4 Constraining the WIMP-parameter space

As for the standard analysis the optimum interval method was used to compute the 90% C.L. upper limit on the spin-independent cross section as a function of WIMP mass and splitting. All eleven WIMP candidates were included as possible signal with no background subtraction. Regions allowed by DAMA/LIBRA at two different C.L.s $(90, 99.9\%)$ were computed, as discussed in chapter 2.3, based on the published modulation spectrum in [41] from an exposure of 1.17 ton-years. Note, that the results shown in Fig 6.26 were based on the spectrum shown in [40] from an exposure of 0.82 ton-years, which was the most recent result at the time that analysis was performed. Therefore, the regions allowed by DAMA/LIBRA shown in the current chapter are slightly more restrictive.

Selected results from these computations are shown in Fig. 7.42 in the cross-section versus WIMP-mass plane for two chosen WIMP-mass splittings. The left plot shows the standard case with $\delta = 0$ keV, equivalent to assuming elastic scattering, while $\delta = 120$ keV is used for the right plot, a value, which is not experimentally excluded by the standard analysis. Apart from the DAMA/LIBRA allowed regions, and constraints emerging from the iDM analysis, the plots also contain cross-section limits from the standard analysis of the 10–100 keV energy range. Constraints from the iDM analysis are less stringent. This

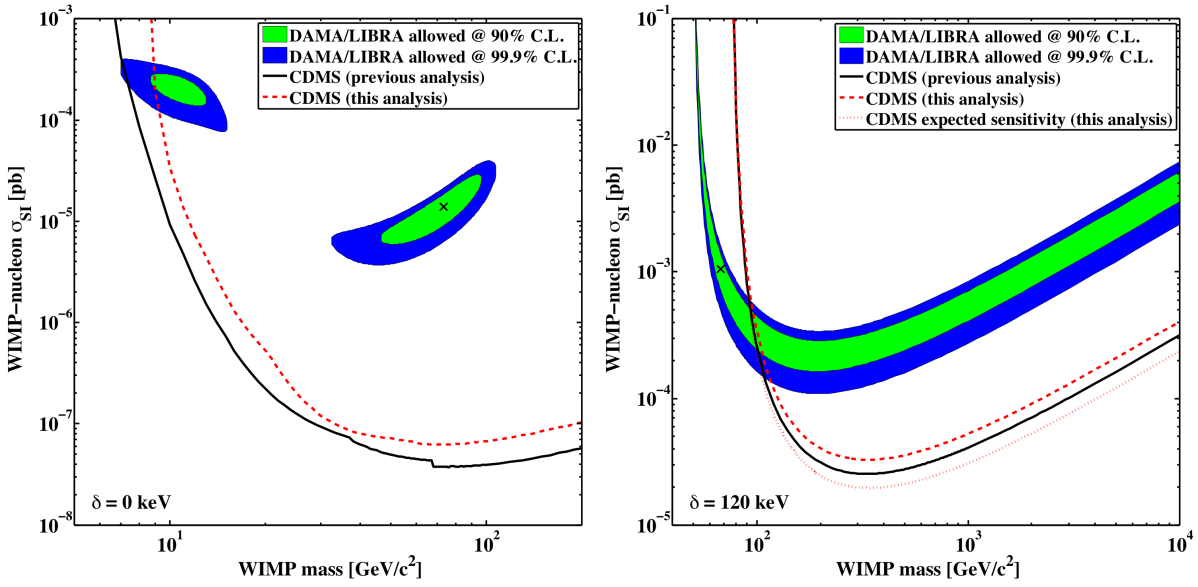

Figure 7.42: 90% C.L. upper limits on the scalar WIMP-nucleon cross section for WIMP-mass splittings of 0 keV (left) and 120 keV (right) from the iDM analysis (red/dashed) and from the standard analysis (black/solid). The red/dotted line in the right plot indicates the expected sensitivity for this analysis based on the estimate of the total background. The colored regions represent DAMA/LIBRA allowed regions at two different C.L.s $(90, 99.9\%)$ calculated following a χ^2 goodness-of-fit technique as discussed in chapter 2.3. The cross $(\times)$ marks the parameter-space point, which yields the minimum χ^2 in the shown cross-section versus WIMP-mass plane given the WIMP-mass splitting.

was anticipated for the elastic scattering case and low WIMP-mass splittings in general, since more surface-background events were expected at low energies due to the looser timing cut defined in the 25–150 keV energy range. The limits are slightly weaker at $\delta = 120$ keV, due to the occurrence of the three candidates above 25 keV, where the rate is expected to peak for higher WIMP-mass splittings. The eight low-energy events have no effect on this part of the parameter space due to the utilization of the optimum interval method. WIMP masses above $\sim$100 GeV/c^2 are excluded for this mass splitting by the current and previous analysis. The expected sensitivity, shown in the right plot, was calculated very similar to the approach leading to the sensitivity shown in Fig. 7.20. However, in order to obtain those results, an expectation value of 0.6, the value which the cut was fixed at, was applied for the expectation value of the number of surface-background events. For the current plot, the improved knowledge of the background distribution was considered: For each Monte Carlo, the number of 0.6 was replaced by a random number drawn from the background distribution shown in Fig. 7.37. The rest of the Monte Carlo approach remained the same. Additionally, the neutron background was included for the current sensitivity estimate.

Since the iDM parameter space is three-dimensional, consisting of the cross section, WIMP mass, and WIMP-mass splitting, excluded regions were defined (as in chapter 6.8) by requiring the 90% C.L. upper limit on the cross section from CDMS to completely rule out the corresponding DAMA/LIBRA allowed cross sections (also at 90% C.L.) for given WIMP mass and WIMP-mass splitting. The results are shown in Fig. 7.43. The only remaining allowed parameter space is within a narrow region at WIMP masses of $\sim$100 GeV/c^2 and WIMP-mass splittings between 85 keV and 135 keV. In the case of the iDM analysis there is also a tiny area in the low-mass region, which is not excluded. The black/dashed line represents the maximum reach in the shown parameter space of an experiment using a Ge target like CDMS. It is computed based entirely on kinematics by demanding $v_{\mathrm{min}} = v_{\mathrm{esc}} + v_{\mathrm{E}}$, and is therefore independent of the cross-section parameter. If v_{min} is larger the predicted rate is zero as discussed in great detail in chapter 2.1.4. Even with higher exposure and increased sensitivity, CDMS cannot rule out the entire DAMA/LIBRA allowed parameter space simply because (relative to an I nucleus) the Ge nucleus is too light. This is the main reason why the constraints from ZEPLIN-III [112] and XENON100 [110], which employ Xe targets, are more stringent. Note, that the results from the latter publication exclude an iDM interpretation of the DAMA/LIBRA results at 90% C.L.

As discussed in chapter 2.1.4, the iDM scenario with a non-zero δ is particularly sensitive to the high-velocity tail of the dark matter velocity distribution due to the increased minimal velocity (2.11). Therefore, it exhibits a strong dependence on the velocity-distribution parameters v_0 (the dispersion) and v_{esc} (the galactic escape velocity) [113]. To examine these dependencies, in Fig. 7.44 plots similar to Fig. 7.43 but with different values of v_{esc} and v_0 are shown. The top plots explore the v_{esc} 90% C.L. lower and upper limits found in [18] (498 km/s and 608 km/s), while all other parameters remain unchanged relative to Fig. 7.43. In the bottom plots only v_0 is varied, assigning a (convenient) lower value of 200 km/s for the left plot and a higher value of 254 km/s (the preferred value according to

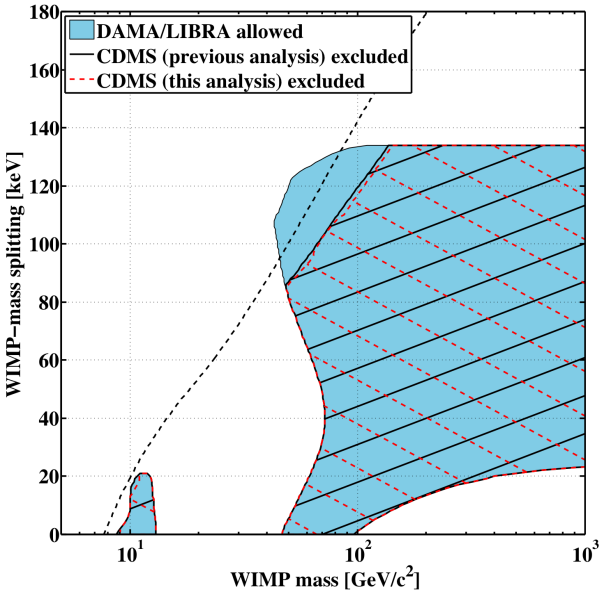

Figure 7.43: The blue/shaded regions represent WIMP masses and WIMP-mass splittings for which cross sections exist that are compatible with the modulation spectrum observed by DAMA/LIBRA at 90% C.L. The hatched regions show constraints on these parameters from the iDM analysis (red/dashed) and from the standard analysis (black/solid). The black/dashed line represents the maximum reach of the CDMS II experiment.

[114]) for the right plot. The capability of CDMS to constrain an iDM interpretation of the DAMA/LIBRA results is relatively independent of the actual velocity-distribution parameters. However, the shape and location of the parameter-space region, which is still allowed by CDMS, has a considerable dependence on v_{esc} and v_0, as expected. Non-Maxwellian velocity distributions, as discussed in [23, 115], are beyond the scope of this study.

As shown in this chapter, the results from the specialized iDM analysis are slightly weaker than from the standard analysis. However, this is due to the fact that three events were observed between 25 keV and 150 keV passing all selection criteria for WIMPs. All of these events, especially the one at 129.5 keV in detector T1Z2, which is far above the timing-cut boundary, may be interpreted as signal, though it was refrained from doing this here due to the low statistical significance. Finally, though this analysis was performed with regard to the iDM scenario, the expansion of the analysis range to 150 keV could be useful to test other models predicting a signal at tens of keV recoil energy.

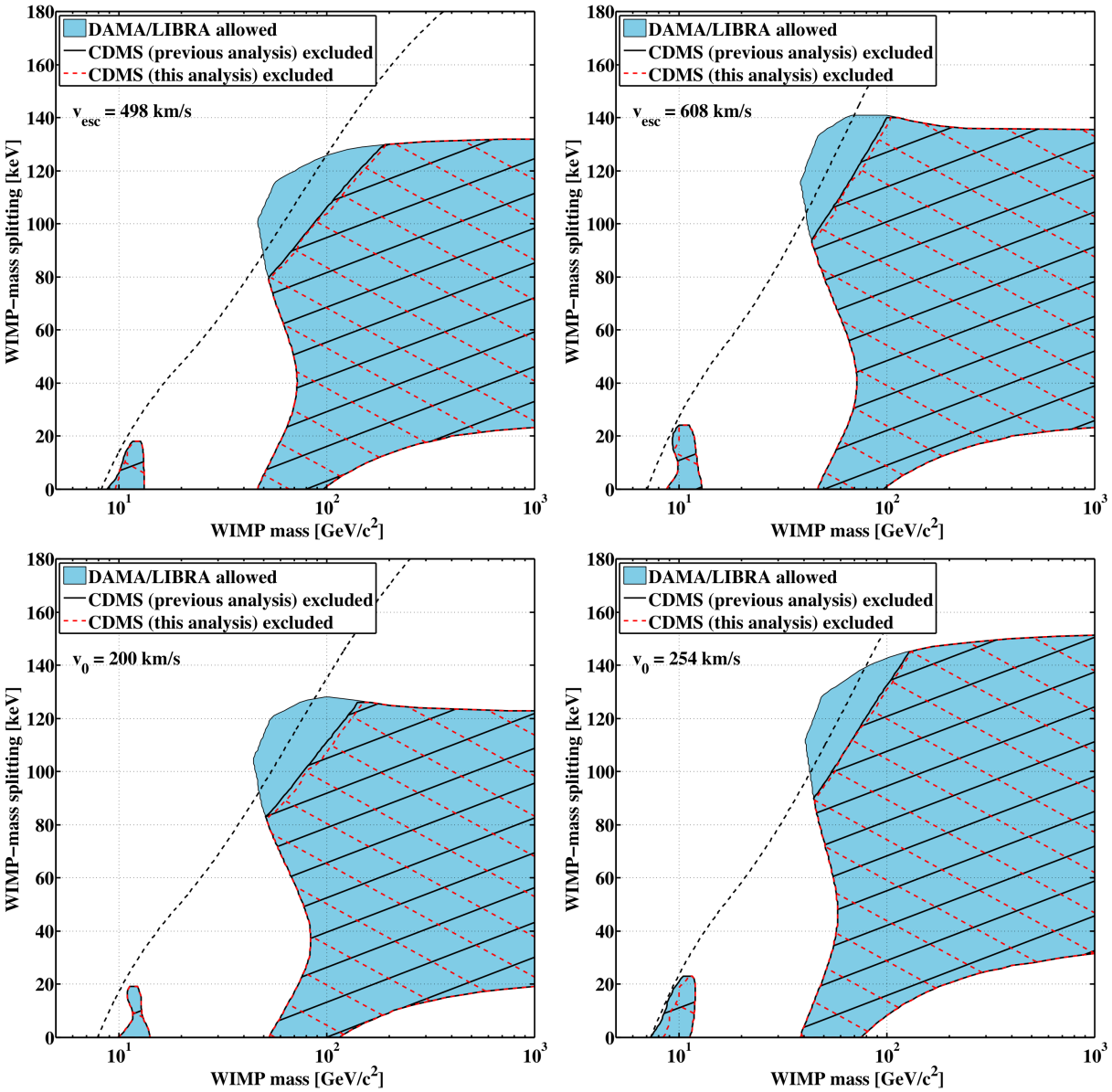

Figure 7.44: Constraints from CDMS on the iDM parameter space allowed by DAMA/LIBRA. Same as Fig. 7.43 but with different velocity-distribution parameters, as given in the plots. All other parameters remain unchanged.

Chapter 8

A maximum-likelihood analysis of the CDMS data

Chapter 5.1.2 introduced the framework of a maximum-likelihood method, which was shown to be an interesting alternative to the cut-based method. So far, the latter approach was the standard method applied by the CDMS collaboration (and most other collaborations of the direct detection dark matter community[1]) to the problem of background rejection. Since no explicit cuts have to be introduced for the discrimination of background events, the maximum-likelihood approach does not suffer from a severe reduction of the signal acceptance. Note, that e.g. regarding the standard analysis, the application of the surface-event rejection cut reduced the efficiency from ∼60% to ∼30%, as shown in Fig. 6.18.

As discussed in chapter 6.6, one of the two observed WIMP candidates suffered from an ambiguity regarding the exact determination of its start time because of the applied charge reconstruction scheme: The start time was obtained by maximizing the amplitude of the signal rather than by minimizing the χ^2 between the acquired trace and the template of the pulse. It was mentioned that, regarding events at low energies, this was a general, previously overlooked issue, and that only a proper reprocessing of the whole data set could reveal, whether a hint for a WIMP detection was evident in the CDMS data.

In the standard WIMP scenario the spectrum nearly falls exponentially with recoil energy. Hence, a signal is expected at low-energies, where the two candidates occurred. However, as shown in Fig. 7.17, the background spectrum has a similar shape, which makes background rejection particularly difficult in that range. A signal at low recoil energies translates into a preferred parameter-space region at low WIMP masses. Indeed, the DAMA/LIBRA collaboration [41] and recently the CoGeNT collaboration [79] claimed hints for a signal in this part of the parameter space. Moreover, some theorists have applied likelihood methods to the CDMS data, yielding a closed region (which would imply a detection) at low WIMP masses, but only at 1σ confidence level [117, 118]. However, these analyses were solely based on the two observed candidates and a very simple estimate

[1] Up to now, only XENON100 published a likelihood-based analysis of their data [116].

of the surface event's energy spectrum. In particular, the background rejection itself was still mainly based on the applied timing cut rather than an on its explicit inclusion in the likelihood method.

In summary, a full likelihood analysis of the CDMS data, reprocessed based on the proper χ^2-minimization and with a lower threshold of ∼5 keV rather than 10 keV, which was previously used, seems like a very promising approach, in particular regarding the low-mass range of the WIMP-parameter space. A threshold, as low as 5 keV, can certainly be achieved after the reprocessing. Note, that the main reason for choosing a 10 keV threshold for the standard analysis was the need for high statistics in order to define the timing cut adequately, which is not necessary in the given approach. Since the detectors show different response to a particle interaction, it is necessary to consider all detectors separately. Moreover, it is appropriate to include three parameters for this approach, recoil energy, ionization yield and the timing parameter. Indeed, such an analysis was performed, however the code has only been applied to the *unreprocessed* data so far, since reprocessing and preparation of the updates on some cuts was still ongoing at the time this thesis was written. Note, that only the data of runs 125–128, but none of the previous runs, are planned to be reprocessed, due to the very long computation time of the algorithm. Thus, this chapter merely serves the purpose of documentation and elaboration of the method. All shown results, in particular regarding low WIMP masses, have to be considered as highly preliminary. It is hoped that the developed machinery can be applied to the reprocessed data in the very near future.

The following discussion is based on the extended log-likelihood function, introduced in formula (5.12):

$$\log L(\nu_s, \nu_b) = -(\nu_s + \nu_b) + \sum_{i=1}^{n} \log \left(\nu_s f_s(\underline{p}_i) + \nu_b f_b(\underline{p}_i) \right), \tag{8.1}$$

where ν_s and ν_b denote the expectation values of signal and surface-event background respectively. The corresponding distributions are denoted f_s and f_b. The parameter $\underline{p}$ represents the rejection variable(s), which, in the given case, is a 3-tuple, consisting of the recoil energy, ionization yield and timing parameter. For the moment, the formula should be considered as being valid for only one particular detector, so that the index i runs over all acquired events in that detector from the WIMP-search runs passing miscellaneous pre-selection cuts. Obtaining the result from all detectors combined is quite simple and is discussed below.

8.1 Determination of signal and background distributions

The main difficulty regarding the application of the likelihood approach certainly is the appropriate estimation of the signal and background distributions f_s and f_b. As mentioned

before, these distributions were considered to be three-dimensional and had to be determined for each detector separately. Moreover, as in the case of the cut-based analysis, it could be expected that modeling of the tails of these distributions is particularly difficult. Finally, one single approach should be sufficient to deal accurately with all of these issues in order to prevent fine-tuning by applying special algorithms to some of the distributions. Such estimates were already discussed very briefly in chapter 6.7. However, only the distributions regarding the two detectors, which the candidates occurred in, had to be estimated for this analysis. A detailed discussion of the determination of the distributions is given in the current section.

So, given a particular detector, it is necessary to estimate the signal and surface-event background distributions as functions of the parameters energy E, ionization yield y and timing parameter t. As in chapter 6.7, it is assumed that yield and timing are independent. A few comments regarding this assumption are given at the end of this section, however, for the current discussion, this should hold true. Thus, the two-dimensional distributions $f_s(t, E)$, $f_s(y, E)$, $f_b(t, E)$ and $f_b(y, E)$ were determined separately and combined afterwards. This was useful, since the determination of two-dimensional distributions is certainly easier than estimating the full three-dimensional distributions right away. Moreover, different data sets were used for determining these distributions as discussed in the following.

All *unreprocessed* data from runs 125–128 between 5 keV and 100 keV were included for this analysis. The runs were combined for each detector in order to increase statistics. This was valid, since run-to-run variations were comparably small. Note, that regarding the unreprocessed data, it would not have been possible to naively include runs 123–124 in the analysis because of the differences, regarding the timing-parameter distributions discussed in the context of the iDM analysis. See Fig. 7.3 and the corresponding discussion. Before starting the actual analysis, all cuts as in the case of the standard WIMP analysis, except for the nuclear-recoil cut (ionization yield) and the surface-event rejection cut (timing parameter), were applied to the data sets, discussed in the following.

Regarding the timing distributions of the signal $f_s(t, E)$, nuclear recoils from the californium calibration data within the 2σ nuclear-recoil band, so obeying the standard definition of nuclear recoils (illustrated in Fig 5.3), were used. The yield distributions of the signal $f_s(y, E)$ were also based on events from californium calibration data but within the 3σ nuclear-recoil band to get better estimates in the tails of the distributions. Including more events at higher yield would probably contaminate the population with too many surface events to prevent a reliable estimate.

Barium events obeying the standard beta definition (illustrated in Fig 5.10) were used for the timing distributions of surface events $f_b(t, E)$. The yield distributions of the surface events $f_b(y, E)$ were based on WIMP-search multiple scatters due to known systematic differences between calibration and WIMP-search data, as discussed in chapter 7.1. This sample suffered from particular low statistics and should therefore be regarded as the main source of uncertainties. The charge threshold (illustrated in Fig 6.13) and the lower edge of the 3σ electron-recoil band were used as the lower and upper boundaries regarding the event selection in ionization yield. This region was also used as the "signal region" for

the WIMP-search discussed in this chapter. The index i in formula (8.1) runs over all WIMP-search single scatters in this region.

After the determination of the data sets, which the distributions had to be based upon, the actual estimates could be performed. Parametric approaches were used to model two-dimensional distributions for a similar but much less advanced study of CDMS detectors in [88]. However, the used functions were quite complicated and depended on numerous parameters rendering the correct convergence of the fitting algorithm comparably involved. Moreover, since it was necessary to model 56 distributions (4 distributions for 14 detectors) with the same approach, it was desirable to apply a more flexible algorithm. Finally, it was decided to apply kernel density estimates (KDE).

KDEs are based on the idea of describing arbitrary distributions by a normalized sum over so-called kernel functions, which in fact are just simple, normalized distribution functions, located at the respective observations. Extensive discussions of the subject can be found in [119, 120]. Since the distributions, which were about to be estimated, were two-dimensional, it would have been possible to use kernels, which include correlations between both variables. However, in order to keep the approach simple, a multiplicative ansatz was chosen:

$$f(x_1, x_2|h_1, h_2) = \frac{1}{n\, h_1 h_2} \sum_{i=1}^{n} K\left(\frac{x_1 - X_{1i}}{h_1}\right) \cdot K\left(\frac{x_2 - X_{2i}}{h_2}\right), \tag{8.2}$$

where x_1 and x_2 denote the two considered variables, e.g. energy and timing, and the sum over X_{1i} and X_{2i} runs over the corresponding two sets of observations. Moreover, K denotes the kernel function, which is supposed to be normalized, and h_1 and h_2 the bandwidths of this function regarding the two considered parameters. Given, that

$$\int_{-\infty}^{\infty} \mathrm{d}u\, K(u) = 1\,, \tag{8.3}$$

it is easy to show that

$$\int_{-\infty}^{\infty} \mathrm{d}x_1 \int_{-\infty}^{\infty} \mathrm{d}x_2\, f(x_1, x_2|h_1, h_2) = 1\,, \tag{8.4}$$

as required. There are infinite possibilities for the choice of kernel function. Two common choices are the standard Gaussian and the Epanechnikov kernel given by the following two functions respectively:

$$\begin{aligned} K_G(u) &= \frac{1}{\sqrt{2\pi}}\, e^{-\frac{1}{2}u^2} \\ K_E(u) &= \frac{3}{4}(1 - u^2) \cdot \mathrm{I}(|u| \leq 1)\,. \end{aligned} \tag{8.5}$$

$\mathrm{I}(|u| \leq 1)$ is equal to 1, if the condition in brackets is fulfilled and 0 otherwise. The Epanechnikov kernel is the kernel, which theoretically leads to the best convergence with the Gaussian having an efficiency, which is worse by $\sim$4% [119]. Moreover, in contrast to the

Gaussian kernel, the Epanechnikov kernel does not extend to infinity, so that at a particular position in parameter space only a limited number of calibration events contributes to the KDE estimate. A comparison of the two functions is shown in Fig. 8.1. The Gaussian kernel is obviously much wider than the Epanechnikov kernel. So it can be expected that larger bandwidths should be used for the latter. Note, that even though it is advisable to check it explicitely, the choice of kernel is not expected to change the results significantly. The authors of [119] use the concept of canonical kernels to separate the problem of the choice of bandwidth and kernel function. The conclusion is that "for practical purposes the choice of the kernel function is almost irrelevant for the efficiency of the estimate" considering its convergence to the true, unknown function. The determination of the bandwidths is the critical part of the KDE estimate.

Since the convolutions of these kernels with themselves are needed for one of the algorithms applied to determine the optimal bandwidths, these convolutions are given here for completeness:

$$\begin{aligned} K_G * K_G(u) &= \frac{1}{2\sqrt{\pi}}\, e^{-\frac{1}{4}u^2} \\ K_E * K_E(u) &= \left(\frac{3}{20}(4-5u^2) + \frac{3}{160}(20-u^2)\,|u|^3\right) \cdot \mathrm{I}(|u| \leq 2)\,, \end{aligned} \tag{8.6}$$

where $*$ denotes the convolution. The first formula represents the well known result that the distribution of a sum of two random variables, which obey Gaussian distributions with means μ_1 and μ_2 and standard deviations σ_1 and σ_2, is again a Gaussian with mean

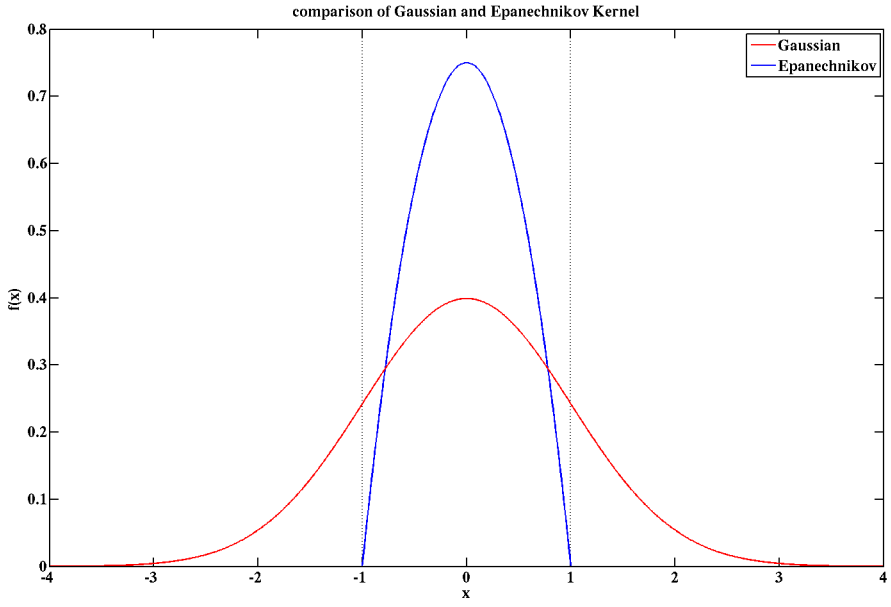

Figure 8.1: Comparison of the Gaussian and the Epanechnikov kernel.

$\mu_{1+2} = \mu_1 + \mu_2$ and standard deviation $\sigma_{1+2} = \sqrt{\sigma_1^2 + \sigma_2^2}$.

As just mentioned, determination of the bandwidths is the main issue regarding KDEs. A good way to start is to compute bandwidths according to Silverman's rule of thumb, which is given by

$$h_j = \left(\frac{4}{d+2}\right)^{\frac{1}{d+4}} n^{-\frac{1}{d+4}} \sigma_j \overset{d=2}{=} \frac{\sigma_j}{\sqrt[6]{n}}, \tag{8.7}$$

where h_j denotes the bandwidth corresponding to the variable x_j, and σ_j is the standard deviation computed based on the observations X_{ji}. n denotes the number of observations and d is the dimension of the distribution. Thus, in the given case $d = 2$. Silverman's rule of thumb yields the optimal bandwidth, given that the actual distribution is a multivariate Gaussian with uncorrelated parameters. Of course, under normal circumstances it is not known whether the distribution is Gaussian. In fact, if it was known, there would be no need to apply KDEs to determine the distribution. It would be much easier to use simple estimates to obtain the mean and standard deviation of the Gaussian. However, if the actual distribution is not too different from a Gaussian distribution, formula (8.7) should yield values, which are near the optimal ones. At least, the obtained values can be used as the start values for more advanced algorithms. Two frequently used methods are discussed in the following.

For both approaches it is necessary to consider the so-called "leave-one-out" estimator at the location of the j^{th} observation

$$f_{-j}(X_{1j}, X_{2j}|h_1, h_2) = \frac{1}{(n-1)\,h_1 h_2} \sum_{\substack{i=1 \\ i\neq j}}^{n} K\left(\frac{X_{1j} - X_{1i}}{h_1}\right) \cdot K\left(\frac{X_{2j} - X_{2i}}{h_2}\right), \tag{8.8}$$

which is just the normal KDE estimate, given in (8.2), neglecting the observation, which the distribution is evaluated at. This is necessary in order to get an unbiased estimate of the distribution at the position of the j^{th} observation.

One possible algorithm to determine the optimal bandwidth is referred to as "maximum-likelihood cross-validation". The likelihood function is given by the product of (8.8) over all observations:

$$L(h_1, h_2) = \prod_{j=1}^{n} f_{-j}(X_{1j}, X_{2j}|h_1, h_2)\,. \tag{8.9}$$

As usual, it is convenient to use the log-likelihood function

$$\begin{aligned} \log L(h_1, h_2) &= \frac{1}{n}\sum_{j=1}^{n} \log f_{-j}(X_{1j}, X_{2j}|h_1, h_2) \\ &= \frac{1}{n}\sum_{j=1}^{n} \log\left(\sum_{\substack{i=1 \\ i\neq j}}^{n} K\left(\frac{X_{1j} - X_{1i}}{h_1}\right) \cdot K\left(\frac{X_{2j} - X_{2i}}{h_2}\right)\right) \\ &\quad - \log\Big((n-1)h_1 h_2\Big), \end{aligned} \tag{8.10}$$

since it is easier to handle numerically. The factor of $1/n$ is added by convention. Optimal values of h_1 and h_2 are determined by searching for the maximum of the log-likelihood function, starting the maximization at the values determined from Silverman's rule of thumb (8.7). It should be noted that this function can be problematic, if the algorithm is used applying kernel functions with a finite support like the Epanechnikov kernel. If an observation is particularly far away form all other observations, it is necessary to apply very large bandwidths in order to prevent the log-likelihood function from diverging ($\to -\infty$). This can lead to an oversmoothing of the distribution.

The second algorithm is denoted "least-squares cross-validation". It is based on the minimization of the integrated squared error (ISE), defined by

$$\mathrm{ISE}(h_1, h_2) = \int_{-\infty}^{\infty} \mathrm{d}x_1 \int_{-\infty}^{\infty} \mathrm{d}x_2 \left(f(x_1, x_2|h_1, h_2) - f(x_1, x_2) \right)^2 , \tag{8.11}$$

where the second function without the parameters h_1 and h_2 denotes the true but unknown distribution, which is about to be approximated with the KDE. Given that the true distribution does not depend on the bandwidths, so that terms, which do not depend on the KDE, can be neglected, and that the expectation value of $f(x_1, x_2|h_1, h_2)$ is defined by

$$E\Big[f(x_1, x_2|h_1, h_2)\Big] = \int_{-\infty}^{\infty} \mathrm{d}x_1 \int_{-\infty}^{\infty} \mathrm{d}x_2 \, f(x_1, x_2|h_1, h_2) \cdot f(x_1, x_2) \, . \tag{8.12}$$

(8.11) can be written as

$$\mathrm{ISE}(h_1, h_2) = \int_{-\infty}^{\infty} \mathrm{d}x_1 \int_{-\infty}^{\infty} \mathrm{d}x_2 \left(f(x_1, x_2|h_1, h_2) \right)^2 - 2\, E\Big[f(x_1, x_2|h_1, h_2)\Big] \, . \tag{8.13}$$

The expectation value can be estimated based on the leave-one-out estimator:

$$E\Big[f(x_1, x_2|h_1, h_2)\Big] = \frac{1}{n} \sum_{j=1}^{n} f_{-j}(X_{1j}, X_{2j}|h_1, h_2) \, . \tag{8.14}$$

Finally, the integrated error can be determined to be given by:

$$\begin{aligned} \mathrm{ISE}(h_1, h_2) \;=\; & \frac{1}{n^2\, h_1 h_2} \sum_{j=1}^{n} \sum_{i=1}^{n} \left(K * K \left(\frac{X_{1j} - X_{1i}}{h_1} \right) \right) \cdot \left(K * K \left(\frac{X_{2j} - X_{2i}}{h_2} \right) \right) \\ & - \frac{2}{n(n-1)\, h_1 h_2} \sum_{j=1}^{n} \sum_{\substack{i=1 \\ i \neq j}}^{n} K \left(\frac{X_{1j} - X_{1i}}{h_1} \right) \cdot K \left(\frac{X_{2j} - X_{2i}}{h_2} \right) , \end{aligned} \tag{8.15}$$

where $*$ denotes the convolution, which is given for both considered kernels in (8.6). The optimal values of h_1 and h_2 are determined by minimizing ISE. Similar to the likelihood cross-validation the optimization is started at the values obtained from Silverman's rule of thumb. Even though both approaches only depend on two parameters, the optimization is

quite tricky due to the complicated form of the considered functions. Note, that the sums run over all acquired events in a given sample. Regarding the samples for the distributions based on nuclear-recoils, it can be up to a few thousand events. Moreover, the functions are usually quite flat around the extreme values rendering the proper determination of these values even more difficult.

Another topic, that needs to be discussed in this context, is adaptive smoothing. If the point density, which the estimate of the distribution is based on, is quite inhomogeneous, with some regions of a particularly high point density and some regions with a particularly low point density, fixed bandwidths for all data points might yield inappropriate results. Consider, a distribution with a high point density in the bulk of the distribution and a low point density in the tails, for example. If the final result is dominated by the bulk population, the obtained bandwidths might be quite small yielding a good, smooth estimate of the bulk, while the tails might be severly undersmoothed and thus exhibit spurious peaks. However, it can also be the other way around, so that the bandwidths are particularly large. In that case, the tails might be adequately described by the KDE estimate, while important features in the bulk might be washed out. In order to deal with this issue the method of adaptive smoothing was developed, which assigns different bandwidths to the kernel functions at each event's location based on the local point density. The approach is quite simple and works as follows. At first, a so-called pilot KDE is determined, where the optimum bandwidths h_1 and h_2 are determined by applying either the maxim-likelihood cross-validation (8.10) or the least-squares cross-validation (8.15). Subsequently, local bandwith factors λ_i are defined for each data point i by

$$\lambda_i = \left(\frac{g}{f(X_{1i}, X_{2i}|h_1, h_2)} \right)^{\alpha}, \tag{8.16}$$

where g denotes the geometric mean

$$g = \sqrt[n]{\prod_{i=1}^{n} f(X_{1i}, X_{2i}|h_1, h_2)}\,, \tag{8.17}$$

and $0 \leq \alpha \leq 1$ is the sensitivity parameter. It can be shown [121] that, regarding two-dimensional distributions, $\alpha = 0.5$ is expected to show the best performance. However, for this study, $\alpha = 0$, which is equivalent to omit the smoothing, since it yields $\lambda_i = 1$, and $\alpha = 1$ were also tested. Finally, the bandwidths are multiplied by the local bandwidth factors, which essentially yields different bandwidths at each event's location. Application of this scheme leads to the following update of the KDE estimate defined in (8.2):

$$f(x_1, x_2|h_1, h_2, \alpha) = \frac{1}{n\, h_1 h_2} \sum_{i=1}^{n} \frac{1}{\lambda_i^2} K\left(\frac{x_1 - X_{1i}}{\lambda_i h_1} \right) \cdot K\left(\frac{x_2 - X_{2i}}{\lambda_i h_2} \right). \tag{8.18}$$

In summary, all 56 distributions were estimated based on different ingredients of the KDE method. The Gaussian and the Epanechnikov kernel (8.5) were both tested by applying the maxim-likelihood cross-validation (8.10) and the least-squares cross-validation

(8.15). Moreover, adaptive smoothing parameters α of 0, 0.5 and 1 were used. Extensive investigations of the obtained results, based on KS-tests and visual inspection of the distributions, were necessary, in order to decide, which combination of these approaches finally gave the most reliable results. The remainder of this paragraph summarizes the most important conclusions drawn from this analysis. Regarding the Gaussian kernel, both cross-validation methods worked fine and gave very similar results in most cases. The maximum-likelihood cross-validation did not work properly for the Epanechnikov kernel, which was not unexpected, since this method tends to be unreliable applying kernel functions with a finite support, as mentioned before. The main issues were maxima at unreasonable large bandwidths or no true maxima at all. Therefore, results regarding the Epanechnikov kernel were only considered as trustworthy applying the least-squares cross-validation. As expected, it was observed that the bandwidths, obtained for the Epanechnikov kernel, were always significantly larger than those obtained for the Gaussian kernel. An example, illustrating the just discussed behaviour, is given in Fig. 8.2, which

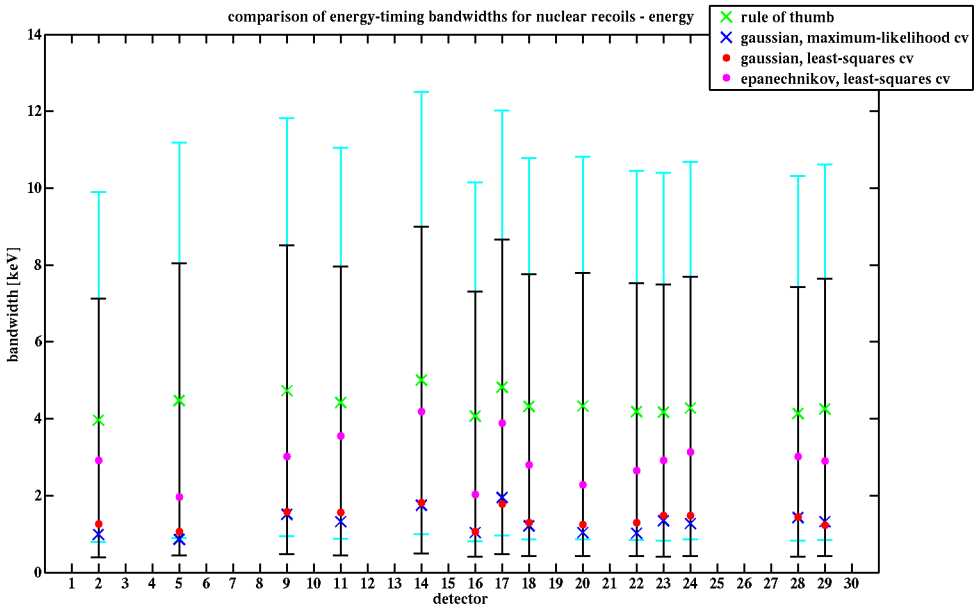

Figure 8.2: Comparison of the bandwidths for the KDEs regarding the recoil-energy for the timing distributions of the signal $f_s(t, E)$, obtained by applying the methods given in the legend. The results considering Gaussian kernels were very similar regarding the maximum-likelihood cross-validation (blue crosses) and the least-squares cross-validation (red dots). As expected, the bandwidths, considering the Epanechnikov kernel based on the least-squares cross-validation (magenta dots), were always significantly larger. The shown intervals were scanned applying a small step-size in order to test the accuracy of the optimization routines. The black intervals ($[0.1h_{\text{rot}}, 1.8h_{\text{rot}}]$) and the cyan intervals ($[0.2h_{\text{rot}}, 2.5h_{\text{rot}}]$) were respectively used for the Gaussian and the Epanechnikov kernel, where h_{rot} denotes the bandwidth obtained by applying Silverman's rule of thumb.

shows a comparison of the obtained bandwith regarding the recoil-energy for the timing distributions of the signal $f_s(t, E)$ for all used detectors. Regarding the three methods, Gaussian kernel applying the maxim-likelihood cross-validation, Gaussian kernel applying the least-squares cross-validation and Epanechnikov kernel applying the least-squares cross-validation, it seemed that the first approach yielded the most appropriate results considering the timing and yield distributions of the signal as well as the timing distributions of the background. The two other methods tended to undersmooth the distributions. Moreover, adaptive smoothing should be omitted, so $\alpha = 0$ should be used, particularly regarding the distributions of the signal. At high energies the point densities are very low due to the familiar low statistics problem of nuclear recoils. Thus, the KDEs, including adaptive smoothing, tended to be very wide with a much to low maximum. On the other hand, the distributions were extremely undersmoothed at low energies. Nevertheless, applying $\alpha = 0$ showed very convenient results. Examples for the three just discussed distributions for representative detectors can be found in Fig. 8.3 and in the top plot of Fig. 8.4. Determination of the yield distribution of the background was a special case. Since it was based on WIMP-search multiple scatters, statistics were very low and estimates for the individual detectors were quite difficult. At the end it was decided to combine the statistics from all detectors into a single distribution. This was adequate, since the yield distributions were quite similar in all detectors. Such a combination would not be possible for the timing distributions of the background, which however was not necessary, since they were based on barium calibration data with high statistics. Moreover, even though the optimization routines of the cross-validation methods found proper extrema, the results did not describe the distribution of the combined data adequately. The bandwidths were extremely small, so that the KDE exhibited spurious spikes and peaks. Unexpectedly, it turned out that the simple result from Silverman's rule of thumb, again with $\alpha = 0$, provided an adequate estimate of the distribution, which is shown in the bottom plot of Fig. 8.4. The discussed choices have a significant impact on the shapes of the final KDEs. Therefore, extreme care has to be taken when this scheme will be applied to the reprocessed data. This is by far the most delicate part of the likelihood analysis.

Since the discussed distributions are two-dimensional, an important part of the visual inspection was the comparison of slices through the estimated distributions at fixed recoil-energies with the data. If these slices are normalized to unity, they represent the conditional probability distributions of the ionization yield/timing parameter given the particular energy. For example, the top plot in Fig. 8.5 shows the conditional yield distribution at $E_0 = 30$ keV for detector T2Z3 and the previously discussed method. It is defined by

$$f_s(y|E_0) = \frac{f_s(y, E_0)}{\int \mathrm{d}y\, f_s(y, E_0)}\,. \tag{8.19}$$

The comparison to the data was performed by making normalized histograms of all data points within a thin slice around the considered energy E_0. If the width of this interval was too small, the histograms would be based on very low statistics, if it was too large, local trends might be washed out. For this study, an energy range of 4 keV, centered around

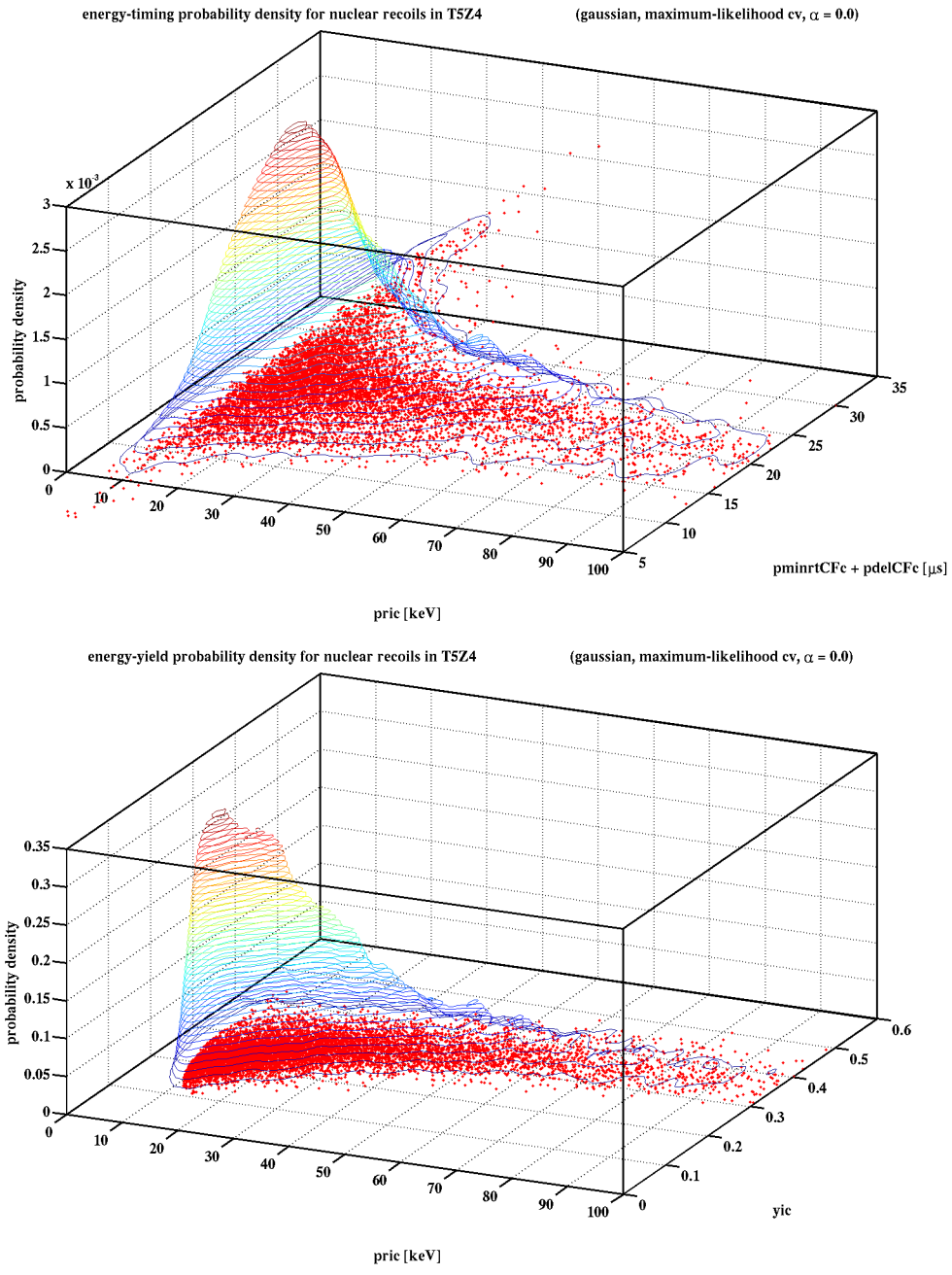

Figure 8.3: Timing $f_s(t, E)$ (top) and yield $f_s(y, E)$ (bottom) distributions of the signal as obtained from californium calibration data for detector T5Z4 applying the preferred method as given in the titles and discussed in the text.

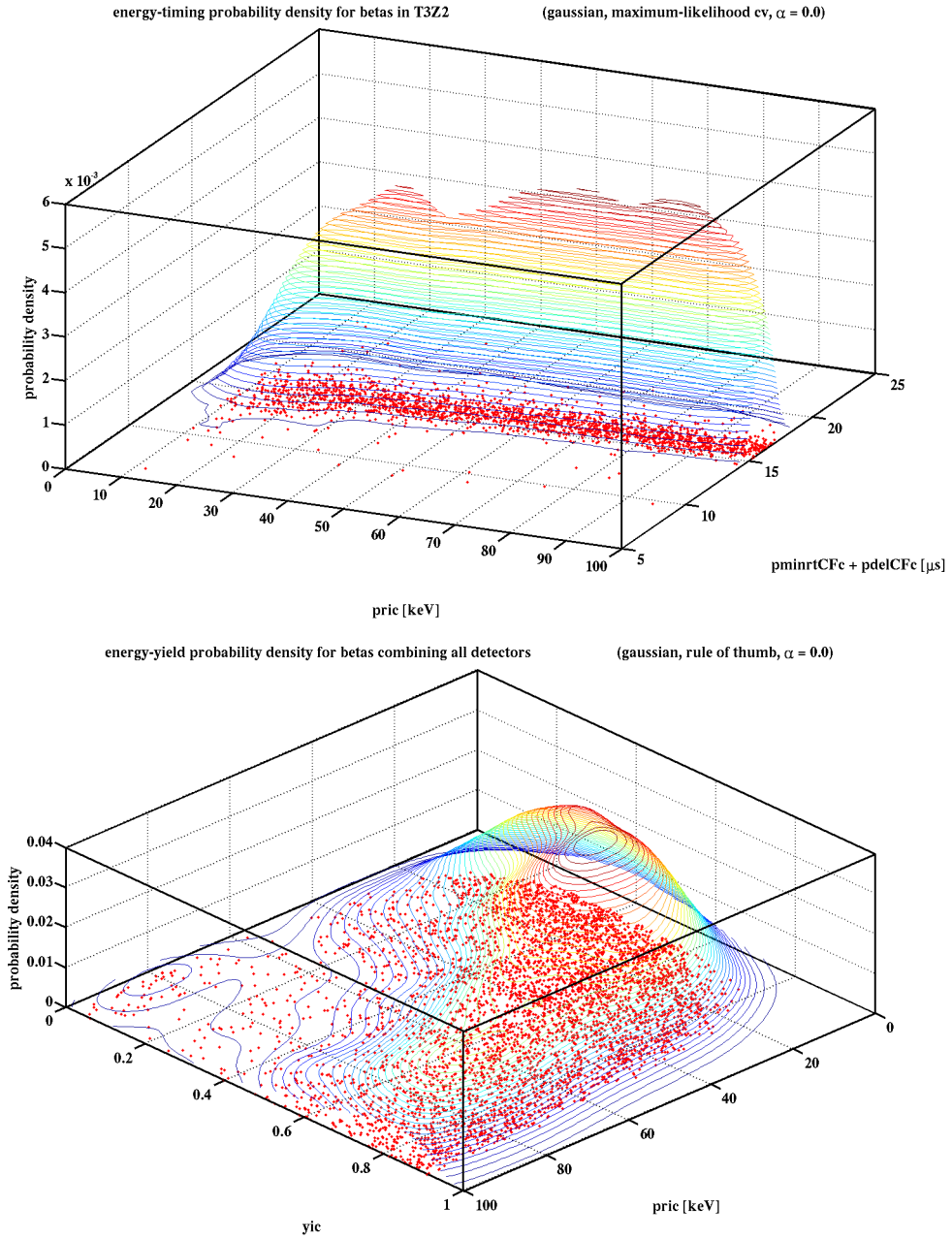

Figure 8.4: Timing distribution of the background $f_b(t, E)$ (top) as obtained from barium calibration data for detector T3Z2 applying the preferred method as given in the title and discussed in the text. The bottom plot shows the yield distribution of the background $f_b(y, E)$ based on WIMP-search multiple scatters. Events from all detectors were combined due to low statistics. Note, that the plot was rotated with respect to the top plot to improve the information value.

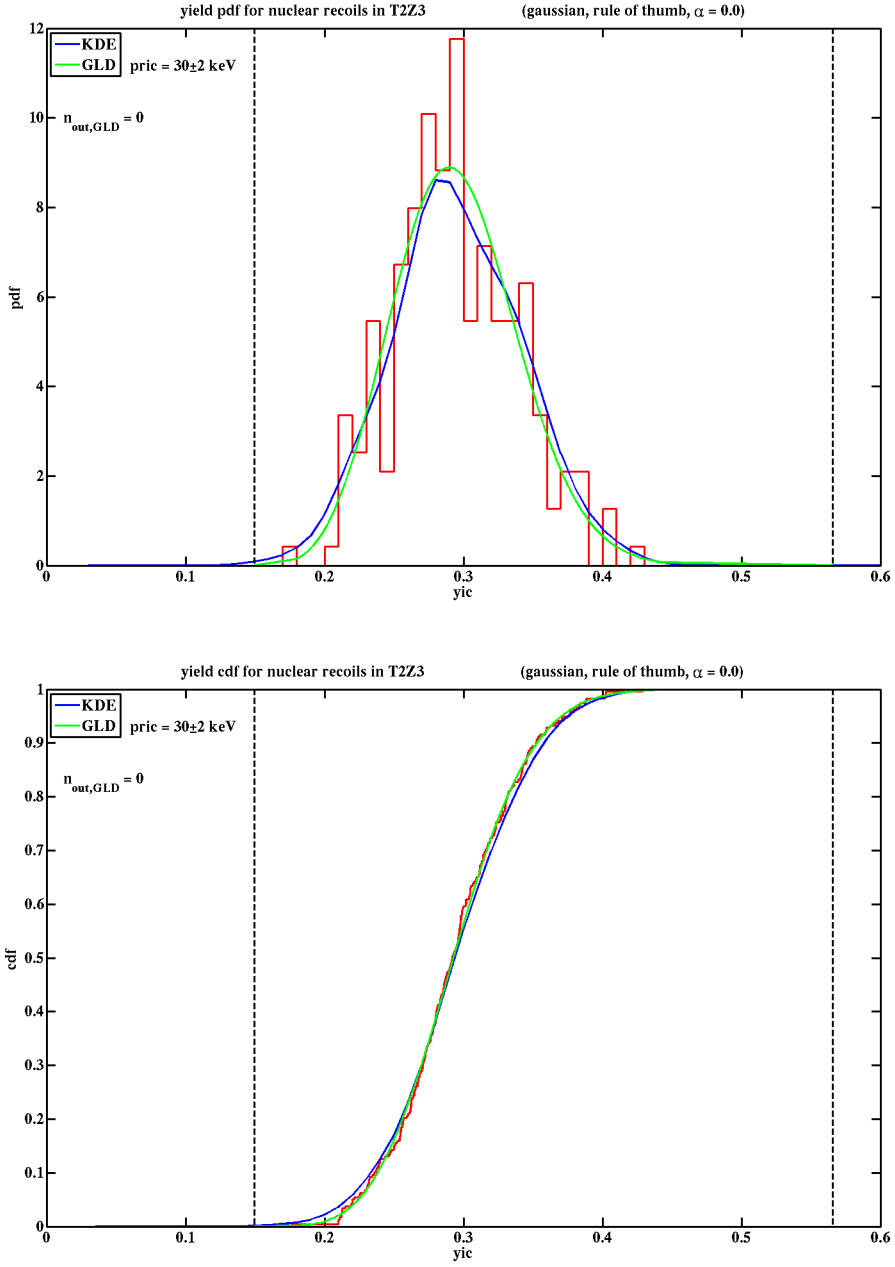

Figure 8.5: Probability distribution (top) and cumulative distribution (bottom) for the ionization yield (yic) parameter of the signal at a fixed recoil energy of 30 keV for detector T2Z3. Both plots show normalized slices through the KDE (blue), a histogram (top)/the empirical cumulative distribution function (bottom) based on the data ±2 keV around 30 keV (red) and the results obtained by fitting a GλD to the data (green). Both estimates describe the data very well, although the GλD fit seems to be slightly better. The vertical dashed lines denote the domain of the fitted GλD, and $n_{\text{out,GLD}}$ denotes the number of events outside that interval. See text for details.

E_0, was applied. Obviously, the histogram in the example plot is very similar to the KDE. Note, that the shown plot is representative for the quality of the estimates for the slices at different tested energies and for all discussed distributions. The corresponding cumulative distribution functions are shown in the bottom plot of the same figure, which can be used to perform KS-tests to check their similarity.

Apart from the normalized slices through the KDE, representing the conditional probability of the yield parameter at the fixed recoil energy, the plots also show the distributions obtained by fitting generalized lambda distributions (GλD) to the data, which was used for the histogram. A discussion of the methods, applied for this study, can be found in [122]. GλDs are not defined as parametrizations of the distributions themselves but as parametrizations of the corresponding quantiles. So slices of the cumulative distributions show whether a fit is a good one rather than the slices of the probability distributions. As an annotation, the definition via the quantile is quite useful regarding Monte Carlo studies, since random numbers obeying the corresponding distribution can be generated very quickly by just drawing random numbers from the standard uniform distribution (uniform between 0 and 1) and plugging them into the quantile function. The so-called FMKL parametrization [122], which is given by

$$x := Q(u) = \lambda_1 + \frac{1}{\lambda_2}\left(\frac{u^{\lambda_3} - 1}{\lambda_3} - \frac{(1-u)^{\lambda_4} - 1}{\lambda_4}\right), \tag{8.20}$$

was used for this analysis. The parameters λ_1 and λ_2 respectively determine the location and the scale of the distribution, while λ_3 and λ_4 determine its shape. The most important feature of these GλDs is the wide variety of shapes it can take. With this approach nearly all kinds of unimodal distributions can be described very accurately. However, this versatility comes with a price: The GλDs are very sensitive to the values of their four parameters, and their proper determination is quite challenging. Even though it is usually not possible to obtain a simple analytic form for the probability distribution itself, it can easily be plotted. Since Q denotes the quantile, it is the inverse of the cumulative distribution function F. From the identity $F(x) = F(Q(u)) = u$ it directly follows that

$$f(x) = \frac{1}{\frac{\partial}{\partial u}Q(u)} = \frac{\lambda_2}{\Big(u(x)\Big)^{\lambda_3 - 1} + \Big(1 - u(x)\Big)^{\lambda_4 - 1}}, \tag{8.21}$$

where u implicitly depends on x. Thus, plots of the probability distribution can be obtained by calculating x according to (8.20) and $f(x)$ according to (8.21) for a range of values for u between 0 and 1. Its domain is bounded by $Q(0)$ and $Q(1)$ yielding

$$\lambda_1 - \frac{1}{\lambda_2\lambda_3} \leq x \leq \lambda_1 + \frac{1}{\lambda_2\lambda_4}. \tag{8.22}$$

The distribution function $f(x)$ is normalized in this range, which can easily be shown:

$$\int_{\lambda_1 - \frac{1}{\lambda_2\lambda_3}}^{\lambda_1 + \frac{1}{\lambda_2\lambda_4}} \mathrm{d}x\, f(x) = \int_0^1 \mathrm{d}u\, \frac{\partial}{\partial u}Q(u)\, \frac{1}{\frac{\partial}{\partial u}Q(u)} = \int_0^1 \mathrm{d}u = 1\,. \tag{8.23}$$

Note, that the authors of some papers consider it to be a main drawback, if the number of events outside this interval is not zero and reject a fit, even though it seems appropriate otherwise. This was occasionally the case for the given analysis. However, these events were all very extreme outliers.

The actual estimation of the parameters was performed following the least-squares method outlined in [122], which was considered to be more appropriate than, for example, the moment-matching method discussed in the same paper. It is based on the minimization of the function

$$G(\lambda_1, \lambda_2, \lambda_3, \lambda_4) = \sum_{i=1}^{n} \Big(x_i - E_i(\lambda_1, \lambda_2, \lambda_3, \lambda_4) \Big)^2 , \tag{8.24}$$

where the sum runs over all observations n at the values x_i and E_i denotes the corresponding expectation values given the GλD with parameters λ_1, λ_2, λ_3 and λ_4. It can be written as

$$E_i(\lambda_1, \lambda_2, \lambda_3, \lambda_4) = \lambda_1 + \frac{Z_i(\lambda_3, \lambda_4)}{\lambda_2} \tag{8.25}$$

with

$$Z_i(\lambda_3, \lambda_4) = \frac{1}{\lambda_3} \left(\frac{\Gamma(n+1)\,\Gamma(i+\lambda_3)}{\Gamma(i)\,\Gamma(n+\lambda_3+1)} - 1 \right) - \frac{1}{\lambda_4} \left(\frac{\Gamma(n+1)\,\Gamma(n-i+\lambda_4+1)}{\Gamma(n-i+1)\,\Gamma(n+\lambda_4+1)} - 1 \right) , \tag{8.26}$$

where Γ is the gamma function. The parameters λ_3 and λ_4 have to be calculated numerically by minimizing the function

$$H(\lambda_3, \lambda_4) = -\Big(r_{xZ}(\lambda_3, \lambda_4) \Big)^2 , \tag{8.27}$$

where r_{xZ} is the correlation coefficient of x_i and Z_i. The numerical calculation is quite involved, since H often exhibits numerous local minima and thus finding the absolute one is difficult. Subsequently, λ_1 and λ_2 can be calculated analytically and are given by

$$\begin{aligned} \lambda_1 &= \mu_x - b_{xZ}\,\mu_z \\ \lambda_2 &= \frac{1}{b_{xZ}} , \end{aligned} \tag{8.28}$$

where μ_x and μ_Z denote the means of x_i and Z_i respectively, while b_{xZ} is the regression coefficient of x_i and Z_i.

From examining plots of the cumulative distributions, as shown in the bottom plot of Fig. 8.5, for slices at different recoil energies and for all considered distributions, it seemed that the GλDs often described the data slightly better than the best KDEs did. However, since the GλDs only describe one-dimensional distributions, it would be necessary to rely on an energy binning and to fit the obtained parameters to get distributions, which vary smoothly with energy. As expected due to the sensitivity of the GλDs to their parameters, the parameters varied considerably with energy, and often there was not even a clear trend to be seen. Thus, performing reasonable fits to these parameters is nearly impossible.

Usage of a very fine energy binning would finally amount to a scenario, where the fits could just be performed directly to the distributions around the energies of the WIMP candidates, and this seems quite artificial. It is rather desirable to obtain global estimates of the distributions and the described KDEs provide a very good way to achieve this. Thus, for the analysis of the reprocessed data it is planned to apply KDEs based on the aforementioned methods and to converge on the best possible estimates based on KS-tests and visible inspection. After having applied these estimates to the WIMP-search data, the obtained probability densities at the events' locations in parameter space could be cross checked by performing GλD fits to the timing and yield distributions at the events' energies. But this should just be a cross check and not the primary analysis approach as just discussed. Such a test seems more appropriate than comparing the results from slighlty different KDE estimates based on different methods.

The next step is to combine the two-dimensional distributions $f_{s,b}(t, E)$, $f_{s,b}(y, E)$ to the full three-dimensional estimates $f_{s,b}(t, y, E)$. Regarding simple probabilities p of single "events" t, y and E the result could be computed according to

$$p(t \cap y \cap E) = p(y \cap E) \cdot p(t|y \cap E) = p(y \cap E) \cdot p(t|E) = p(t|E) \cdot p(y|E) \cdot p(E)\,, \quad (8.29)$$

where $p(t|y \cap E) = p(t|E)$ only holds, because t and y are assumed to be independent. Applying this reasoning to the used probability distributions yields

$$f_{s,b}(t, y, E) = \frac{f_{s,b}(t, E)}{\int \mathrm{d}t f_{s,b}(t, E)} \cdot \frac{f_{s,b}(y, E)}{\int \mathrm{d}y f_{s,b}(y, E)} \cdot f_{s,b}(E)\,, \quad (8.30)$$

where the first two factors are the conditional distributions of the single random variables t and y respectively, as in (8.19), which can be taken from the KDE estimates. Here, the recoil energy E is just treated as a constant parameter. These distributions correspond to the slices through the two-dimensional distributions, as shown in the top plot of Fig. 8.5. The third factor simply is the energy distribution.

For the surface events the energy distribution is estimated based on WIMP-search multiple scatters, the same event population, which was used for the yield distribution of the background. Thus, with

$$f_b(E) = \int \mathrm{d}y f_b(y, E)\,, \quad (8.31)$$

which is the distribution of E regardless of the value of y, the full surface-event background distribution is given by

$$f_b(t, y, E) = \frac{f_b(t, E) \cdot f_b(y, E)}{\int \mathrm{d}t f_b(t, E)}\,. \quad (8.32)$$

For the energy distribution of the signal it was assumed that WIMPs obey the differential event rate $\frac{\mathrm{d}R}{\mathrm{d}E}$, given in (2.21), which depends on the WIMP mass m_W and the WIMP-nucleon cross section σ. The efficiency of each detector was taken into account introducing a slight detector-dependent difference of the spectra. Since the charge threshold and the lower edge of the 3σ electron-recoil band were used as the boundaries of the signal region,

the efficiency of the analysis needed here could be directly inferred from the efficiency of the standard anlysis discussed in chapter 6.4. However, it was necessary to neglect the nuclear-recoil cut and the timing cut, which were not applied for the likelihood analysis. Figure 8.6 shows the obtained final efficiency for detector T1Z2, where the result was exposure-weighted over the four considered runs. Except for low recoil energies the efficiency is roughly between 60% and 70%, which holds true for all detectors. The significant increase compared to the efficiency of the standard analysis, which is ∼30% as shown in Fig. 6.18, is due to the fact that the two aforementioned cuts, in particular the surface-event rejection cut, were not applied here. This increase in signal acceptance is an important advantage of cut-free methods like the maximum-likelihood approach. Including the efficiency, the energy distribution of the signal was given by:

$$f_s^{m_W}(E) = \frac{\dfrac{\mathrm{d}R}{\mathrm{d}E} \cdot \mathrm{eff}(E)}{\displaystyle\int_{E_{\mathrm{lower}}}^{E_{\mathrm{upper}}} \mathrm{d}E \, \frac{\mathrm{d}R}{\mathrm{d}E} \cdot \mathrm{eff}(E)} \,, \tag{8.33}$$

where the additional index m_W indicates that the distribution depends on the WIMP mass. Since the cross section just appears as a multiplicative factor in the rate, the distribution

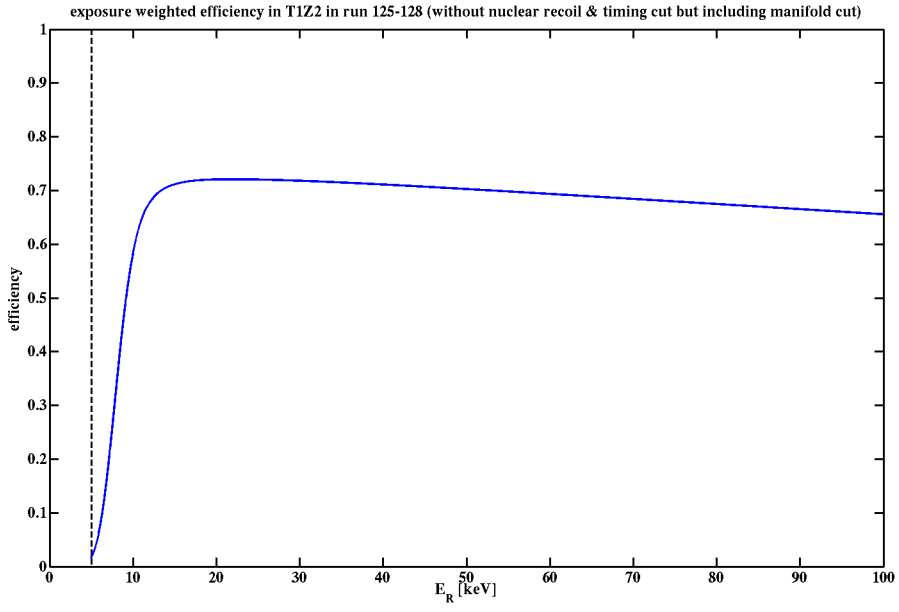

Figure 8.6: Exposure-weighted efficiency for detector T1Z2 used for the likelihood analysis. The nuclear-recoil cut and the timing cut were neglected with respect to the standard analysis. All other cuts were inherited from that analysis.

is independent of σ. Thus, the full three-dimensional distribution is given by

$$f_s^{mw}(t,y,E) = \frac{f_s(t,E)}{\int \mathrm{d}t f_s(t,E)} \cdot \frac{f_s(y,E)}{\int \mathrm{d}y f_s(y,E)} \cdot \frac{\dfrac{\mathrm{d}R}{\mathrm{d}E} \cdot \mathrm{eff}(E)}{\displaystyle\int_{E_{\mathrm{lower}}}^{E_{\mathrm{upper}}} \mathrm{d}E \, \frac{\mathrm{d}R}{\mathrm{d}E} \cdot \mathrm{eff}(E)} \,. \tag{8.34}$$

In other words, the theoretical prediction is applied for the energy distribution, and it is assumed that for a given energy the yield and timing distributions are the same for WIMPs as for neutrons from the californium calibrations.

As an annotation, it was also tried to consider neutrons as a possible background. In this case, the energy distribution was obtained from the applied KDEs similar to the case of surface events. In particular, the distribution was based on nuclear recoils from the californium calibration data within the 2σ nuclear-recoil band, so the events considered for the determination of the timing distribution of the signal. Thus, with

$$f_b^n(E) = \int \mathrm{d}t f_s(t,E) \,, \tag{8.35}$$

the full neutron background distribution was given by

$$f_b^n(t,y,E) = \frac{f_s(t,E) \cdot f_s(y,E)}{\int \mathrm{d}y f_s(y,E)} \,, \tag{8.36}$$

where the additional index n indicates that this is the distribution of neutrons and not of surface events, which is the primary background. Note, that in this model the distributions of WIMPs and neutrons have the same timing and yield dependence. Thus, only the energy dependence can be used to distinguish between both kinds of events. Including neutrons the log-likelihood function, given in (8.1), should be updated to

$$\log L(\nu_s, \nu_b, \nu_b^n) = -(\nu_s + \nu_b + \nu_b^n) + \sum_{i=1}^{n} \log\left(\nu_s f_s(\underline{p}_i) + \nu_b f_b(\underline{p}_i) + \nu_b^n f_b^n(\underline{p}_i)\right) , \tag{8.37}$$

where ν_b^n denotes the expectation value of the neutron background. However, the routine, discussed in the next chapter, yielded the result that this expectation value, treated as a free (nuisance) parameter, was exactly zero in most detectors, independent of the assumed WIMP parameters. This was not a numerical issue. It rather indicates that it is not possible to identify a very small contribution of neutrons to the total event sample, particularly because the WIMP and neutron distributions are quite similar. Apart from the yield and timing distributions, which were explicitly assumed to be identical, the energy spectra also had a very similar shape, which of course depended on the WIMP mass determining the actual energy spectrum of the signal. This is illustrated in Fig. 8.7, which shows a comparison of the energy spectra of the neutron background, surface-event background and WIMPs for three different assumed WIMP masses. Thus, it was not a reliable approach to determine the neutron contribution directly from the likelihood method. Since Monte Carlo

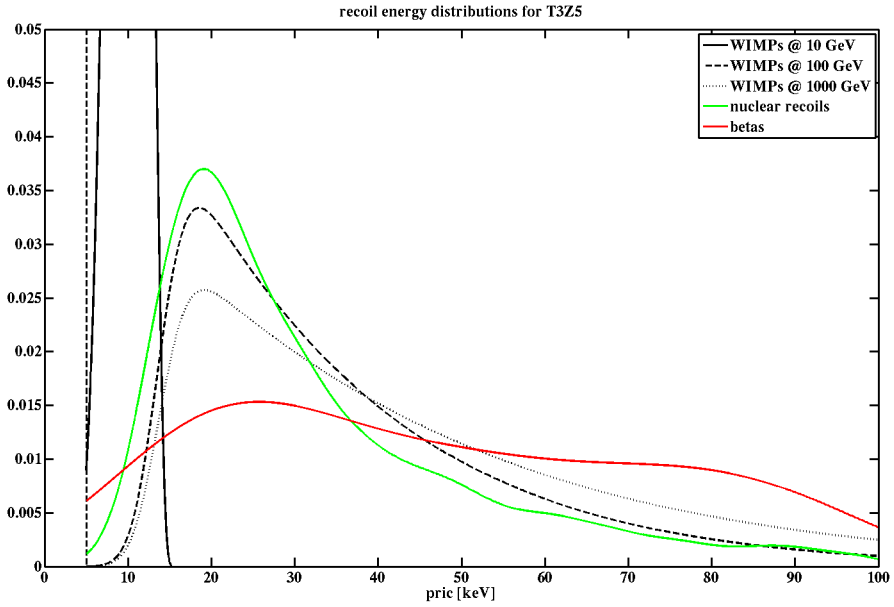

Figure 8.7: Comparison of the energy (pric) spectra of the neutron background (green), surface-event background (red) and WIMPs for three different assumed WIMP masses (black, as given in the legend) for detector T3Z5. The WIMP spectrum for $m_W = 10$ GeV/c^2 is localized at very small recoil energies and thus extends to densities high above the shown range. The drop down of the spectra near the threshold of 5 keV is induced by the decreasing acceptance, as shown in Fig. 8.6. The necessary inclusion of this efficiency yields different WIMP spectra for different detectors. The WIMP spectrum for $m_W = 100$ GeV/c^2 and the spectrum of the neutron background are very similar. The surface event-spectrum is comparably flat.

simulations indicated that it should be very small (see Table 6.3), it should be appropriate to just neglect this contribution, which is done in the discussion in the remainder of this chapter.

There are three possible improvements, which might be considered for the analysis of the reprocessed data. First of all, the just mentioned Monte Carlo simulations could be used to constrain the parameter ν_b^n, so that the neutron background could be included but did not have to be determined as a by-product from the likelihood analysis.

The second improvement is related to an update of the yield part of the WIMP-distribution itself. As discussed before, it was assumed that WIMPs and neutrons from the californium calibration data have the same yield distribution. However, WIMPs should be single scatters, while a large part of the neutrons scatter multiple times in a single detector. So far, a correction regarding systematic differences between single and multiple scatters was only incorporated in the CDMS analysis in the context of the fiducial-volume cut, as discussed in chapter 6.4.3.5. However, there should also be systematic differences between the yield distributions of single-scatter nuclear recoils expected from WIMPs and neutrons from the californium calibration data. Since, as shown in Fig. 5.3, the ionization yield of

events within the nuclear-recoil band is increasing with energy, a multiple scatter event, where the total measured recoil energy is split between several lower-energy recoils, should appear at lower yield than a single internal scatter of the same recoil energy. For the discussion of this effect it is appropriate to denote the yield parameter in the distribution of the calibration data y_C and the one in the (unknown) distribution of single scatters y_W. The distributions themselves are respectively denoted $f_s^C(y_C, E)$ and $f_s^W(y_W, E)$. Since differences should be only slight, the approach

$$f_s^W(y_W, E) = a\, f_s^C(a\, y_W + b, E) \tag{8.38}$$

should be sufficient to unfold the observed neutron-yield distribution from the calibrations into the expected WIMP-yield distribution. This transformation is capable of including a shift and rescaling, while maintaining the proper normalization of the distribution f_s^C obtained by applying the KDE approach to the calibration data. The recoil energy is assumed to require no correction. The expectation values E and variances V of y_C and y_W for given recoil energy E are connected by the two conditions

$$\begin{aligned} \mathrm{E}[y_W|E] &= \frac{\mathrm{E}[y_C|E] - b}{a} \\ \mathrm{V}[y_W|E] &= \frac{\mathrm{V}[y_C|E]}{a^2}\,, \end{aligned} \tag{8.39}$$

which can easily be verified by direct calculation. At the same time, the difference between y_C and y_W could be parameterized by an energy dependent offset $s(E)$: $y_C = y_W + s$. This ansatz also yields two simple conditions regarding the expectation values and the variances:

$$\begin{aligned} \mathrm{E}[y_W|E] &= \mathrm{E}[y_C|E] - \mathrm{E}[s|E] \\ \mathrm{V}[y_W|E] &= \mathrm{V}[y_C|E] - \mathrm{V}[s|E]\,. \end{aligned} \tag{8.40}$$

Equalizing (8.39) and (8.40) results in the following expressions for the unknown parameters a and b:

$$\begin{aligned} a &= \sqrt{\frac{\mathrm{V}[y_C|E]}{\mathrm{V}[y_C|E] - \mathrm{V}[s|E]}} \\ b &= a\,\mathrm{E}[s|E] + (1-a)\,\mathrm{E}[y_C|E]\,. \end{aligned} \tag{8.41}$$

$\mathrm{E}[y_C|E]$ and $\mathrm{V}[y_C|E]$ are the expectation value and the variance of the nuclear recoils in the californium calibration data, which, in fact, were already used for the definition of the nuclear-recoil bands. $\mathrm{E}[s|E]$ and $\mathrm{V}[s|E]$ need to be estimated based on Monte Carlo simulations. They should be relatively insensitive to the actual input of the Monte Carlo. E.g., if the used distribution $f_s^W(y_W, E)$ was comparably narrow, the estimates of $\mathrm{E}[s|E]$ and $\mathrm{V}[s|E]$ should still be realistic. In summary, going back to the original notation of this chapter, $f_s(y, E)$, as obtained from californium calibration data, should not be evaluated

at y but at $ay+b$ when performing the likelihood analysis. Subsequently, the result should be multiplied by the factor a. A preliminary correction following this scheme has already been calculated. Figure 8.8 shows the effect of the obtained transformation $y \rightarrow ay + b$. The red lines represent the mean and 2σ nuclear-recoil bands as obtained from californium calibration data, exposure-weighted over all detectors. The corresponding band, which should be valid for single scatters like WIMPs, are shown as blue lines. Obviously, the transformation $y \rightarrow ay+b$ shifts the yield to lower values and also widens the distribution. So, to summarize, the true WIMP distribution is expected to have slightly higher yield and also be slightly tighter than the distribution obtained from calibration neutrons. This correction can be approximated by the simple deconvolution from the neutron distribution given in formula (8.38) with the parameters given in (8.41). However, it was observed that this slight correction has only a minor impact on the results of the likelihood analysis, which are discussed in the next section.

So far, a possible dependence of the ionization yield and timing parameter, in particular regarding the background distribution, has been neglected. However, as mentioned before, such a correlation would not be surprising, since both parameters are sensitive to the depth of an interaction. As both distributions are determined based on different data sets, the ionization yield on WIMP-search multiple scatters and the timing parameter on barium calibration data, which is necessary due to systematic differences, it is also unclear

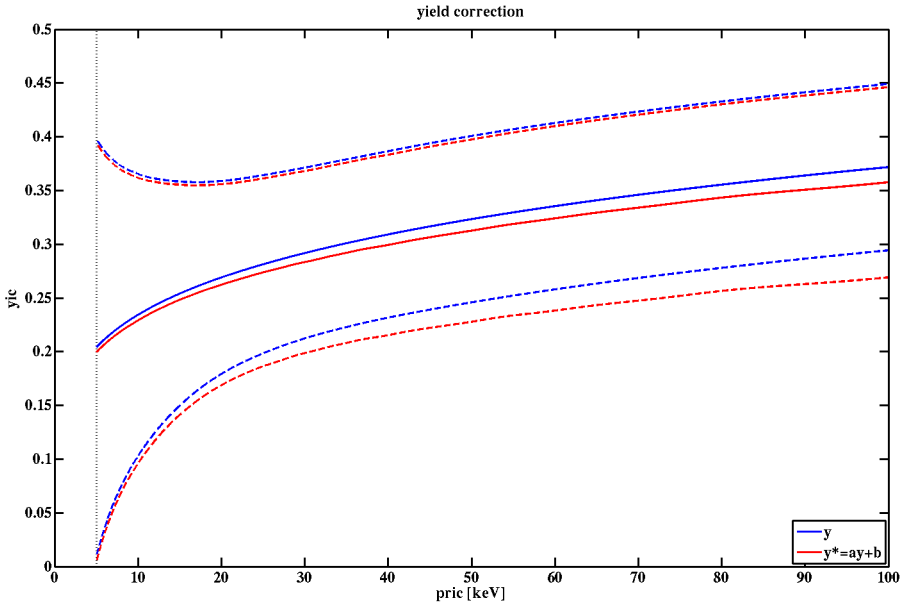

Figure 8.8: Estimated difference between the yield bands of nuclear-recoils from calibration neutrons (red), which induce single and multiple scatters, and single scatters, as expected from WIMP interactions (blue). The solid lines represent the means of the bands, while the dashed lines denote the corresponding 2σ bands. The applied transformation is discussed in the text.

how to investigate such a correlation properly. Nevertheless, tests have been performed to check a possible dependence of both parameters based on the barium calibration data, since statistics are much higher. For each detector the surface events, which additionally resided within the nuclear-recoil band, were divided into several energy bins. An illustration of this segregation for detector T3Z4 is shown in Fig. 8.9. Subsequently, for each energy bin the timing distribution of the events in the upper half of the nuclear-recoil band was compared to the corresponding distribution in the lower half of the band applying a KS-test. Figure 8.10 shows a color-coded summary of the p-values from the KS-tests obtained for each detector and considered energy bin. The p-values give the probability for a KS-test statistic, defined as the maximum difference between the two compared cumulative distribution functions, to be larger than the observed one. For example, a p-value of 0.05 means that the null hypothesis, which states that both compared samples are drawn from the same distribution, is rejected at 95% C.L. In other words, low p-values, shown as dark/blue in the plot, indicate that both samples are quite different. It can be observed that for most detectors and energy bins the KS-test does not indicate that the null hypothesis should be rejected, which gives confidence in the decision to neglect a dependence of ionization yield and timing parameter. It might be argued that this conclusion was only due to the comparably low statistics of surface events from the barium calibration data within the nuclear-recoil band. However, similar tests were performed based on surface events at higher ionization yield with higher statistics, which lead to the same result.

Nevertheless, a correction was developed to approximately take a dependence of both

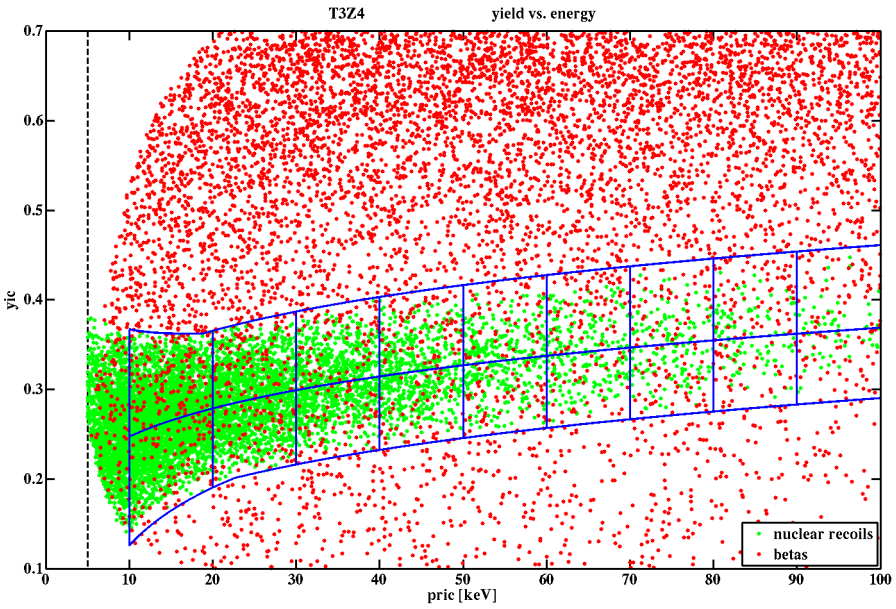

Figure 8.9: Segregation of surface events for the KS-test, performed in order to test the assumption that the ionization yield and the timing parameter of surface events are nearly independent.

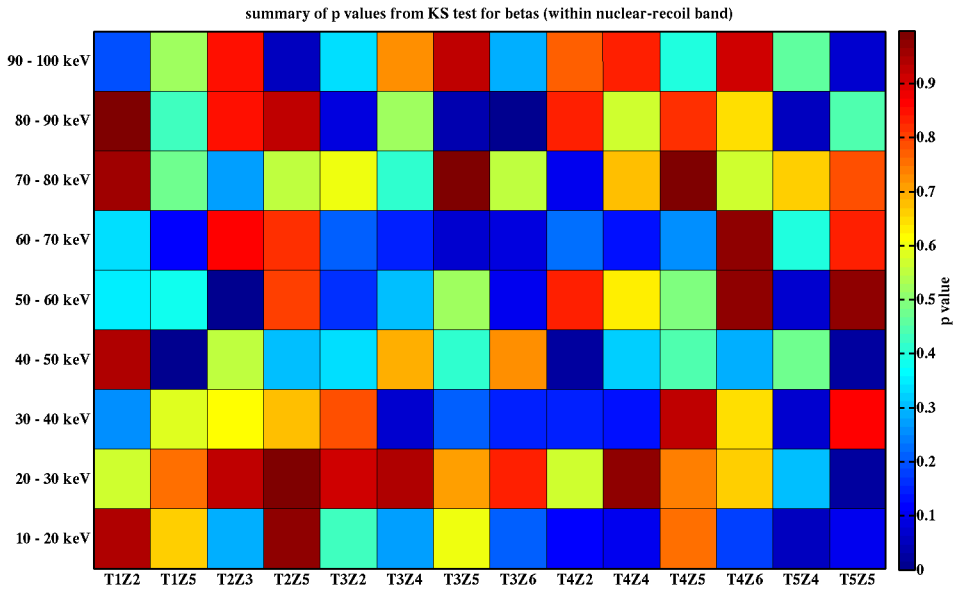

Figure 8.10: Summary of p-values from KS-tests performed to check the independence of the ionization yield and the timing parameter. Low p-values, represented by dark/blue colors, indicate that the tested distributions (see text) are quite different. They are obviously similar in most detectors and energy bins.

parameters into account. This approach, which is discussed in the following, will be tested considering the analysis of the reprocessed data. To introduce this correction, it is useful to write the estimate for the surface-event background (8.32) in its original form (8.30)

$$f_b(t,y,E) = \frac{f_b(t,E)}{\int \mathrm{d}t f_b(t,E)} \cdot \frac{f_b(y,E)}{\int \mathrm{d}y f_b(y,E)} \cdot \int \mathrm{d}y f_b(y,E) = f_b(t|E) \cdot f_b(y|E) \cdot f_b(E)\,. \quad (8.42)$$

The first two factors denote the combined distribution of ionization yield y and timing parameter t for given recoil energy E. In its current form

$$f_b(t,y|E) = f_b(t|E) \cdot f_b(y|E) \quad (8.43)$$

a possible dependence is neglected. An approximate way to incorporate such a dependence is given by

$$f_b^C(t,y|E) = f_b(t|E) \cdot f_b(y|E) \cdot \left(1 + \rho[t,y|E] \cdot \frac{t - \mathrm{E}[t|E]}{\sqrt{\mathrm{V}[t|E]}} \cdot \frac{y - \mathrm{E}[y|E]}{\sqrt{\mathrm{V}[y|E]}}\right), \quad (8.44)$$

where the term in the large brackets represents a correction factor. As before, E and V denote the expectation value and variance for given recoil energy E. They can be estimated

based on the approach neglecting correlations between y and t (8.43), which yields

$$\begin{aligned} \mathrm{E}[y|E] &= \frac{\int \mathrm{d}y\, y\, f_b(y,E)}{\int \mathrm{d}y f_b(y,E)} \\ \mathrm{E}[y^2|E] &= \frac{\int \mathrm{d}y\, y^2\, f_b(y,E)}{\int \mathrm{d}y f_b(y,E)} \\ \mathrm{V}[y|E] &= \mathrm{E}[y^2|E] - \Big(\mathrm{E}[y|E]\Big)^2 , \end{aligned} \tag{8.45}$$

and similar formulae for the timing parameter. Since

$$\begin{aligned} \mathrm{E}\Big[y - \mathrm{E}[y|E]\Big|E\Big] &= 0 \\ \mathrm{E}\Big[t - \mathrm{E}[t|E]\Big|E\Big] &= 0 , \end{aligned} \tag{8.46}$$

the corrected distribution is still properly normalized. Moreover, the marginal distributions, where one of the two variables is integrated out, are not affected by the correction, as it should be:

$$f_b^C(y|E) = \int \mathrm{d}t\, f_b^C(t,y|E) = f_b(y|E) \tag{8.47}$$

$$f_b^C(t|E) = \int \mathrm{d}y\, f_b^C(t,y|E) = f_b(t|E) \tag{8.48}$$

The parameter ρ denotes the correlation coefficient between y and t. If it is calculated based on the estimate (8.43), it would be zero as expected. However, if it is evaluated directly based on the data (in several energy bins), correlations will render it non-zero. A very small correlation coefficient would indicate that its effect can be neglected. Otherwise, usage of the corrected distribution (8.44) can take much of it into account.

As discussed in this section, estimating the signal and background distributions is a highly non-trivial issue with many difficulties. The next sections contain discussions of various methods, which can be applied in order to obtain preferred regions (or upper limits) in the parameter space of the WIMP mass and WIMP-nucleon cross section based on the maximum-likelihood method.

8.2 "Standard" approach to the likelihood analysis

After having discussed estimates of the signal and background distributions, the actual likelihood analysis based on the log-likelihood function (8.1) can be performed. It was indicated that it depends on the expectation values of the signal ν_s and the surface-event background ν_b. However, the expectation value of the signal is given as a function of the WIMP-nucleon cross section σ and WIMP mass m_W:

$$\nu_s(\sigma, m_W) = \mathrm{MT} \cdot \int_{E_{\mathrm{lower}}}^{E_{\mathrm{upper}}} \mathrm{d}E\, \frac{\mathrm{d}R}{\mathrm{d}E} \cdot \mathrm{eff}(E) , \tag{8.49}$$

with the exposure MT, the differential event rate $\frac{\mathrm{dR}}{\mathrm{d}E}$, which introduces the dependence on σ and m_W, and the energy-dependent efficiency eff. Only spin-independent scattering is considered for this analysis. Moreover, in the previous section it was argued that the signal distribution $f_s^{m_W}(t, y, E)$ depends on the WIMP mass. So the likelihood function should not just be considered as a function of ν_s and ν_b. It is rather given as a function of three parameters, the WIMP-nucleon cross section (via ν_s), the WIMP mass (via ν_s and $f_s^{m_W}$) and the background expectation value ν_b. ν_b enters the computation as a nuisance parameter, whose actual value is not of interest. So the correct approach is

$$L = L\big(\sigma, m_W, \nu_b\big) \; . \tag{8.50}$$

There are two convenient ways to deal with nuisance parameters, the Frequentist and the Bayesian approach. In the latter it is assumed that the nuisance parameters are random variables, which can be removed from the likelihood function via integration. This approach is discussed in the next section.[2] In the Frequentist approach the nuisance parameters are considered to be fixed parameters with an unknown value, which can be effectively removed by constructing the profile-likelihood function L_p. For the given case it is defined by

$$L_p(\sigma, m_W) = L\Big(\sigma, m_W, \widehat{\nu}_b(\sigma, m_W)\Big) \; , \tag{8.51}$$

where $\widehat{\nu}_b(\sigma, m_W)$ denotes the values of ν_b, which maximize the likelihood function for fixed σ and m_W. So in the Frequentist approach the nuisance parameters are removed via maximization, while they are integrated out in the Bayesian approach.

In order to obtain L_p, it was necessary to calculate ν_s (8.49) on a very tiny grid in the cross-section versus WIMP-mass plane first. These computations were performed separately for all used detectors taking the appropriate efficiency and exposure into account. The total number of expected WIMPs, summed over all detectors, is shown in Fig 8.11. The lower black line is the 90% C.L. upper limit of all runs combined, while the upper blue line is the limit using only runs 125–128, which emerged from the analysis presented in chapter 6. Both limits were already shown in Fig. 6.24. As only data of runs 125–128 were included in the likelihood analysis, its result should be compared to the limit shown in blue.

In the next step, the values of $\widehat{\nu}_b$ were calculated by maximizing the logarithm of the likelihood function for all detectors separately. This was a very simple calculation, since for given σ and m_W there was only one remaining unknown parameter (the nuisance parameter) per detector. Moreover, for given σ and m_W, the likelihood function, considered as a function of ν_b, was always nearly Gaussian with a clear maximum. This was due to the large number of events in the considered WIMP-search region. Note, that the number of events passing all selection criteria in the cut-based analysis was extremely small (just two events), since the nuclear-recoil cut and the timing cut were applied. As a byproduct of this calculation, the values of the profile-likelihood function at each considered parameter point were directly obtained.

[2] Note, that this method was already discussed in the context of the Bayesian leakage estimate in chapter 7.2.

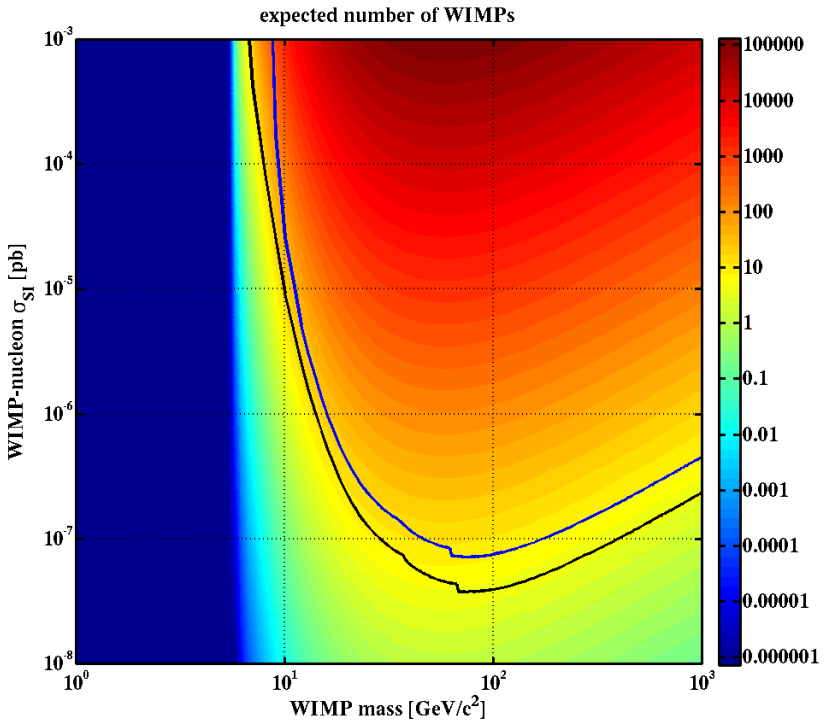

Figure 8.11: Total expected number of WIMPs in runs 125–128 as indicated by the color-code. Due to the recoil-energy threshold of 5 keV, no WIMPs are expected in the blue region below WIMP masses of ∼6 GeV/c^2. The lower black line is the 90% C.L. upper limit from all runs combined, while the upper blue line is the limit only using runs 125–128, which were both already shown in Fig. 6.24.

The results of the individual detectors were combined in the following way: The full likelihood function simply is the product of the single likelihood functions of all detectors, and the log-likelihood function is accordingly given by the sum of the individual log-likelihood functions. So actually it would be necessary to sum-up all log-likelihood functions, and thus compute the full profile-log-likelihood function. However, this function would contain 14 nuisance parameters (one for each considered detector), so that the maximization might be computationally difficult. Fortunately, this can be done much easier. The profile-log-likelihood function is obtained by sampling over σ and m_W and subsequently varying only the nuisance parameters to find the maximum. However, σ and m_W are the only parameters appearing in the likelihood functions of all detectors. If these parameters are fixed, as it is done computing the profile-likelihood function, the contributions of all detectors are independent. Thus, the values of the nuisance parameters, which maximize the individual likelihood functions, are also the ones which maximize the full likelihood function (for

given σ and m_W). In short, the full profile-log-likelihood function is simply given by the sum over the profile-log-likelihood functions from each detector. This is very convenient since, as discussed in the previous paragraph, determining the “best” values of ν_b is a very simple calculation for individual detectors. The profile-likelihood function for all detectors combined is shown in Fig. 8.12. It exhibits a distinct maximum near WIMP masses of $\sim$15 GeV/c^2 and cross sections of $\sim 10^{-6}$ pb.

As mentioned in chapter 5.1.2, confidence regions at a confidence level C can be determined by finding all parameter values, which the log-likelihood function decreases at by $Q_{C,n}/2$, where $Q_{C,n}$ denotes the quantile of order C of the χ^2 distribution with n degrees of freedom, from its maximum value:

$$\log L_p(\sigma, m_W) = \log L_p^{\max} - \frac{Q_{C(\sigma,m_W),n}}{2} \,. \tag{8.52}$$

This equation is frequently used in maximum-likelihood analyses. It is designed to yield a certain probability by choosing a fraction of the integrated likelihood, which is a Bayesian probability with a flat prior. However, this equation is actually correct, only if the likelihood function is Gaussian, which usually is only true in the case of high statistics. Regard-

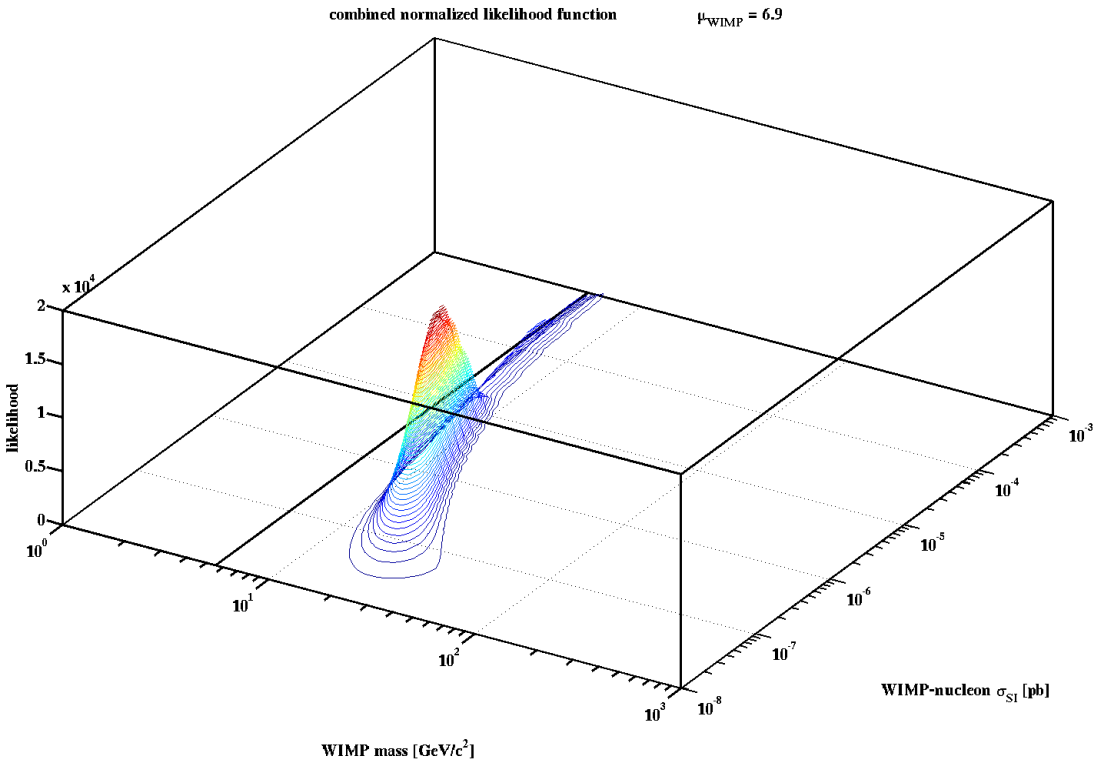

Figure 8.12: Profile-likelihood function for all detectors combined. A distinct maximum resides near WIMP masses of $\sim$15 GeV/c^2 and cross sections of $\sim 10^{-6}$ pb. The experiment is insensitive to WIMP masses below $\sim$6 GeV/c^2 indicated by the black line, because of the 5 keV threshold.

ing Fig 8.12 it can be argued that this simple method will yield quite reasonable results, but that it is desirable to additionally investigate other methods in order to estimate favored regions in parameter space. This is done in subsequent sections of this chapter, where, among other things, favored regions are defined by explicit integration of the likelihood function. The application of this equation was the main reason for denoting the approach discussed in this section "standard" method, since it is frequently used, even in cases where its applicability is questionable. Note, that this approach has a Frequentist/Bayesian character, since the nuisance parameters were treated as constant parameters and removed via maximization of the likelihood function.

Equation (8.52) can be solved for C yielding:

$$C(\sigma, m_W) = F_{\chi^2,n}\left(-2\log\frac{L_p(\sigma, m_W)}{L_p^{\max}}\right), \tag{8.53}$$

where $F_{\chi^2,n}$ denotes the cumulative distribution function of the χ^2 distribution. For two degrees of freedom this formula can be simplified, since the χ^2 distribution, given by

$$f_{\chi^2,2}(u) = \frac{1}{2}e^{-\frac{u}{2}}, \tag{8.54}$$

can be analytically integrated:

$$C(\sigma, m_W) = \int_0^{-2\log\frac{L_p(\sigma,m_W)}{L_p^{\max}}} \mathrm{d}u\, f_{\chi^2,2}(u) = 1 - \frac{L_p(\sigma, m_W)}{L_p^{\max}}. \tag{8.55}$$

Thus, the confidence level at each considered parameter point can be easily calculated from the profile-likelihood function.

In roughly one half of the detectors upper limits were obtained, while in the other half an indication for a signal at low WIMP masses was found. Figure 8.13 shows the results based on the combination of all detectors, which exhibits a closed contour at 2σ confidence level around WIMP masses of $\sim$15 GeV/c^2 and cross sections of $\sim 10^{-6}$ pb. The WIMP parameters, which maximize the profile-likelihood function yield 6.9 expected events in the exposure of runs 125–128. Note, that this does not contradict the observation of just two WIMP candidates in the standard analysis discussed in chapter 6. First of all, the efficiencies used for the likelihood analysis were more than a factor of two higher, since the timinig cut and the nuclear-recoil cut could be neglected. Moreover, a threshold of 5 keV was used here, while the threshold for the standard analysis was set to 10 keV, which greatly improves the sensitivity to low-mass WIMPs. This is evident from the shown WIMP spectrum assuming a WIMP mass of 10 GeV/c^2 in Fig. 8.7. The preferred region is of similar shape as the ones computed by some theorists and shown in [117, 118], which were already mentioned at the beginning of this chapter, though it is closed at a much higher confidence level, due to the higher accuracy of the applied likelihood method. Note, however, that these results are highly preliminary, since they are based on the unreprocessed data. Especially the low-mass region, where a hint for a WIMP signal is found, is very sensitive to changes of the parameters of WIMP candidates at low energies. Thus, it is not possible to draw a final conclusion from the results shown here. The discussed approach will be applied to the reprocessed data in the very near future.

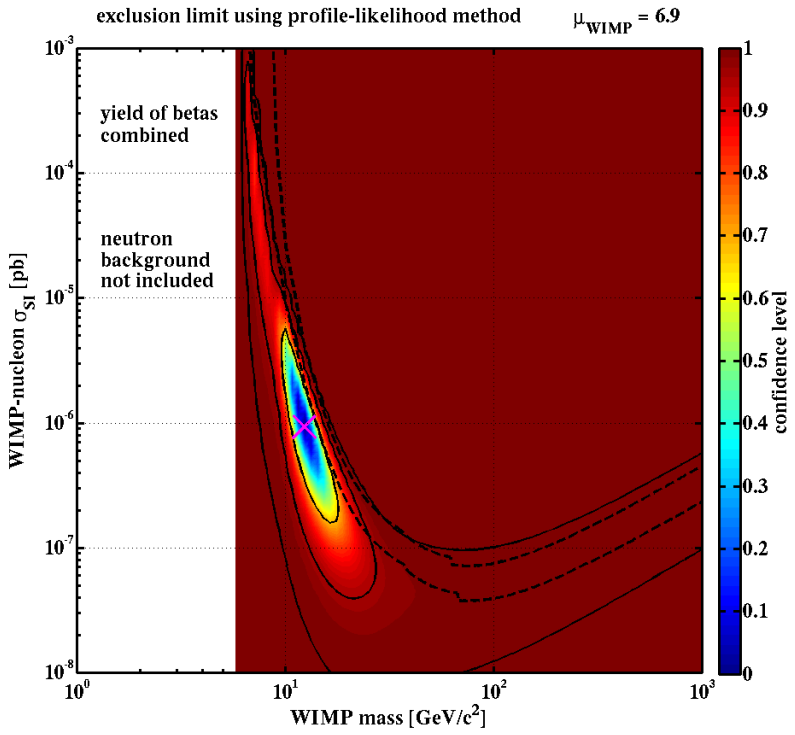

Figure 8.13: Preferred regions from the "standard" likelihood analysis of the CDMS data. The color-code denotes the confidence level of each considered point in parameter space. The three black/solid lines correspond to confidence levels of 1σ, 2σ and 3σ (from inside to outside). The magenta cross marks the parameters, which maximize the profile-likelihood function. They yield an expected number of 6.9 WIMPs for the analyzed exposure. The dashed lines denote the upper limits of the standard analysis also shown in Fig. 8.11. The upper line is the limit of runs 125–128 and the lower line is the one of all Soudan runs combined. Note, that these results are highly preliminary, since they were calculated based on the unreprocessed data. See text for details.

8.3 Computing allowed regions with a Bayesian approach

In the last section, the nuisance parameters of the likelihood function were treated as fixed parameters and removed via maximization of the likelihood function, which is a Frequentist approach. The method to calculate preferred regions was based on a Bayesian method, however the used equation (8.52) was only an approximation. A correct Bayesian treatment regarding the nuisance parameters and the parameters of interest is discussed in the current section.

Bayesian techniques were already used in chapter 7.2 regarding the calculation of the

surface event leakage. Application of Bayes' theorem (7.15) essentially means that the posterior likelihood function is obtained by multiplying the given likelihood function with an appropriate prior and a factor assuring proper normalization. In this scheme all parameters are considered as random variables. At first, it is necessary to remove the nuisance parameters via integration to obtain a likelihood function L_B, which only depends on the parameters of interest. This is the analogon to the profile-likelihood function discussed in the previous section and defined in (8.51). At first, only one detector is considered. Given an estimate $h(\nu_b)$ of the distribution of ν_b, which can be used as the prior, the posterior is defined by

$$L_B(\sigma, m_W) = c \cdot \int_{-\infty}^{\infty} \mathrm{d}\nu_b \, L\big(\sigma, m, \nu_b\big) \cdot h(\nu_b) \,, \tag{8.56}$$

where the factor c denotes the normalization constant. In case of a perfectly known background ($\nu_b = \nu_{b0}$) this approach yields a very intuitive result, since with $h(\nu_b) = \delta(\nu_b - \nu_{b0})$, where δ denotes Dirac's delta function, $L_B(\sigma, m_W) = L\big(\sigma, m, \nu_{b0}\big)$ is obtained. However, in the given case no background estimate was available. Therefore, a simple uniform prior, which is a common choice in such cases, with a cutoff at $\nu_b = 0$ was used:

$$h(\nu_b) = \begin{cases} 1 & \text{if } \nu_b \geq 0 \\ 0 & \text{if } \nu_b < 0 \,, \end{cases} \tag{8.57}$$

which yields

$$L_B(\sigma, m_W) = c \cdot \int_{0}^{\infty} \mathrm{d}\nu_b \, L\big(\sigma, m, \nu_b\big) \,. \tag{8.58}$$

It should be noted that in the given case the actual form of the prior was not expected to have a significant impact on the final result, since, as mentioned in the previous section, the likelihood function, considered as a function of ν_b, was always nearly Gaussian with a clear maximum.

The full likelihood function, combined over all detectors, is simply the product of the contributions of the individual detectors:

$$L\big(\sigma, m_W, \underline{\nu}_b\big) = \prod_{i=1}^{14} L_i\big(\sigma, m_W, \nu_{b,i}\big) \,. \tag{8.59}$$

In order to remove the nuisance parameters it was necessary to integrate them out. This is an integral over 14 parameters, but similar to the approach regarding the maximization discussed in the previous section, the evaluation of this integral can be greatly simplified:

$$L_B(\sigma, m_W) = c \cdot \left(\prod_{i=1}^{14} \int_0^{\infty} \mathrm{d}\nu_{b,i} \right) L(\sigma, m_W, \underline{\nu}_b) = c \cdot \prod_{i=1}^{14} \int_0^{\infty} \mathrm{d}\nu_{b,i} \, L_i\big(\sigma, m_W, \nu_{b,i}\big) = c \cdot \prod_{i=1}^{14} L_{B,i}(\sigma, m_W) \,. \tag{8.60}$$

In other words, the posterior distribution for all detectors combined is obtained by simply multiplying the posterior distributions from the individual detectors. The final result was equal to the profile-likelihood function, which was shown in Fig. 8.12. This was a very

convenient result, since it indicated that the difference between removing the nuisance parameters by maximization of the likelihood function or by integration of the likelihood function over these parameters seems to be negligible.

Subsequently, Bayesian credibility regions had to be calculated. In the previous section, this was done by applying the approximation (8.52) or rather (8.55). However, the analysis in the current section follows the correct Bayesian scheme. At first, it is necessary to consider appropriate priors for σ and m_W. Unlike the case of the nuisance parameters even the order of magnitude of these parameters is completely unknown. Thus, uniform priors are not a good choice here. The Jaynes prior, again with a cutoff at zero, defined by

$$h(\sigma) = \begin{cases} \frac{1}{\sigma} & \text{if } \sigma \geq 0 \\ 0 & \text{if } \sigma < 0\,, \end{cases} \tag{8.61}$$

for σ and in the same way for m_W, is much more appropriate, since it is equivalent to a uniform prior on a logarithmic scale. Finally, credibility regions were obtained by integrating the product of L_B and the two priors, demanding that they were bounded by contours of constant probability:

$$C(\sigma, m_W) = \frac{\iint_{L_B(\sigma', m'_W) \geq L_B(\sigma, m_W)} \mathrm{d}\sigma'\, \mathrm{d}m'_W\, L_B(\sigma', m'_W) \frac{1}{\sigma'} \frac{1}{m'_W}}{\int_0^\infty \int_0^\infty \mathrm{d}\sigma'\, \mathrm{d}m'_W\, L_B(\sigma', m'_W) \frac{1}{\sigma'} \frac{1}{m'_W}}\,. \tag{8.62}$$

Even though L_B was normalized to unity, the denominator had to be added to ensure proper normalization, since non-uniform priors were used.

The final result based on this procedure is shown in Fig. 8.14. It should be compared to Fig. 8.13 of the previous section. The fact, that both approaches yield very similar results, assures confidence in the likelihood approach to the CDMS data. Note again, that these results are highly preliminary.

8.4 Computing allowed regions with a Feldman and Cousins approach

In the previous two sections it was discussed that the choice of the method for removing the nuisance parameters, maximization or integration, was nearly irrelevant for obtaining a likelihood function, which only depends on the two parameters of interest, the WIMP-nucleon cross section and the WIMP mass. So Bayesian and Frequentist methods yield very similar results in this regard. However, considering the actual calculation of preferred regions in the parameter space of σ and m_W, only Bayesian techniques have been investigated yet. Thus, the CDMS collaboration is also developing a Frequentist approach for this part of the likelihood analysis. It is based on the so-called Feldman and Cousins method [123], which has achieved good acceptance in the particle physics community. This approach

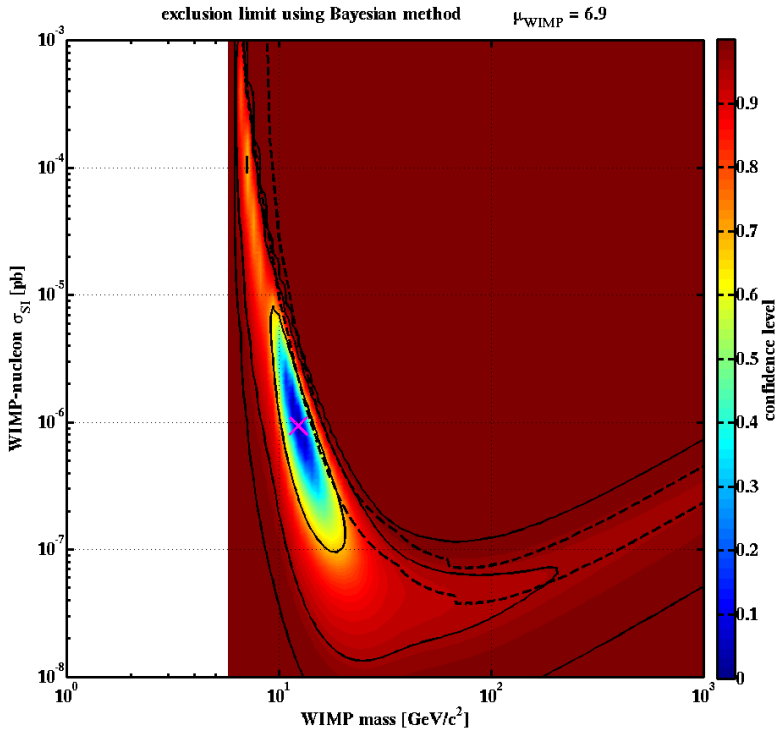

Figure 8.14: Preferred regions from a Bayesian likelihood analysis of the CDMS data. The color-code denotes the confidence level of each considered point in parameter space. The three solid black lines correspond to confidence levels of 1σ, 2σ and 3σ (from inside to outside). The magenta cross marks the parameters with the highest probability. They yield an expected number of 6.9 WIMPs for the analyzed exposure. The dashed lines denote the upper limits of the standard analysis also shown in Fig. 8.11. The upper line is the limit of runs 125–128 and the lower line the one of all Soudan runs combined. Note, that these results are highly preliminary, since they were calculated based on the unreprocessed data. See text for details.

has not be finalized yet, so the current section just outlines the method and discusses the emerging difficulties.

In a Bayesian framework, where the parameters are considered as random variables, the obtained credibility regions include a certain fraction of the likelihood function (multiplied by the priors) by definition. This means that e.g. the degree of belief, that the parameters are within the 90% region, is 90%. As mentioned in the introduction, the Feldman and Cousins method is a Frequentist approach. In this case, the meaning of the obtained confidence regions is entirely different.[3] They are defined by demanding, that if the same

[3]Note, that in the context of Bayesian statistics preferred regions are called "credibility" regions, while they are called "confidence" regions in Frequentist statistics.

experiment was repeated a large number of times and preferred regions were constructed, e.g. the 90% C.L. region would contain the fixed unknown value in 90% of the experiments.

The Feldman and Cousins method was developed to deal with issues related to the statistical analysis of small signals, so it is appropriate for the analysis of dark matter direct detection experiments like CDMS. An ordering principle based on likelihood ratios is used to determine classical (Frequentist) confidence regions, which provide exact coverage. The main advantage of this method is the fact, that the decision of whether an upper limit or a two-sided confidence region should be computed is directly incorporated into the algorithm and does not depend on the experimenter's choice. This is of particular importance, since the developers of the method have shown in their paper that otherwise the obtained regions can substantially undercover, which means that the confidence level of an estimated 90% region can actually be much lower.

In the following, the method is presented for a simple example of a Gaussian with a cutoff at zero following [123]. Afterwards some annotations are made regarding its application to the CDMS data. Assuming $\sigma = 1$ for simplicity, the Gaussian distribution is given by

$$p(x|\mu) = \frac{1}{\sqrt{2\pi}} e^{-\frac{1}{2}(x-\mu)^2}, \tag{8.63}$$

where μ is demanded to be non-negative ($\mu \geq 0$). In this notation x represents the measured value of μ, which obeys fluctuations because of Gaussian noise. The best estimate of μ denoted $\widehat{\mu}$ is the one, which maximizes $p(x|\mu)$ obeying the mentioned constraint on μ. It is given by

$$\widehat{\mu} = \begin{cases} x & \text{if } x \geq 0 \\ 0 & \text{if } x < 0\,. \end{cases} \tag{8.64}$$

In the Feldman and Cousins approach confidence regions are defined based on the likelihood ratio

$$R(x|\mu) = \frac{p(x|\mu)}{p(x|\widehat{\mu})} = \begin{cases} e^{-\frac{1}{2}(x-\mu)^2} & \text{if } x \geq 0 \\ e^{x\mu - \frac{\mu^2}{2}} & \text{if } x < 0\,. \end{cases} \tag{8.65}$$

For given μ, 90% confidence intervals $[x_1,\, x_2]$ are constructed by adding values of x to the given interval in decreasing order of R until the total likelihood reaches 0.9. In other words, for each μ the interval is obtained by finding x_1 and x_2, so that $R(x_1|\mu) = R(x_2|\mu)$ and

$$\int_{x_1}^{x_2} \mathrm{d}x\, p(x|\mu) = 0.9\,. \tag{8.66}$$

This construction is shown for a particularly small and a quite large value of μ in Fig. 8.15. In the latter case, where μ is far away from the boundary at zero, the obtained result is equal to the classical central confidence interval as it must. It is defined by demanding

$$\begin{aligned} \int_{-\infty}^{x_1} \mathrm{d}x\, p(x|\mu) &= \frac{1-0.9}{2} \\ \int_{x_2}^{\infty} \mathrm{d}x\, p(x|\mu) &= \frac{1-0.9}{2}\,. \end{aligned} \tag{8.67}$$

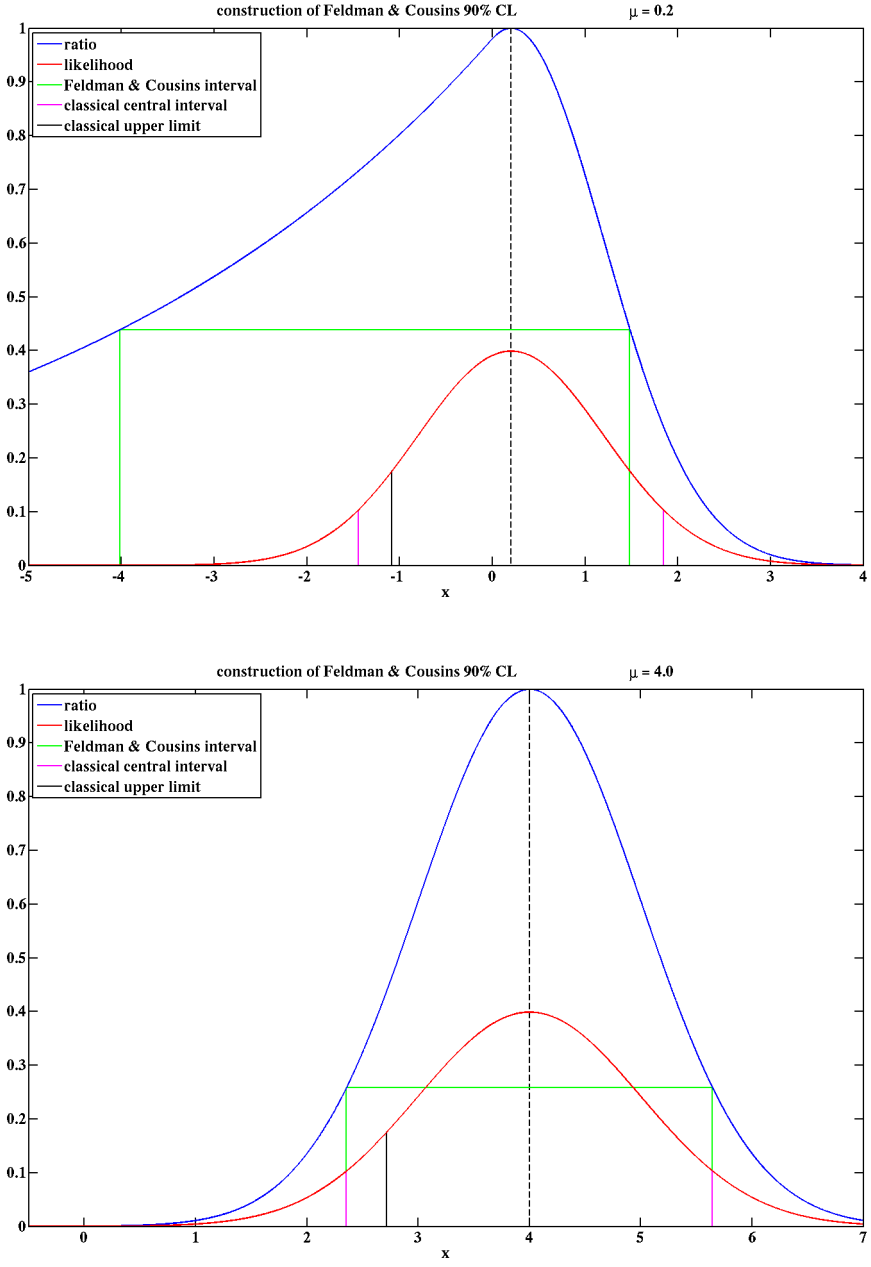

Figure 8.15: Construction of Feldman and Cousins 90% confidence intervals for a Gaussian (with $\sigma = 1$) with a boundary at the origin for $\mu = 0.2$ (top) and $\mu = 4.0$ (bottom). The red and the blue curves are the Gaussians and the likelihood ratios, which the ordering for the Feldman and Cousins approach is based on, respectively. Apart from the Feldman and Cousins intervals (green), the plots also contain the classical central intervals (magenta) and the classical upper limits (black). For large μ, as in the bottom plot, the Feldman and Cousins intervals and the classical central intervals are identical.

Classical upper limits x_u are defined by simply demanding

$$\int_{-\infty}^{x_u} \mathrm{d}x\, p(x|\mu) = 1 - 0.9\,. \tag{8.68}$$

See the summary at the beginning of [123] for a short discussion of the construction of classial confidence belts.

Calculating the Feldman and Cousins intervals for various values of μ led to the confidence belt shown as the green/dashed line in Fig. 8.16. From this plot it should also be clear that the lower boundaries on x for given μ yield upper boundaries on μ for given x, which was the reason for denoting x_u an upper limit. Note, that x is the measured variable. Obviously, there is a smooth transition from two-sided confidence intervals for large values of x to upper limits for small values of x.

In situations that are more complicated, it is usually necessary to obtain the distributions of R for each considered point in parameter space based on Monte Carlo simulations. For the simple example of the Gaussian with a cutoff at the origin this approach would be as follows: For each value of μ, that should be tested, perform a large number of Monte Carlo simulations by drawing e.g. 10000 random numbers x from the Gaussian given in (8.63).

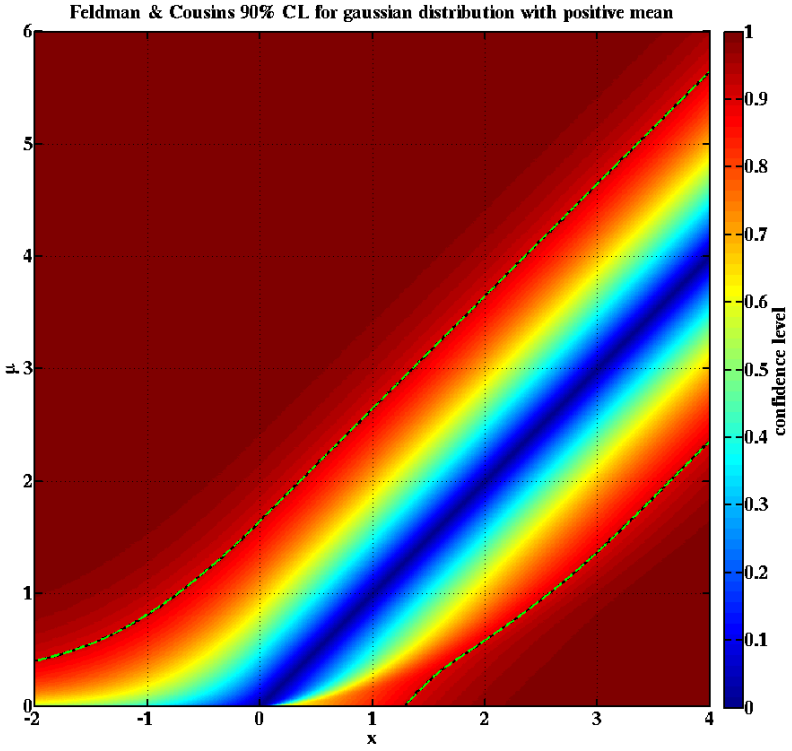

Figure 8.16: Confidence levels for the mean of a Gaussian with a cutoff at the origin. The color-code represents the results from the Monte Carlo approach. The 90% level is given by the confidence belt represented by the black/solid lines, which perfectly coincides with the belt obtained analytically (green/dashed).

For each of these possible experimental outcomes calculate the likelihood ratio (8.65). A histogram of the obtained values represents the distribution of the likelihood ratio for given μ denoted $g(R_\mu)$. Subsequently, calculate the likelihood ratio for the result x_0, that was actually observed, for each tested value of μ denoted $R_\mu(x_0)$. Finally, the confidence level $C(\mu)$, which each parameter point is accepted at, is given as the fraction of $g(R_\mu)$, which is larger than $R_\mu(x_0)$:

$$C(\mu) = \int_{R_\mu(x_0)}^{1} \mathrm{d}R_\mu \; g(R_\mu) \; . \tag{8.69}$$

Results from this Monte Carlo approach are also shown in Fig. 8.16. The color-code denotes the confidence levels at each point in parameter space. The 90% level is given by the confidence belt represented by the black/solid lines. Statistics from the Monte Carlo were high enough, so that this result perfectly coincides with the belt obtained with the simpler approach discussed before.

Before continuing with the discussion of this method in the context of the CDMS analysis, it is interesting to note, that in the case of high statistics the (Frequentist) Feldman and Cousins approach yields exactly the same results as the (Bayesian) "standard" method based on equation (8.52). It is quite simple to show this explicitly. As given in (8.53) the standard method yields the following confidence level at a given parameter η:

$$C_{\text{standard}}(\eta) = F_{\chi^2,n}\Big(-2\log\frac{L(\eta)}{L^{\max}}\Big) = F_{\chi^2,n}\Big(-2\log R_\eta(x_0)\Big) \, , \tag{8.70}$$

where n denotes the dimension of η, and x_0 denotes the actual observation. Considering the application to the CDMS data η represents σ and m_W. In the case of high statistics it can be assumed that Wilk's theorem holds, which states that $Z_\eta := -2\log R_\eta$ obeys a χ^2-distribution with n degrees of freedom $f_{\chi^2,n}$. In order to calculate confidence levels following Feldman and Cousins it is necessary to determine the distribution of R_η. It is given by

$$g(R_\eta) = \int_0^\infty \mathrm{d}Z_\eta \, f_{\chi^2,n}(Z_\eta) \cdot \delta\Big(R_\eta - e^{-\frac{Z_\eta}{2}}\Big) = f_{\chi^2,n}\Big(-2\log R_\eta\Big) \cdot \frac{2}{R_\eta} \, , \tag{8.71}$$

and defined in the interval $(0,\, 1]$. Note, that $g(R_\eta) = 1$ for two degrees of freedom, which is the case for the analysis of the CDMS data. Subsequently, the Feldman and Cousins confidence levels can be calculated to be

$$C_{\text{FC}}(\eta) = \int_{R_\eta(x_0)}^{1} \mathrm{d}R_\eta \; g(R_\eta) = \int_0^{-2\log R_\eta(x_0)} \mathrm{d}u \; f_{\chi^2,n}(u) = F_{\chi^2,n}\Big(-2\log R_\eta(x_0)\Big) \, , \tag{8.72}$$

which is equal to (8.70). As an annotation, this definition of confidence regions is in fact equal to the standard approach used for fits performed via χ^2-minimization, too. In that case, the argument of the cumulative distribution function of the χ^2-distribution is given by $\Delta\chi^2$, which is the difference of the χ^2 at the considered point in parameter space and its absolute minimum. The main improvement of the Feldman and Cousins method is the

fact, that no assumptions about the asymptotic behaviour of the likelihood ratio is made. Its distribution is rather explicitly determined, which is of special importance regarding small signals and also parameters near physical boundaries.

In summary, regarding a Feldman and Cousins analysis of the CDMS data, it can be assumed that the likelihood ratio as discussed below will be uniformly distributed between 0 and 1, and that the confidence levels will be the same as those obtained with the standard approach, if the statistics are sufficiently high. In the context of the discussion of the profile-likelihood method it was already mentioned (see page 223) that statistics are indeed quite high due to the fact, that the nuclear-recoil cut and in particular the timing cut were omitted for the likelihood analysis. The question might arise, why it should be useful to perform a computationally demanding Feldman and Cousins analysis, as it can be expected that the results will be the same as those of the standard approach. To answer this question it should be kept in mind that it can be expected, that a large number (or even all) of the events in the data sample are due to background. Thus, the statistics are only high because a large number of background events were allowed to enter the data sample. The number of potential WIMP candidates is still extremely small. Therefore, it is unclear, whether approximations, based on the assumption of high statistics, are valid in order to draw conclusions on the parameters of the signal. On the other hand, the Feldman and Cousins approach is designed to treat small signals correctly.

The Feldman and Cousins method based on the Monte Carlo approach is applicable to the CDMS data, which is discussed in some detail for one detector in the remainder of this section. Combination of the detectors to obtain the final results can be performed with techniques previously described in this chapter. So the likelihood function

$$L = L\big(\sigma, m_W, \nu_b\big) \tag{8.73}$$

with the nuisance parameter ν_b is considered. There are three main difficulties regarding the application of the Feldman and Cousins approach.

The first issue is the presence of ν_b. The standard way to deal with this parameter is to consider an ordering principle based on the likelihood ratio

$$R_{\sigma,m_W} = \frac{L\Big(\sigma, m_W, \widehat{\nu}_b(\sigma, m_W)\Big)}{L\Big(\widehat{\sigma}, \widehat{m}_W, \widehat{\nu}_b\Big)}\,. \tag{8.74}$$

The values, which maximize the full three-dimensional likelihood function, have to be used in the denominator. $\widehat{\nu}_b(\sigma, m_W)$ denotes the values of the nuisance parameters, which maximize the likelihood function for the actual data for given σ and m_W. This is identical to the profile-likelihood approach. The values of $\widehat{\nu}_b(\sigma, m_W)$ are kept constant at the given parameter point. Though coverage is not guaranteed for all values of ν_b, which in principle should be the case, previous studies show that this approach is appropriate [124].

The main problem regarding Monte Carlos of this likelihood ratio is the fact that three dimensional distibutions, depending on recoil energy, ionization yield and timing parameter, are used for the background discrimination. Drawing random numbers from

multi-dimensional distributions is extremely time consuming, since in general only brute-force methods (acceptance-rejection method) are applicable. In the given case, however, the dependence of timing and ionization yield is neglected, which allows for a much faster Monte Carlo method, based on the inverse transform method applied to one-dimensional distributions.

To explain this approach in more detail consider, as an example, the derivation of a Monte Carlo generator for a correlated two-dimensional Gaussian distribution function. In general, a two-dimensional distribution $f(x, y)$ can be decomposed as follows:

$$f(x,y) = \frac{f(x,y)}{\int \mathrm{d}x\, f(x,y)} \cdot \int \mathrm{d}x\, f(x,y) = f(x|y) \cdot f(y)\,, \tag{8.75}$$

where the two factors are the probability distribution of x for a given fixed value of y (conditional distribution) and the distribution of y regardless of the value of x (marginal distribution) respectively. Assuming a two-dimensional Gaussian, which can be written as

$$f(x,y) = \frac{1}{2\pi\sigma_x\sigma_y\sqrt{1-\rho^2}} e^{-\frac{1}{2(1-\rho^2)}\left(\left(\frac{x-\mu_x}{\sigma_x}\right)^2 - 2\rho\left(\frac{x-\mu_x}{\sigma_x}\right)\left(\frac{y-\mu_y}{\sigma_y}\right) + \left(\frac{y-\mu_y}{\sigma_y}\right)^2\right)}\,, \tag{8.76}$$

both distributions can easily be derived and are given by one-dimensional Gaussians N:

$$\begin{aligned} f(x|y) &= N\left(\mu_x + \rho\frac{\sigma_x}{\sigma_y}(y-\mu_y), \sigma_x\sqrt{1-\rho^2}\right) \\ f(y) &= N(\mu_y, \sigma_y)\,, \end{aligned} \tag{8.77}$$

where the two arguments denote the mean and standard deviation respectively. The Monte Carlo can now be performed by drawing two random numbers g_x and g_y from $N(0,1)$ and subsequently compute

$$\begin{aligned} Y &= \mu_y + \sigma_y g_y \\ X &= \mu_x + \rho\frac{\sigma_x}{\sigma_y}(Y-\mu_y) + \sigma_x\sqrt{1-\rho^2}g_x = \mu_x + \rho\sigma_x g_y + \sigma_x\sqrt{1-\rho^2}g_x\,. \end{aligned} \tag{8.78}$$

This is an algorithm frequently used for drawing random numbers from a two dimensional correlated Gaussian. In short, it is applicable to draw a random number Y from the marginal distribution $f(y)$ in the first step and to subsequently draw another random number X from the conditional distribution of $f(x|y)$, where the parameter y is fixed at the random number Y generated in the first step.

For the CDMS analysis the signal and background distributions are directly given in a form, which is applicable for the Monte Carlo simulation (see e.g. equation (8.42)).

$$f_{s,b}(t,y,E) = f_{s,b}(t|E) \cdot f_{s,b}(y|E) \cdot f_{s,b}(E)\,. \tag{8.79}$$

Note, that this approach is not valid, if any corrections for a possible dependence of ionization yield and timing parameter are included. The Monte Carlo is performed as follows:

For each considered parameter point (σ, m_W) the number of WIMP events is Poisson fluctuated around ν_s, computed according to (8.49), and the number of background events is drawn from a Poisson distribution with mean $\widehat{\nu}_b(\sigma, m_W)$. Subsequently, values for E, t and y have to be assigned to each event. At first, a value for E is drawn from the corresponding marginal distribution, which in the case of the signal distribution depends on the WIMP mass. Subsequently, a value for t is assigned from the conditional distribution of t, where the parameter E is fixed at the value assigned in the previous step. The last step is repeated in a similar way for the parameter y. This Monte Carlo method has already been tested successfully, and the computation speed was found to be excellent.

The third difficulty, which should only be mentioned shortly, is also related to the computation speed. Assume, that a grid of only 100×100 points is considered in the cross-section versus WIMP-mass plane. In order to have sufficient statistics for a proper determination of the distributions of the likelihood ratios it is necessary to perform at least 10000 Monte Carlo experiments at each point. This means that 10^9 maximizations of the likelihood function have to be performed. Due to the complexity of the likelihood function this requires significant resources.

Finally, the distributions $g(R_{\sigma,m_W})$ of R_{σ,m_W} will be known for each parameter point with an accuracy given by the number of Monte Carlo experiments and by uncertainties from the determination of the signal and background distributions. As before, the confidence levels for given σ and m_W are given by the fractions of this distribution, which are larger than the likelihood ratio computed based on the actual data. From equation (8.55) it can be seen that it is given by $1-C(\sigma, m_W)$ where C is the confidence interval calculated according to the standard method.

Even though the Feldman and Cousins approach cannot be expected to yield perfect coverage, which is due to the occurrence of nuisance parameters, it can be assumed that it shows a better performance than the previous two discussed methods. Thus, a direct comparison is desirable. However, as shown in this section, its application is quite demanding, particularly regarding the required computation speed.

Chapter 9

Conclusion

Even though there are numerous hints for dark matter, it has not been measured directly yet. However, its detection and the subsequent determination of its properties are of utmost importance regarding the question what the universe is made of. There are several ways to approach the dark matter issue. In this thesis, the search for WIMPs, which scatter off the target nuclei in a dedicated detector, was discussed in great detail.

At first, the general formalism regarding the direct detection of dark matter was presented. In particular, deviations from the "standard" WIMP scenario, which is based on the assumption that the WIMPs in the Milky Way's dark halo obey a truncated Maxwell-Boltzmann velocity distribution, were considered. Unless the minimum velocity was extremely high, so that only WIMPs in the high-velocity tail of the distribution were capable of scattering off the target nuclei, it was shown that an analysis, based on velocity distributions obtained from dark matter simulations, yielded very similar results as an analysis based on the simple truncated Maxwell-Boltzmann distribution. Thus, usage of the latter seems adequate.

Moreover, the implications of inelastic scattering, where the dark matter particles scatter off the target nuclei by transition into an excited state was discussed. In this framework, the expected rate peaks at tens of keV recoil energy, while the recoil spectrum is nearly exponential assuming elastic scattering. This model was applied to investigate the annual modulation observed by the DAMA collaboration and to determine regions in parameter space, which are in agreement with their observation.

Subsequently, a particular WIMP model, based on the assumption that additional flat compactified space dimensions exist, was investigated. It was shown that constraints from direct detection experiments, collider studies and cosmology (relic density studies) are highly complementary, and that combining them substantially diminishes the relevant parameter space. This emphasizes the necessity to approach the problem of the missing mass from different directions. It was discussed that the expected sensitivity of the next-generation direct detection experiments is sufficient to cover the whole parameter space for the Kaluza-Klein photon γ_1, which is the most natural WIMP candidate in this extension of the standard particle physics model.

After these rather general considerations, the CDMS experiment was discussed in great

detail. The main focus was on background rejection, which is the main issue for experiments like CDMS searching for extremely rare signals. Two techniques, based on "cuts" and a maximum-likelihood approach, which can be used to discriminate against the dominant background, surface electron recoil events, were presented.

The first one was used for the "standard" WIMP-search and a dedicated analysis considering inelastic scattering. Both analyses gave rise to events passing all selection criteria, however, their numbers, two and three (in the region of interest) respectively, were too low to interpret these results as statistically significant detections of dark matter: Based on the background estimates, the probabilities to have more than the observed events in the signal regions were 23% and 11% respectively. Thus, upper limits were computed in both cases. The constraints from the "standard" analysis were the world-leading upper limits on the spin-independent WIMP-nucleon cross section for WIMP masses above $\sim$44 GeV/c^2 at the time, when the results were published. Limits from this analysis were also used to constrain an inelastic dark matter interpretation of the DAMA claim. Only the ZEPLIN collaboration set more stringent limits on this scenario at that time. The constraints emerging from the dedicated inelastic dark matter analysis were slightly weaker than those from the "standard" analysis due to the occurrence of the three WIMP candidates at recoil energies, where a signal would be expected.

Finally, a likelihood-based analysis of the CDMS data was presented. The performance of this approach seems very promising. However, the shown results are only very preliminary as the charge pulses of the used events have to be refitted with an algorithm based on a proper χ^2-minimization algorithm. Thus, currently, conclusions regarding low WIMP masses, which heavily depend on events at low recoil energies $\lesssim$10 keV, are not reliable. Application of the developed algorithm to the reprocessed data will be performed in the very near future.

Given that the CoGeNT collaboration recently claimed a hint for dark matter at low WIMP masses near the DAMA allowed region (assuming elastic scattering), and the XENON100 collaboration heralded the era of the direct detection experiments, which are capable of probing spin-independent cross sections beyond the zeptobarn (10^{-9} pb) benchmark, it is obvious that exciting times lie ahead for the dark matter community.

Acknowledgment

First of all, I would like to thank my advisor Laura Baudis for giving me the opportunity to work on an exciting experiment like CDMS. I greatly benefitted from her knowledge of dark matter and astrophysics in general. I appreciate her encouragement and advise particularly regarding new ideas like the developed likelihood analysis. It was a pleasure to be part of her research group.

I want to thank the whole CDMS collaboration. Apart from the pure science, I can say that I enjoyed the atmosphere in the team, and it has been a great time working with you. In the following I would like to mention some members of the collaboration whom I owe a special debt of gratitude. I learned a great deal about cryogenics from Angela Reisetter, Cathy Bailey, Jodi Cooley, Kyle Sundqvist and Darren Grant while I was on shift at Soudan. Regarding these shifts, I am also particularly grateful to Dan Bauer for his advice and Jim Beaty for always being more than helpful. Thanks for "fixing" my car by the way. Besides, a lot of people supported me by performing quality checks for the WIMP candidates from the inelastic dark matter analysis: Matt Fritts, Oleg Kamaev, Scott Hertel, Dave Moore, Tobias Bruch and Lauren Hsu. Extra thanks go to Matt Fritts for determining the radiogenic neutron background. Moreover, I enjoyed advice and suggestions regarding data analysis in general from Richard Schnee, Bernard Sadoulet, Jeff Filippini, Jonghee Yoo and particularly from Steven Yellin. I learned a lot from all of you.

I am indebted to Larry Widrow for providing me with some samples from the GHalo simulation and for many fruitful discussions.

I enjoyed working on the UED project with Konstantin Matchev, Kyoungchul Kong and Jonghee Yoo. Thanks for the insights into particle physics beyond the standard model.

Many thanks to Laura's whole Zürich group, previous and current members: Tobias Bruch, Alfredo Davide Ferella, Aaron Manalaysay, Teresa Marrodan Undagoitia, Marc Schumann, Ali Askin, Annika Behrens, Francis Froborg, Alexander Kish, Michal Tarka, Manuel Walter, Christopher Geis, Marijke Haffke, Eirini Tziaferi, Manuel Walter and Roberto Santorelli. I am particularly indebted to Tobias Bruch for many discussions on the CDMS analysis and proof-reading of this thesis. I really learned a lot from you.

On a more personal level, I want to thank my two best friends from home, Mike Rummler and Amir Movahed Nia, and my family. Many thanks to my mother Silvia Arrenberg for her support and encouragement. Thanks to Ssico for being there. I am also indebted to my "new" family from Korea: Bonghak Kim, Yeon Ok Jeon, Jiyeon Kim, Morea Kim and Eunwoo Jeong. Last but not least, to my lovely wife Jihye Kim: Without you I could not have made it this far and together with you the future looks bright.

Bibliography

[1] J. D. Lewin and P. F. Smith, Astropart. Phys. **6**, 87 (1996).

[2] S. Arrenberg, L. Baudis, K. Kong, K. T. Matchev and J. Yoo, Phys. Rev. D **78**, 056002 (2008).

[3] Z. Ahmed *et al.*, Science **327**, 1619 (2010).

[4] Z. Ahmed *et al.*, Phys. Rev. D **83**, 112002 (2011).

[5] Z. Ahmed *et al.*, Phys. Rev. Lett. **103**, 141802 (2009).

[6] T. Bruch, PhD thesis, University of Zürich (2010).

[7] I. Zlatev, L. Wang and P. J. Steinhardt, Phys. Rev. Lett. **82**, 896 (1999).

[8] http://map.gsfc.nasa.gov

[9] G. Bertone, D. Hooper and J. Silk, Phys. Rept. **405**, 279 (2005).

[10] G. Jungman, M. Kamionkowski and K. Griest, Phys. Rept. **267**, 195 (1996).

[11] D. Hooper and S. Profumo, Phys. Rept. **453**, 29 (2007).

[12] K. G. Begeman, A. H. Broeils and R. H. Sanders, Mon. Not. Roy. Astron. Soc. **249**, 523 (1991).

[13] D. Clowe *et al.*, Astrophys. J. **648**, 109 (2006).

[14] R. Narayan and M. Bartelmann, arXiv:astro-ph/9606001 (1997).

[15] M. R. Nolta *et al.*, Astrophys. J. Suppl. **180**, 296 (2009).

[16] J. J. Binney and S. Tremaine, Galactic Dynamics, Princeton University Press, Second Ed. (2008).

[17] W. Dehnen and J. J. Binney, Mon. Not. Roy. Astron. Soc. **298**, 387 (1998).

[18] M. C. Smith *et al.*, Mon. Not. Roy. Astron. Soc. **379**, 755 (2007).

[19] J. D. Vergados and D. Owen, Phys. Rev. D **75**, 043503 (2007).

[20] A. S. Eddington, Mon. Not. Roy. Astron. Soc. **76**, 572 (1916).

[21] J. Stadel *et al.*, Mon. Not. Roy. Astron. Soc. **398**, 21 (2009).

[22] M. Vogelsberger *et al.*, Mon. Not. Roy. Astron. Soc. **395**, 797 (2009).

[23] M. Kuhlen *et al.*, J. Cosmol. Astropart. Phys. **02**, 030 (2010).

[24] A. Klypin, S. Gottlöber, A. V. Kravtsov and A. M. Khokhlov, Astrophys. J. **516**, 530 (1999).

[25] D. Smith and N. Weiner, Phys. Rev. D **64**, 043502 (2001).

[26] M. Weber and W. d. Boer, Astron. and Astrophys. **509**, A25 (2010).

[27] A. Kurylov and M. Kamionkowski, Phys. Rev. D **69**, 063503 (2004).

[28] R. H. Helm, Phys. Rev. **104**, 1466 (1956).

[29] G. Fricke *et al.*, At. Data Nucl. Data Tables **60**, 177 (1995).

[30] G. Dũda, A. Kemper and P. Gondolo, J. Cosmol. Astropart. Phys. **04**, 012 (2007).

[31] H. de Vries *et al.*, At. Data Nucl. Data Tables **36**, 495 (1987).

[32] D. R. Tovey *et al.*, Phys. Lett. B **488**, 17 (2000).

[33] J. Engel, S. Pittel and P. Vogel, Int. J. Mod. Phys. E **1**, 1 (1992).

[34] V. I. Dimitrov, J. Engel and S. Pittel, Phys. Rev. D **51**, 291 (1995).

[35] M. T. Ressel and D. J. Dean, Phys. Rev. C **56**, 535 (1997).

[36] C. Savage, P. Gondolo and K. Freese, Phys. Rev. D **70**, 123513 (2004).

[37] A. K. Drukier, K. Freese and D. N. Spergel, Phys. Rev. D **33**, 3495 (1986).

[38] P. Gondolo and G. Gelmini, Phys. Rev. D **71**, 123520 (2005).

[39] R. Bernabei *et al.*, Phys. Lett. B **480**, 23 (2000).

[40] R. Bernabei *et al.*, Eur. Phys. J. C **56**, 333 (2008).

[41] R. Bernabei *et al.*, Eur. Phys. J. C **67**, 39 (2010).

[42] E. Aprile *et al.*, Phys. Rev. Lett. **105**, 131302 (2010).

[43] J. Angle *et al.*, Phys. Rev. Lett. **101**, 091301 (2008).

[44] E. Behnke *et al.*, Science **319**, 933 (2008).

[45] H. S. Lee *et al.*, Phys. Rev. Lett. **99**, 091301 (2007).

[46] V. N. Lebedenko *et al.*, Phys. Rev. D **80**, 052010 (2009).

[47] C. Savage, G. Gelmini, P. Gondolo and K. Freese, J. Cosmol. Astropart. Phys. **04**, 010 (2009).

[48] M. Maltoni and T. Schwetz, Phys. Rev. D **68**, 033020 (2003).

[49] R. Bernabei *et al.*, Phys. Lett. B **389**, 757 (1996).

[50] R. Bernabei *et al.*, Nucl. Instrum. Meth. A **592**, 297 (2008).

[51] R. Bernabei *et al.*, INFN-AE-98-23 (1998).

[52] K. S. Hoberg and M. W. Winkler, J. Cosmol. Astropart. Phys. **09**, 010 (2009).

[53] R. Bernabei *et al.*, Eur. Phys. J. C **53**, 205 (2008).

[54] N. Bozorgnia, G. B. Gelmini and P. Gondolo, J. Cosmol. Astropart. Phys. **11**, 019 (2010).

[55] T. Kaluza, Preuss. Akad. Wiss., Phys. Math. Kl. 966, (1921).

[56] O. Klein, Z. Phys. **37**, 895, (1926).

[57] G. D. Kribs, arXiv:hep-ph/0605325 (2006).

[58] J. R. Ellis, A. Ferstl and K. A. Olive, Phys. Lett. B **481**, 304 (2000).

[59] H. C. Cheng, J. L. Feng and K. T. Matchev, Phys. Rev. Lett. **89**, 211301 (2002).

[60] B. A. Dobrescu, D. Hooper, K. Kong and R. Mahbubani, J. Cosmol. Astropart. Phys. **10**, 012 (2007)

[61] Z. Ahmed *et al.*, Phys. Rev. Lett. **102**, 011301 (2009).

[62] J. Angle *et al.*, Phys. Rev. Lett. **100**, 021303 (2008).

[63] R. W. Schnee *et al.*, arXiv:astro-ph/0502435 (2005).

[64] E. Aprile *et al.*, arXiv:1107.2155 (2011).

[65] G. K. Mallot, Int. J. Mod. Phys. A **15S1**, 521 (2000).

[66] F. Burnell and G. D. Kribs, Phys. Rev. D **73**, 015001 (2006).

[67] K. Kong and K. T. Matchev, J. High Energy Phys. **01**, 038 (2006).

[68] H. C. Cheng, K. T. Matchev and M. Schmaltz, Phys. Rev. D **66**, 056006 (2002).

[69] A. Datta, K. Kong and K. T. Matchev, Phys. Rev. D **72**, 096006 (2005); **72**, 119901(E) (2005).

[70] S. P. Martin, Phys. Rev. D **75**, 115005 (2007).

[71] H. Baer, A. Box, E. K. Park and X. Tata, J. High Energy Phys. **08**, 060 (2007).

[72] J. Dunkley *et al.*, Astrophys. J. Suppl. **180**, 306 (2009).

[73] I. Gogoladze and C. Macesanu, Phys. Rev. D **74**, 093012 (2006).

[74] T. Appelquist and H. U. Yee, Phys. Rev. D **67**, 055002 (2003).

[75] V. Mandic, PhD thesis, University of California, Berkeley (2004).

[76] R. W. Ogburn, PhD thesis, Stanford University (2008).

[77] J. P. Filippini, PhD thesis, University of California, Berkeley (2008).

[78] I. Ambats *et al.*, NUMI-L-337 (1998).

[79] C. E. Aalseth *et al.*, Phys. Rev. Lett. **106**, 131301 (2011).

[80] D. Abrams *et al.*, Phys. Rev. D **66**, 122003 (2002).

[81] T. Shutt *et al.*, Phys. Rev. Lett. **69**, 3531 (1992).

[82] B. S. Neganov and V. N. Trofimov, Otkryt. Izobret. **146**, 215 (1985).

[83] P. N. Luke, J. Appl. Phys. **64**, 6858 (1988).

[84] H. J. Maris and S. Tamura, Phys. Rev. B **47**, 727 (1993).

[85] H. J. Maris, J. Low Temp. Phys. **93**, 355 (1993).

[86] K. D. Irwin, Appl. Phys. Lett. **66**, 1998 (1995).

[87] R. J. Gaitskell *et al.*, Nucl. Phys. B (Proc. Suppl.) **51**, 279 (1996).

[88] V. Mandic, B. Sadoulet and R. W. Schnee, Nucl. Instrum. Meth. A **553**, 459 (2005).

[89] M. C. Fritts, PhD thesis, University of Minnesota (2011).

[90] R. Hennings-Yeomans, PhD thesis, Case Western Reserve University (2009).

[91] V. A. Kudryavtsev, Comp. Phys. Comm. **180**, 339 (2009).

[92] S. Agostinelli *et al.*, Nucl. Instrum. Meth. A **506**, 250 (2003).

[93] J. Allison *et al.*, IEEE Trans. Nucl. Sci. **53**, 270 (2006).

[94] A. Fasso, A. Ferrari, J. Ranft and P. R. Sala, Report No. CERN-2005-010 (2005).

[95] G. Battistoni *et al.*, AIP Conf. Proc. **896**, 31 (2007).

[96] M. Tarka, Diploma thesis, RWTH Aachen (2007).

[97] X. Qiu, PhD thesis, University of Minnesota (2009).

[98] J. Lindhard *et al.*, K. Dan. Vidensk. Selsk. Mat. Fys. Medd. **33**, 10 (1963).

[99] T. Shutt *et al.*, Nucl. Instrum. Meth. A **444**, 340 (2000).

[100] S. Yellin, Phys. Rev. D **66**, 032005 (2002).

[101] E. Aprile *et al.*, Phys. Rev. C **79**, 045807 (2009).

[102] E. Armengaud *et al.*, Phys. Lett. B **687**, 294 (2010).

[103] E. Aprile *et al.*, Phys. Rev. Lett. **107**, 131302 (2011).

[104] J. Ellis *et al.*, Phys. Rev. D **71**, 095007 (2005).

[105] L. Roszkowski *et al.*, J. High Energy Phys. **07**, 075 (2007).

[106] V. N. Lebedenko *et al.*, Phys. Rev. Lett. **103**, 151302 (2009).

[107] J. Angle *et al.*, Phys. Rev. D **80**, 115005 (2009).

[108] J. I. Collar *et al.*, arXiv:1005.0838 (2010); arXiv:1005.3723 (2010); arXiv:1006.2031 (2010); arXiv:1010.5187 (2010); arXiv:1106.0653 (2011).

[109] A. Manzur *et al.*, Phys. Rev. C **81**, 025808 (2010).

[110] E. Aprile *et al.*, Phys. Rev. D **84**, 061101 (2011).

[111] M. Greenwood, Rep. Pub. Health Med. Sub. **33**, 1 (1926).

[112] D. Yu. Akimov *et al.*, Phys. Lett. B **692**, 180 (2010).

[113] J. March-Russell, C. McCabe and M. McCullough, J. High Energy Phys. **05**, 071 (2009).

[114] M. J. Reid *et al.*, Astrophys. J. **700**, 137 (2009).

[115] M. Lisanti, L. E. Strigari, J. G. Wacker and R. H. Wechsler, Phys. Rev. D **83**, 023519 (2011).

[116] E. Aprile *et al.*, Phys. Rev. D **84**, 052003 (2011).

[117] J. Kopp, T. Schwetz and J. Zupan, J. Cosmol. Astropart. Phys. **02**, 014 (2010).

[118] A. Bottino, F. Donato, N. Fornengo and S. Scopel, Phys. Rev. D **81**, 107302 (2010).

[119] W. Härdle, M. Müller, S. Sperlich and A. Werwatz, Nonparametric and semiparametric models, Springer, 1 edition (2004).

[120] W. Härdle, Smoothing Techniques, Springer, 1 edition (1990).

[121] S. R. Sain, PhD thesis, Rice University (1994).

[122] A. Lakhany and H. Mausser, Algo Research Quarterly **3**, 47 (2000).

[123] G. J. Feldman and R. D. Cousins, Phys. Rev. D **57**, 3873 (1998).

[124] Proceedings of talk by G. J. Feldman, PHYSTAT 05, Statistical problems in Particle Physics, Astrophysics and Cosmology, Oxford, UK, September 15, 2005.